

Development and Validation of Efficient Multifluid and Population Balance Models for Dispersed Gas-Liquid Processes

Vom Fachbereich Maschinenbau und Verfahrenstechnik
der Rheinland-Pfälzischen Technischen Universität Kaiserslautern-Landau
zur Erlangung des akademischen Grades

Doktor-Ingenieur (Dr.-Ing.)

genehmigte

Dissertation

vorgelegt von

M.Sc. Ferdinand Breit

aus Kaiserslautern

Dekan: Prof. Dr. rer. nat. Roland Ulber

Prüfungskommission:

Prüfungsvorsitzender: Jun. Prof. Dr.-Ing. Dr. rer. nat. Simon Stephan

1. Berichterstatter: Prof. Dr.-Ing. Erik von Harbou

2. Berichterstatter: Prof. Dr.-Ing. Hugo Atle Jakobsen

Tag der mündlichen Prüfung: 15.11.2024

Kaiserslautern 2024

D386

Abstract

Reactive multiphase systems, in which at least one phase is dispersed, are ubiquitous in chemical and biotechnological processes. The complexity of these systems, involving multiple interacting phases and a wide range of process conditions, presents significant challenges to experimental analysis alone. Consequently, there is a need for reliable and computationally efficient models to predict system behavior, optimize reactor design, and facilitate process scale-up from laboratory to production scale. This thesis develops and validates novel models for three reactor types: jet loop reactors (JLRs), bubble columns (BCs), and stirred tank reactors (STRs). For JLRs, a one-dimensional momentum balance model was developed that allows local resolution of key process variables. This model revealed significant effects of gas consumption on internal circulation and reactor performance. For BCs, a one-dimensional multifluid population balance model (MPB) was developed. The model accurately predicts gas holdup and the bubble size distribution using a one-point calibration. The prediction performance was evaluated on the basis of new experimental data encompassing the variation of gas and liquid fluxes, design of gas sparger, liquid holdup and liquid composition. However, limitations are apparent at higher gas and liquid fluxes. The thesis also addresses converting a number-based population balance equation (PBE) to a mass-based PBE, introducing a mass transfer term that enhances the understanding of the conservation properties of the PBE. Finally, the MPB was applied to a non-reactive semi-batch STR. A newly proposed finite volume method with Gauss quadrature (FVMG) was found to be fast, robust, and accurate compared to other numerical methods. In a parameter and sensitivity study, most trends from the literature could be confirmed. Preliminary experimental validation showed good agreement with simulation results, although further work is needed to generalize the model. The models developed offer computationally efficient tools for extensive parameter studies, enhancing the understanding of dispersed multiphase reactive processes, essential for reactor design and optimization.

Kurzfassung

Reaktive Mehrphasensysteme, bei denen mindestens eine Phase dispergiert ist, sind in chemischen und biotechnologischen Prozessen weit verbreitet. Die Komplexität dieser Systeme, die mehrere interagierende Phasen und eine Vielzahl von Prozessbedingungen umfasst, stellt eine große Herausforderung für die experimentelle Analyse dar. Daher besteht ein Bedarf an zuverlässigen und rechnerisch effizienten Modellen, um das Systemverhalten vorherzusagen, die Reaktorkonstruktion zu optimieren und die Prozessskalierung vom Labor- auf den Produktionsmaßstab zu erleichtern. In dieser Arbeit werden solche Modelle für drei Reaktortypen entwickelt und validiert: Strahlschlaufenreaktoren (JLRs), Blasensäulen (BCs) und Rührkesselreaktoren (STRs). Für JLRs wurde ein eindimensionales Impulsbilanzmodell entwickelt, das eine lokale Auflösung der wichtigsten Prozessvariablen ermöglicht. Dieses Modell zeigte signifikante Auswirkungen einer gasverbrauchenden Reaktion auf die interne Zirkulation und die Reaktorleistung. Für Blasensäulen wurde ein eindimensionales Multifluid-Populationsbilanzmodell (MPB) entwickelt. Das Modell ermöglicht eine effektive und genaue Vorhersage des Gasanteils und der Blasengrößenverteilung mithilfe einer Ein-Punkt-Kalibrierung. Die Vorhersagekraft wurde anhand neuer experimenteller Daten bewertet, die die Variation von Gas- und Flüssigkeitsströmen, des Designs des Gasverteilers, des Flüssigkeitsanteils und der Flüssigkeitszusammensetzung umfassten. Allerdings zeigen sich Einschränkungen bei höheren Gas- und Flüssigkeitsströmen. Darüber hinaus befasst sich diese Arbeit mit der Transformation einer anzahlbasierten Populationsbilanzgleichung (PBE) in eine massenbasierte PBE, wobei ein Massentransfer-Term eingeführt wurde, der das Verständnis der Erhaltungseigenschaften der PBE verbessert. Schließlich wurde das MPB auf einen nicht-reaktiven semi-batch STR angewendet. Eine neu vorgeschlagene Finite Volumen Methode mit Gauss-Quadratur (FVMG) erwies sich im Vergleich zu anderen numerischen Methoden als schnell, robust und genau. In einer Parameter- und Sensitivitätsstudie konnten die meisten Trends aus der Literatur bestätigt werden. Eine vorläufige experimentelle Validierung zeigte eine gute Übereinstimmung mit den Simulationsergebnissen, obwohl weitere Arbeiten erforderlich sind, um das Modell zu verallgemeinern. Die entwickelten Modelle bieten rechnerisch effiziente Werkzeuge für umfangreiche Parameterstudien und verbessern das Verständnis von dispergierten mehrphasigen reaktiven Prozessen, welches für die Reaktorkonstruktion und -optimierung unerlässlich ist.

Contents

| | |
|---|------------|
| Abstract | I |
| Kurzfassung | III |
| 1. Introduction | 1 |
| 2. Jet Loop Reactor | 7 |
| Abstract | 7 |
| 2.1. Introduction | 8 |
| 2.2. The Principle of the Jet Loop Reactor | 9 |
| 2.3. Modelling and Simulation | 11 |
| 2.3.1. Governing Equations | 11 |
| 2.3.2. Compartment Model of the Jet Loop Reactor | 13 |
| 2.3.3. Implementation and Simulation | 14 |
| 2.4. Simulation Results | 18 |
| 2.4.1. Variation of Process Parameter | 18 |
| 2.4.2. Variation of Design Parameter | 20 |
| 2.4.3. Influence of Process and Design Parameters | 24 |
| 2.5. Conclusion and Outlook | 26 |
| 3. Bubble Column Study I | 29 |
| Abstract | 29 |
| 3.1. Introduction | 30 |
| 3.2. Experimental Setup | 32 |
| 3.3. Modeling and Simulation | 34 |
| 3.3.1. Governing Equations | 34 |
| 3.3.2. Method of Solution | 35 |
| 3.3.3. Regression Model | 35 |
| 3.4. Results and Discussion | 38 |
| 3.4.1. Evaluation of the Calibration Methods | 38 |
| 3.4.2. Investigation of Prediction Performance | 41 |
| 3.4.3. Scenario Test | 47 |
| 3.5. Conclusion and Outlook | 50 |
| 4. Bubble Column Study II | 51 |
| Abstract | 51 |
| 4.1. Introduction | 53 |

| | |
|---|------------|
| 4.2. Materials and Methods | 55 |
| 4.2.1. Experimental Setup and Procedure | 55 |
| 4.2.2. Measurement Techniques | 56 |
| 4.2.3. Overview of Experiments | 58 |
| 4.3. Modelling and Simulation | 59 |
| 4.3.1. Multifluid Population Balance Model | 59 |
| 4.3.2. Sparger Model | 60 |
| 4.3.3. Error Measure | 61 |
| 4.4. Results and Discussion | 62 |
| 4.4.1. Semi-Batch Mode – Gas Flux and Sparger Study | 62 |
| 4.4.2. Continuous Mode – Gas and Liquid Flux Study | 67 |
| 4.5. Conclusion and Outlook | 70 |
| 5. Insights Into PBE Modelling | 73 |
| Abstract | 73 |
| 5.1. Introduction | 74 |
| 5.2. The Number-Based Population Balance Equation | 75 |
| 5.3. Transformation from Number-Based to Mass-Based PBE | 77 |
| 5.4. Discussion | 80 |
| 5.4.1. Extra Mass Transfer Term | 80 |
| 5.4.2. Mass-based Breakage and Coalescence Sources and Sinks | 82 |
| 5.4.3. Nondimensionalization of the PBE | 83 |
| 5.5. Conclusion and Outlook | 86 |
| 6. Stirred Tank Reactor | 87 |
| Abstract | 87 |
| 6.1. Introduction | 88 |
| 6.2. Experimental Setup | 90 |
| 6.3. Modelling and Simulation | 92 |
| 6.3.1. System Description and Assumptions | 92 |
| 6.3.2. Governing Equations | 93 |
| 6.3.3. Constitutive Equations | 94 |
| 6.3.4. Methods of Solution | 95 |
| 6.3.5. Implementation Details and Tools | 96 |
| 6.3.6. Analytical Solutions and Error Measure | 96 |
| 6.3.7. Definition of Sensitivity and Parameter Studies | 97 |
| 6.3.8. Preliminary Application to Measured BSD and Parameter Estimation | 98 |
| 6.4. Results and Discussion | 99 |
| 6.4.1. Comparison of the Numerical Solution Methods | 99 |
| 6.4.2. Sensitivity and Parameter Analysis | 102 |
| 6.4.3. Model Demonstration: Application to Experimental Data | 106 |
| 6.5. Conclusion and Outlook | 107 |
| 7. Conclusion and Outlook | 109 |

| | |
|---|------------|
| Nomenclature | 113 |
| References | 136 |
| A. Supplementary Information for Chapter 2 | 137 |
| A.1. Parameter Applied in the Simulation Studies | 137 |
| A.1.1. Constant Parameters | 137 |
| A.1.2. Parameters Study I | 137 |
| A.1.3. Parameters Study II | 138 |
| A.1.4. Parameters Study III | 138 |
| A.2. Modeling Details | 140 |
| A.2.1. Pressure Loss Coefficient | 140 |
| A.2.2. Ideal Reactor Models | 141 |
| A.2.3. Inlet Conditions Draft Tube | 141 |
| A.2.4. Damköhler Number | 142 |
| A.2.5. Residence Behavior | 142 |
| A.3. Additional Figures | 144 |
| A.4. Implementation Details | 148 |
| B. Supplementary Information for Chapter 3 | 149 |
| B.1. Overview Experimental Data | 149 |
| B.2. Constitutive and Additional Equations | 150 |
| B.3. Additional Equations | 154 |
| B.3.1. Moments | 154 |
| B.3.2. Normalization | 154 |
| B.3.3. Interfacial Area Density | 154 |
| B.4. Additional Figures | 155 |
| C. Supplementary Information for Chapter 4 | 157 |
| C.1. Additional Equations | 157 |
| C.1.1. Transformation of Mass to Number Based Density Function | 157 |
| C.1.2. Moments | 157 |
| C.1.3. Normalization | 158 |
| C.1.4. Local Gas Volume Fraction | 158 |
| C.2. Sparger Model | 159 |
| C.3. Applied Parameters in the Simulations | 161 |
| C.4. Detail about the Experimental Setup | 163 |
| C.5. Additional Figures | 165 |
| D. Supplementary Information for Chapter 5 | 169 |
| D.1. Derivation of a Generalized Transport Equation in \mathbb{R}^N | 169 |
| D.1.1. Mathematical Preamble | 169 |
| D.1.2. Model Development | 170 |
| D.1.3. Initial and Boundary Conditions | 171 |
| D.2. Derivation of Growth Velocity | 173 |

| | |
|--|----------------|
| E. Supplementary Information for Chapter 6 | 175 |
| E.1. Additional Studies | 175 |
| E.1.1. Variation of Physiochemical Properties | 175 |
| E.1.2. Design of the Gas Sparger | 177 |
| E.2. Model Details | 179 |
| E.2.1. Constitutive Equations | 179 |
| E.2.2. Additional Equations | 180 |
| E.2.3. Applied Parameters in the Simulations | 181 |
| E.3. Model Derivations | 183 |
| E.3.1. Derivation of the Outlet Mass Flow Rate | 183 |
| E.3.2. Simplification of the Generalized PBE to STR Application | 184 |
| E.3.3. Conversion Rules for Comparison Experiment and Simulation | 185 |
| E.4. Finite Volume Method with Gauss Quadrature – FVMG | 186 |
| E.4.1. Grid points | 186 |
| E.4.2. Convection | 186 |
| E.4.3. Interpolation | 187 |
| E.4.4. Gauss Quadrature | 188 |
| E.5. Used Packages and Version | 189 |
| E.6. Geometric Dimension of STR Used in the Experiments | 190 |
| E.7. Additional Figures | 191 |
| Detailed Contributor Roles Taxonomy | 193 |
| Publication List | 195 |
| Journal Articles | 195 |
| Lectures and Speeches | 195 |
| Conference Posters | 196 |
| Data Sets | 196 |
| Supervised Student Theses | 197 |
| Curriculum Vitae | 199 |

1. Introduction

Many industrially important syntheses involve reactive multiphase systems [1, 2]. Examples include homogeneously or heterogeneously catalyzed oxidation, hydrogenation, carboxylation, or hydroformylation reactions. To scale up these processes from laboratory to production scale and to design the required reactor vessels, the engineer needs insight into the influence of process conditions (e.g. temperature, pressure, power input), system properties (e.g. reaction rate, gas solubility) and reactor geometry (e.g. vessel height and diameter, geometry of internals) on the behavior of the multiphase process (e.g. space-time yield achieved). In many cases, these insights into the complex interactions cannot be obtained by experiments alone, mostly because of the large number of parameter combinations and the difference in scale between laboratory and production (e.g. ratio of shell area to volume, ratio of bubble size to reactor diameter). Therefore, models are needed that can reliably describe these interactions over a wide range of parameters. The engineer can use these models to find the optimal reactor design for a given synthesis task or to predict the behavior of a given reactor under varying process conditions.

Many complex interactions of different processes and properties, as shown in Fig. 1.1, can be relevant to the general behavior of dispersed reactive multiphase systems and must be considered in the model.

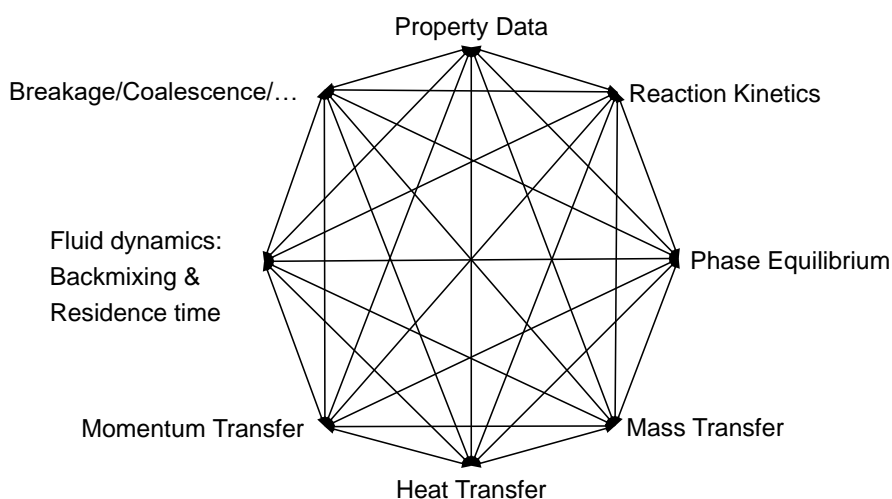


Figure 1.1.: Illustration of reactive multiphase flow interactions. Adapted from [3].

In principle, all the processes and properties shown in the Fig. 1.1 are well understood and can be described by models. Multiphase computational fluid dynamics (CFD) methods exist that combine these models. Thus, CFD methods can potentially provide the required detailed

insight into the complex behavior of reactive multiphase processes [4, 5]. However, their computational and time requirements are still high [6, 7]. Consequently, comprehensive studies of process and design parameters are often impractical when employing these methods. Such studies are frequently required by engineers in the initial stages of process development. Moreover, predicting the exact behavior of the apparatus with high temporal and spatial resolution is often not the primary interest of the engineer. Instead, the general trends of the interaction between system properties, process conditions, and reactor geometry must be represented. Thereby identifying unfavorable operating windows or reactor designs, or to supporting the interpretation of real production processes observations. Therefore, engineers often use a variety of correlations from the literature to describe the influence of the property data, geometry and process conditions on the behavior of the process (e.g. mass and heat transfer, gas holdup) and to design reactors. The disadvantage of these correlations is that, for simplicity, they are often strongly empirical in nature and contain little physical knowledge. Thus, they can often only be used to describe the behavior of the reactor within the range of conditions for which reliable experimental data exist, and not to extrapolate to new conditions. The enormous variation in the composition of the gas and liquid phases alone makes it almost impossible to predict the behavior of an unstudied chemical system on the basis of these correlations. It is therefore necessary to develop a modelling approach that takes into account the interactions of the different processes occurring in multiphase systems. This approach should be capable of reliably describing the general behaviour of such systems, while also being computationally inexpensive, thus enabling large-scale parameter studies.

This thesis presents the development, application and validation of such reliable and efficient modelling approaches to three different reactor types: jet loop reactors, bubble columns and stirred tank reactors (see Fig. 1.2).

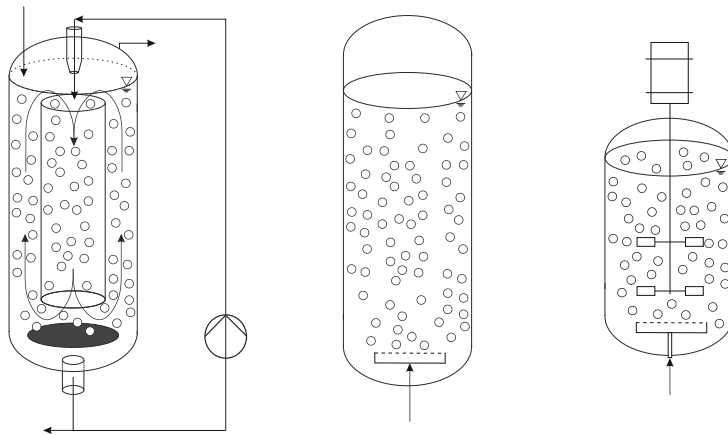


Figure 1.2.: Studied reactor types. From left to right: jet loop reactor, bubble column, stirred tank reactor.

The first reactor examined in this thesis is the jet loop reactor (JLR) in Chapter 2. JLRs are multiphase reactors commonly used in chemical, biological, and environmental processes [8]. The JLR operates with a continuous liquid phase and, depending on the process, with one or more dispersed phases, e.g. gas bubbles and/or solid particles. It is therefore used for heterogeneous or homogeneous catalyzed gas-liquid reactions (e.g. hydrogenation or hydroformylation

reactions [9]) or for multiphase biotechnological processes (e.g. wastewater treatment with bacteria [9, 10]). They exhibit complex fluid dynamics with an internal circulation between a draft tube and the resulting annulus driven by a jet (see Fig. 1.2). This internal circulation determines the concentration profile of the chemical species in the reactor via the degree of backmixing and the stability of the loop. In order to describe this internal circulation, Bey *et al.* [11] developed a model based on an integral balance of momentum for the draft tube and the annular gap. This model makes it possible to analyze the influence of a gas-consuming reaction on the internal circulation and the performance (yield, turnover) of the reactor. However, this model has the disadvantage that the integral consideration is a strong simplification, especially when large local variations of the gas consumption rate occur. Furthermore, the model can only be applied to simple isothermal reactions for which an analytical solution of the local conversion rates exists.

Therefore, an extension of the model of Bey *et al.* [11] is presented in Chapter 2. Instead of an integral, a one-dimensional differential momentum balance is used to describe the internal circulation flow in JLRs. The model allows locally resolved calculation of the volume fraction of the phases, the pressure, the concentration of the species and the velocity of the phases in the JLR. A detailed parameter and sensitivity study of process and design parameters was performed. The influence of gas consumption, power input by the jet and reactor geometry on the internal circulation was investigated and optimized. It has been shown that even small changes in gas consumption can lead to a collapse of the circulation due to an unfavorable gas distribution in the reactor. Furthermore, complex correlations between reactor geometry and operating conditions have been found. These complex correlations indicate that the couplings in Fig. 1.1 must be considered simultaneously during design and optimization.

Although the model presented in Chapter 2 has proven valuable for understanding the behavior of the JLR, it does not encompass all phenomena influencing the internal circulation and gas consumption, as depicted in Fig. 1.1. For instance, local gas volume fraction variations in the JLR, discussed in Chapter 2, can result not only from reactions but also from variations in bubble rising velocity. The bubble rising velocity is directly dependent on bubble size or more precisely on the bubble size distribution (BSD) and is influenced by several parameters, including reactor geometry, internals (e.g. stirrers, baffles), gas sparger, physicochemical properties of the fluids, and the power input from supplied fluids and internals. The BSD governs the gas phase residence time and thus the gas holdup. It also determines the interfacial area density, which is crucial for interfacial mass, energy, and momentum transport. Therefore, understanding the BSD behavior is essential for a reliable description of reactors, in which dispersed multiphase systems are found.

This issue is addressed in this thesis by utilizing the population balance equation (PBE). The PBE is a well-established tool for describing the behavior of the BSD [12–18]. The unique feature of PBE modeling is that it does not rely solely on the external physical space coordinates (e.g. x, y, z) commonly used in mass, momentum, and energy balance equations. Instead, the PBE incorporates the consideration of transport processes within property space using internal coordinates such as bubble-length, -shape, and -concentration. This allows the highly complex dispersed phase phenomena such as bubble breakage, coalescence, growth,

and nucleation including their effect on variables such as gas volume fraction, Sauter mean diameter, and interfacial density to be studied on a statistical basis with a single transport equation.

Considering the PBE only in addition to the common multifluid model will give a better estimation of some gas phase variables. But this sequential or ad hoc approach results in weak one-way coupling, which is common practice in the CFD community [19] due to the high computational demands. Hence, more sophisticated approaches are needed to account for the influence of dispersed phase phenomena on the other state variables such as species mass, momentum and energy of the dispersed phase. For example, to account for the fact that small bubbles remain in the reactor longer than larger ones due to the lower rising velocity, the residence time behavior of the bubbles must be size dependent. Thus, the momentum balance of the gas phase must also be size dependent.

A common approach to describe a size-dependent dispersed phase velocity is the inhomogeneous multiple size group (MUSIG) approach [20], where velocity classes of the dispersed phase are defined and assigned to certain bubble size ranges. However, if the complex interactions as shown in Fig. 1.1 are to be considered, further classes in the sense of the inhomogeneous MUSIG (e.g. composition and temperature classes) would have to be introduced. Alternatively, the composition and temperature of the dispersed phase are introduced into the PBE as additional state variable dimensions in the property space [21–23]. When multicomponent reactions and separation processes are considered in future work, the number of classes and the dimension of the PBE would become very large. It is expected that this high dimension of the property space or the large number of classes will be numerically very demanding, contradicting the basic requirement for an efficient model.

A suitable alternative which avoids the need of additional classes or state variable dimensions in the property space is the kinetic theory approach with size resolution (KTAWSR) developed by Jakobsen and coworkers [24–26]. They derived new transport equations (mass, species mass, energy, momentum) for the dispersed phase which, like the PBE, depend on the bubble size. The incorporation of the bubble size as additional dimension into all dispersed phase transport equations allows a direct investigation of the effects like bubble breakage and coalescence on the dispersed phase transport variables. This approach is therefore both straightforward and based on physical principles.

The KTAWSR, which in principle can represent all the couplings shown in Fig. 1.1, will be used to extend the reactor models commonly used in process engineering. Reactor models usually apply strong simplifications with respect to spatial resolution, e.g. zero spatial gradients result in ideal mixed systems or cross-sectional area averaging results in plug flow behavior. For more complex systems, the two assumptions are combined in compartment models (cf. Chapter 2). Despite the strong simplifications made, these so-called pseudo-continuous models (which means phases are treated as continuous phases) are well established and have proven their practical value even for complex reactive multiphase systems for decades [27, 28]. However, in dispersed multiphase systems, these models cannot determine important quantities and couplings such as gas holdup, interfacial density and bubble diameter, or only with the aid of empirical correlations. These correlations are strongly limited to the experimental range

and conditions investigated and therefore do not adequately reflect the complex interactions between the dispersed phases.

This thesis combines the KTAWSR and the well-tested spatial resolution assumptions leading to the multifluid population balance model (MPB) approach. The MPB aims to reduce the need for empirical correlations and to map the complex interphase couplings in order to make reliable and efficient predictions and estimates over a wide range of parameters.

The MBP is applied to describe the second reactor type of this thesis, bubble columns (BCs). BCs are standard multiphase reactors used in processes such as fermentation, gas adsorption, oxidation, and hydrogenation [1, 2]. In a previous study conducted by the author of this thesis [16], the MPB was successfully applied to a non-reactive semi-batch miniplant bubble column. This study [16] is not included in the present thesis. It was found that the simplifying assumptions made concerning the flow field in the reactor and the breakage and coalescence behavior of the bubbles necessitated the fitting of model parameters. These parameters of the breakage and coalescence kernel had to be adjusted to experimental data in order to describe the behavior of the dispersed phase in the BCs in a satisfying manner. Rather than being determined by independent experiments, the parameters used to describe breakage and coalescence were adjusted directly to the data from the bubble column. There is a theoretical possibility that the parameters are correlated. Additionally, inaccuracies in other submodels, such as the model describing the turbulent energy dissipation rate, may also be accounted for by these parameters. Nevertheless, the findings demonstrate that despite the simplicity of the parameter estimation method, which involves only four fitting parameters, the model is capable of accurately predicting experimental results, as evidenced by the findings of Breit *et al.* [16]. However, the range investigated was limited and all measured BSDs were used to calibrate the model parameters. In order to investigate the prediction performance of the model over a wide range, a large database was measured and is presented in Chapter 3. Different gas fluxes, vertical measurement positions, liquid holdups, and concentrated aqueous solutions of e.g. ethanol and sodium chloride were studied. Furthermore, a cross-validation was performed to reduce the measured BSD required for calibration compared to [16]. It was possible to predict the BSD and the gas holdup with a one-point calibration in an aqueous system within the experimental range analyzed. Chapter 4 extends the study of Chapter 3 to different gas spargers, higher gas fluxes in semi-batch mode, and applies and validates the model predictions for the first time in continuous mode where the liquid phase is also fed. In addition, the possibility of replacing the measured inlet BSD (necessary mathematical boundary condition), as used in [16] and Chapter 3, by a sparger model was investigated. Furthermore, instead of the optical multimode online probe (OMOP) [29], needle probes were utilized to measure the BSD required for validation. It was shown that the MPB is able to describe the new experiments with sufficient accuracy (about 10 %) without recalibration. The new sparger model also shows promising results, although overall limitations of the MPB could be identified.

So far, mass transfer between phases has not been considered in the MPB. The next step towards a multiphase reactive MPB approach is the investigation of non-reactive mass transfer processes. The KTAWSR already features mass transfer as a function of bubble size and its

influence on the BSD. Furthermore, the PBE of the KTAWSR balances the mass instead of the usual number of bubbles. This has the numerical advantages such as scaling to smaller numbers that are less subject to round-off errors and is a common conservation quantity for engineers. However, to obtain the necessary understanding of the size-dependent mass transfer needed for reactive multiphase processes, the commonly used number-based PBE derived from continuum mechanics has been transformed into a mass-based PBE in Chapter 5. After the transformation, an additional extra mass transfer term was obtained, which is also found in the KTAWSR from kinetic gas theory. The exact origin and interpretation of this term is discussed in detail. It is shown that the appearance of the extra term is due to the conservation properties of the original equations, which are preserved after the transformation. Furthermore, the transformations from different original equation reveal a deeper understanding of the conservation properties of the growth rate.

The investigation in this thesis is concluded with Chapter 6. Here the results of the application of the MPB to the third reactor type, a non-reactive semi-batch stirred tank reactor, are presented focusing on the influence of mass transfer. In industrial production processes, the stirred tank reactor (STR) is a widely used standard reactor. It is ideal for carrying out chemical or biotechnological gas-liquid syntheses, such as fermentations [30, 31]. In Chapters 3 and 4 the orthogonal collocation method (OC) developed by Solsvik *et al.* [32] was used to discretize the governing equations. The OC is a higher-order discretization method providing high accuracy but is complex, unfamiliar to engineers, and prone to oscillations and instabilities, especially in PBE applications. Instead, a robust and efficient method is needed to cover large parameter spaces when using the MPB for reactor design and optimization. For this reason, in Chapter 6, four different methods for solving the PBE for to the density function, including one newly proposed method, the finite volume method with Gauss quadrature (FVMG), were compared with each other. It was found that none of the methods clearly outperformed the others. The proposed FVMG proved to be robust, sufficiently accurate, and its components are familiar to engineers. To demonstrate the robustness of the FVMG and to study the operating behavior of the STR in detail, almost all model parameters were varied in a one-at-a-time parameter and sensitivity analysis. The results were compared to literature trends where available. Most of the literature trends were reliably reproduced, confirming that the number of empirical correlations for reactor design can be reduced with the help of the MBP. In addition, the result of a preliminary experimental investigation of the operating behavior of a non-reactive semi-batch STR is presented. The model can reproduce the measured data, but there are certain limitations that will be addressed in future studies.

Despite the successes achieved in the thesis, limitations of the MPB are already apparent, e.g. insufficient description of the dissipation rate and residence time behavior of the gas phase in the case of the STR. These and other limitations will be investigated and solved in future research projects. However, the content of this thesis contributes to a deeper understanding of dispersed multiphase reactive processes, which is essential for reactor design and optimization. For this purpose, simple, efficient and robust models have been developed, which can nevertheless represent the complex multiphase interactions, and have been validated by parameter studies and comparison with own experiments.

2. Model-Based Investigation of the Interaction of Gas-Consuming Reactions and Internal Circulation Flow Within Jet Loop Reactors

Contributor Roles Taxonomy

Ferdinand Breit: conceptualization; methodology; software; validation; formal analysis; investigation; data curation; writing - original draft; writing - review & editing; visualization

Chapter redrafted after the following main publication:

F. Breit, O. Bey, and E. von Harbou, "Model-based investigation of the interaction of gas-consuming reactions and internal circulation flow within jet loop reactors," *Processes*, vol. 10, no. 7, 2022. DOI: <https://doi.org/10.3390/pr10071297>.

Abstract

Jet loop reactors are standard multiphase reactors used in chemical, biological and environmental processes. The strong liquid jet provided by a nozzle enforces both internal circulation of liquid and gas as well as entrainment and dispersion of the gas phase. We present a one-dimensional compartment model based on a momentum balance that describes the internal circulation of gas and liquid phase in the jet loop reactor. This model considers the influence of local variations of the gas volume fraction on the internal circulation. These local variations can be caused by coalescence of gas bubbles, additional gas feeding points and gas consumption or production. In this chapter, we applied the model to study the influence of a gas consuming reaction on the internal circulation. In a comprehensive sensitivity analysis, the interaction of different parameters such as rate of reaction, power input through the nozzle, gas holdup, reactor geometry, and circulation rate were investigated. The results show that gas consumption can have a significant impact on internal circulation. Industrially relevant operating conditions have even been found where the internal circulation comes to a complete standstill.

2.1. Introduction

In this chapter an extension of model approach of Bey *et al.* [11] is presented in order to describe a reactive multiphase jet loop reactor (JLR). Instead of the integral balance applied by Bey *et al.* [11], a one-dimensional differential balance of momentum is applied to describe the internal circulation flow in JLRs. The model enables locally resolved calculation of the volume fraction of the phases, the pressure, the concentration of species and the velocity of the phases in the JLR. Certain properties of the multiphase flow, such as the bubble size distribution, are deliberately not considered in the model. The goal of the model is not to get a precise representation of the state of the multiphase flow in the JLR but to enable quick test of different scenarios of possible interactions of reaction and internal circulation. Therefore, we applied the developed model for extensive sensitivity studies based on a case adapted from industry. To the best of the authors' knowledge, the interaction between reaction and multiphase fluid dynamics in JLR as well as in similar reactors has not been systematically studied in the literature. The reaction is indeed frequently included in the calculation [5, 33–36], but a systematic investigation and the effect on the operating behavior and reactor design is mostly missing. This is the gap we would like to close with our model and parameter studies.

In the first study, the influence of different process parameters such as power input and rate of reaction constant on the internal circulation flow is investigated for a given reactor design. In the second study, the impact of variation of the reactor design on the internal circulation flow is assessed. In the third study, both the process and the design parameters were varied simultaneously.

We found that the internal circulation flow can be very sensitive to gas consumption in a broad and industrially relevant range of process and design parameters. These results show that the sensitivity studies carried out with help of the model developed in this chapter, provide comprehensive insights into the complex interplay between reaction and fluid dynamics in JLRs. From these insights, important conclusions can be drawn for the reliable design, and robust and safe operation of multiphase reactors.

2.2. The Principle of the Jet Loop Reactor

A wide variety of designs of JLRs exist. A good overview can be found in [37–40]. In this chapter, we look at a design where the liquid is injected from the top, see Fig. 2.1. However, the model developed in this chapter is not limited to this particular design, but can easily be adapted to other designs such as airlift reactors, reactors with liquid injection from the bottom or with additional gas feeding points.

In this chapter, two phases are considered: a continuous liquid phase (l) and a dispersed gas phase (g). The vessel (R) of the JLR contains the nozzle (N) at the top, the draft tube (DT), and the baffle plate (BP). The liquid is fed into the reactor via the nozzle with the volume flow rate $\dot{V}_{l,N}$. In the nozzle, the liquid flow is accelerated so that it is injected with high velocity into the liquid phase present in the reactor. Due to the high velocity of the jet, gas is drawn from the gaseous headspace into the circulating flow and dispersed, resulting in a downward bubble flow in the draft tube ($\dot{V}_{l,DT}$). At the baffle plate, the flow is divided. One part goes upward through the annular gap (AG) ($\dot{V}_{l,AG}$). The other part of the flow continuous downwards into the bottom space (BS) and is removed at the bottom of the reactor from where it is fed back into the reactor via the external liquid recycle (ER). The external liquid recycle is driven by a pump ($\dot{V}_{l,ER}$).

The gas phase flows dispersed as bubbles in co-current with the continuous liquid phase. However, not all gas bubbles follows the 180° redirection into the draft tube at the top but some leaves the surface into the gaseous headspace of the reactor. From there, the gas is either driven back into the liquid phase by the liquid jet or it leaves the reactor through the gas purge ($\dot{V}_{g,purge}$). The gas purge is needed to prevent accumulation of non-condensable gaseous inerts.

Typically, the reactor diameter is chosen so that the flow velocity of the liquid phase in the bottom space (especially in the gap between the baffle plate and the reactor wall) is smaller than the rise velocity of the gas bubbles. In this way, entrainment of gas bubbles into the external liquid recycle and into the pump, respectively is minimized.

JLRs are commonly used for hydrogenation, carbonylation, hydroformylation and oxygenation. In simplified form, the reactions that take place can be represented as a single irreversible gas consuming reaction that takes place in the liquid phase. The brutto reaction can be written as:



In our example, species A is a high-boiling reactant and species C a high-boiling product. Both are mainly present in the liquid phase. B is a gaseous species for example hydrogen or carbon monoxide that must be absorbed into the liquid phase upon reaction. In this chapter, it is assumed for the sake of simplicity that the liquid phase consists only of reactants A and B (dissolved from the gas phase), product C and an inert solvent. The gas phase consists of species B as only species B can change the phase. Note that the model could easily be extended to system with more complicated phase behavior. The reactants are fed via the two-phase nozzle ($\dot{V}_{l,feed}, \dot{V}_{g,feed}$). The liquid product ($\dot{V}_{l,product}$) is withdrawn from the external

recycle as shown in Fig. 2.1. As these type of reactions are typically exothermic reactions, a heat exchanger is installed in the external liquid recycle to control the temperature of the reaction mixture.

A special feature of this design of JLR is that the gas holdup in the reactor can be controlled. If the flow rate of the product stream is increased for a short time, the liquid holdup in the reactor decreases and therefore also the gassed height. This increases the distance between the surface of the gasified liquid and the tip of the nozzle. The increased distance leads to an intensification of entrainment of gas by the jet into the liquid phase. As a result, the gas holdup in the circulating liquid phase increases and the gassed height rises again until an equilibrium is reached between entrainment, discharge and consumption of gas bubbles so that the gas holdup stays constant.

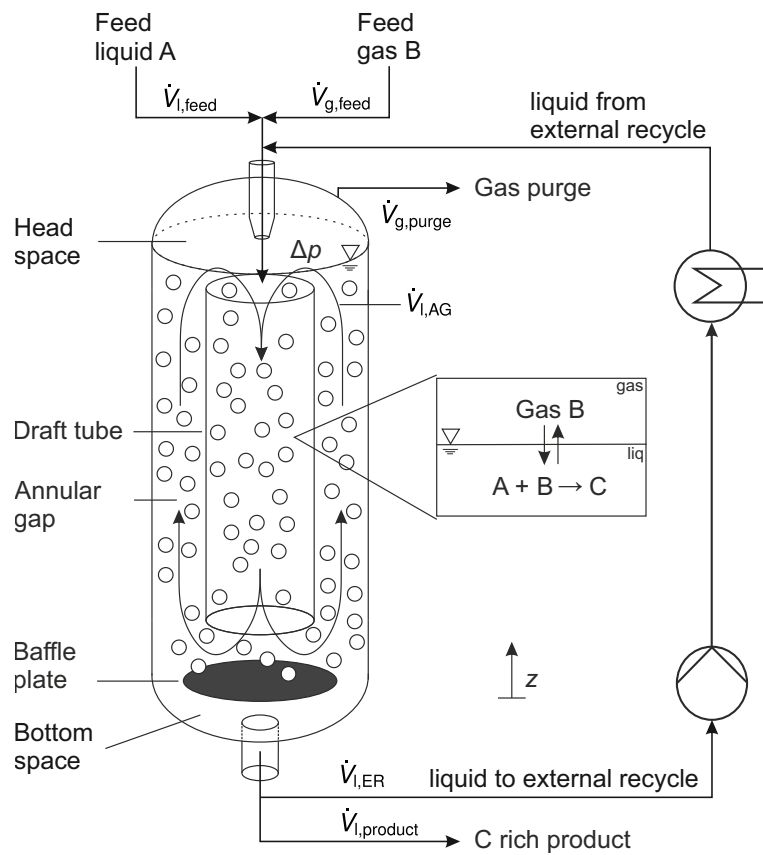


Figure 2.1.: Schematic drawing of a jet loop reactor.

2.3. Modelling and Simulation

2.3.1. Governing Equations

The model used to describe the internal flow in the JLR is based on a one-dimensional balance of momentum along the internal circulation flow path of the liquid phase. The internal circulation flow path or just flow path starts at the inlet of the draft tube ($z = h_{DT}$) leads further in negative z -direction to the outlet of the draft tube ($z = 0$). The flow path continues then in the annular gap ($z = 0$) in positive z -direction. The end of the flow path coincide with the outlet of the annular gap ($z = h_{DT}$). That is the flow path describes one complete circulation. The following assumptions were made to simply the balance of momentum:

- Stationary process
- Constant property data (e.g. density and viscosity of liquid phase)
- No viscous effects
- Only gravity acts as body force.
- No momentum transfer between liquid and gas phase, resulting in the zero-slip condition between gas bubbles and liquid phase.
- No change of momentum due to phase change.
- Only friction forces act on the interface of the liquid phase.

Applying these assumptions, the balance of momentum of the liquid phase in vertical z -direction is:

$$\rho_1 u_1 \alpha_1 \frac{\partial u_1}{\partial z} = -\alpha_1 \frac{\partial p}{\partial z} + \rho_1 \alpha_1 g + F_1 \quad (2.1)$$

where ρ_k , u_k and α_k denotes the mass density, the velocity and the volume fraction of phase k (liquid: $k = l$, gas: $k = g$). Furthermore is p the pressure, g the gravitational acceleration constant and F_1 the friction force per unit volume acting on the liquid phase, with

$$F_1 = \rho_1 \frac{\zeta}{2d_i} u_1^2 \quad (2.2)$$

Here, d_i is the hydraulic diameter of the compartment i (the compartments are introduced in Section 2.3.2), ζ is the pressure loss coefficient that describes friction in the draft tube and annular gap as well as the 180° redirection. The pressure loss coefficient is a function of the given geometry and the velocity of the liquid phase. In this chapter, ζ is calculated with the model presented by Zehner [41]. Details are given in the Supplementary Information A.2.1. The volume fraction, the volume flow rate (\dot{V}_k), and the velocity of the phases are coupled via Eq. (2.3).

$$u_k = \frac{\dot{V}_k}{A_i \alpha_k} \quad (2.3)$$

A_i is the cross-sectional area of compartment i . It is assumed that the liquid volume flow rate is constant within each compartment i (see Section 2.3.2).

The balance of momentum of the gas phase is not considered in this chapter. The gas phase is described with closing conditions: the gas volume fraction (α_g) results from the volume fraction constrain given in Eq. (2.4), the velocity of the gas phase (u_g) is obtained from the zero-slip condition (see Eq. (2.5)).

$$\text{Volume fraction constrain : } \alpha_g = 1 - \alpha_l \quad (2.4)$$

$$\text{No-slip condition : } u_g = u_l \quad (2.5)$$

It is important to note that the model approach is not limited to the zero-slip condition but can be easily extended with models describing the gas-liquid slip velocity. This extension, however, was not in the scope of the present chapter and will be considered in further work.

The change of molar concentration of reactant A in the liquid phase along the flow path is calculated with a kinetic model assuming plug flow behavior [42], see Eq. (2.6).

$$u_l \alpha_l \frac{\partial c_{l,A}}{\partial z} = \alpha_l \nu_{l,A} r_I \quad (2.6)$$

Where $c_{l,A}$ is the molar concentration of species A in the liquid phase, $\nu_{l,A}$ is stoichiometric coefficient of species A in Reaction (I) and r_I is the rate of reaction per unit volume of Reaction (I). It is assumed that the rate of reaction follows a simple power law:

$$r_I = k_I c_{l,A} \quad (2.7)$$

where k_I is the rate of reaction constant. The power law is of first order with respect to the molar concentration of liquid species A and of zeroth order with respect to the gaseous species B. This type of reaction kinetics can be found in systems, in which the gas-liquid mass transfer is fast so that the liquid phase is always saturated with dissolved gaseous species. In this chapter, this simplification is justified as our focus is to study the general influence of a gas consuming reaction on the internal circulation flow. However, it is important to note that the presented model approach is not limited to this simplification but can be easily extended both with more complicated kinetic models and with models describing mass transfer between gas and liquid phase.

The consumption of gas along the flow path of the gas phase is reflected as a reduction of the internal volume flow rate of the gas phase. It is calculated directly from the conversion of the liquid species A according to the stoichiometry of the given chemical reaction (see Reaction (I)).

$$\dot{V}_{g,i}(z) = \dot{V}_g(z_{IN,i}) - \frac{M_B}{\rho_g} \frac{\nu_{l,B}}{\nu_{l,A}} \dot{V}_l(z_{IN,i}) (c_{l,A}(z_{IN,i}) - c_{l,A}(z)) \quad \text{for } z_{IN,i} = \begin{cases} h_{DT} & i = DT \\ 0 & i = AG \end{cases} \quad (2.8)$$

Here, $z_{IN,i}$ is the initial position in the direction of the flow path of compartment i and M_B is

the molar mass of species B.

2.3.2. Compartment Model of the Jet Loop Reactor

To describe the JLR reactor with its internal circulation flow with the one-dimensional model equations presented above the reactor is divided into compartments as shown in Fig. 2.2. Where h_i is the height of compartment i with $h_{DT} = h_{AG}$. The balance of momentum is only considered in those compartments, in which gas-liquid flow is present. That are: draft tube (DT) and annular gap (AG). The conversion of species A, which takes only place in the liquid phase, is considered in all compartments including the external recycle (ER) and the bottom space (BS). As shown in Eq. 2.6 plug flow (PFR) behavior is assumed in the draft tube, the annular gap and the external recycle. The bottom space (BS) is described as ideally mixed (CSTR). It is assumed that the mixing of the liquid feed ($\dot{V}_{l,feed}$), the liquid jet ($\dot{V}_{l,ER}$) and the internal circulation flow ($\dot{V}_{l,AG}$) is instantaneous. Note that the head space (HS), the upper flow redirection (HR) and the lower flow redirection (BR) are not modeled.

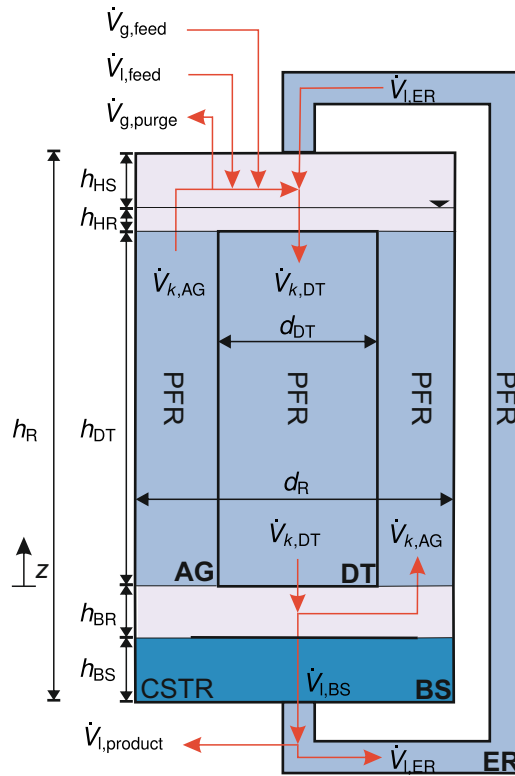


Figure 2.2.: Compartment model of the jet loop reactor. The abbreviations denote: AG annular gap, DT draft tube, BS bottom space, HS head space, ER external liquid recycle, BR lower flow redirection, HR upper flow redirection, R reactor, CSTR continuous stirred tank reactor and PFR plug flow reactor.

2.3.3. Implementation and Simulation

Boundary Conditions

Using the presented Eq. (2.1) - Eq. (2.8), the gas and liquid volume fractions (α_g, α_l), the pressure (p), the molar concentration of species A in the liquid phase ($c_{l,A}$) and the velocity of the gas and liquid phase (u_g, u_l) can be calculated as function of the flow path z . The possibility to represent the influence of the reaction on the gas volume fraction and to express the gas volume fraction as a function of the location in the JLR is the main difference of this model approach to the so far well-established integral models of JLRs of for example Zehner and co-workers [38, 39, 43].

When all geometry parameters including the diameter of the nozzle mouth are given, the following process parameters (i.e. boundary conditions) have to be specified to close the system of Eq. (2.1) - Eq. (2.8):

- $\dot{V}_{l,ER}$, the volume flow rate of liquid jet, which is equivalent to the volume flow rate of the external liquid recycle
- $\dot{V}_g(z_{IN,i})$, the volume flow rate at the entry of the draft tube and the annular gap
- $\dot{V}_{l,feed}$, the volume flow rate of liquid feed
- p_0 , the pressure in the headspace of the JLR

The volume flow rate of liquid jet can be calculated using a simple pressure drop correlation and the definition of the volume flow rate (see Eq. (2.3)):

$$\dot{V}_{l,ER} = \sqrt{\frac{\Delta p_N}{8\zeta_N \rho_l}} \pi d_N^2 \quad (2.9)$$

d_N is the diameter of the nozzle mouth, Δp_N is the pressure drop over the nozzle and ζ_N the pressure loss coefficient of the nozzle, whose value is assumed to be constant with $\zeta_N = 1.1$. Instead of the pressure drop over the nozzle, the (specific) power input φ can also be specified,

$$\varphi = \frac{P}{V_R} = \frac{\Delta p_N \dot{V}_{l,ER}}{V_R} \quad (2.10)$$

P is the power introduced into the reactor by the liquid jet and V_R is the reactor volume. Thus, we have four parameters ($\varphi, \Delta p_N, \dot{V}_{l,ER}, d_N$) and two equations (Eq. (2.9), Eq. (2.10)) resulting in a degree of freedom of two. Hence, when two parameters are specified the other two are fixed. All values specified in this chapter are summarized in the Supplementary Information A.1.

The volume flow rate of the liquid feed is specified in this chapter so that a space-time-yield in the reactor is obtained that is typical for industrial reactors.

The volume flow rate of gas phase at the inlet of the draft tube ($z = h_{DT}$) must be specified to calculate the volume flow rate of gas phase along the flow path (see Eq. (2.8)). It is the sum of the volume flow rate of gas that is entrained by the liquid jet and of gas bubbles recirculated from the flow through annular gap. The volume flow rate of the gas that is

entrained by the liquid jet into the liquid phase depends on the distance of nozzle mouth to the surface of the gassed liquid. The volume flow rate of recirculated gas bubbles depends on many parameters such as reactor geometry and properties of the fluids. Both flow rates are not explicitly calculated in this chapter. Instead the volume flow rate of gas phase at the inlet of the draft tube is specified using the volume flow rate of the gas feed, see Eq. (2.12). The gas feed is calculated from the stoichiometric amount required to enable (at least theoretically) full conversion of species A, which is fed via the liquid phase into the reactor (see Eq. (2.11)). Two factors are used: f_r and f_s . They are defined in the interval $[0, \infty)$. f_r is the stoichiometric excess factor applied to ensure that more gas is fed into the liquid phase than the maximum that can be consumed in the reaction. The factor f_s reflects the internal recycle of gas bubbles from the annular gap into the draft tube.

As no additional gas is fed into the annular gap, the volume flow rate of gas phase at the inlet of the annular gap ($z = 0$) is the same as the volume flow rate at the outlet of the draft tube, see Eq. (2.13).

$$\dot{V}_{g,\text{feed}} = \frac{\rho_l}{\rho_g} \frac{M_B}{M_A} \frac{\nu_{l,B}}{\nu_{l,A}} \dot{V}_{l,\text{feed}} \quad (2.11)$$

$$\dot{V}_g(z_{\text{IN,DT}}) = \dot{V}_{g,\text{feed}} f_s f_r \quad (2.12)$$

$$\dot{V}_g(z_{\text{IN,AG}}) = \dot{V}_g(z_{\text{IN,DT}}) \quad (2.13)$$

Further details on the modeling can be found in the Supplementary Information A.2.

Method of Solution

The solution of the differential equation of the balance of momentum (Eq. (2.1)) is done by the finite volume method. Because of the simple kinetic model, the species balance can be solved for each compartment analytically (for details see Supplementary Information A.2.2).

The discretized system of non-linear equations is solved with a damped Newton algorithm implemented in MATLAB[®] in the Version R2019a (9.6.0.1072779) from the publisher The MathWorks Inc. (Natick, Massachusetts, USA). For details on the implementation see Supplementary Information A.4.

Definition of the Simulation Studies

Three different simulation studies are carried out in this chapter: I) variation of process parameter, II) variation of design parameter and III) variation of process and design parameter.

In the variation of process parameter study, the reactor design (including the design of the nozzle) is given and the following process parameters are varied: the rate of reaction constant and the specific power input. This study represents the case of optimizing the process conditions such as internal circulation flow or conversion of reactants for an existing reactor. In real processes, a variation of the rate of reaction constant can be achieved e.g. by varying the

amount of catalyst or the temperature of the reacting mixture. For a given design, the variation of the specific power input can only be realized by varying the volume flow rate of liquid phase through the nozzle (i.e. by varying the power output of the pump). Variations of the volume flow rate results directly in variations of the pressure drop over the nozzle. Tab. A.2 in the Supplementary Information give details on the varied parameters of this study.

The variation of design parameter study reflects the case in which the specifications for the reaction process are given and the internal design of the reactor is chosen for example to achieve maximum internal circulation. Specifications for the reaction process are typically the space-time-yield, the production rate or feed rate, respectively and the composition of the feed. The space-time-yield and production rate result in a defined reactor volume. When the reactor volume is given, the following design parameters that determine the internal geometry of the reactor can be varied: ratio of diameter of draft tube to diameter of reactor d_{DT}/d_R (short: diameter ratio), ratio of reactor height to reactor diameter h_R/d_R (short: slenderness ratio). To study the influence of the consumption of gas on the internal circulation flow also the rate of reaction constant was varied in this study. Tab. A.3 and Tab. A.4 in the Supplementary Information give details on the varied parameters of this study.

To get deep insights into the complex interactions of both design and process parameters, the following parameters were varied in the last study (variation of process and design parameter): ratio of diameter of draft tube to diameter of reactor, specific power input, the rate of reaction constant and the gas holdup in the reactor. Tab. A.5 in the Supplementary Information give details on the varied parameters of this study.

The constant parameters e.g. property data applied the for all simulation studies is listed in the Supplementary Information Tab. A.1.

Output Parameters

For the evaluation of the simulation results, the following output parameters are defined:

- N_{circ} : circulation number
- $\bar{\alpha}_{g,AG}$: gas holdup in the annular gap
- $\Delta\bar{\alpha}_{g,DT,AG}$: difference of gas holdup in draft tube and annular gap
- $c_{l,A,DT,IN}$: molar concentration of species A in the liquid phase at the inlet ($z = h_{DT}$) of the draft tube
- $c_{l,A,DT,OUT}$: molar concentration of species A in the liquid phase at the outlet ($z = 0$) of the draft tube
- $c_{l,A}(z)$: molar concentration of species A in the liquid phase along the flow path
- $\alpha_g(z)$: volume fraction of gas along the flow path

The circulation number N_{circ} describes the ratio of the liquid volume flow rate of the internal circulation flow ($\dot{V}_{\text{l,AG}}$) to the external recycle ($\dot{V}_{\text{l,ER}}$):

$$N_{\text{circ}} = \frac{\dot{V}_{\text{l,AG}}}{\dot{V}_{\text{l,ER}}} \quad (2.14)$$

The gas holdup in the annular gap or in the draft tube is the volume weighted average of the gas volume fraction in that section.

$$\bar{\alpha}_{\text{g},i} = \frac{1}{h_i} \int_0^{h_i} \alpha_{\text{g},i}(z) \, dz \quad \text{for } i \in \{\text{AG, DT}\} \quad (2.15)$$

The gas holdup difference between draft tube and annular gap is

$$\Delta\bar{\alpha}_{\text{g,DT,AG}} = \bar{\alpha}_{\text{g,DT}} - \bar{\alpha}_{\text{g,AG}} \quad (2.16)$$

For brevity, in the following the output parameter $\Delta\bar{\alpha}_{\text{g,DT,AG}}$ is called just gas holdup difference.

2.4. Simulation Results

2.4.1. Variation of Process Parameter

Fig. 2.3A depicts the circulation number N_{circ} and the molar concentration of A in the liquid phase at the inlet of the draft tube $c_{1,A,DT,IN}$ as function of the rate of reaction constant k_I for different power inputs φ . Fig. 2.3B shows the gas holdup in the annular gap $\bar{\alpha}_{g,AG}$ and gas holdup difference $\Delta\bar{\alpha}_{g,DT,AG}$ as a function of the rate of reaction constant k_I for different power inputs φ . The effect of the variation of the rate of reaction constant and the specific power input on a given reactor design is investigated here at a low excess of gas ($f_s = 1.1$) that is a low gas holdup. The influence of the gas holdup on the internal circulation is discussed in Section 2.4.2.

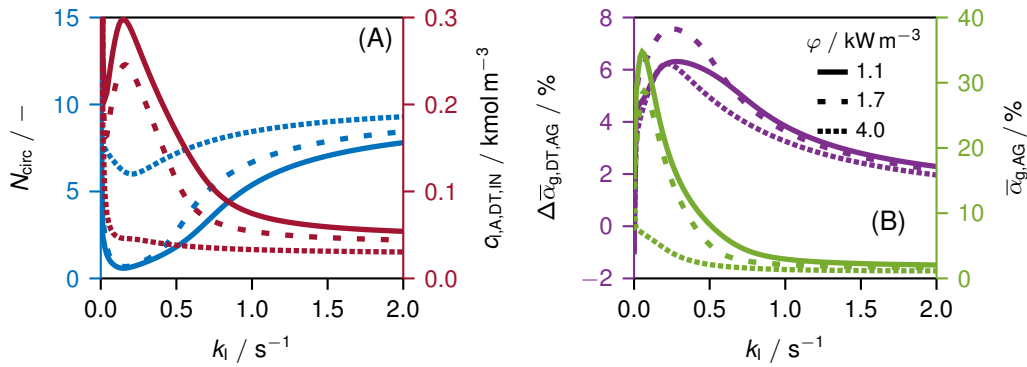


Figure 2.3.: (A): Circulation number N_{circ} (blue) and molar concentration of A in the liquid phase at the inlet of the draft tube $c_{1,A,DT,IN}$ (red), and (B): gas holdup difference $\Delta\bar{\alpha}_{g,DT,AG}$ (purple) and gas holdup in the annular gap $\bar{\alpha}_{g,AG}$ (green), as a function of the rate of reaction constant k_I . Variation of the specific power input φ (line style). Applied parameter see Tab. A.1 and Tab. A.2.

If no reaction takes place ($k_I = 0$), no gas is consumed and \dot{V}_g is constant along the whole flow path. Because of the injection of liquid at the top and removal at the bottom, the volume flow rate of liquid in the draft tube is larger than in the annular gap. Therefore, the gas holdup in the draft tube is smaller than in the annular gap (i.e. $\Delta\bar{\alpha}_{g,DT,AG} < 0$). Hence, the hydrostatic pressure in the draft tube is larger than in the annular gap. This pressure gradient promotes the internal circulation flow in the JLR. Thus, a high circulation number at $k_I = 0$ is found for all power inputs.

With the onset of the reaction, gas is consumed. Due to the larger cross-sectional area and the lower liquid volume flow rate in the annular gap, the residence time in the annular gap is longer than in the draft tube. Consequently, more gas is consumed in the annular gap than in the draft tube so that the gas holdup decreases in the annular gap with increasing rate of reaction constant. The result is that the gas holdup difference becomes positive $\Delta\bar{\alpha}_{g,DT,AG} > 0$. Now, the hydrostatic pressure gradient acts against the direction of the internal circulation flow. Thus, the circulation number decreases rapidly with increasing rate of reaction constant. Surprisingly, the gas holdup in the annular gap initially increases. The explanation for this observation is that the internal circulation flow decreases faster at low rate of reaction constants

than the gas volume flow rate in the annular gap. Only when the reaction becomes even faster and the gas consumption in the annular gap increases further, does the gas holdup in the annular gap also decrease.

If the reaction rate continues to increase, there is no more consumption of gas in the annular gap but only in the draft tube. This reduces the difference of the gas holdup again and the decelerating effect of the hydrostatic pressure difference on the internal circulation flow diminishes. Thus, the circulation number increases again. If the reaction is so fast that the reactants are completely converted immediately after being injected into the draft tube, the gas consumption has no effect on the circulation number and it is similar to that of the non-reactive case.

The strong variation of the circulation number depending on the rate of reaction constant, also affects the concentration profiles within the JLR. If the circulation number is large, backmixing is enhanced. Thus, the spatial concentration gradients of the reacting species along are small within the reactor. In contrast, a reduction of the internal circulation number leads to lower backmixing, which results in larger concentration gradients along the flow path. This behavior shows how important it is that the gas consumption is considered in the model so that the internal circulation flow is properly captured by the model. Whereby in future work, the model predictions should be confirmed by experiments to prevent an overestimation of the influence of a reaction on the fluid dynamics by the model. However, the observations from industrial processes described in [11] support the model predictions.

If the influence of gas consumption on the internal circulation flow is not account for in the fluid dynamic model of the JLR, the internal circulation number and thus also the backmixing can be significantly overestimated in the design of the reactor compared to the real behavior of the JLR. In case of reaction systems in which unwanted side reactions occur that are of higher order with respect to the reactants the reduction of internal backmixing decreases the selectivity. Or the increase of the concentration of reactants at the reactor inlet can cause an increase of the deactivation rate of the catalyst. Furthermore, reduction of backmixing means that the rate of reaction, and thus also the required gas-liquid mass transfer, is significantly higher at the inlet of the JLR than that at the upper end of the annular gap. If this increased demand for mass transfer was not considered when designing the reactor that is the power input is chosen too low (because the model did not considered these effects), it may result in a deficiency of dissolved gas species. In many cases, this deficiency of reactants results in increased rate of formation of unwanted side-products. For the case of internal heat exchanger surfaces, similar problems could arise. If the degree of backmixing is smaller in reality than expected in the design of the reactor, hot spots may arise at the reactor entrance (top of the draft tube) due to the high concentration of reactants and therefore high rate of reactions. These examples show that negligence of the influence of the gas consumption on the internal circulation during the design of the reactor can lead to the reactor not reaching the desired target values (e.g. conversion of reactants, selectivity to target products) later in operation.

As demonstrated above, many operation conditions can be found in which the consumption of gas influences the internal circulation in the JLR. This means that the results of non-reactive test runs in real JLRs (e.g. runs without catalyst or with inert gas), which are carried out

during start-up (e.g. for calibration of instruments, understanding of reactor behavior), may not provide information that can be directly transferred to reactive operation when gas is consumed.

Fig. 2.3 shows clearly that high power inputs mitigate the influence of the rate of reaction constant and the gas consumption, respectively on the internal circulation. At high power inputs, the accelerating or decelerating contribution of the hydrostatic pressure difference is small compared to the input of momentum of the liquid jet. For this reason, variations of the hydrostatic pressure difference due to gas consumption are less significant when the power input is large.

As expected the sensitivity of the internal circulation on the power input is largest in the range of rate of reaction constants ($k_I = 0.1 \text{ s}^{-1} - 0.2 \text{ s}^{-1}$) where the decelerating effect of the hydrostatic pressure difference is largest and the internal circulation number reaches a minimum. In the following, this region is called "sensitive reactive" range.

The influence of the power input on the internal circulation is not linear in the sensitive reactive range. For power inputs smaller than $\varphi \lesssim 2.0 \text{ kW m}^{-3}$, a small change of the power leads to a significant change of the internal fluid dynamics. It is most likely that the strong reduction of the internal circulation flow of the liquid phase in the sensitive reactive range for power inputs less than (2.0 kW m^{-3}) would lead to a complete collapse of the circulation in reality. In the simulation, the low internal circulation flow is only possible because zero-slip condition between gas and liquid phase is assumed. For small liquid velocities, the slip velocity of the gas phase (that is the rise velocity of the gas bubbles) is significant especially when coalescence of gas bubbles occurs at large values of the gas holdup.

In addition, at high gas volume fractions and low liquid velocities, complex two-phase flows and flow patterns can occur [44]. The prediction of the collapse of the internal circulation flow, however, was not in the scope of this chapter and will be considered in future work. For the design of JLRs the information provided by the model presented in this chapter are sufficient to identify sensitive regions. For JLRs used in industry, robust operation must be ensured. Therefore, the reactor should be operated far outside these sensitive regions.

2.4.2. Variation of Design Parameter

Variation of the Draft Tube to Reactor Diameter Ratio

Fig. 2.4A shows the circulation number N_{circ} and the gas holdup difference $\Delta\bar{\alpha}_{g,\text{DT,AG}}$ as a function of the diameter ratio $d_{\text{DT}}/d_{\text{R}}$, for different rate of reaction constants k_I . Thereby, the investigated rate of reaction constants, based on the findings from the previous section, stand for: I) non-reactive case (i.e. $k_I = 0.0 \text{ s}^{-1}$), II) non-sensitive reactive case (i.e. $k_I = 2.0 \text{ s}^{-1}$) and III) sensitive reactive case (i.e. $k_I = 0.2 \text{ s}^{-1}$). Fig. 2.4B illustrates the molar concentration of A in the liquid phase at the inlet of the draft tube $c_{1,\text{A,DT,IN}}$ and at its outlet $c_{1,\text{A,AG,OUT}}$ as a function of the diameter ratio for different rate of reaction constants.

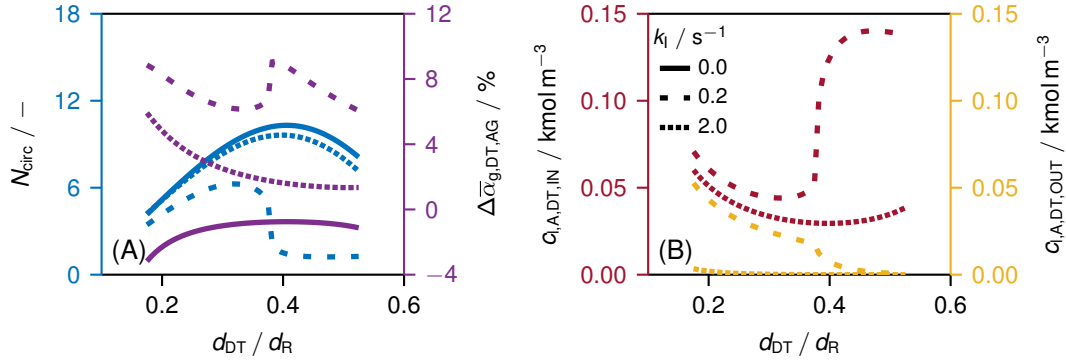


Figure 2.4.: (A): Circulation number N_{circ} (blue) and gas holdup difference $\Delta\bar{\alpha}_{g,DT,AG}$ (purple), and (B): molar concentration of A in the liquid phase at the inlet $c_{1,A,DT,IN}$ (red) and outlet $c_{1,A,AG,OUT}$ (yellow) of the draft tube as a function of diameter ratio d_{DT}/d_R . Variation of the rate of reaction constant k_I (line style). Applied parameter see Tab. A.1 and Tab. A.3 with $\varphi = 4.0 \text{ kW m}^{-3}$.

In the non-reactive case, the circulation number shows a convex shape with a maximum at a diameter ratio of 0.42. Blenke *et al.* [45] determined semi-empirical 0.59 for a single-phase case and Gao *et al.* [46] determined CFD-based 0.66 for a two-phase case. Both cases are non-reactive and in contrast to the case of this chapter, the nozzle is located in the bottom space, which may explain the discrepancy with our non-reactive case. The maximum of the circulation number is caused by a minimum of the overall frictional losses in the reactor that are dominated by losses from the redirection of the internal flow at the inlet ($z = h_{DT}$) and the outlet of the draft tube ($z = 0$). In the non-sensitive reactive case with very high rate of reaction constants ($k_I = 2.0 \text{ s}^{-1}$), a similar pattern is observed as in the non-reactive case though the circulation number is somewhat smaller in the reactive case. As already described in the previous section (see Section 2.4.1), the reaction has little effect on the internal fluid dynamics for very fast reactions where the gas consumption takes place only in the upper part of the draft tube. The reduction of the circulation number observed for the non-sensitive reactive case is caused by consumption of gas. This leads to a positive gas holdup difference as shown in Fig. 2.4A, which in turn decelerates the internal circulation flow.

Just as in the previous section, the results show a clear influence of gas consumption on internal circulation number when the rate of reaction constant is in the sensitive reactive range (here: $k_I = 0.2 \text{ s}^{-1}$). After the circulation number has reached a maximum at a diameter ratio of about 0.34 the circulation number decreases abruptly to a constant value of about 1.2. To get a better understanding for the cause of the significant change of the circulation number, the gas volume fraction is plotted as a function of the flow path and the diameter ratio in Fig. 2.5. The length of the flow path is normalized with its total length of $2h_{DT}$.

At low values of the diameter ratio the circulation number increases with increasing diameter ratio (see Fig. 2.4A). As in the other two cases, this trend is initially due to the decrease in internal friction. Because the gas flow entrained by the nozzle remains constant in the simulation, the gas volume fraction at the inlet of the draft tube decreases as the circulation number increases (see Fig. 2.4A). Consequently, the gas holdup difference decreases. Simultaneously, the increase of backmixing leads to a reduction of the concentration of reactant A at the inlet

of the draft tube (see Fig. 2.4B), the complete plot of the concentration profile of reactant A as a function of the flow path is shown in the Supplementary Information Fig. A.1 and Fig. A.2. So far, the trend for both reactive cases (non-sensitive and sensitive) is the same. However, the decrease of the molar concentration of reactant A at the inlet of the draft tube reduces the rate of reaction and therefore also the gas consumption in that region of the reactor. Hence, in the sensitive case the gas volume fraction starts to increase again at the value of the diameter ratio of about 0.31 where the circulation number reaches its maximum. This leads to an increase of the decelerating effect of the gas holdup difference (see Fig. 2.4A) when the diameter ratio is increased further. In addition to that, the residence time of the liquid phase in the draft tube increases because both the volume of the draft tube increases compared to the volume of the annular gap and the internal circulation flow rate of the liquid phase decreases. Thus, the increase of the concentration of the reactant A at the inlet of the draft tube and the increase of the residence time in the draft tube caused by the reduction of the circulation number lead both to an unfavorable distribution of gas consumption and gas holdup between draft tube and annular gap. As a result, the gas holdup difference increases rapidly at a value of the diameter ratio of 0.38 (see Fig. 2.4A) and so does its decelerating effect. Hence, the flow rate of the internal circulation is very small for values of the diameter ratio of more than 0.4. In this case, the draft tube acts almost like a PFR where all conversion of reactant A takes place (see concentration difference between inlet and outlet of the draft tube plotted in Fig. 2.4B). To summarize, in the sensitive reactive case, the reactor characteristics change in dependence of the diameter ratio (see Fig. 2.5). For small diameter ratios the circulation number is large, the reactor behaves like a CSTR with small local difference of the concentration of reactants and gas volume fraction. For large diameter ratios, however, the circulation number is small so that the draft tube acts as a PFR, which results in strong local gradients of the concentration of reactants and gas volume fraction. The strong differences between the behavior of the JLR for the non-reactive and the reactive (and kinetically sensitive) case demonstrate that the gas consumption can have a significant influence on the internal circulation flow.

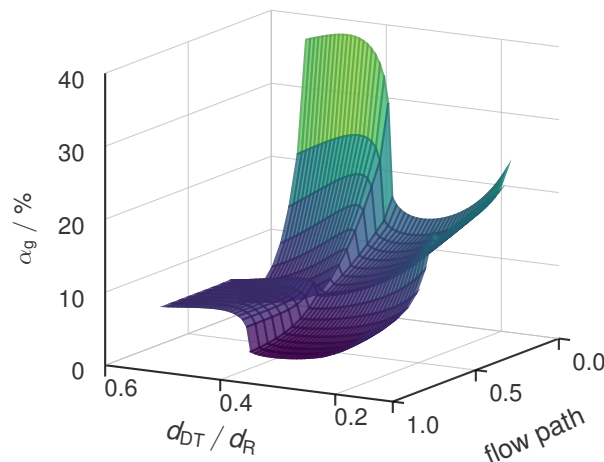


Figure 2.5.: Gas volume fraction α_g as a function of the diameter ratio d_{DT}/d_R and the normalized flow path. Applied parameter see Tab. A.1 and Tab. A.3 with $k_I = 0.2 \text{ s}^{-1}$ and $\varphi = 4.0 \text{ kW m}^{-3}$ where the reactor volume where kept constant.

Variation of the Reactor Height to the Reactor Diameter

Fig. 2.6A shows the circulation number and the gas holdup difference as a function of the slenderness ratio. Fig. 2.6B illustrates the molar concentration of A in the liquid phase at the inlet and the outlet of the draft tube as a function of the slenderness ratio. As in the previous section, three cases are considered: I) non-reactive case (i.e. $k_I = 0.0 \text{ s}^{-1}$), II) non-sensitive reactive case (i.e. $k_I = 2.0 \text{ s}^{-1}$) and III) sensitive reactive case (i.e. $k_I = 0.2 \text{ s}^{-1}$).

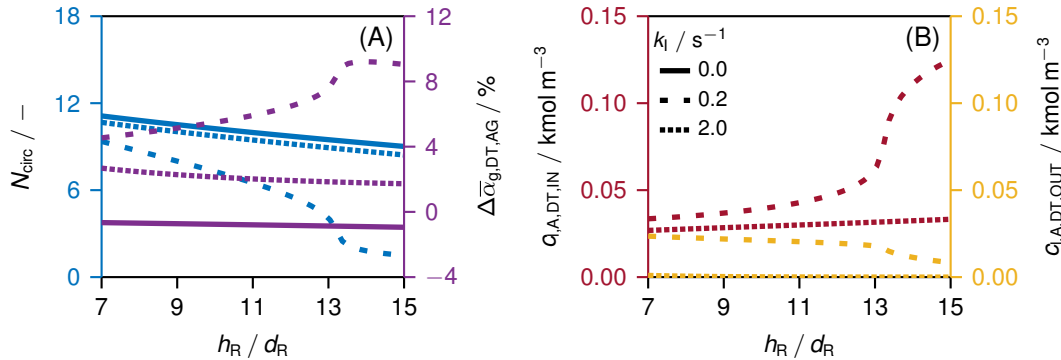


Figure 2.6.: (A): Circulation number N_{circ} (blue) and gas holdup difference $\Delta\bar{\alpha}_{g,DT,AG}$ (purple), and (B): molar concentration of A in the liquid phase at the inlet $c_{l,A,DT,IN}$ (red) and outlet $c_{l,A,DT,OUT}$ (yellow) of the draft tube as a function of slenderness ratio h_R/d_R . Variation of the rate of reaction constant k_I (line style). Applied parameter see Tab. A.1 and Tab. A.4 with $\varphi = 4.0 \text{ k W m}^{-3}$.

For the non-reactive and the non-sensitive reactive case (i.e. $k_I = 2.0 \text{ s}^{-1}$), the circulation number decreases with increasing h_R/d_R because internal friction increases when the reactor becomes slimmer. The difference between the non-reactive and non-sensitive reactive case in terms of circulation number are due to gas consumption and its decelerating effect explained above.

Similar to the results presented in the previous study in which the diameter ratio is varied, the sensitive reactive case ($k_I = 0.2 \text{ s}^{-1}$) deviates significantly from the two other cases (see Fig. 2.6). Also here, a sharp drop in circulation number is observed if the design parameter that is the slenderness ratio is increase over a certain value (about 13). The explanation for this behavior is basically the same as the one we presented in the previous section. When the slenderness ratio is increased over a certain value the decreases of the internal circulation and its feedback effect on the gas consumption caused by the increases of the concentration of reactants at the inlet of the draft tube (see Fig. 2.6B) induces a change of the regime of the reactor behavior. Fig. 2.7 depicts the concentration of reactant A as a function of the normalized length of flow path and of the slenderness ratio. While the local concentration gradients in the JLR are small at low slenderness ratios they become more than three times larger at high slenderness ratios. Thus, the reactor characteristics change from a well backmixed system (CSTR) to the behavior of a PFR. The gas volume fraction shows similar trends (see Supplementary Information A.3).

In this study, however, it is noticeable that the change in circulation number is not as abrupt as in the case of the change in the diameter ratio (compare Fig. 2.4 with Fig. 2.6). While the

increase of the diameter ratio causes a change of the regime of the reactor characteristics via two effects (backmixing and ratio of residence time in draft tube and annular gap), in this case it only acts via the reduction of backmixing caused by the reduction of the circulation flow rate.

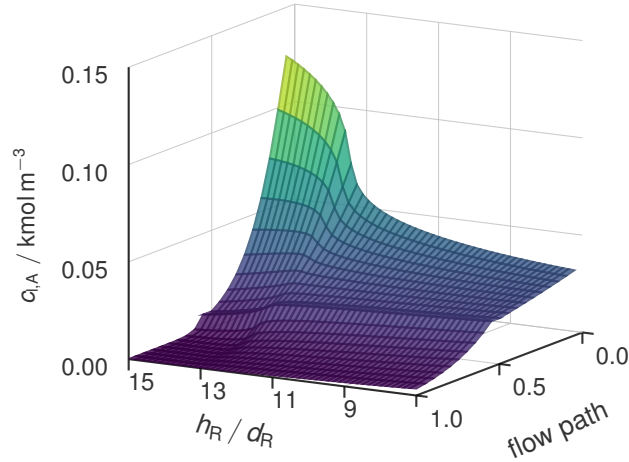


Figure 2.7.: Molar concentration of A in the liquid phase $c_{l,A}$ as a function of the slenderness ratio h_R/d_R and the normalized flow path. Applied parameter see Tab. A.1 and Tab. A.4 with $k_I = 0.2 \text{ s}^{-1}$, $\varphi = 4.0 \text{ kW m}^{-3}$ and diameter ratio $d_{DT}/d_R = 0.5$ where the reactor volume kept constant.

2.4.3. Influence of Process and Design Parameters

In the simulation studies presented in the previous sections, the volume flow rate of entrained gas is kept at a constant value that results in an gas holdup of about 10 %. Fig. 2.8 summarizes the results of a simulation studies in which the gas holdup (i.e. volume flow rate of entrained gas), the power input, the diameter ratio, and the rate of reaction constant are varied. Note that in contrast to Section 2.4.1, the specific power input was adjusted by varying the nozzle diameter resulting in variation of the pressure drop over the nozzle. The liquid volume flow rate through the nozzle (i.e. the flow rate of the external recycle) was kept constant, so that the different reactor concepts remain comparable. The bottom row in Fig. 2.8 shows the non-reactive case ($k_I = 0.0 \text{ s}^{-1}$). The results are in line with the expectation. High power input, low gas holdup and a diameter ratio of about 0.5 facilitate high circulation numbers. Similar trends are found for the non-sensitive reactive case ($k_I = 2.0 \text{ s}^{-1}$). In this case, only the absolute values of the circulation number is somewhat lower compared to the non-reactive case due to the decelerating effect of the gas consumption on the circulation (see explanation in Section 2.4.1).

In the sensitive reactive case ($k_I = 0.2 \text{ s}^{-1}$), a similar behavior compared to the other two cases is found but only if the gas holdup is large. If the gas holdup is decreased to values smaller than 20 %, the circulation number drops sharply (for a diameter ratio of 0.5) and no solution is found by the solver (both diameter ratios). These results suggest that the internal circulation flow collapse at this point. Only with very high power input ($\varphi = 4.0 \text{ kW m}^{-3}$), a stable circulation (for the given assumptions) can be achieved. The drastic decreases (or even

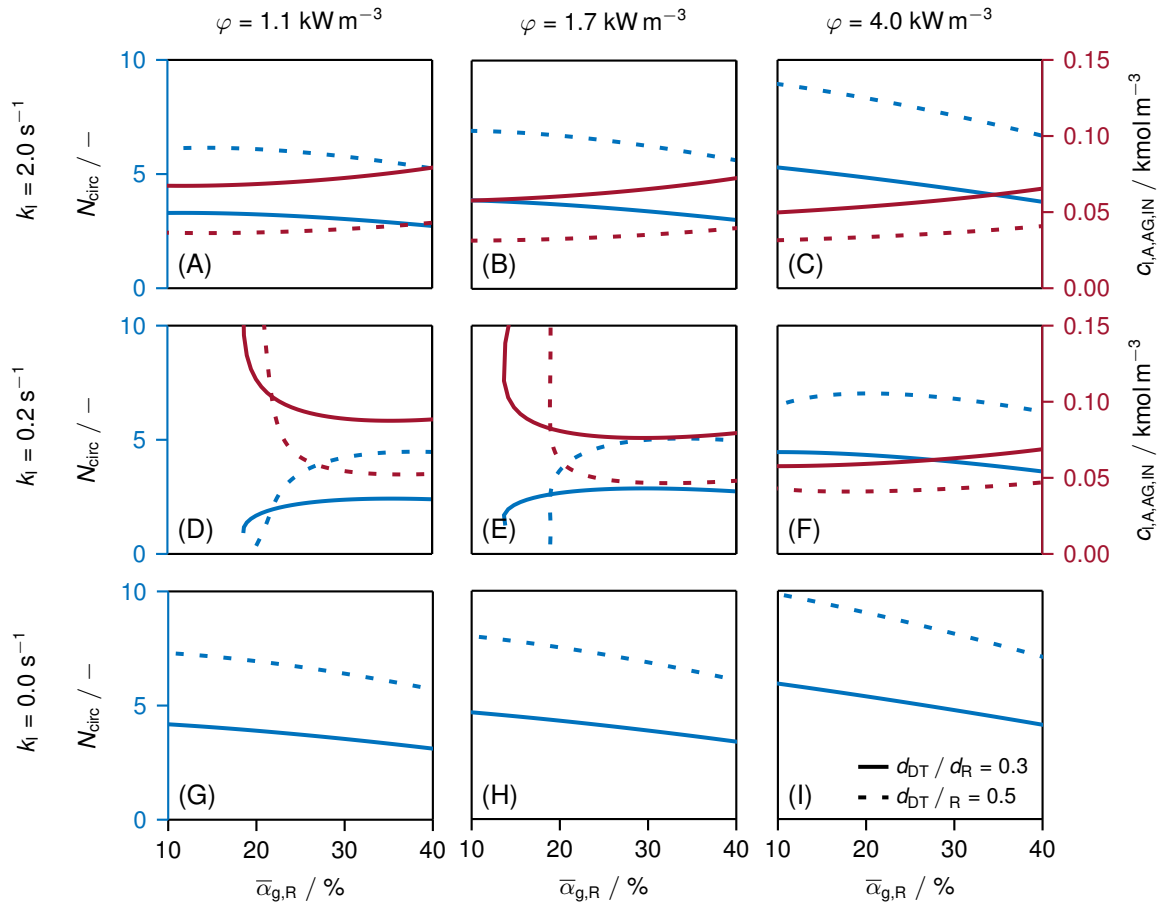


Figure 2.8.: (A)-(I) Influence of rate of reaction constant k_I , power input φ on the circulation number N_{circ} (blue line) and the molar concentration of component A in the liquid phase at the inlet of the draft tube $c_{1,AG,IN}$ (red line) as a function of the gas holdup $\bar{\alpha}_{g,R}$ at different diameter ratios of the DT to R d_{DT}/d_R (line style). Applied parameter see Tab. A.1 and Tab. A.5 where the reactor volume was kept constant.

collapse) of the internal circulation observed for the sensitive reactive case at low values of the gas holdup corresponds to the results shown in Fig. 2.4. Obviously, a small gas holdup is not beneficial for the circulation flow in this case. As discussed in the previous sections, the unfavorable local distribution of gas consumption and the resulting differences between the gas holdup in the draft tube and in the annular gap have a decelerating effect on the internal circulation. However, at large values of the gas holdup the flow rate of the circulating gas is much larger than stoichiometrically required for the reaction. Thus, the consumption of gas causes only small variations of the gas volume fraction along the flow path. Consequently, the influence of the reaction and gas consumption on the circulation flow diminishes at large values of the gas holdup.

The results show that the operating window of feasible gas holdups is significantly smaller for the sensitive reactive case than for the other two cases. It is also likely that commissioning of the JLR is more difficult in the sensitive reactive case. Here, operation with high power input or additional gas feeding points in the draft tube are possible countermeasures that can be taken during operation or design of the JLR.

2.5. Conclusion and Outlook

A one-dimensional model of a jet loop reactor (JLR), which is based on a balance of momentum, is presented in this chapter. It facilitates the local resolution of important process variables such as species concentration, gas volume fraction, pressure, and velocity of gas and liquid phases. For example, the influence of gas consumption by reaction on the gas volume fraction and its feedback on the internal circulation flow can be investigated with the model. Due to its simplicity, simulation with the model are fast and robust. Thus, large ranges of both process and design parameters can be studied with the model. We do not claim that our model predicts the real behavior of the reactor precisely. But the presented model enables tests of different scenarios (that are different combination of process and design parameters). Thereby it provides insights into the complex interactions of the processes taking place simultaneously in the JLR.

Despite the simplification of the model, the influence of the reaction on the fluid dynamics is clearly evident. In general, gas consumption has a decelerating effect on the internal circulation. In addition to that we found unfavorable combination of process conditions (rate of reaction constant, gas holdup and power input) under which the gas consumption causes a drastic reduction of the internal circulation, which would lead in reality most likely to a complete collapse of the internal circulation. If a JLR is designed for a synthesis whose rate of reaction constant is in the sensitive reactive region, the strong influence of the gas consumption has to be considered. Most important, the operational window for possible gas holdups in the reactor is significantly narrowed down. Both at too high and at too low values of the gas holdup the reactor cannot be operated in a stable manner. The results suggest that start-up of this reaction in the JLR has to be done with care. Even the reduction of internal circulation and backmixing alone can have negative effects on the synthesis.

The results show that neglecting the influence of gas consumption on the internal circulation can lead to strong overestimation of the reactor performance (i.e. conversion of reactants and selectivity to target products). That means information gained either from non-reactive calibration and test runs in the production reactor or from laboratory kinetic studies carried out in well-mixed stirred tank reactors cannot be transferred to the reactive case in the production scale.

The presented model does not only enable identification of parameter regions in which strong sensitivity of the internal circulation on gas consumption can be expected but also assessment of different countermeasures. For example the stabilizing effect of additional gas feeding points or of an increase of power input on the internal circulation can be evaluated by means of the model.

Even though observations from industrial JLR support the findings of this chapter no comprehensive experimental data basis exist so far that allows verification of the model predictions. These experimental studies will be carried out in future work. Furthermore, not only gas consumption but also coalescence of gas bubbles can influence the internal circulation. For example, internals such as cooling tubes can enhance coalescence. The structure of the model facilitates easy and swift extensions in future work, so that phase slip and coalescence can be

accounted for in the model. Thereby, these industrially relevant phenomena could be included in sensitivity studies in the future.

The presented model closes the gap between classical process models used for example in flow sheet simulators and detailed CFD simulations. Process models usually do not consider the balance of momentum and therefore cannot describe internal flow phenomena. CFD models enable deep insights into flow phenomena in reactors. However, they are computationally too expensive to cover large parameter spaces. This is where our model comes in. Even though it is not strictly predictive due to its simplicity, the model can be used to study the complex interactions that occur in gas-liquid reactors and apparatus. Thereby, it gives valuable insights both for the design and scale-up as well as for the operation of these processes.

The aim of future studies will be to generalize the observations made in this chapter on concrete example processes. The development and selection of suitable dimensionless indicators could be useful in this regard. Furthermore, an easy-to-calculate stability criterion of the internal circulation would be very helpful for users in industry as well as a validation of the performed simulation studies by experiments.

3. Application and Parameterization of a 1D Multifluid Population Balance Model to Bubble Columns

Contributor Roles Taxonomy

Ferdinand Breit: conceptualization; data curation; investigation; methodology; software; validation; visualization; writing – original draft; writing – review & editing

Chapter redrafted after the following main publication:

F. Breit, C. Weibel, and E. von Harbou, "Application and parameterization of a one-dimensional multifluid population balance model to bubble columns," *AIChE Journal*, 2024. DOI: <https://doi.org/10.1002/aic.18424>.

Abstract

A 1D multifluid population balance model approach is presented as a compromise between computational effort and accuracy. The approach is used to test process scenarios, perform sensitivity analysis, and provide a reliable reactor scale-up and optimization tool. This chapter focuses on a miniplant semi-batch bubble column, where the scale-up behavior in terms of bubble column height, gas flux, and composition of the liquid phase is investigated. Although simplifications were made, the model requires calibration to experimental data using different calibration methods. An optimal calibration procedure is found that minimizes experimental effort while maximizing scalability. The model was tested on various liquid-phase compositions, and it was found to reproduce experimental data accurately. However, the model cannot reproduce flow regime changes and does not perform well across substance systems. This chapter shows that the applied 1D multifluid population balance approach is a valuable and reliable tool in multiphase reactor scale-up and optimization.

3.1. Introduction

In this chapter, the multifluid population balance model (MPB) is applied to bubble columns (BCs) as a standard multiphase reactor. In a previous work of Breit *et al.* [16], the MPB based on kinetic theory approach with size resolution (KTAWSR) developed by Jakobsen and coworkers [24–26] was already successfully applied to BC, and this chapter continues this work. Since the equations are cross-sectional area averaged resulting in a one-dimensional (1D) physical space along the vertical axis, local information about turbulence, backmixing or radial gradients of the gas volume fraction cannot be calculated by the model. This assumption is both the greatest strength and weakness of the developed approach. On the one hand, it provides a significant performance advantage over computational fluid dynamics (CFD) enabling large parameter studies necessary for reactor design. On the other hand, the model cannot predict these effects and is not fully predictive, so the predictions should be taken carefully and be experimentally tested as done this chapter by random sampling. In particular, the turbulent energy dissipation rate must be estimated from integral properties such as inlet gas flux. But local information on the turbulence and the bubble size distribution (BSD) are required in the model to calculate local values for breakage and coalescence of bubbles. Therefore, due to the strong simplifications and the assumptions made, our model was not able to predict the properties of the dispersed phase correctly when all model parameters were adopted directly from literature [16]. However, good agreement between model predictions and experiments was obtained when only a few parameters (four) of the models describing coalescence and breakage of bubbles were fitted to the measurement of local BSD in the bubble column. Obviously, the fitted parameters lump all the specific information of the process (e.g. turbulence) and the chemical system. Thus, our approach makes it possible to describe the complex behavior of dispersed phases in multiphase processes with little computational effort.

So far, the model approach has only been used to describe bubble columns for a few variations of process conditions (superficial gas velocity) [16]. Therefore, no reliable statements can be made about the ability of the model to predict the process reliably over a wide range of parameters. In particular, it is important to know whether the model can predict process conditions outside the parameter range for which the model was trained. Therefore, in this chapter we present a comprehensive study of the influence of process conditions, system properties and reactor geometry on the BSD and integral gas holdup. For this purpose, the superficial gas velocity, the column height and the composition of the liquid phase were systematically varied. The composition of the continuous liquid phase was altered by using different concentrated aqueous (aq.) solutions of sodium chloride, sodium sulfite, ethanol and glycerol. The BSD was measured at 3-11 different vertical positions along the bubble column using an optical imaging probe. The optical imaging probe had been developed in-house [29]. In total, about 600 data sets including BSD and gas holdup were measured in this chapter. To the best of our knowledge, this is the first time that such a comprehensive database of bubble column behavior has been presented in the literature.

In order to find an optimal compromise between experimental effort (size of the training data set) and prediction performance of the model (that is the accuracy of the model prediction for both the training and validation data), a cross-validation was performed. During this

cross-validation, different calibration methods, which differ in their training data set, were compared in a structured hierarchical manner, evaluated using the data of the water + air system. The resulting optimized calibration method was then applied to the water + air system to investigate in detail the model prediction with respect to variations in column height and gas flux. As the model is to be used for reactive processes in the future, it is necessary to ensure that the accuracy of the model predictions is not sensitive to changes in property data caused by concentration changes due to reaction or mass transfer. For this study, we applied the optimized calibration method to a single composition for a given chemical system. We then examined the extent to which the model can be extrapolated to describe other compositions in that chemical system.

The results show that the model, calibrated with only two BSDs at a single vertical height, can be used to interpolate and extrapolate bubble column behavior over a wide range of gas flux, column height, measurement position, and compositions within a given chemical system.

Furthermore, we demonstrate the usefulness of the presented model approach in two exemplary studies. In these tests, the influence of process conditions and different designs on important local properties of the dispersed flow, such as the interfacial area density, are investigated. The results show that the model approach, thanks to a good compromise between the accuracy of the model predictions and the computational effort required to solve the model equations, is a perfect tool for simulation studies of multiphase systems. It provides new insights into the complex behavior of dispersed multiphase processes.

3.2. Experimental Setup

Fig. 3.1 depicts the experimental setup used in this chapter. This setup is based on the design applied in the work by Breit *et al.* [16] but without the air saturator. The primary function of the saturator was to ensure complete saturation of the air with water, thereby minimizing the interfacial mass transfer of water from the liquid phase into the gas bubbles. However, both experimental data and simulation results indicated that the saturator had no significant effect on the system behavior. The following sections provide a brief description of the experimental setup and measurement methodology. Detailed information are available in the source publication [16].

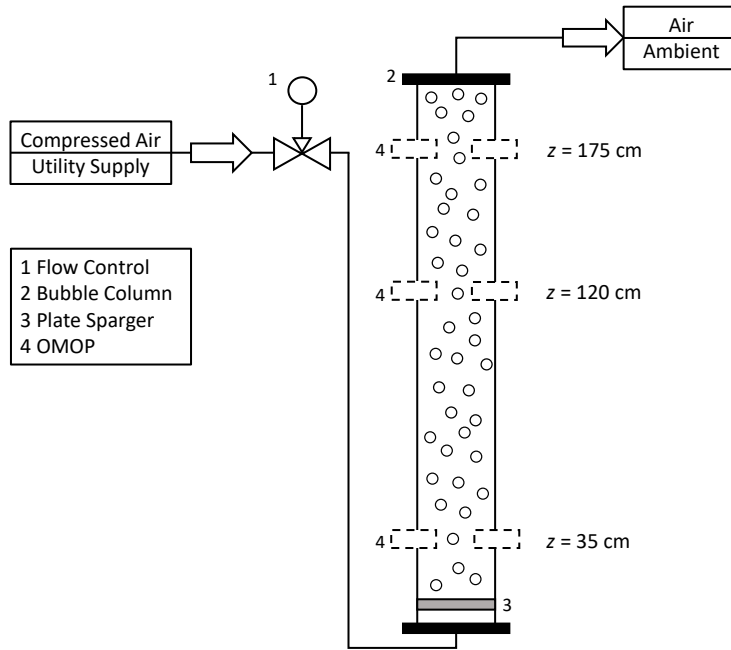


Figure 3.1.: Schematic illustration of the experimental setup. More details are given by Breit *et al.* [16].

Compressed air from the utility supply was introduced into a Polymethylmethacrylat (PMMA) bubble column (BC) (2, the number refer to Fig. 3.1) through a plate sparger (3) with 163 holes of diameter 0.4 mm and a triangular hole pitch of 7.0 mm at $z = 0$ m. The inner diameter of the BC was $d_{BC} = 0.1$ m. The gas flux j_d was regulated by a Brooks Instrument (Hatfield, Pennsylvania, USA) mass flow controller (1) of type GF040 (GF040CXXC-0008030L-N2AVS5-XXXXXX-00C). The air passes through the liquid phase of the column before it leaves the column at the upper end ($z = z_{max}$) into the environment. The BC was filled before starting the gas flow to a height of h_c , which corresponds to the ungasified liquid height, with osmosis water (conductivity about 0.01 mS cm^{-1}), in the following just called water, or different concentrated aqueous solutions of sodium chloride (NaCl), ethanol (EtOH), glycerol (Gly) or sodium sulfite (Na_2SO_3). Note, that the aqueous solution of sodium sulfite reacts with air. However, the uncatalyzed reaction is negligible [47]. The ungasified liquid height corresponds to the BC height and is used synonymously in the following. The BSD and the gas holdup were measured for different measuring heights (just for the BSD), gas fluxes, BC heights and compositions

of aqueous solutions (summary of performed experiments, see Supplementary Information Tab. B.1). All measurements were carried out at ambient conditions ($T^0 \approx 293$ K, $p^0 \approx 1.0 \times 10^5$ Pa).

To determine the gas holdup, either the method of Mühlbauer *et al.* [48] was used or the gasified height was repeatedly read from a scale attached to the outside of the column. In both cases, the relative measurement error is estimated to be less than 1 % based on the standard deviation. Therefore, the error is not indicated in the following figures.

The in-house developed optical multimode online probe (OMOP) (4) was used to determine the BSD. It records telecentric shadowgraph images of the bubbly flow in a measuring gap (typical values are 12 mm or minimum two times the maximum bubble size). Then, an automatic algorithm detects and evaluates the bubbles so that the BSD can be calculated. Details of the setup and evaluation can be found elsewhere [29, 49]. In comparison to other image based optical measurement methods, the OMOP is characterized by its high degree of automatization for the analysis method and high number of bubbles (several thousand to ten thousand) used to calculate the BSD.

As maximal accuracy 6.4 % is specified according to Schulz *et al.* [50] for micrometer-range particles. Therefore, we estimate an error of less than 1.0 % for particles in the millimeter range as they were found in the experiments of this chapter. From own repetition measurements, it is known that the percentage standard deviation of a single operation point (water + air, $z = 80$ cm, $h_c = 1.0$ m, $j_d = 4.0$ cm s⁻¹) is about 1 % for the Sauter mean diameter and about 4 % for the variance [51]. Besagni *et al.* [52] use a similar analysis method and specify an error of 10 % - 15 % . The OMOP should also be in this order of magnitude, tending to be better due to the used telecentric lenses and the computer-aided evaluation. A detailed investigation of the measurement accuracy is still pending. However, the existing uncertainty in the measurement error does not influence the general results and statements of this chapter. All of the recorded and used experimental data are summarized in [51] and are available to the public.

3.3. Modeling and Simulation

3.3.1. Governing Equations

In this chapter, the KTAWSR approach is applied for the balance of momentum and mass of the gas phase so that the velocity and mass of the dispersed phase (here: bubbles) becomes a function of the bubble diameter. For the continuous liquid phase, the common multifluid model was used. To simplify the complex model, the following key assumptions are made:

- Only the momentum and mass balance of both liquid and gas phase are considered
- Cross-sectional averaging, resulting in one physical space dimension along main flow direction (the column height, in the following just z -direction)
- Stationary process
- No mass transfer between phases

In addition to the assumptions made by Breit *et al.* [16], the viscous effects and the influence of the virtual added mass force are neglected because their influence on the simulation results was found to be negligible. Furthermore, these simplifications lead to a significant speed-up of the simulation runs. The Eq. (3.1) - Eq. (3.4), adopted from [16, 25, 26], summarize the governing equations of the applied model.

Population balance equation of gas phase:

$$\begin{aligned} \frac{\partial}{\partial z} (f_d^m(z, \xi) u_d(z, \xi)) + \frac{\partial}{\partial \xi} (f_d^m(z, \xi) \dot{\xi}(z, \xi)) \\ = -B_D(z, \xi) + B_B(z, \xi) - C_D(z, \xi) + C_B(z, \xi) \end{aligned} \quad (3.1)$$

Momentum balance of gas phase:

$$\begin{aligned} u_d(z, \xi) f_d^m(z, \xi) \frac{\partial u_d(z, \xi)}{\partial z} + \dot{\xi}(z, \xi) f_d^m(z, \xi) \frac{\partial u_d(z, \xi)}{\partial \xi} \\ = -\frac{f_d^m(z, \xi)}{\rho_d(z)} \frac{\partial p(z)}{\partial z} - f_d^m(z, \xi) g + m_d(z, \xi) \end{aligned} \quad (3.2)$$

Mass balance of liquid phase:

$$\alpha_c(z) \rho_c \frac{\partial u_c(z)}{\partial z} + u_c(z) \rho_c \frac{\partial \alpha_c(z)}{\partial z} = 0 \quad (3.3)$$

Momentum balance of liquid phase:

$$\alpha_c(z) \rho_c u_c \frac{\partial u_c(z)}{\partial z} = -\alpha_c(z) \frac{\partial p(z)}{\partial z} - \alpha_c(z) \rho_c g + M_c(z) \quad (3.4)$$

Here $f_d^m(z, \xi)$ is the mass density function, z is the vertical position in the bubble column, ξ is the bubble diameter, and $u_d(z, \xi)$ and $u_c(z)$ is the velocity of the dispersed phase, and of the continuous phase, respectively. $\dot{\xi}(z, \xi)$ describes the growth rate in the property space ξ . $B_D(z, \xi)$, $B_B(z, \xi)$ are sink and source with respect to bubble breakage, $C_D(z, \xi)$, $C_B(z, \xi)$ are sink and source with respect to bubble coalescence. $\rho_k(z)$ is the mass density of phase k ,

(with dispersed phase: d, continuous phase: c), $p(z)$ the pressure, g gravitational acceleration constant, $m_d(z, \xi)$ momentum transfer per bubble diameter from the continuous phase, α_k the volume fraction of phase k , $M_c(z)$ interfacial momentum transfer to the continuous liquid phase.

Note, that the PBE given in Eq. (3.1) replaces the mass balance for the dispersed gas phase and that the volume fraction constrain see Eq. (B.9) is used to close the system of equations. The necessary boundary conditions and constitutive equations, including the equations for the estimation of the mixture properties, are summarized in the Supplementary Information B.2. The breakage and coalescence kernel are calculated with the model of Coualoglou *et al.* [53]. This model proved to be a good compromise between accuracy and speed. The turbulent energy dissipation rate (see Eq. (B.17)) is estimated from the superficial velocity of the dispersed phase as suggested by Baird *et al.* [54].

As boundary conditions for the mass density function, the experimental BSD [51] is used directly. The property data of pure water and air as well as the parameters used to calculate the property data of the aqueous solutions are summarized in Tab. B.2 and Tab. B.3 in the Supplementary Information. The boundary conditions applied and further model parameters are listed in Tab. B.4 and Tab. B.3 in the Supplementary Information.

3.3.2. Method of Solution

The Eq. (3.1) - Eq. (3.4) are discretized using the orthogonal collocation method as presented in [55]. This discretization leads to a set of nonlinear equations per balance equation, which are solved separately using the Picard iteration method. In addition, the entire system of equations is solved simultaneously using the Picard algorithm. During each Picard iteration of the entire system, the grid is updated to correspond to the height of the bubble column calculated from the total liquid phase mass balance. This allows us to predict the gas holdup. See Breit *et al.* [16] for more information.

3.3.3. Regression Model

To calibrate the model, the following regression approach is used. The independent variables \mathbf{X} are the gas flux j_d , the ungasified liquid height h_c , the measurement position z , the solute concentration c_s and the solute s . The dependent variables \mathbf{Y} are the bubble size distribution \hat{f}_d^n , moments of bubble size distribution ξ_{32}, σ, ω (see. Eq. (B.44) together with Tab. B.5) and the gas holdup $\bar{\alpha}_d$ (see Eq. (B.10)). The unknown parameters β are the empirical parameters C_1 to C_4 of the breakage and coalescence kernel of Coualoglou *et al.* [53]. After a preliminary study, it was found that the parameter C_2 is not significant and has a large confidence interval. Thus, this parameter is set to the value $C_2 = 1.0 \text{ m}^{-2}$. The parameters C_1, C_3, C_4 of the used breakage and coalescence kernel of Coualoglou *et al.* [53] have no units, so that a physical interpretation based on the unit is not possible. If future work involves kernels with parameters that have units, it is important to consider how these units relate to the characteristics of the system being investigated. In order to determine the parameters $\beta = (C_1, C_3, C_4)$ of the model

function f_{model} the minimization problem Eq. (3.5) is solved using the function `lsqnonline` with the trust-region-reflective algorithm provided in the Optimization Toolbox of the software MATLAB[®] Version R2019a (9.6.0.1072779) from the publisher The MathWorks Inc. (Natick, Massachusetts, USA). The sum of the squared absolute percentage error is used as loss function, f_{loss} .

$$\min_{\boldsymbol{\beta}} f_{\text{loss}}(\boldsymbol{\beta}, \mathbf{X}, \mathbf{Y}) = \min_{\boldsymbol{\beta}} \left(\sum_i \left| \frac{\mathbf{Y}_i - f_{\text{model}}(\boldsymbol{\beta}, \mathbf{X}_i)}{\mathbf{Y}_i} \right|^2 \right) \quad (3.5)$$

Here is i a unique identifier for an experiment characterized by the values of \mathbf{X}_i . A detailed preliminary investigation with the Global Optimization Toolbox of MATLAB[®] shows that it can be assumed that there is only one global minimum. The following values were used as initial guess for the parameter estimation: $C_1 = 0.0203$, $C_3 = 0.697$, $C_4 = 5.63$. The values were adopted from our previous work [16].

The termination condition during the calculation of the Picard iteration on the entire system and the one for the solution of the PBE (cf. Section 3.3 [16]) were reduced to $\epsilon = 1 \times 10^{-4}$ in order to save computing resources. In a preliminary study, the reduction of the termination condition did not have a significant effect on the subsequent fit result. The calibrated parameters of the different simulations can be found in the Supplementary Material of the publication [3].

Model Validation: Cross-Validation

In order to validate the model and to measure the prediction performance, a cross-validation is performed. The aim of this chapter is to find an optimal compromise between experimental effort (size of the training data set known to the model) and prediction performance. Therefore, a manual cross-validation was applied in a structured hierarchical manner in which different calibration methods were compared on the basis of the mean absolute percentage error (*MAPE*, see Eq. (3.6)) and the percentage error (*PE*, see Eq. (3.7)) to measure the prediction performance. The calibration methods differ in the size and selection of the training data set and in the selection and number of the dependent variables. Whereby the different training data sets result from the selection and number of the independent variables.

$$MAPE = \frac{1}{N_j} \sum_i^{N_j} \left| \frac{\mathbf{Y}_i - f_{\text{model}}(\boldsymbol{\beta}, \mathbf{X}_i)}{\mathbf{Y}_i} 100 \% \right| \quad (3.6)$$

$$= \frac{1}{N_j} \sum_i^{N_j} |PE| \quad (3.7)$$

Where N_j is a set of experiments included in the calculation. A calibration method encompasses four components. First, which dependent variables \mathbf{Y} are included, second to fourth, which measurement positions z , gas fluxes j_d and bubble column height h_c are included in the training data set. The selection of the dependent variables is intended to investigate which of these variables is best suited for optimization. The selection and number of independent variables determines the size of the training data set on which Eq. (3.5) is trained. In order

to distinguish between the calibration methods, a composite label system is used. The labels of the data sets that were included in the training data are defined in Tab. 3.1.

Table 3.1.: Composite label system to identify a calibration method.

| Y_i | Method label - included variable | | |
|-----------------------------|--|-------------------------------|---------------------------------------|
| | H - $\bar{\alpha}_{d,i}$ | M2 - $\xi_{32,i}, \sigma_i^2$ | M3 - $\xi_{32,i}, \sigma_i^2, \omega$ |
| | M2H - $\xi_{32,i}, \sigma_i^2, \bar{\alpha}_{d,i}$ | D- $\hat{f}_{d,i}^n$ | |
| X_i | Method label - included value | | |
| $j_{d,i} / \text{cms}^{-1}$ | jd3 - (3) | jd2,3 - (2,3) | jd2,4 - (2,4) |
| | jd14 - (1,4) | jd234 - (2,3,4) | jd1234 - (1,2,3,4) |
| z_i | z1 - (high) | z2 - (middle, high) | z3 - (low, middle, high) |
| $h_{c,i}$ | hc60 - (60) | hc60 - (80) | hc100 - (100) |

The label Mz2jd234hc140 for example states that Eq. (3.5) was solved respectively trained based on the Sauter mean diameter and the variance of the experimental data set consisting of all measurements at $z = (80, 140)$ cm and $j_d = (2, 3, 4)$ cms^{-1} in a 140 cm high bubble column.

Optimization of the calibration method is performed only in the water + air system. This means that data with variations in the solute and its concentration are not taken into account. It is important to note that the different calibration methods have different training data sets but are all evaluated after training, for a given simulation study, on the same test data set with the *MAPE*. The *MAPE* is always calculated using the two dependent variables Sauter mean diameter (ξ_{32}) and variance (σ^2) of the measured BSDs. The adjusted parameters β of all simulations and study's can be taken from the Supplementary Material of the publication [3].

3.4. Results and Discussion

3.4.1. Evaluation of the Calibration Methods

Choice of the Dependent Variables

In the first study, the influence of the choice and number of dependent variables is investigated. The data set of the water + air system acquired with a bubble column height of $h_c = 140$ cm was used for that study. To shorten the notation, the label of the bubble column height is omitted. The results are shown in the Supplementary Information B.4 and are only briefly summarized here.

As expected, if the gas holdup is included as the only dependent variable in the parameter estimation (method H), a *MAPE* of > 60 % is obtained. If the parameter estimation is related to two moments of the BSD (method M2), the result is a *MAPE* of 12 % in average (over j_d and z). If the gas holdup is further added to the two moments of the method M2 as a dependent variable (resulting in method M2H), the *MAPE* and the *PE* with respect to the gas holdup remains more or less the same (cf. Fig. B.1).

Including another moment to the method M2, the kurtosis (method M3), shows that the *MAPE* increases to 20 % in average (over j_d and z , cf. Fig. B.2). This finding can be attributed to the large experimental uncertainty of this quantity so that an overfitting (the model memorizes the training data set instead of generalizing it) takes place. Additionally, it is important to note that no more than two independent moments should be included in the calibration method if the underlying BSD can be described by a two-parametric distribution function, e.g. Gaussian, Log-normal or Weibull, otherwise overfitting may occur.

When complete BDS (method D) is considered for calibration, the *MAPE* becomes 26 % on average (over j_d and z) and is thus larger compared to method M2. This is due to the fact that the moments are integral and therefore averaged quantities that are less sensitive to outliers and measurement noise. If the complete BSD is used instead of the two moments for the estimation of the model parameters, there is the risk that random measurement errors are represented by the model parameters. This worsens the overall prediction performance of the model for method D compared to method M2.

In summary, as expected, the calibration of the model to integral measures alone, such as the gas holdup, is not sufficient to achieve good prediction performance of the model. Instead, information is needed that reflects the specific behavior of the dispersed phase for the given process and chemical system. The BSD, or more precisely the two moments of the BSD, provides exactly this information. In the following, only two moments (Sauter mean diameter, variance) are used as dependent variables to calculate the loss function Eq. (3.5).

Choice of the Independent Variables: Gas Flux and Vertical Position

In the second study, the influence of the choice and number of independent variables on the prediction performance is investigated. For that study, the data sets from the water + air system with a bubble column height of $h_c = 140$ cm were used and the gas flux and vertical measuring position was chosen as variable independent parameters. Again, to shorten the notation, the label of the bubble column height is omitted.

Fig. 3.2 shows the influence of the choice and number of independent variables of method M2 on the *MAPE*. When only one vertical position and only one gas flux are used to calibrate the model, the largest *MAPE* occurs. Obviously, the training data do not represent enough information about the system. Furthermore, it can be observed that when more vertical positions are included in the training data, there is a slight trend towards an improved prediction performance of the model (cf. Fig. 3.2A). However, this improvement is small. Therefore, the authors believe that the laboratory effort associated with each additional measurement position is not justified.

In contrast, if the training data set includes at least two experiments carried out with different gas fluxes, the prediction performance increases as shown in Fig. 3.2B. However, when data from more than two gas flows are included in the calibration, the increase in prediction performance is small compared to the case calibrated with data obtained for two gas fluxes. Obviously, these two data sets provides enough information of the behavior of the multiphase system so that a good model fit is obtained.

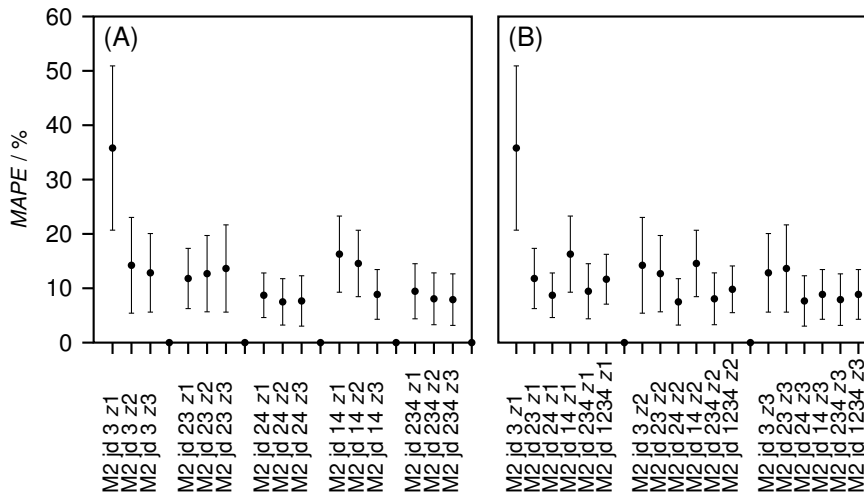


Figure 3.2.: Mean absolute percentage error *MAPE* (see Eq. (3.6)) evaluated on the water + air data set with $h_c = 140$ cm for different calibration methods (see Section 3.3.3). Grouping of the observations: **(A)** the number of included gas fluxes in ascending order, **(B)** vertical measurement position. Internal sorting of the groups: **(A)** the additional vertical measurement positions in ascending order, **(B)** gas flux and number in ascending. Evaluation data set: $h_c = 140$ cm.

It can also be observed that the *MAPE* increases when the lowest gas flux is included in the calibration method (cf. Fig. 3.2B). This may be attributed to the fact that the multiphase flow is in a different flow regime under these conditions. That means that the turbulence,

which influences e.g. breakage, coalescence and internal backmixing, is different compared to the experiments with higher gas flux ($j_d > 1 \text{ cm s}^{-1}$). A detailed discussion on that subject is given in Section 3.4.2.

In summary, the model can describe (interpolate) the behavior of the dispersed flow in the bubble column well for gas fluxes between $j_d = 2 \text{ cm s}^{-1}$ and $j_d = 4 \text{ cm s}^{-1}$. The calibration method that uses two moments of the BSD (Sauter mean diameter, variance), which is measured at one vertical position only but for two different gas fluxes, is the best compromise between prediction performance of the model and experimental effort. This calibration method (M2jd24z1) is referred to in the following as the optimized calibration method.

Choice of the Independent Variables: Column Height

In the third and final study, the optimized calibration method (M2jd24z1) is used to investigate the influence of the choice of the bubble column height on the prediction performance. As mentioned above, the bubble column height is an independent variable that was not considered in the optimization of the calibration method. For this purpose, method M2jd24z1 is applied to various h_c and evaluated on the basis of the complete data set (all gas fluxes, measurement positions and BC heights). The Fig. 3.3 shows the violin plot of the percentage error PE as a function of the BC height $h_{c,cal}$ which was used as the calibration data set.

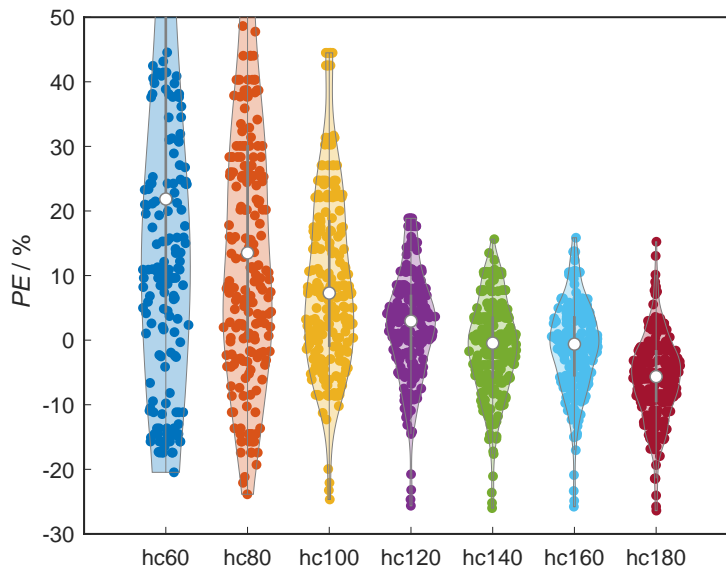


Figure 3.3.: Violin plot of the percentage error PE as function of the BC height which was used as calibration data set. Calibration method variation hc (see Section 3.3.3) based on M2jd24z1. Evaluation data set: complete water + air dataset.

It can be seen that the mean value of the PE becomes smaller with increasing bubble column height (i.e. liquid holdup), and that there are only fewer outliers. A possible explanation for this observation could be that with a small column height, the deviation from the ideal plug flow, which is assumed in the model, is expressed more strongly than with a large column. In addition, the applied measurement probe (OMOP) is invasive. That means, that the volume

of the column influenced by the probe is relatively large in comparison to the total holdup of the column when the height of the column is small.

In summary, the higher the bubble column, the better the predication performance. A height of 1.4 m is considered as sufficient (cf. Fig. B.3).

3.4.2. Investigation of Prediction Performance

Bubble columns height and Gas Flux

Fig. 3.4 shows the Sauter mean diameter as a function of the z -direction for different BC heights (A)-(F) and gas fluxes j_d (colors). The boundary values are marked as stars. The values that are used for the calibration are marked by a crosshair (see Fig. 3.4D). The model was calibrated using the optimized method (M2jd24z1) with the $h_c = 1.4$ m data set (see Section 3.4.1). Note that Fig. 3.4 corresponds to the data series measured with a bubble column height of 1.4 m shown in Fig. 3.3.

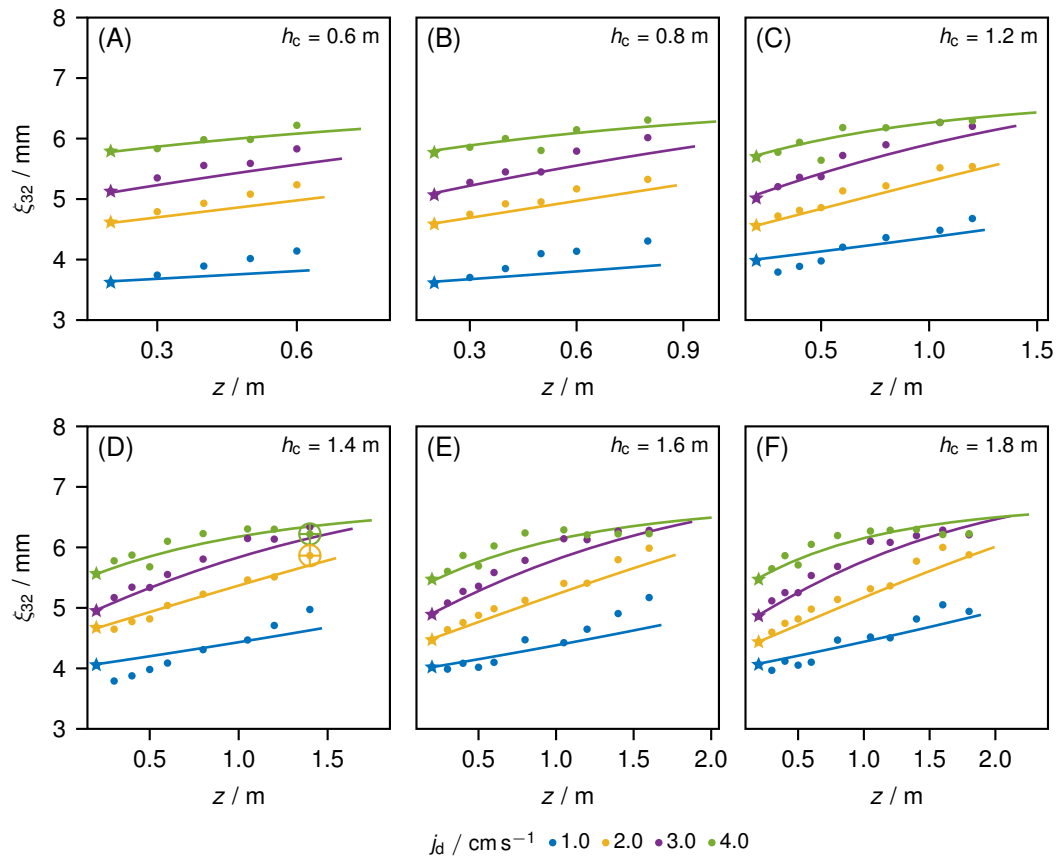


Figure 3.4.: (A)-(F): Sauter mean diameter ξ_{32} as a function of the z -direction for different gas fluxes j_d (color) and different bubble column heights h_c . Calibrated with method Mjd2,4z1 with $h_c = 1.4$ m. Definitions: Experiments (symbols), model predictions (lines), calibration points (crosshairs), boundary values (stars). Chemical system: water + air.

The experimental data reflect the expectations: the Sauter mean diameter increases with increasing vertical position and gas flux. The latter observation is mainly due to the fact that

as the gas flux increases, more turbulence is introduced into the system, which in turn leads to an increased coalescence frequency. The vertical position corresponds with the residence time of the gas phase and thus the total number of coalescence events. Therefore, the bubble diameter increases with residence time and vertical position, respectively. After a certain vertical position in the column, the Sauter mean diameter no longer increases linearly. Instead, its slope decreases. This decrease in slope can be attributed to the higher breakup frequencies of larger bubbles. On the other hand, at that position the fraction of bubbles whose size is larger than the maximum bubble diameter that can be captured by the OMOP is no longer negligible.

In addition, it can be observed that the increase in Sauter mean diameter is approximately equidistant for gas fluxes $j_d = (2.0, 3.0, 4.0) \text{ cm s}^{-1}$. Between $j_d = 2.0 \text{ cm s}^{-1}$ and $j_d = 1.0 \text{ cm s}^{-1}$, however, a larger difference in Sauter mean diameter can be observed. This increase may indicate a change in the flow regime, as described above. This changes the turbulence in the column and thus the breakage and coalescence of the bubbles. Obviously, the simple turbulence model used in this chapter (see Section 3.3.1), which describes a linear relationship between the turbulent energy dissipation rate and the gas flux, is not able to correctly reproduce this change in the flow regime.

The comparison of experimental data and simulation results shows that the model can reliably predict the Sauter mean diameter in a wide range of process parameters (i.e. BC heights and gas fluxes). The deviation of the model measured with the *MAPE* evaluated within the respective BC height is shown in Fig. B.3 in the Supplementary Information. It is important to mention that only the two data, which are shown with crosshairs in the Fig. 3.4, were used for the calibration of the model.

Even the transformation from a linear shape at a lower BC height (cf. Fig. 3.4A) to a more curved shape at a higher BC height (cf. Fig. 3.4F) can be reproduced by the model without any prior knowledge of that behavior which indicates that the OMOP was not yet at its measurement limit as mentioned above. The largest deviations between model predictions and experimental data are found for a gas flux of $j_d = 1.0 \text{ cm s}^{-1}$.

In all likelihood, these large deviations are again caused by the change of flow regime discussed above, which obviously cannot be adequately described by the model. A different model to describe the turbulent energy dissipation rate, other than the extremely simple approach taken in this chapter by Baird *et al.* [54] (see Eq. (B.17)), could probably improve the prediction accuracy. However, this optimization of the model was not the focus of this chapter and will be considered in more detail in a future work. It is important to note that despite these limitations of the model, the general trend of the dispersed flow behavior is well predicted for the low gas fluxes.

Chemical System

Fig. 3.5 shows the Sauter mean diameter as a function of concentration of solute c_s for the aqueous solutions of ethanol (A), glycerol (B) sodium chloride (C) and sodium sulfite (D) for the lowest vertical measurement position available. The gas flux was varied depending on the chemical system in the range $j_d = (1.0, \dots, 5.0) \text{ cm s}^{-1}$. For the sake of clarity, not all gas fluxes have been depicted, but are available in the Supplementary Material of the publication [3]. The liquid holdup (BC height) was constant at $h_c = 180 \text{ cm}$ during these measurements.

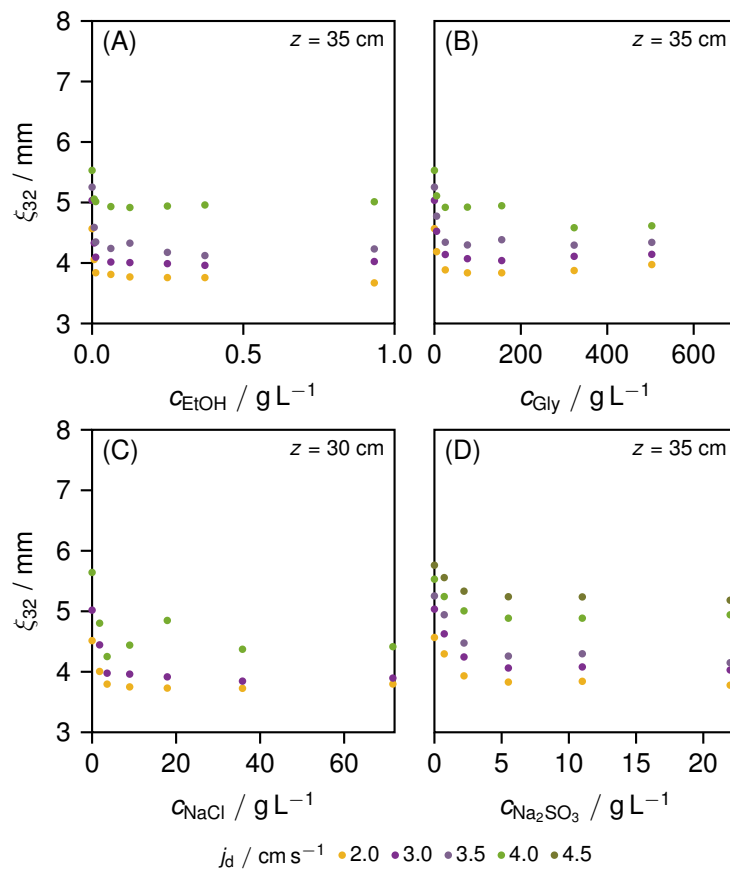


Figure 3.5.: Sauter mean diameter ξ_{32} as a function of the solute concentration c_s for different aqueous mixtures for different superficial gas velocity j_d (color) at the lowest available measuring position z . Solutes: ethanol (A), glycerol (B), sodium chloride (C) and sodium sulfite (D).

Fig. 3.5 shows that regardless of the chemical system, the Sauter mean diameter initially decreases with increasing concentration and then remains almost constant. This form of the curve indicates that the addition of the solutes inhibits coalescence of bubbles. Similar observations are reported in other works, e.g. [52, 56–59].

The aqueous mixtures with glycerol show a somewhat different behavior than the other mixtures. First the Sauter mean diameter decreases but it begins to increase again at higher concentrations of glycerol. This behavior was also found by Samaras *et al.* [59] and is attributed by the author to the influence of the viscosity of the liquid phase.

The comparison between experimental data and model prediction for the different aqueous

solutions is summarized in Fig. 3.6. It shows the Sauter mean diameter as a function of the z -direction for differently concentrated aqueous solutions of glycerol (A)-(D), sodium chloride (E)-(H), sodium sulfite (I)-(L) and ethanol (M)-(P). In addition, the gas flux was varied for each system. The calibration was performed only once for each chemical system with the optimized calibration method (i.e. one distinct concentration of solute, two gas fluxes and one additional vertical position). This data set is marked with a crosshair in the figure.

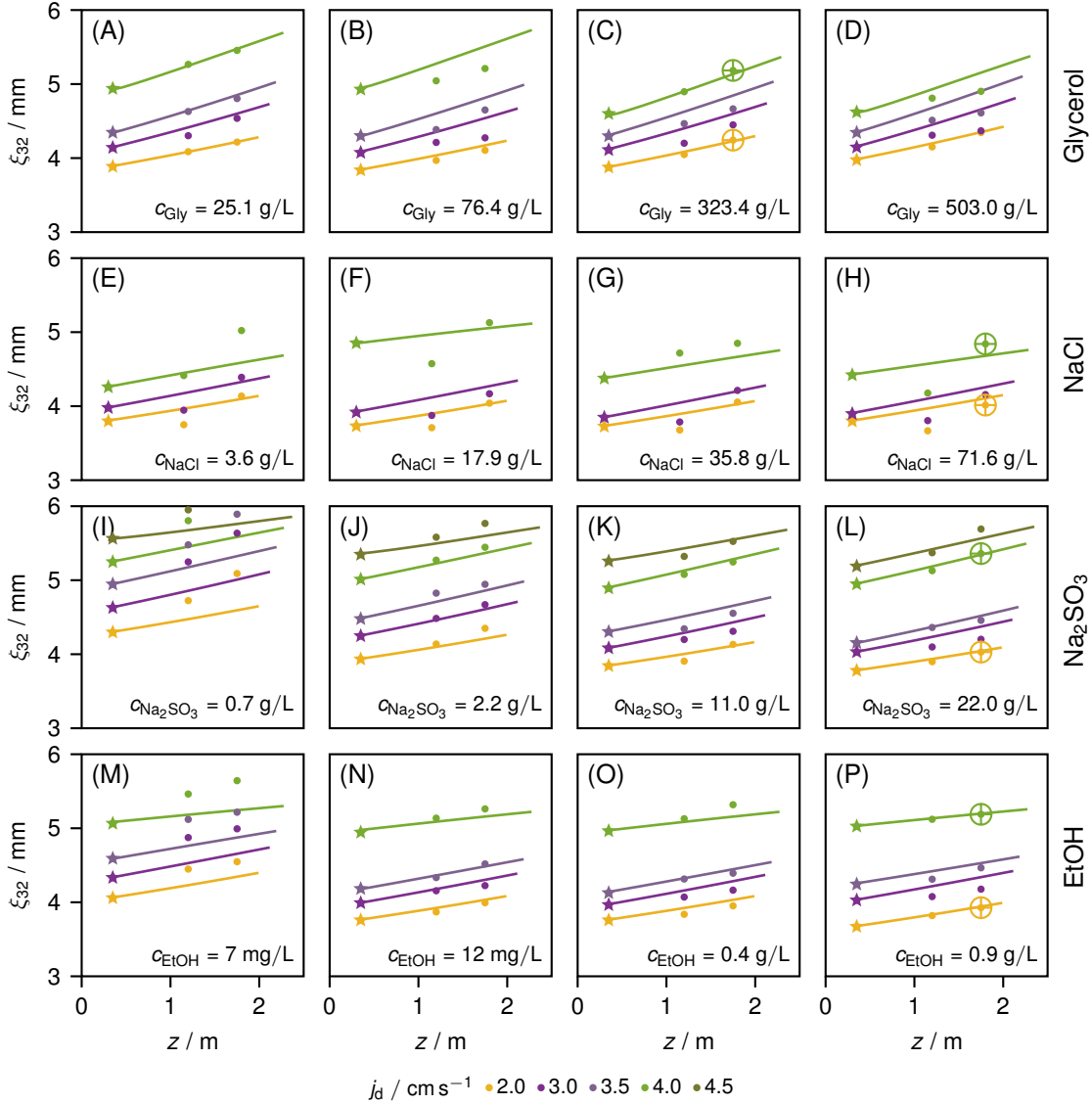


Figure 3.6.: Sauter diameter ξ_{32} as a function of the z -direction for different gas fluxes j_d (color) and different aqueous mixtures of glycerol (A)-(D), sodium chloride (E)-(H), sodium sulfite (I)-(L) and ethanol (M)-(P) at different concentrations. Definitions: Experiments (symbols), simulations (lines), calibration points (crosshairs), boundary values (stars).

Fig. 3.6 shows that all chemical systems, including the water + air system discussed in the previous section, behave similarly as the vertical position or gas flow is increased, namely that the bubble diameter becomes larger. Furthermore, Fig. 3.6 shows that the model can predict the Sauter mean diameter over a wide range of concentrations of solute and gas fluxes. However, it is noticeable that the model mostly underestimates the Sauter mean diameter and

that the lowest concentration of solute (farthest from the calibration point) has the lowest prediction performance.

This is to the fact that although the breakage and coalescence kernel of Coualoglou *et al.* [53] used in this chapter contains the concentration-dependent property data of viscosity, surface tension and mass density of gas and liquid phase, the model is not capable to describe the observed change in breakage and coalescence behaviour with constant parameters C_i across aqueous solution. Therefore applying the fitted parameters directly from one system (e.g. water + air) to another (e.g. aq. EtOH + air) is not recommended, the prediction performance of the model decreases significantly. The reason for that could be that the used kernel underestimate the dependency of the just slightly changing property data within and across the aqueous solution. Furthermore the kernel of Coualoglou *et al.* [53] do not reflect the effect of impurities and surfactants. The literature [60–62] suggests kernels that can take such effects into account. But Li *et al.* [61] also shows that these kernels are not necessarily better than kernels that do not take this effect into account. As summarised well in Falzone *et al.* [62] we are still far away from having kernels that describe all the different breakage and coalescence mechanics at once and the influence of surfactants. We hope that we can contribute to the development of new kernels with our measured data. However, using constant parameter across the aqueous solution the general trends are still correctly described (not shown here). On the other hand, if calibration is carried out once per aqueous solution, the measured data can be reproduced well as described above. This means that sufficient information reflecting the properties of the considered chemical system must be contained in the fitted model parameters and the inlet BSD. Thus, in order to predict the behavior of bubbles in bubble columns for any chemical system without having to measure the inlet BSD for the given system and process conditions in each case, a reliable model of bubble formation in the installed disperser is necessary. First attempts have been made by the authors with the adaptation and extension of the model suggested by Geary *et al.* [63]. However, the development of a model describing the behavior of bubble formation is not in the scope of this chapter.

For the system aq. NaCl + air, large deviations between the measured and predicted Sauter mean diameter can be observed at a vertical measurement position of 1.2 m (see Fig. 3.6P to Fig. 3.6H). This deviation could be a measurement error or it could be a feature of the real system behavior that cannot be adequately described by the model.

To get a further impression of the prediction performance of the model, Fig. 3.7 shows comparison of the predicted and measured normalized number density distribution \hat{f}_d^n (see Eq. (B.45) and Eq. (B.46)) as a function of diameter ξ for different vertical positions z and gas fluxes j_d for the system aq. NaCl + air. The model can predict the experimental results (figures in the second and third column) well for different process parameters even though the model was calibrated using data from measurements with a different concentration of NaCl.

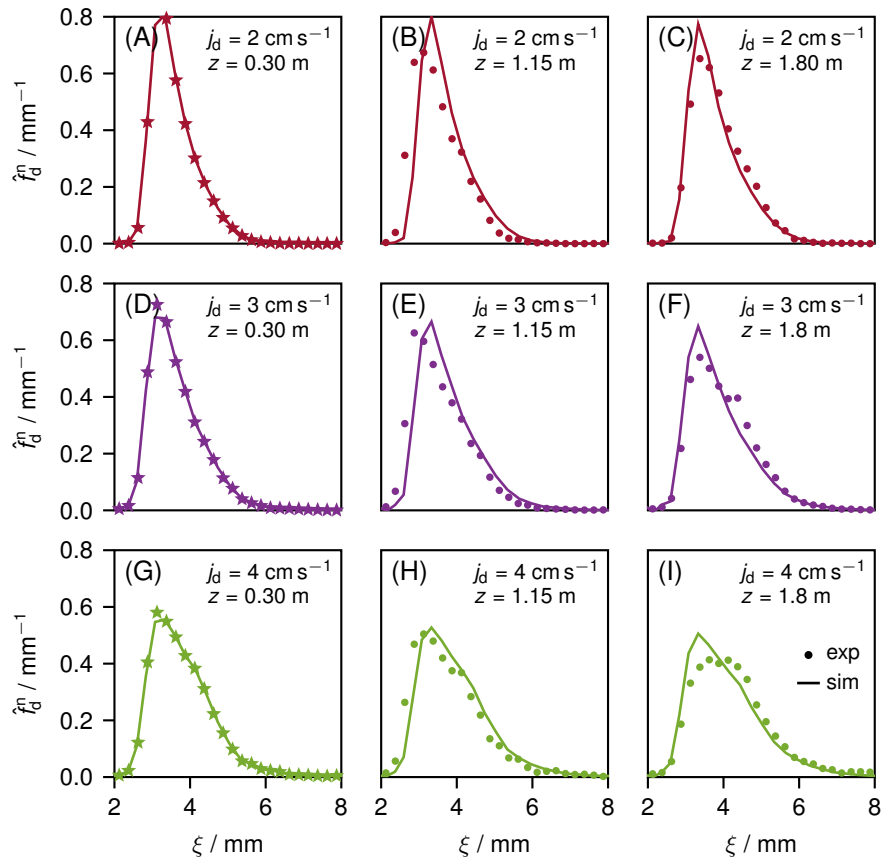


Figure 3.7.: Normalized number density distribution \hat{f}_d^n as a function of bubble diameter ξ for different gas fluxes j_d (color, along rows) and vertical positions z . Chemical system: aq. NaCl + air ($c_{\text{NaCl}} = 3.6 \text{ g L}^{-1}$). Simulated with the fit parameters of aq. NaCl + air ($c_{\text{NaCl}} = 71.6 \text{ g L}^{-1}$). Experiments: symbols, simulations: lines, boundary values: stars.

3.4.3. Scenario Test

Chemical System

In the first scenario, the influence of the chemical system on the local interfacial area density is investigated. Fig. 3.8 shows the influence of the concentration of ethanol on the profiles of the interfacial area density a , mean diameter ξ_{10} and gas volume fraction α_d .

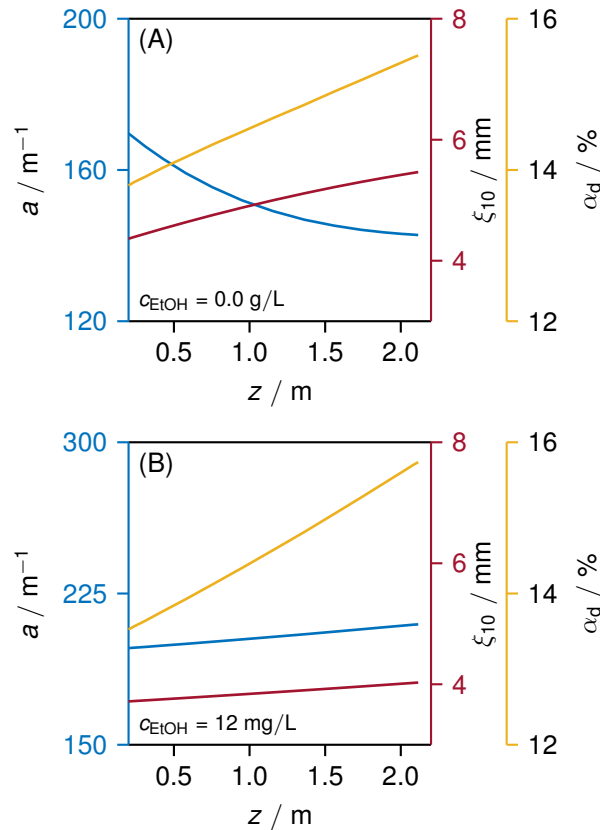


Figure 3.8.: Interfacial area density a (blue), gas volume fraction α_d (yellow) and mean diameter ξ_{10} (red) as a function of vertical height z for (A) water and (B) aq. EtOH + air.

For both chemical systems, the gas volume fraction and the mean diameter increase as expected with the height. The interfacial area density, however, shows a complete different profile for both chemical systems. While it increases in the water system, it decreases in the system aq. EtOH + air. The different trends are caused by the complex interaction of local BSD and gas volume fraction. The interfacial area density has a major influence on the local mass transfer. The local gas (or liquid) volume fraction is important for local conversion rates or they can even influence the internal fluid dynamics (see e.g. Chapter 2). If classical correlations [64, 65] are used to determine this local change cannot be mapped. Thus, this study shows the importance of being able to correctly predict the local properties of the dispersed flow (bubble diameter, gas fraction, gas velocity, interfacial area) in order to be able to predict local phenomena such a mass transport and reaction rates. In addition to considering local resolution, the determination of crucial design parameters, including phase volume fraction,

interfacial area density, Sauter mean diameter, as well as mass and heat transport, often relies on the application of empirical correlations, as consolidated in references [64, 65]. These correlations encompass numerous empirical parameters tailored to specific systems from diverse origins. In contrast, our proposed model reduces this multitude of parameters to three, which increases the efficiency and simplicity of the modeling process.

Sparger

In the second scenario, the influence of the geometry parameters of the used sparger on the behavior of the dispersed flow is investigated. Two different types of spargers are considered: a sparger that generates small bubbles (called fine sparger) and a sparger that generates large bubbles (called coarse sparger). The assumed BSDs generated by the two different spargers are depicted in Fig. 3.9A and B. At the same gas flux, the fine sparger would cause a higher pressure drop and thus higher operating costs than the coarse sparger. As an engineer, the question now arises whether these additional operating costs are compensated for by improved mass transfer (and thus e.g. higher conversion rates and space-time-yields in the bubble column). For this purpose, the engineer must be able to estimate the influence of the initial BSD on the interfacial area and thus on mass transfer. Fig. 3.9C and D shows that the model presented in this chapter can do exactly this prediction.

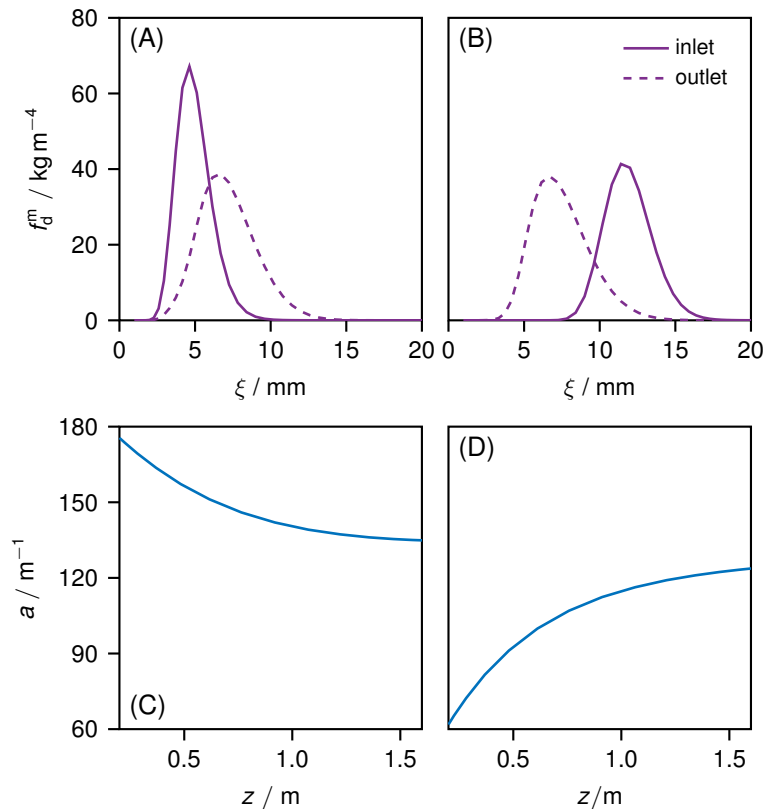


Figure 3.9.: Mass density distribution f_d^m as a function of the bubble diameter ξ at the inlet and outlet (line style) and the interfacial area density a as a function of the z -direction for the fine sparger (A,C) and coarse sparger (B,D).

Comparing Fig. 3.9A with Fig. 3.9B, it is noticeable that in the case of the fine sparger the bubbles tends to coalesce while flowing upward. In contrast, the bubbles leaving the coarse sparger break rather than coalesce. As a result, the interfacial density decreases along the column height when the fine sparger is used (cf. Fig. 3.9C) and it increases when the coarse sparger is used (cf. Fig. 3.9D). Since the growth of bubbles is negligible, both the BSD and the interface density of the two different spargers converge to similar values at the outlet of the column, due to an equilibrium of breakage and coalescence. If the model were now coupled in a next step with mass transfer and reactions in the liquid phase, a statement could be made whether the additional operating costs are worthwhile.

3.5. Conclusion and Outlook

In this chapter, a 1D multifluid population balance model (1D-MPB) approach to predict the behavior of dispersed flow in bubble columns was presented. The approach represents a compromise between computational effort and accuracy. The model enables scenarios test that can reveal the complex interaction of process parameters (e.g. gas flux), geometry parameters (e.g. column height) and properties of the chemical system.

Due to the simplifications made, it is necessary to calibrate the model to experimental data. Different calibration methods were compared in a structured hierarchical manner. An optimal calibration method could be found that minimizes the experimental effort (i.e. the number of measurements needed) while maximizing accuracy of the prediction. We found a calibration method that requires only data from one local measurement position in the bubble column acquired for two different gas fluxes. Data from approximately 600 different experiments was used to evaluate the performance of the calibration method. For this purpose, the gas flux, the bubble column height and the composition of the liquid phase were systematically varied. The calibrated model can reproduce and predict the experimental data well. Only for the smallest gas flux larger deviations were found. We assume that these larger deviations are attributable to a change in the flow regime. Obviously, the very simple turbulence model cannot adequately describe this change. Nevertheless, the model predicts the general trends correctly. To investigate the performance of the model for an even larger range of parameters, more experiments in bubble columns will be carried out. Especially, the accuracy of the model predictions for larger column diameters and columns height will be of interest. Furthermore, the influence of the flow rate of the liquid phase will be studied.

To demonstrate the usefulness of the presented method, the model was applied to two scenario tests. These tests show that the model is well suited to predict the influence of process conditions and different designs on important local properties of the disperse flow, such as interfacial area density.

The presented modeling approach was applied in this chapter to describe dispersed flow in bubble columns. In principle, even complex (three-dimensional) internal flow characteristics as they can be found for example in jet loop reactors (cf. Chapter 2) can be described by this approach. In this case, the reactor must be subdivided into characteristic compartments. Then each compartment can be described with the MPB approach. This application to more complex reactors and the inclusion of further couplings as shown in Fig. 1.1 is subject of future work.

Overall, it has been demonstrated that the applied 1D multifluid populations balance approach is able to describe the general behavior of complex multiphase flow. Therefore, it is a valuable tool for engineers to get insights into the complex interactions that can occur in these systems.

4. A Quantitative Evaluation of the Prediction Performance of a One-Dimensional Multifluid Population Balance Model in Continuous and Semi-Batch Bubble Columns

Contributor Roles Taxonomy

Ferdinand Breit: conceptualization; formal analysis; investigation; methodology; project administration; software; validation; visualization; writing - original draft; writing - review & editing

Chapter redrafted after the following submitted manuscript:

F. Breit, C. Zipp, C. Weibel, and E. von Harbou, "A Quantitative Evaluation of the Prediction Performance of a One-Dimensional Multifluid Population Balance Model in Continuous and Semibatch Bubble Columns," *Chemical Engineering Research and Design*, 13.09.2024. Manuscript number: CHERD-D-24-02143.

Abstract

The objective of this chapter was to evaluate the efficacy of a one-dimensional multifluid population balance model (1D-MPB) in predicting the axial variation of the bubble size distribution (BSD), gas phase velocity, and gas volume fraction in a bubble column. The bubble column was operated in either a semi-batch mode, without liquid feed, or a continuous mode, with co-current liquid and gas feed. The model's predictions were compared with experimental data obtained through minimal invasive fiber optic needle probes. The experiments were carried out with different spargers and varying gas and liquid fluxes. The model parameters were previously determined in a different study. The findings indicate that the model accurately predicts the BSD, Sauter mean diameter and local gas volume fractions, particularly at medium gas fluxes in semi-batch mode. The application of a modified sparger model to predict inlet BSDs demonstrated potential, although limitations were observed at higher fluxes. In continuous co-current mode, the model (parameterized with data from semi-batch experiments), exhibited

robust prediction performance without the need for recalibration, indicating the soundness of the underlying physical principles and the value of the method for scale-up. Future work will focus on refining the turbulent energy dissipation model to enhance the model's accuracy and applicability for industrial bubble column design and optimization.

4.1. Introduction

In this chapter, the study of evaluating the prediction performance of the multifluid population balance model (MPB) applied to bubble columns (BCs) of Chapter 3 is continued. In order to demonstrate the applicability of our methodology for the scale-up of bubble columns, it is necessary to prove that the model is capable of predicting states that are situated even further outside the regime to which it was calibrated. Thus, a new series of experiments was conducted with the objective of determining the influence of the different designs of gas spargers on the properties of the dispersed gas phase in the column operated in semi-batch mode. Furthermore, the operation mode was altered to a continuous co-current mode with feed of gas and liquid phase. The experimental data was subjected to a comparison with the model predictions. Nevertheless, the model was not recalibrated; rather, the four model parameters from the previous Chapter 3 (estimated with experimental data obtained in the semi-batch model), were utilized.

Further in the previous studies (Breit *et al.* [16], Chapter 3), an optical image measurement technique, the optical multimode online probe (OMOP) [29], was used in order to measure the BSDs. A key issue in the use of OMOP is the extent to which it affects the measured bubble size distribution (BSD), given its invasive nature. In this chapter instead, fiber optic needle probes (NP) based on Laser Doppler Anemometry [66] were used, which are significantly less invasive than the OMOP and are practically unrestricted in terms of gas volume fraction and gas velocity. The NP enables the recording of BSDs at higher gas fluxes, and it can also determine the local gas volume fraction. This feature allows for the comparison of predicted and measured local gas volume fractions. However, it is challenging to directly compare the size distributions determined with different measurement techniques, even when the invasiveness of the measurement technique on the flow and the BSD are disregarded. This is because both OMOP and NP measure different size distributions. The OMOP measures the size based on a two-dimensional shadowgraphic image of the bubbles [67], whereas the NP measures the distribution of the piercing length (for details please refer to Section 4.2 and Lefebvre *et al.* [66]). Consequently, the absolute values measured are not comparable in principle. This also applies to other measurement techniques, such as grating sensors or lasers [68]. In essence, however, our primary objective is not to ascertain the absolute BSDs, but rather to utilize the measured BSDs to estimate model parameters and to evaluate the prediction performance. It is hypothesized that the choice of measurement technique has no influence on the resulting model parameters and predictions. The estimated model parameters exert an influence on the occurrence of breakage and coalescence, which in turn affects the manner in which the BSD and dispersed phase velocity change along the height of the column (shape and appearance). The position of the BSD (corresponding to the mean bubble diameter) is primarily influenced by the inlet distribution generated by the sparger. Consequently, provided that the different measurement techniques reflect the same trends of the BSD with respect to the parameter variations, the model parameters determined for the different measurement data should be similar. To assess the hypothesis, the model parameters, calibrated with the OMOP, are applied without recalibration to the BSD measured with the NP and the prediction performance is evaluated.

As previously stated, the inlet BSD produced by the gas sparger exerts a significant influence on the BSD along the column height. In order to solve our model equations, it is necessary to specify the inlet BSD as a mathematical boundary condition (for further details, please refer to Supplementary Information B). In the previous studies (Breit *et al.* [16], Chapter 3), we utilised the BSD measured just above the gas sparger (about 20 cm) as the boundary condition. The application of a measured BSD as a boundary condition restricts the scope of our model approach. It is not feasible to employ this approach for scaling up of bubble columns, as in industrial-scale bubble columns, the inlet BSD is rarely, if ever, measured. A model is required that can reliably predict the BSD produced by the gas sparger as a function of the sparger geometry and the operating conditions. Consequently, in this chapter, a modified model approach, as proposed by Ribeiro *et al.* [69], was tested. The BSDs predicted by the sparger model were compared to the measured inlet BSDs.

In this chapter, we were able to successfully apply the MBP without recalibration to different spargers in semi-batch operation and for the first time to continuous co-current operation. Thereby, the experimental reference data was acquired using needle probes instead of an optical imaging method. The model was able to reproduce the measured data by the needle probe, but limitations were found at higher gas fluxes. The results demonstrate that the proposed one-dimensional multifluid population balance model is capable of adequately describing the local bubble size distribution and the local gas volume fraction in the BC for diverse operational conditions (without liquid feed, co-current feed of gas and liquid, and different gas spargers) with a single set of model parameters. Overall, the findings suggest that the presented MPB is a valuable tool for the scale-up of bubble columns.

4.2. Materials and Methods

4.2.1. Experimental Setup and Procedure

Fig. 4.1 depicts the experimental setup employed in this chapter. Two operating modes were possible: 1) continuous gas feed without continuous liquid feed (referred to as semi-batch mode), and 2) continuous co-current gas and liquid feed (referred to as continuous mode). The bubble column (2, the number refers to Fig. 4.1) consisted of three column sections. The longest column section in the bottom (5) was made of austenitic stainless steel up to a height of $h \approx 200$ cm with an internal diameter of $d_{BC} \approx 10.6$ cm. This column section was followed by a small transparent pipe section (6) made of polymethyl methacrylate ($(d, h) \approx (10, 30)$ cm). It is used as a viewing window. The upper column section (7) is a T-piece ($(d, h) \approx (11, 50)$ cm) made of unplasticized polyvinyl chloride. It serves as a side overflow ($d \approx 5$ cm).

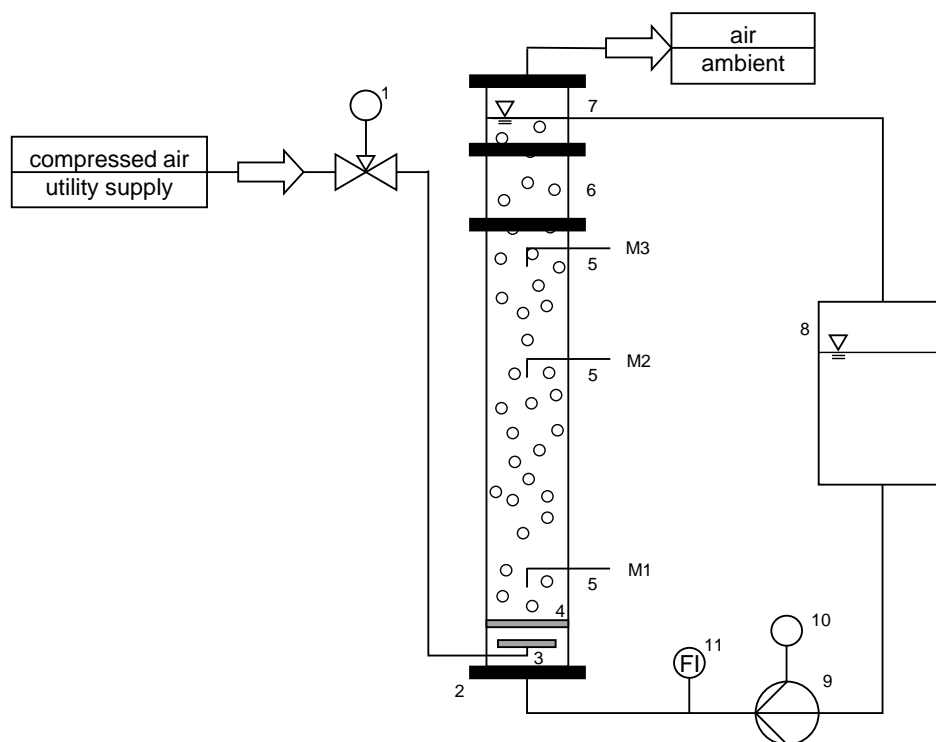


Figure 4.1.: Schematic illustration of the experimental setup.

In both operating modes, compressed air from the utility supply was dispersed at the bottom ($z = 0$ cm) into the column through a plate sparger (4, PIS) in semi-batch mode or a spider sparger (3, SpS) in continuous mode. The air was purged to the ambient at the column top. Geometric details of the employed spargers including there abbreviations are summarized in the Supplementary Information Tab. C.7. The gas flux j_d was regulated by a mass flow controller (1) from the manufacturer Brooks Instrument (Hateld, Pennsylvania, USA) of the GF040 series (GF040CXXC-0008030L-N2AVS5-XXXXXX-00C). In semi-batch mode the column was filled with with osmosis water (conductivity about 0.01 mS cm^{-1} , in the following referred just as water) before starting the gas flow. The level of the ungasified liquid h_c was measured from the plate sparger. In continuous mode, the liquid (water) was fed into the column from the buffer

tank (8) and it left the column via the side overflow ($z \approx 2.535$ m) from where it flowed back into the buffer tank (8). The buffer tank also served the function of a gas-liquid separator. A centrifugal pump (9) of type MPN170PP from manufacturer SCHMITT Kreiselpumpen GmbH & Co. KG (Ettlingen, Germany) was used to convey the liquid. The liquid inlet was situated in a central position at the base of the column ($d \approx 3.44$ cm, $z \approx -10.5$ cm). The liquid volume flow rate, or the liquid flux j_c , was determined using a Coriolis mass flow meter (11) of type PROMASS 80 (80F15-10H0/0) from manufacturer Endress+Hauser (Reinach, Switzerland). The liquid flow rate was manually controlled using the frequency inverter (10) of type DC1 (DC1-349D5NB-A6SCE1) from the manufacturer EATON (Bonn, Germany) to adjust the rotational speed of the pump.

4.2.2. Measurement Techniques

To determine the BSD at the three axial positions (M1, M2, M3, see Tab. C.9 for details) along the height of the BC, fiber optic needle probes (5, NP) of type M2 from manufacturer A2 Photonic Sensors (Grenoble, France) were used. Fiber optic needle probes are based on laser Doppler anemometry [66, 70]. A comprehensive description of the measuring principle and application of NP can be found in [66, 70]. The following paragraph provides a concise overview based on these sources:

A laser beam generated by an optoelectronic module (OPTOEM) is sent via an optical fiber to the conical glass fiber tip of the probe. The laser is reflected from the surrounding phase back into the tip to the OPTOEM, whereby the intensity of the reflected signal depends on the refractive index of the surrounding phase. Since the refractive index of the dispersed and continuous phase is different, the surrounding phase can be determined. The OPTOEM converts the reflected light signal into a digital signal and uses this to determine the penetration time and the pierced phase. In addition, the velocity of the pierced bubble can be determined from the signal using the Doppler effect. With the information of the velocity and piercing time, the size of a individual bubble can be calculated. The validity of each measured bubble is evaluated using the detected signal based on the velocity measurement. A valid velocity measurement occurs whenever the tip of the probe pierces the surface of the bubble almost perpendicularly. In addition to the size and the velocity of the bubbles, the local gas volume fraction can be determined in a separate measurement using the NP. The ratio of sum of the piercing time to the total measurement time gives the local gas volume fraction.

The advantages and disadvantages of this measuring technique result from the design and the measuring principle. On one hand, it is minimally invasive (tip diameter 0.125 mm, for further dimensions see Fig. C.1) and the size and velocity of the bubbles as well as the local gas volume fraction can be determined with a single measurement technique. The recorded data is considered to be accurate (5 % - 15 %) according to Lefebvre *et al.* [66]. The OMOP should also be in this order of magnitude of accuracy ([16], Chapter 3). On the other hand, only a 1D chord length measurement takes place. This disadvantage is further exacerbated by the validity check, which has the consequence that only bubbles that are pierced near their center, where the angle between tip and surface is close to 90° are incorporated. This has

the overall consequence that we do not obtain a chord length distribution (CLD) in which all chords of the bubbles are recorded, for which at least semi-empirical conversion methods to a volume equivalent based BSD [71, 72] exist. The distributions recorded with the NP are somewhat akin to filtered CLD, or, according to the manufacturer, can be considered to be size distributions. Due to this filtering, the size distributions will be shifted towards smaller bubbles compared to the ground truth. Notwithstanding this difference, this size distribution is also referred to as BSD in the following.

In contrast, the OMOP [29] employed in the preceding studies (Breit *et al.* [16], Chapter 3) records two-dimensional images from which the area and various diameters of the individual bubbles can be calculated, resulting in a BSD. However, this measurement technique presents several disadvantages, including invasiveness, a limitation of the maximum detectable bubble size due to optics and measurement gap size, and superposition of bubbles in the measurement gap that requires separation by computer-aided techniques (see, for example, [67]). In sum, these limitations restrict the application of the OMOP to lower phase fractions (approximately 20 %) for least non-spherical bubbles. Furthermore, due to shadow-graphic technology, e.g. umbrella bubbles are detected significantly larger in volume. Overall, it is estimated that the OMOP within its operating conditions measures larger bubble diameters compared to the ground truth.

Fig. C.2 in the Supplementary Information provides a comparison of the two measurement techniques measured BSD under the same operating conditions. However, the objective of this chapter is not to provide a comprehensive comparison between NP and OMOP, nor to assess the precision of the associated measurement techniques. This is a topic that is left to other authors and future studies. The objective of this chapter is to assess the prediction performance of the 1D-MPB in greater detail. In this context, the NP is a valuable tool as it is less invasive than the OMOP, can measure at higher gas fluxes and gas volume fractions, and additionally measures the local gas volume fraction. Consequently, the potential of the NP as an alternative to the OMOP is being investigated in this chapter. Moreover, the ground truth of the bubble size is of lesser importance, given that the objective is to identify trends and order of magnitude detection.

The OPTOEM and software settings used and further details about the NP are in the Supplementary Information C.4. A bubble size measurement contained at least 3000 valid bubbles and a local volume gas fraction measurement was performed for 30 s. The measured BSD and the measurement data for determining the gas volume fraction are provided in the Supplementary Material of the publication.

4.2.3. Overview of Experiments

An overview of the experiments is given in Tab. 4.1, the abbreviated sparger property's can be found in Tab. C.7 and the axial measuring position in Tab. C.9 in Supplementary Information. All experiments were carried out under ambient conditions ($T^0 \approx 293$ K, $p^0 \approx 1.0 \times 10^5$ Pa).

Table 4.1.: Summary of the experiments carried out.

| Operation mode | $j_d / \text{cm s}^{-1}$ | $j_c / \text{cm s}^{-1}$ | Sparger | Measuring position |
|----------------|--------------------------|--------------------------|-------------|--------------------|
| Semi-batch | 1.0, 2.0, | 0.0 | PIS 04-187, | M1, M2, |
| | 3.0, 4.0, 5.0 | | PIS 05-120 | M3 |
| Continuous | 1.0, 2.0, | 1.0, 2.0, 3.0 | SpS 04-56 | M1, M2, |
| | 3.0, 4.0 | | | M3 |

4.3. Modelling and Simulation

4.3.1. Multifluid Population Balance Model

The model employed in this chapter is based on the assumption of steady-state conditions. All space-dependent quantities have been subjected to cross-sectional area averaging, resulting in the generation of a one-dimensional (1D) model aligned with the axial main flow direction (z). That is the plug-flow assumption. In the case of the continuous liquid phase (mass and momentum), the common multifluid model [73] is employed, while the KTAWSR [26] is utilized for the balance of momentum and mass of the gas phase. This allows for the velocity and mass of the dispersed phase (in this instance, bubbles) to be considered as a function of both the physical space (axial position, z) and the property space (bubble diameter, ξ). It should be noted that the size-dependent mass balance of the gas phase is represented by the population balance equation (PBE).

In this chapter, we employed the mass-based formulation of the PBE, as detailed in Chapter 5. The solution of the equations of the MPB yields the mass density function, designated as f_d^m , and the velocity of the gas phase as functions of the axial position and bubble size. The mass density function enables the calculation of both the Sauter mean diameter (SMD) ξ_{32} (which represents a moment of the density function) and the local gas volume fraction α_d . The calculation formulas are summarized in the Supplementary Information C.1.

The model implementation and solution strategy are identical to those presented by Breit *et al.* [16], using the same simplification as suggest in Chapter 3. Furthermore, the bubble growth due to axial pressure variations was neglected in this chapter. The growth of bubbles near the lower boundary of the property space leads to numerical artifacts mainly due to the denominator of the coalescence birth term. The denominator of the mass-based coalescence birth term contains the diameter and the volume of the bubble to be coalesced. Multiplying these two numbers, especially at the integration limits, produces extremely small numbers. If a number that is not sufficiently close to zero is divided by this extremely small number, values are created that are not physical (see detailed explanation and discussion Chapter 5 and 6). This problem did not occur in the previous studies (Breit *et al.* [16], Chapter 3) because the lower boundary was at larger bubble diameters (compare 1×10^{-3} m to 5×10^{-5} m) where f_d^m was close to zero. Since the employed NPs enables detection of smaller bubbles than the OMOP (c.f. Section 4.2), the BSDs measured in this chapter are shifted to towards smaller bubbles (cf. Fig. C.2) compared to the BSDs measured in our previous studies ([16], Chapter 3) so that f_d^m is non-zero at that small bubble sizes leading to the issue. In Chapter 5 and 6, we discuss possible solutions, and in Chapter 6 we use a finite volume method instead of the spectral orthogonal collocation method used in current chapter, which significantly reduces this problem. However, after a preliminary study it could be shown that in the cases considered here, growth has hardly any influence on the BSD compared to breakage and coalescence, so that the solution strategy and its advantages over the finite volume method (cf. Chapter 6) can be retained for the time being.

The turbulent energy dissipation rate was estimated using $\varepsilon = \sum_k j_k g$ according to [74, 75], where j_k is the flux of phase k and g the gravitational acceleration constant. This model is

based on an energy balance about the reactor volume. For further detailed information on the model equations and solution strategy, please refer to the source publications ([16], Chapter 3). The parameters used in the simulations of this chapter are summarized in the Supplementary Information C.3.

4.3.2. Sparger Model

In this chapter, the inlet BSD (i.e. the boundary condition in the property space of the PBE) was taken from two different sources: 1) measurements of the BSD from just above the gas sparger as in our previous studies (Breit *et al.* [16], Chapter 3), also referred to as measured inlet BSD below, 2) model predictions.

The model approach employed to describe the BSD at the gas sparger as a function of sparger geometry, property data of the fluids and process conditions (in the following referred to as sparger model) was adopted from Ribeiro *et al.* [69]. Ribeiro *et al.* [69] used the model according to Geary *et al.* [63] to determine the diameter of a single bubble formed at a single orifice. To obtain a distribution, Ribeiro *et al.* [69] fitted the two parameters (ω, χ) of a log-normal distribution to the measured BSD just above the sparger. Ribeiro *et al.* [69] considered one parameter of the log-normal distribution as the sparger parameter, the ω , and assumed it to be constant, although they could detect a dependence on the gas flux. The second parameter, the χ was re-fitted from Ribeiro *et al.* [69] to the bubble diameter formed at a single orifice resulting from the model of Geary *et al.* [63] in a second step. Therefore the model approach of Ribeiro *et al.* [69] allows the inter- and extrapolation to other gas fluxes and does not completely eliminate the need for experiments, it reduces the number of them.

We have modified the approach of Ribeiro *et al.* [69], because we have also found that ω is not constant, since it depends on the gas flux. In our case, however, to an extent that is no longer negligible. Furthermore, we found that the predicted bubble diameter according to Geary *et al.* [63] does not agree with our observations, which is why we additionally adjusted it using a further but constant parameter c for each sparger. Deviations of $\pm 20\%$ of the predicted bubble size according to Geary *et al.* [63] have already been observed by other researchers [76]. Furthermore, due to the available measurement connection ports in the bubble column, we were only able to record the first BSD approx. 20 cm above the sparger. At this distance, the bubbles have already experienced many breakage and coalescence events and the model according to Geary *et al.* [63] applies to a single orifice not to numerous neighboring ones, which may influence each other. However, using this additional parameter, good results could be achieved (cf. Section 4.4). Moreover, instead of using only Geary *et al.* [63] volume-equivalent bubble diameter for parameter estimation, as adapted by Ribeiro *et al.* [69], we included the SMD and standard deviation to fulfill additional moments of the distribution functions. The modified sparger model is briefly summarized in the Supplementary Information C.2.

4.3.3. Error Measure

Two different error measures are used to evaluate the prediction performance of our MPB. First, the mean absolute percentage error *MAPE* of the moments of the distributions according to Eq. (4.1) is employed. Second, the symmetric Chi-Square distance χ^2 (see Eq. (4.2)) is used to evaluate the difference between predicted and measured BSD.

$$MAPE = \frac{1}{N} \sum_i^N \frac{|\mu_{ab,i,\text{exp}} - \mu_{ab,i}|}{\mu_{ab,i,\text{exp}}} \quad (4.1)$$

$$\chi^2 = \sum_j \frac{\left(\hat{f}_d^n(\xi_j) - \hat{f}_{d,\text{exp}}^n(\xi_j) \right)^2}{\hat{f}_d^n(\xi_j) + \hat{f}_{d,\text{exp}}^n(\xi_j)} \quad (4.2)$$

Here $\mu_{ab,i}$ is the ab 'th moment ratio of a distribution function, ab is the order of the moment ratio (see Supplementary Information C.1), i is the index of incorporated moments and/or experiments, N is the number of incorporated moments and experiments, the subscript "exp" indicate a measured value, \hat{f}_d^n is the normalized number density function (see Eq. (C.4)), ξ is the bubble size and j is the index of the bubble size class. For a single statement about the χ^2 across several experiments, these are arithmetically averaged resulting in $\overline{\chi^2}$. The experiments to be averaged are marked in the superscript (M: for the measuring position, j_d, j_c for the gas resp. liquid fluxes), and the model is marked in the subscript (sim: simulation with measured inlet BSD, sim-SPM simulation with inlet BSD from sparger model, SPM: sparger model). In the case of the *MAPE*, the moment(s) with which it was formed is/are also identified in the subscript.

4.4. Results and Discussion

4.4.1. Semi-Batch Mode – Gas Flux and Sparger Study

Fig. 4.2 depicts both the measured and predicted Sauter mean diameter (SMD) ξ_{32} and the local gas volume fraction α_d as a function of the axial position z in the BC (semi-batch mode) for different gas fluxes j_d and for the two different spargers investigated. The simulation results were obtained using as boundary condition either the measured inlet BSD (sim) or the BSD predicted by the sparger model (sim-SPM).

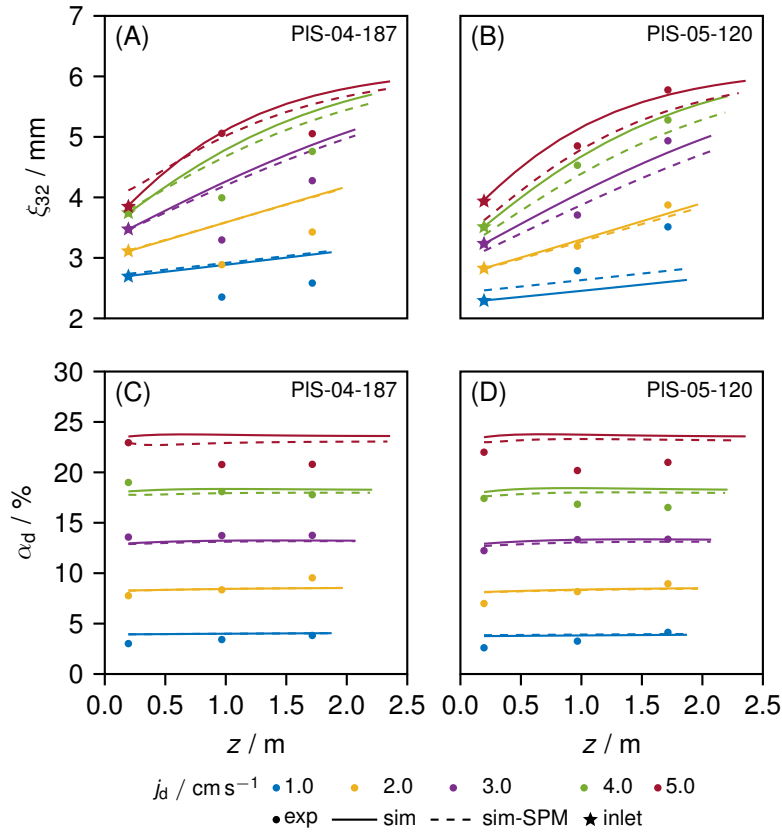


Figure 4.2.: Top row (A)-(B): Sauter mean diameter ξ_{32} and bottom row (C)-(D): local gas volume fraction as function of the axial position z for different gas fluxes j_d (color) and spargers. Left column (A),(C): sparger type PIS-04-187 and right column (B),(D): sparger type PIS-05-120. Operating conditions: semi-batch mode. Symbols: experiments, inlet marked with star. Solid lines: simulation with measured inlet BSD. Dashed line: simulation with inlet BSD obtained by the sparger model.

As anticipated, the measured SMD and the local gas volume fraction demonstrate the expected trends. Both values increase with increasing gas flux, irrespective of sparger type and axial position. The rise in gas volume fraction is attributable to the fact that a greater volume of gas must traverse the column (cf. [16]).

For the sparger PIS-05-120, an almost linear correlation was observed between the measured SMD and the axial position for each gas flux (see Fig. 4.2B). While rising in the column

the number of coalescence events increases and thus the BSD shifts to larger diameters. In contrast, the profile of the measured SMD along the axial position for the sparger PIS-04-187 (see Fig. 4.2A) is not linear. The measured SMD first decreases and then it increases. Only the curves at higher gas fluxes ($j_d \geq 4.0$ cm/s) show a different form. A similar behavior was already observed in Chapter 3 for a semi-batch bubble column with an aqueous sodium chloride solution as liquid phase. The design of the column was similar to the current chapter (diameter of the column $d_{BC} = 10$ cm, and diameter and number of the sparger orifices $d_h = 0.4$ mm, $N_h = 163$). At that time, we reached the conclusion that this behavior could be attributed to the invasiveness of the OMOP. In this chapter, measurements with the NP, which is significantly less invasive than the OMOP, confirmed that the axial profile of the SMD passes through a minimum. Furthermore, since this profile was not observed for high gas fluxes ($j_d > 4.0$ cm/s) and it did not occur when the sparger PIS-05-120 was employed (see Fig. 4.2B), it is assumed that the non-linear axial profile of the SMD is due to a complex interaction of bubble size-dependent breakage and, more importantly, coalescence (more on this later). A similar explanation applies to the fact that the SMD did not increase further with increasing axial position at the highest gas flux (cf. Fig. 4.2A). Again, this was also observed in our previous experiments with pure water as liquid phase (Chapter 3). We assumed that bubble size detection limitation of the OMOP could be the cause for that behavior. Also here, the new measurements with the NP, which were carried out in this chapter, do not confirm our previous assumption, but the experimental data is still too scarce to completely rule it out.

The local gas volume fraction for both spargers (see Fig. 4.2C and D) the for gas fluxes $j_d = (1 - 3)$ cm s⁻¹ is almost constant along the height of the column. For the two larger gas fluxes, the local gas volume fraction exhibits a slight decrease, which can be attributed to the fact that the large bubbles formed there have a significantly higher rise velocity, resulting in a reduction of the local gas volume fraction.

In general, the agreement between the model prediction and the experimental results is satisfactory. It is noteworthy that no calibration of the model parameters was conducted in this chapter; instead, all model parameters were directly adopted from our previous work presented in Chapter 3. Comparing the model prediction, of the case, in which the measured inlet BSD is used as boundary condition (solid line in Fig. 4.2A and B) for the two different spargers shows that the PIS-04-187 $MAPE_{\xi_{32},sim}^{M>1,j_d} = 13.4$ % is predicted significantly worse than the PIS-05-187 $MAPE_{\xi_{32},sim}^{M>1,j_d} = 7.7$ %. This finding can be attributed to the fact that the parameters calibrated in Chapter 3 and adopted by us in this chapter were obtained from bubble column experiments with similar a dispersed phase behavior to that of sparger PIS-05-187. In other words, no experimental results have been used for the model calibration thus far that show a comparable axial profile of the SMD to that observed with sparger PIS-04-187, in which the bubble diameter initially decreases after leaving the inlet and then increases. It is therefore unsurprising that the set of parameters estimated in our previous work does not yet provide an accurate representation of the complex interplay between coalescence and breakage within the column as it is observed for that type of sparger. It is possible to make an additional adjustment to the second coalescence parameter, namely the coalescence efficiency parameter. This parameter was set in Chapter 3 to unity, as it was deemed to have no significant influence

on the objective value, the error during calibration. When the value is unity, a coalescence efficiency of 100 % is obtained, regardless of bubble size. By modifying this parameter to obtain a bubble size dependent coalescence efficiency, a more complex dispersed phase behavior could be described. However, the aim of this chapter is not to recalibrate the parameters, but to investigate the prediction performance of our model, which has been calibrated with minimal experimental data. And this could be further demonstrated and extended in the case of PIS-05-187, so that higher gas fluxes could also be predicted well by the model, whereby the same limitation of the model at $j_d = 1 \text{ cm s}^{-1}$ as in Chapter 3 can be observed here due to the flow regime change.

When the sparger model is used to predict the inlet BSD (boundary condition), a similar good agreement between experimental and model predictions with respect to the SMD of $MAPE_{\xi_{32}, \text{sim-SPM}}^{M>1, j_d} = 12.6 \%$ for the PIS-04-187 and $MAPE_{\xi_{32}, \text{sim-SPM}}^{M>1, j_d} = 8.5 \%$ for the PIS-05-120 can be observed, especially for lower gas fluxes (see dashed lines in Fig. 4.2). The fact that the model prediction for the case where the sparger model is used to describe the inlet BSD is slightly better than that where the measured inlet BSD is used can be attributed to the two higher gas fluxes (cf. Fig. 4.2A and B).

A comparison between the measured value and the model prediction demonstrates that the sparger model is capable of accurately describing the BSD at the inlet ($M = 1$) for both spargers: $MAPE_{\xi_{32}, \text{SPM}}^{M=1, j_d} = 2.1 \%$ for the PIS-04-187 and $MAPE_{\xi_{32}, \text{SPM}}^{M=1, j_d} = 4.7 \%$ for the PIS-05-120. Therefore, the prediction performance of the axial profiles of the SMD is not significantly affected in our case by the choice of boundary conditions, whether measured values or model predictions of the BSD are used (cf. Fig. 4.3 first column). Obviously, the sparger model adopted from Ribeiro *et al.* [69] and modified in this chapter is able to predict the inlet BSD, taking into account a limitation at higher gas fluxes.

Fig. 4.2C and D demonstrates that the model is capable of accurately predicting the axial profile of the local gas volume fraction, irrespective of the manner in which the inlet BSD is described: $MAPE_{\alpha_d, \text{sim}}^{M, j_d} = 8.2 \%$ and $MAPE_{\alpha_d, \text{sim-SPM}}^{M, j_d} = 7.6 \%$ for PIS-04-187 and $MAPE_{\alpha_d, \text{sim}}^{M, j_d} = 10.5 \%$ and $MAPE_{\alpha_d, \text{sim-SPM}}^{M, j_d} = 10.0 \%$ for the PIS-05-120. Only at higher gas fluxes ($j_d = 5 \text{ cm s}^{-1}$) the model exceeds the trend. It is important to note that no data pertaining to the gas holdup or the local gas volume were employed for the calibration of the model parameters. Therefore, it can be considered a pure model prediction. In particular, the gas volume fraction is a crucial parameter for engineers engaged in the design and optimization of bubble columns. It influences a number of key factors, including the maximum possible liquid holdup in the column, interfacial heat and mass transfer, and the conversion of reactants. The favorable outcome serves to reinforce the efficacy of the proposed model approach.

Fig. 4.3 illustrates a comparison between the measured and predicted BSD for three distinct axial positions within the column, as well as for varying gas fluxes associated with the PIS-05-120 sparger. The same figure for the PIS-04-187 is presented in the Supplementary Information Fig. C.3.

As previously observed in Chapter 3, the distributions become broader with increasing gas flux and axial position, and are shifted towards larger bubble diameters. This can be attributed

to an increase in coalescence events analogous to the moments. Overall, the MPB approach have a prediction performance of $\overline{\chi^2_{\text{sim}}^{M>1,j_d}} = 0.05/\text{mm}$ and $\overline{\chi^2_{\text{sim-SPM}}^{M>1,j_d}} = 0.09/\text{mm}$ for the PIS-04-187 and $\overline{\chi^2_{\text{sim}}^{M>1,j_d}} = 0.07/\text{mm}$ and $\overline{\chi^2_{\text{sim-SPM}}^{M>1,j_d}} = 0.15/\text{mm}$ for the PIS-05-120 sparger.

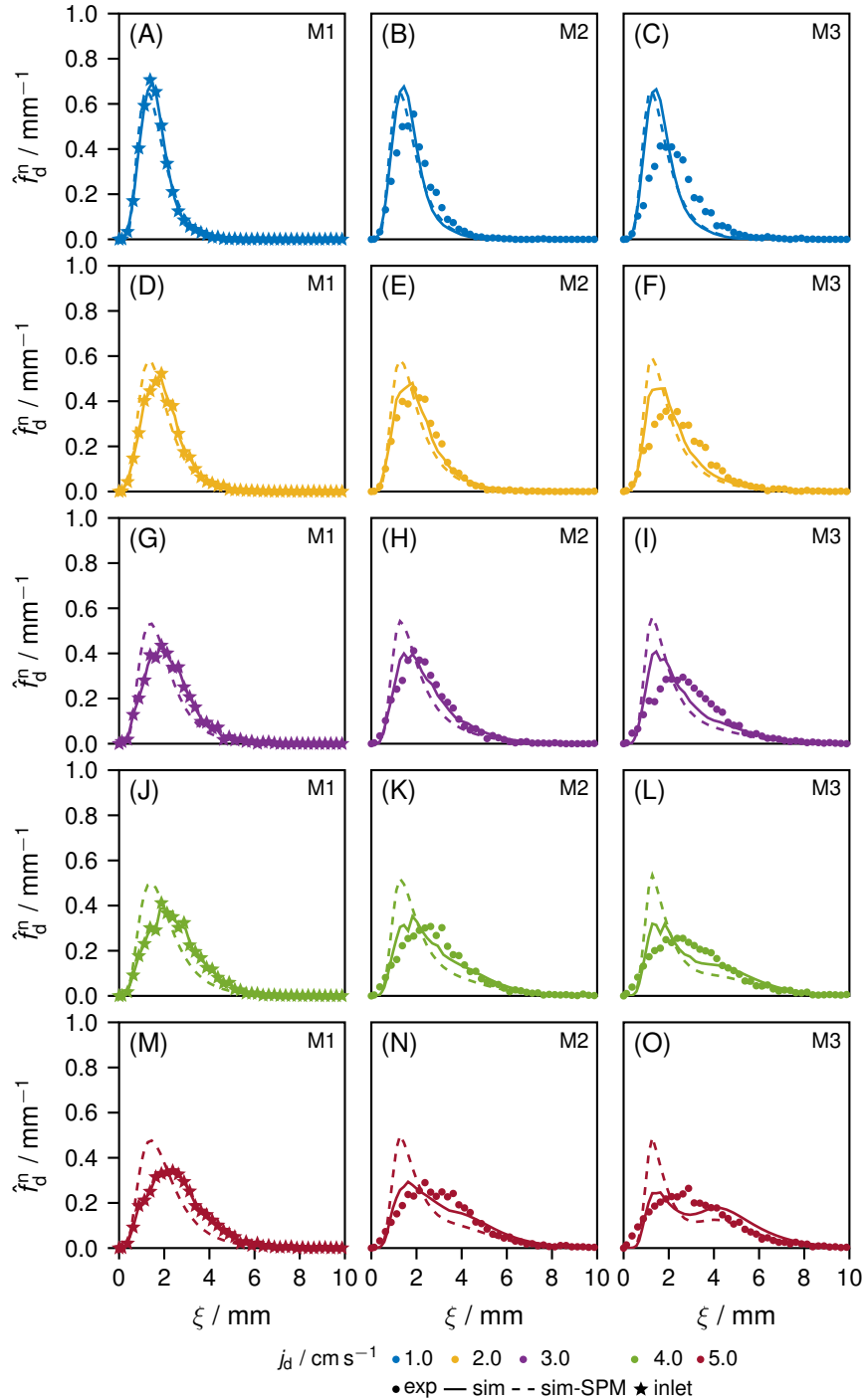


Figure 4.3.: Normalized number density distribution \hat{f}_d^n as a function of bubble diameter ξ for different gas fluxes j_d (color, along rows) and axial positions z (along columns) for the PIS-05-120 sparger in semi-batch mode. Symbols: experiments, inlet marked with star. Solid lines: simulation with measured inlet BSD. Dashed line: simulation with inlet BSD obtained by the sparger model.

The prediction performance of the sparger model with respect to the inlet BSD are $\overline{\chi^2_{\text{sim-SPM}}^{M=1,j_d}}$

= 0.05/mm for the PIS-04-187 and $\overline{\chi^2}_{\text{sim-SPM}}^{M=1, j_d} = 0.07/\text{mm}$ for the PIS-05-120 results. Both the χ^2 -values as well as the BSDs plotted in Fig. 4.3 reveals that the prediction performance is enhanced when the measured inlet BSD is utilized as the boundary condition, as opposed to the inlet BSD predicted by the sparger model. As previously stated, when only the SMD and gas volume fraction (moments) are considered, the origin of the inlet BSD is inconsequential. This illustrates that an evaluation of the model's prediction performance based solely on the moments may lead to wrong conclusions. Moreover, it can be observed that the model with the parameters of Chapter 3 exhibits a tendency to underestimate coalescence and overestimate breakage, as evidenced by a significant discrepancy between the measured BSD and those predicted by the model. Furthermore, the inlet BSD, as predicted by the sparger model, also deteriorates with increasing gas flux and remains overly peaked (see Fig. 4.3A-M). The error persists in the BSDs of axial positions situated at greater distances from the inlet. It is noteworthy that the model predicts a bimodal distribution at the highest flux and position (see Fig. 4.3O), despite the specification of a mono-modal log-normal inlet BSD which is attributed to the complex interplay between breakage and coalescence. It is intensified by the higher gas flux and thus energy dissipation.

It should be mentioned that a better prediction of the distributions is possible with the help of the sparger model, in which, for example, not the moments (ξ_{32}, σ^2) but the χ^2 - distance of the BSDs is added to the objective function for the parameter estimation in the fourth step of the modified sparger model (see Supplementary Information C.2). However, this can lead to a poor prediction of the moments. In essence, neither the SMD nor the BSD is of direct interest to the engineer, but rather, the influence of these values on the apparatus' overall performance is of greater consequence., e.g. on conversion and yield. So far it is not clear which of the properties of the dispersed flow must be predicted most accurately in order to describe the overall performance of the apparatus best. This question will be addressed in future work in which reaction and / or separation processes in dispersed gas-liquid systems will be studied.

Nevertheless, it can be concluded that the parameters of Chapter 3 can be directly applied for other spargers and higher gas fluxes as they have been used in the calibration experiments and still they enable a prediction of the BSDs, the SMD and the local gas volume fraction with a deviation (compared to the experimental data) of less than 10 %. Furthermore, the developed modified sparger model shows good inter- and extrapolation capabilities and provides only a slightly poorer prediction performance than with measured inlet BSD. Moreover, the parameters of Chapter 3 appear to be independent of the measurement technique (OMOP versus NP) employed to quantify the BSD required for parameter calibration and specification of the inlet BSD. The results thus confirm the hypothesis that the choice of measurement technique has no influence on the model parameters and prediction performance (cf. Section 4.1). So no or just little information about the inlet BSD is lumped in to the model parameters while parameter calibration. Furthermore, it can be stated that it is most important for a good parameter calibration to capture the trends how the BSD develops along the axial position in the column and not to measure the absolute values of the BSD. However, the kernels used here and many other kernels depend on the order of magnitude of the bubble size examined, so that the parameters can only be applied to similar size ranges.

4.4.2. Continuous Mode – Gas and Liquid Flux Study

Fig. 4.4 depicts the SMD ξ_{32} and the local gas volume fraction α_d as a function of the axial position in the bubble column for the continuous mode for different gas fluxes j_d now for different liquid fluxes j_c along the columns of the figure.

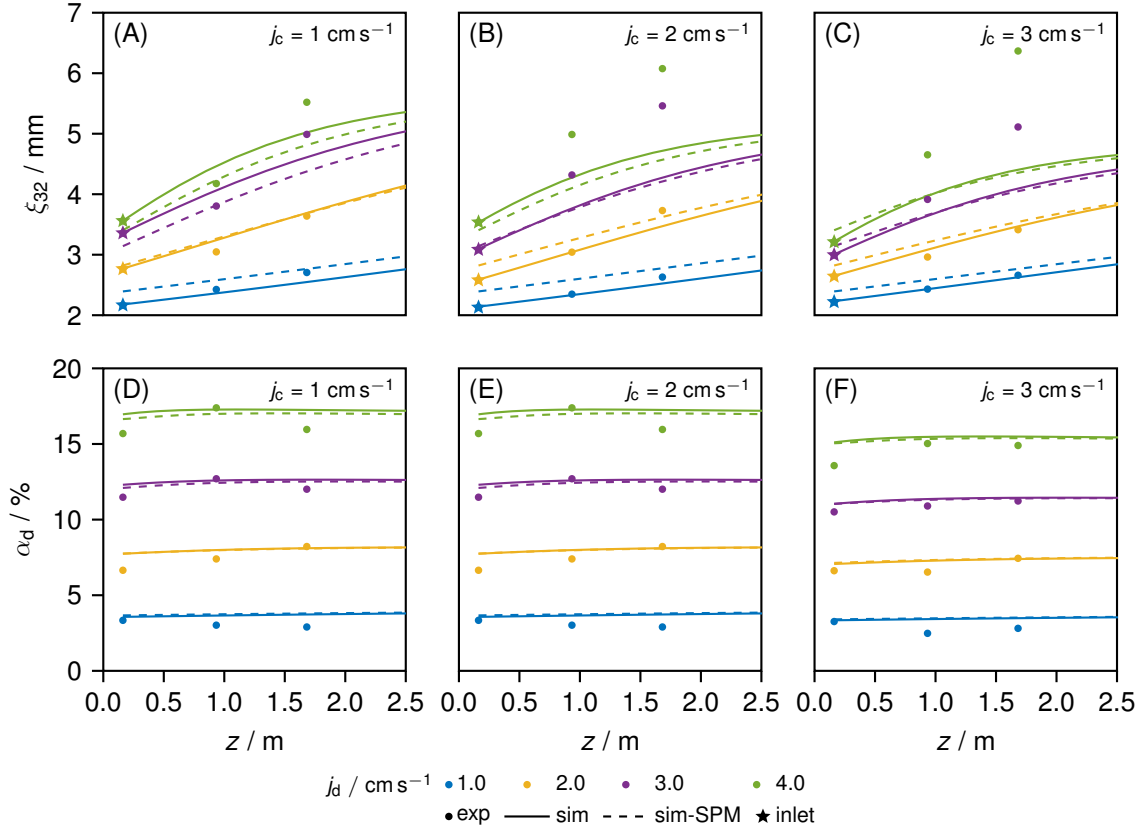


Figure 4.4.: **Top row A-C:** Sauter mean diameter ξ_{32} and **bottom row D-F:** local gas volume fraction as function of the axial position z for different gas fluxes j_d (color) and liquid fluxes j_c (columns). Operating conditions: continuous mode. Symbols: experiments, inlet marked with star. Solid lines: simulation with measured inlet BSD. Dashed line: simulation with inlet BSD obtained by the sparger model.

First, the experimental results shown in Fig. 4.4 are discussed. As expected, the SMD (see Fig. 4.4A-C) increases with the gas flux and axial position analogous. The strongly curved profiles observed for the semi-batch mode, in which the SMD even decreased first, are not found in the experiments of the continuous mode. The slope of the profiles becomes greater with increasing liquid flux, which is attributed to the higher energy dissipation caused by the liquid feed. It is postulated that the nearly linear profile observed in the continuous mode is attributable to the well-defined co-current flow of both the gas and liquid phases. In contrast, in the semi-batch mode, which lacks forced convection of the liquid phase, circulation zones with strong backmixing are evident in the column. Additionally, slightly larger SMD are observed in the continuous mode (for the same gas flux and axial position) in comparison to the semi-batch mode. This finding is attributed to the increased energy dissipation by the liquid flow. The axial profiles of the local gas volume fraction (see Fig. 4.4D-F) show a similar

behavior in the continuous mode as in the semi-batch mode. The local gas volume fraction remains relatively constant along the axial position, which is consistent with the findings observed in the semi-batch mode for the majority of gas fluxes. However, no decrease was detected for the highest gas flux, in contrast to the results obtained in the semi-batch mode (cf. Fig. 4.2D).

A comparison of the model predictions with the experimental data demonstrates that the model is capable of accurately predicting the axial profiles of the SMD and the local gas volume fraction for all liquid fluxes, provided that the gas fluxes are low ($j_d \leq 2.0 \text{ cm s}^{-1}$). The errors are: $MAPE_{\xi_{32}, \text{sim}}^{M>1, \{j_d\} \leq 2, j_c} = 2.9 \%$ and $MAPE_{\xi_{32}, \text{sim-SPM}}^{M>1, \{j_d\} \leq 2, j_c} = 5.3 \%$. The high gas fluxes ($j_d \geq 3.0 \text{ cm s}^{-1}$) can only be predicted for the lowest liquid flux (cf. Fig. 4.4A). It is hypothesized that this behavior is derived from the model employed to describe the turbulent energy dissipation rate. In accordance with the model proposed by Baird *et al.* [54], the turbulent energy dissipation rate is assumed to be constant within the reactor, dependent solely on the gas flux and liquid flux. As the turbulent energy dissipation rate affects both the breakage and coalescence kernels, it exerts a considerable influence on the BSD within the column. A sensitivity analysis (not shown here) indicates that the prediction performance of the model can be enhanced when the turbulent energy dissipation rate is increased. This observation implies that the basic model proposed by Baird *et al.* [54] may underestimate the turbulent energy dissipation rate for higher gas and liquid fluxes. In accordance with the fundamental principles of physics, turbulence is a transient three-dimensional phenomenon. Consequently, it is a gross oversimplification to reduce this phenomenon to a constant value that is applicable throughout the entire column. In future work, the development of turbulent models that provide a more accurate representation of the local turbulent energy dissipation rate while maintaining consistency with the steady-state and one-dimensional MPB approach will be addressed.

A comparison of the two approaches utilized to define the inlet BSD (experimental data or prediction by the sparger model) demonstrates that even for a spider sparger and continuous mode, the sparger model accurately predicts the SMD. The resulting error is: $MAPE_{\xi_{32}, \text{SPM}}^{M=1, j_d, j_c} = 6.3 \%$. It should be noted that only for the smallest liquid flux $j_c = 1 \text{ cm s}^{-1}$ the sparger model parameters were adjusted as described in Supplementary Information C.2. Therefore, the simulation results shown in Fig. 4.4B-F are pure model predictions without any prior knowledge about the experiments to be reproduced. Overall, this results in a $MAPE_{\xi_{32}, \text{sim}}^{M>1, j_d, j_c} = 8.7 \%$ and $MAPE_{\xi_{32}, \text{sim-SPM}}^{M>1, j_d, j_c} = 10.1 \%$ for the model with specification of the measured inlet BSD and for the model with an inlet BSD from the sparger model. The profiles of the gas volume fraction are accurately predicted by the model comparable to the results found for the semi-batch mode (see Fig. 4.4D-F), $MAPE_{\alpha_d, \text{sim}}^{M, j_d, j_c} = 9.8 \%$ and $MAPE_{\alpha_d, \text{sim-SPM}}^{M, j_d, j_c} = 10.2 \%$.

Fig 4.5 depicts the BSD measured in the continuous mode for a liquid flux of $j_c = 2 \text{ cm s}^{-1}$ at different axial positions and for different gas fluxes (the remaining j_c are given in the Supplementary Information Fig. C.4 and C.5). It is evident that the measured distributions exhibit a narrower range for all axial positions and gas fluxes. The degree of prediction performance is comparable to that observed in the semi-batch mode: $\overline{\chi^2}_{\text{sim}}^{M>1, j_d, j_c} = 0.04/\text{mm}$ and $\overline{\chi^2}_{\text{sim-SPM}}^{M>1, j_d, j_c} = 0.10/\text{mm}$. The prediction performance of sparger model for the inlet BSD

is also comparable to that found for the semi-batch mode: $\overline{\chi^2}_{\text{SPM}}^{M=1, j_d, j_c} = 0.05/\text{mm}$. The good agreement between predicted inlet BSD and measured BSD is the reason why the differences between the model predictions of the axial profiles of the BSD, SMD and gas volume fraction obtained from the two different inlet BSD (sparger model and measured) are not significant.

Despite the certain deviations in the model predictions found for higher gas fluxes, it must be emphasized that the model parameters of Chapter 3 were calibrated for the semi-batch mode and could be applied here without adjustment to the continuous mode. This means that the 1D-MPB reflects the underlying physical principles, so that this information was not or only to a small extent lumped into the parameters.

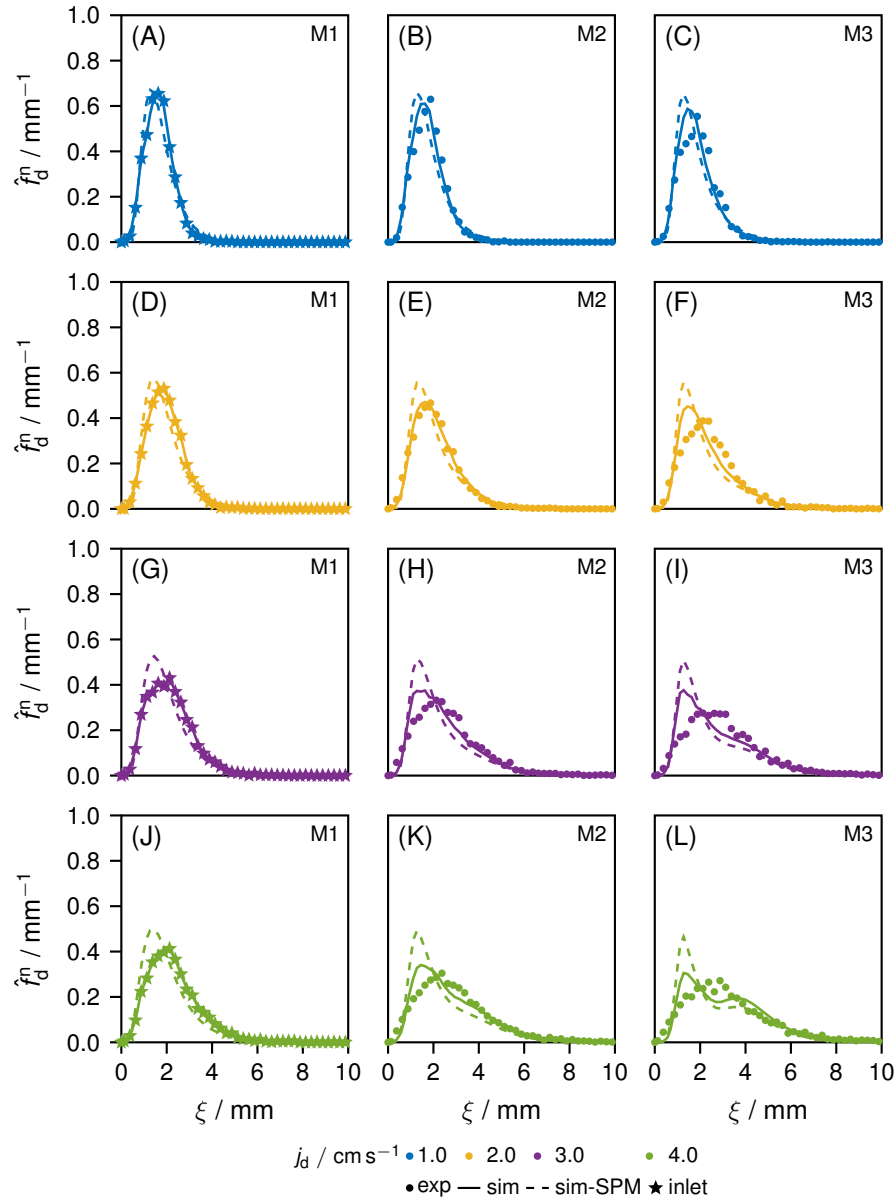


Figure 4.5.: Normalized number density distribution \hat{f}_d^n as a function of bubble diameter ξ for different gas fluxes j_d (color, along rows) and axial positions z (along columns) for the liquid flux $j_c = 2 \text{ cm s}^{-1}$. Symbols: experiments, inlet marked with star. Solid lines: simulation with measured inlet BSD. Dashed line: simulation with inlet BSD obtained by the sparger model.

4.5. Conclusion and Outlook

In this chapter, we extended the assessment of the prediction performance of a one-dimensional multifluid population balance model (1D-MPB) for bubble columns by evaluating its prediction performance in both semi-batch and continuous co-current operation. The model parameters were adopted from previous work (cf. Chapter 3) and were not recalibrated in this chapter. During the experiments, we used a variety of sparger types and varied the gas and liquid fluxes. In this chapter, we employed a fiber optic needle probe for data acquisition, as this method is less invasive than the multimode online optical probe (OMOP) used in previous investigations ([16], Chapter 3). This allowed the acquisition of bubble size distribution (BSD) and local gas volume fraction data at elevated gas fluxes.

The main results of our study highlight that the model showed good prediction performance for different spargers, especially at lower gas fluxes during semi-batch operation. The model predictions of Sauter mean diameter (SMD), local gas volume fraction and BSDs were in good agreement with the experimental data, especially when the inlet bubble size distribution (BSD) was measured. We propose a modified sparger model based on the model of Ribeiro *et al.* [69]. This modified sparger model was calibrated with only two measured inlet BSDs. The use of this modified sparger model to predict the inlet BSD for different sparger types (plate and spider), gas and liquid fluxes showed potential, although limitations were observed at higher gas fluxes.

Our results also show that the model fit parameters are independent of the measurement method used to determine the reference BSD. So that model parameters calibrated with measured BSD using the OMOP could be used to predicted BSD measured with needle probes. This underlines that the parameter calibration, or estimation method, used together with the MPB generalizes to the changes and not to the magnitude of the BSDs. The magnitude of the BSD (e.g. the mean) predicted by the model is determined exclusively by the inlet BSD and is either not or only to a minimal extent lumped into the model parameters.

In continuous co-current operation, the model's prediction performance was also effective, with good agreement between predicted and experimental SMD, local gas volume fractions and BSDs over a range of gas and liquid fluxes. Model parameters were not recalibrated, so parameters obtained in a semi-batch column were applied to the continuous mode. The fact that this was possible supports the physical principles described by the MPB and demonstrates the great potential of this model approach for scaling up dispersed multiphase processes from laboratory experiments.

Despite these achievements presented in our two studies Breit *et al.* [16] and Chapter 3, this chapter identified several limitations in the current model approach. The model's reliance on calibrated parameters from semi-batch mode experiments may not fully capture the dynamics in the continuous mode. In addition, the underestimation of turbulent energy dissipation rates at higher fluxes suggests the need for more sophisticated modeling approaches that account for spatial variations in this value. Further refinement of the sparger model toward a predictive model without the need for experimental data for calibration is also necessary to more accurately predict inlet BSDs over a broader range of operating conditions.

By addressing these areas, the 1D-MPB approach can be further optimized to provide a powerful tool for the design and optimization of bubble columns in various industrial applications. Further development and validation of this model approach will contribute significantly to the understanding and control of multiphase flow processes, facilitating optimization, design and scale-up from laboratory to production scale reactors.

5. Formulation of a Mass-Based Population Balance Equation: Insights Into Derivation, Mass Transfer, and Nondimensionalization

Contributor Roles Taxonomy

Ferdinand Breit: conceptualization; formal analysis; investigation; methodology; project administration; validation; visualization; writing - original draft; writing - review & editing

Chapter redrafted after the following main publication:

F. Breit, H. A. Jakobsen and E. von Harbou, "Formulation of a Mass-Based Population Balance Equation: Insights Into Derivation, Mass Transfer, and Nondimensionalization," *Chemical Engineering Communications*, 2024. DOI: <https://doi.org/10.1080/00986445.2024.2445228>.

Abstract

Population balance equations (PBEs) are well-suited for modeling properties of dispersed phases such as bubbles, droplets and solid particles in processes. Unlike commonly used momentum and energy balance equations, PBEs transcend external spatial coordinates, incorporating internal property dimensions such as length, shape, and concentration. This chapter focuses on transforming the traditional number-based PBEs into a mass-based formulation, offering superior characteristics and insights in engineering applications. The mass-based formulation results in a conservative equation which allows the evaluation of breakage and coalescence kernels as well as the numerical method for mass conservation. The transformation introduces a new source term describing mass increase from outside the balanced system, confirming an approach origin from kinetic gas theory published by other authors. The chapter addresses challenges in discretizing the coalescence birth term denominator by nondimensionalization of the PBE. This research enhances our understanding of PBE modeling, particularly with the inclusion of mass transfer, contributing valuable insights for engineering applications.

5.1. Introduction

Traditionally, population balance equations (PBEs) are formulated in a non-conservative number-based framework, which quantifies the population in terms of discrete entities like bubbles [12, 16], droplets [14] or solid particles [17]. However, in many practical engineering applications, it is more convenient and insightful to work with conserved quantities such as mass, species mass, energy and momentum. In order to couple the PBE with these quantities and to be able to map phenomena such as reaction, mass and heat transfer, a conservative mass-based formulation is more appropriate. This chapter explores the transformation of a number-based PBE into a mass-based one and highlights its significance in engineering contexts.

The mass-based formulation was already introduced and applied to bubble columns by Jakobsen and coworkers [24–26, 77]. In their earlier work [77], a simple transformation was carried out without taking mass transfer into account. In a subsequent work of Nayak *et al.* [24], new transport equations and variables (mass and momentum) were derived on the basis of the kinetic gas theory (KGT) for the dispersed gas phase, which, like the PBE, also have internal coordinates. Vik *et al.* [26] then finally extended the theory to non-isothermal systems with mass transfer within their kinetic theory approach with size resolution (KTAWSR), introducing a particle size, time and spatial position dependent mass, species mass, momentum and energy balance of the dispersed phase.

In their PBE resp. the size-dependent mass balance of the dispersed gas phase, a new term for mass transfer was found, which describes the mass transfer in addition to the one in the growth term. In this chapter, we also derive the additional mass transfer term independently of Vik’s approach and discuss the relevance and necessity of the term. The authors are aware that parts of this chapter have already been considered in other publications. However, to the best of the authors’ knowledge, a common and detailed derivation and discussion of the mass-based PBE is missing in the literature.

Starting from a number-based PBE the mass-based formulation transforms the PBE into a conservative transport equation. This transformation has the advantage of validating the breakage and coalescence kernels and the numerical solution method for mass conservation. In addition, the value of the distribution density function is drastically scaled, which allows an easier and more accurate numerical solution of the PBE [78]. After the transformation, an additional mass transfer source appears in the mass-based formulation, which describes the mass increase due to mass transfer from outside the considered dispersed phase. Our approach from the field of continuum mechanics confirms the correctness of this additional term resulting from the KTAWSR. We found the deeper origin of this term, and the conservation property of the growth rate is discussed and explained.

However, the transformation to a mass-based formulation generates, among other things, a new denominator in the coalescence birth term, which is numerically difficult to discretize. As a possible solution, we propose a way to nondimensionalize the PBE. Overall, this chapter contributes to a better understanding of PBE modeling, especially when mass transfer between phases is included.

5.2. The Number-Based Population Balance Equation

Utilizing a local instantaneous continuum mechanical framework about the modeled system resp. the considered dispersed phase, we can formulate a multidimensional transport equation governing the conserved density function, denoted as ψ , within the phase space \mathbf{C} . This formulation is achieved through the application of the generalized theorems of Gauss and Stokes, as elucidated in Supplementary Information D.1.1. The phase space \mathbf{C} is conventionally partitioned into physical space, characterized by external coordinates $\mathbf{r} = (x, y, z)^T$, and property space, defined by internal coordinates $\mathbf{c} = (c_1, c_2, c_3, \dots)^T$. A comprehensive derivation is available in Jakobsen [73] and Ramkrishna [79] and a summary is provided in Supplementary Information D.1.

$$\frac{\partial \psi(\mathbf{c}, \mathbf{r}, t)}{\partial t} + \nabla_{\mathbf{r}} \cdot (\psi(\mathbf{c}, \mathbf{r}, t) \mathbf{v}_{\mathbf{r}}(\mathbf{c}, \mathbf{r}, t)) + \nabla_{\mathbf{c}} \cdot (\psi(\mathbf{c}, \mathbf{r}, t) \mathbf{v}_{\mathbf{c}}(\mathbf{c}, \mathbf{r}, t)) = \Phi(\mathbf{c}, \mathbf{r}, t) \quad (5.1)$$

In the context of Eq. (5.1), t represents the time dimension, $\mathbf{v}_{\mathbf{r}}$ and $\mathbf{v}_{\mathbf{c}}$ denote velocities in physical and property space, respectively, and Φ represents a source or sink within the phase space.

It should be noted here that, strictly speaking, Eq. (5.1) is only an equation for single-phase systems. In the context of the continuum mechanical framework, for an application to multiphase systems, integral theorems which are generalized to include discontinuities (phase boundary) and averaging procedures, e.g. volume averaging, would have to be applied. This procedure causes additional terms describing the exchange between the phases and turbulence. To the best of the authors' knowledge, this has not yet been done. However, the single-phase PBE has been used successfully in multiphase systems for decades [12–18].

Given the presence of a time derivative and a first-order partial differential operator in Eq.(5.1), it necessitates appropriate initial and boundary conditions. Typically, an open domain is considered in physical space, implying the existence of both inlet and outlet fluxes, with one being specified by the boundary condition. In the properties space, a partially open system is commonly examined, where a flux occurs at a single boundary, such as the nucleation flux at the lower limit. A detailed discussion is available in Ramkrishna [79], with a concise summary presented in Supplementary Information D.1.3.

The number-based PBE emerges by assigning the conserved density function ψ to number density function $f_{\text{d}}^{\text{n}}(\mathbf{c}, \mathbf{r}, t)$.

$$\frac{\partial f_{\text{d}}^{\text{n}}(\mathbf{c}, \mathbf{r}, t)}{\partial t} + \nabla_{\mathbf{r}} \cdot (\mathbf{v}_{\mathbf{r}}(\mathbf{c}, \mathbf{r}, t) f_{\text{d}}^{\text{n}}(\mathbf{c}, \mathbf{r}, t)) + \nabla_{\mathbf{c}} \cdot (\mathbf{v}_{\mathbf{c}}(\mathbf{c}, \mathbf{r}, t) f_{\text{d}}^{\text{n}}(\mathbf{c}, \mathbf{r}, t)) = \Phi(\mathbf{c}, \mathbf{r}, t) \quad (5.2)$$

In most engineering applications, only one inner coordinate in the property space is included, usually the particle size ξ [14–17], which simplifies the PBE to Eq. (5.3), which is called number-based PBE (nPBE) in the following.

$$\begin{aligned} \frac{\partial f_{\text{d}}^{\text{n}}(\xi, \mathbf{r}, t)}{\partial t} + \nabla_{\mathbf{r}} \cdot (\mathbf{v}_{\mathbf{r}}(\xi, \mathbf{r}, t) f_{\text{d}}^{\text{n}}(\xi, \mathbf{r}, t)) + \frac{\partial}{\partial \xi} (v_{\xi}^{\text{n}}(\xi, \mathbf{r}, t) f_{\text{d}}^{\text{n}}(\xi, \mathbf{r}, t)) \\ = -B_{\text{D}}^{\text{n}}(\xi, \mathbf{r}, t) + B_{\text{B}}^{\text{n}}(\xi, \mathbf{r}, t) - C_{\text{D}}^{\text{n}}(\xi, \mathbf{r}, t) + C_{\text{B}}^{\text{n}}(\xi, \mathbf{r}, t) \end{aligned} \quad (5.3)$$

Here, $v_{\xi}^n(\xi, \mathbf{r}, t)$ is the velocity in property space with respect to the 1D particle size dimension in the following just growth rate. In addition, an n has been super-scripted to indicate that this growth rate originates from the number-based formulation. The source term Φ is decomposed into components representing breakage ($B_B^n(\xi, \mathbf{r}, t)$, $B_D^n(\xi, \mathbf{r}, t)$) and coalescence ($C_B^n(\xi, \mathbf{r}, t)$, $C_D^n(\xi, \mathbf{r}, t)$) phenomena, encompassing birth and death events. These terms are formulated through macroscopic considerations, with derivations provided in works by Jakobsen [73] and Solsvik *et al.* [80] or Ramkrishna [79]. Their expressions are articulated as follows:

$$B_D^n(\xi, \mathbf{r}, t) = b(\xi) f_d^n(\xi, \mathbf{r}, t) \quad (5.4)$$

$$B_B^n(\xi, \mathbf{r}, t) = \int_{\xi}^{\xi_{\max}} \nu P(\xi, \zeta) b(\zeta) f_d^n(\zeta, \mathbf{r}, t) d\zeta \quad (5.5)$$

$$C_D^n(\xi, \mathbf{r}, t) = f_d^n(\xi, \mathbf{r}, t) \int_{\xi_{\min}}^{(\xi_{\max}^3 - \xi^3)^{1/3}} c(\xi, \zeta) f_d^n(\zeta, \mathbf{r}, t) d\zeta \quad (5.6)$$

$$C_B^n(\xi, \mathbf{r}, t) = \frac{\xi^2}{2} \int_{\xi_{\min}}^{(\xi^3 - \xi_{\min}^3)^{1/3}} \frac{c([\xi^3 - \zeta^3]^{1/3}, \zeta)}{(\xi^3 - \zeta^3)^{2/3}} f_d^n(\zeta, \mathbf{r}, t) f_d^n([\xi^3 - \zeta^3]^{1/3}, \mathbf{r}, t) d\zeta \quad (5.7)$$

where $b(\xi)$ is the breakage frequency, ν is the average number of daughter particles after breakage, $P(\xi, \zeta)$ is the daughter size distribution function, ξ_{\max} , ξ_{\min} are the maximum and minimum particle sizes, ζ is the integration variable or the mother particle, and $c(\xi, \zeta)$ is the coalescence frequency. The upper integration limits for coalescence terms have been modified by Jakobsen [73] to ensure strict mass conservation, as explained in detail in Solsvik *et al.* [80]. Additionally, Solsvik *et al.* [25] introduces Heaviside functions before birth and death terms to further enforce mass conservation — a practice endorsed by the authors but is not replicated in this chapter for brevity.

5.3. Transformation from Number-Based to Mass-Based PBE

The number-based density function, f_d^n , typically assumes values on the order of $1 \times 10^8 \text{ m}^{-4}$, especially in gas-liquid systems. The precision of numerical calculations becomes a challenge for such large numbers, as they are prone to round-off errors [78]. To address this, the number-based density distribution function, f_d^n , can be transformed and scaled by the single particle mass $m_d(\xi, \mathbf{r}, t)$, where ξ is typically in the micrometer range. This transformation results in a mass-based density distribution function, f_d^m . The scaling operation significantly diminishes the magnitude of f_d^n , allowing for more accurate numerical calculations while maintaining the integrity of the underlying physical system. The relationship for transforming f_d^n to f_d^m is expressed as:

$$f_d^n(\xi, \mathbf{r}, t) = \frac{f_d^m(\xi, \mathbf{r}, t)}{m_d(\xi, \mathbf{r}, t)} \quad (5.8)$$

To effect the transformation, Eq. (5.8) is incorporated into Eq. (5.3). Subsequently, each term in Eq. (5.3) is individually converted, expanded, and then combined.

Accumulation term

$$\frac{\partial}{\partial t} \left(\frac{f_d^m(\xi, \mathbf{r}, t)}{m_d(\xi, \mathbf{r}, t)} \right) = \frac{1}{m_d(\xi, \mathbf{r}, t)} \frac{\partial f_d^m(\xi, \mathbf{r}, t)}{\partial t} - \frac{f_d^m(\xi, \mathbf{r}, t)}{m_d(\xi, \mathbf{r}, t)^2} \frac{\partial m_d(\xi, \mathbf{r}, t)}{\partial t} \quad (5.9)$$

Convection in the physical space

$$\begin{aligned} \nabla_{\mathbf{r}} \cdot \left(\mathbf{v}_{\mathbf{r}}(\xi, \mathbf{r}, t) \frac{f_d^m(\xi, \mathbf{r}, t)}{m_d(\xi, \mathbf{r}, t)} \right) &= \frac{f_d^m(\xi, \mathbf{r}, t)}{m_d(\xi, \mathbf{r}, t)} \nabla_{\mathbf{r}} \cdot \mathbf{v}_{\mathbf{r}}(\xi, \mathbf{r}, t) \\ &+ \frac{\mathbf{v}_{\mathbf{r}}(\xi, \mathbf{r}, t)}{m_d(\xi, \mathbf{r}, t)} \cdot \nabla_{\mathbf{r}} f_d^m(\xi, \mathbf{r}, t) \\ &- \frac{\mathbf{v}_{\mathbf{r}}(\xi, \mathbf{r}, t) f_d^m(\xi, \mathbf{r}, t)}{m_d(\xi, \mathbf{r}, t)^2} \cdot \nabla_{\mathbf{r}} m_d(\xi, \mathbf{r}, t) \end{aligned} \quad (5.10)$$

Convection in the property space

$$\begin{aligned} \frac{\partial}{\partial \xi} \left(v_{\xi}^n(\xi, \mathbf{r}, t) \frac{f_d^m(\xi, \mathbf{r}, t)}{m_d(\xi, \mathbf{r}, t)} \right) &= \frac{f_d^m(\xi, \mathbf{r}, t)}{m_d(\xi, \mathbf{r}, t)} \frac{\partial v_{\xi}^n(\xi, \mathbf{r}, t)}{\partial \xi} \\ &+ \frac{v_{\xi}^n(\xi, \mathbf{r}, t)}{m_d(\xi, \mathbf{r}, t)} \frac{\partial f_d^m(\xi, \mathbf{r}, t)}{\partial \xi} \\ &- \frac{v_{\xi}^n(\xi, \mathbf{r}, t) f_d^m(\xi, \mathbf{r}, t)}{m_d(\xi, \mathbf{r}, t)^2} \frac{\partial m_d(\xi, \mathbf{r}, t)}{\partial \xi} \end{aligned} \quad (5.11)$$

Source and sink terms

$$B_D^{m,*}(\xi, \mathbf{r}, t) = b(\xi) \frac{f_d^m(\xi, \mathbf{r}, t)}{m_d(\xi, \mathbf{r}, t)} \quad (5.12)$$

$$B_B^{m,*}(\xi, \mathbf{r}, t) = \int_{\xi}^{\xi_{\max}} \nu P(\xi, \zeta) b(\zeta) \frac{f_d^m(\zeta, \mathbf{r}, t)}{m_d(\zeta, \mathbf{r}, t)} d\zeta \quad (5.13)$$

$$C_D^{m,*}(\xi, \mathbf{r}, t) = \frac{f_d^m(\xi, \mathbf{r}, t)}{m_d(\xi, \mathbf{r}, t)} \int_{\xi_{\min}}^{(\xi_{\max}^3 - \xi^3)^{1/3}} c(\xi, \zeta) \frac{f_d^m(\zeta, \mathbf{r}, t)}{m_d(\zeta, \mathbf{r}, t)} d\zeta \quad (5.14)$$

$$C_B^{m,*}(\xi, \mathbf{r}, t) = \frac{\xi^2}{2} \int_{\xi_{\min}}^{(\xi^3 - \xi_{\min}^3)^{1/3}} \frac{c([\xi^3 - \zeta^3]^{1/3}, \zeta) f_d^m(\zeta, \mathbf{r}, t)}{(\xi^3 - \zeta^3)^{2/3} m_d(\zeta, \mathbf{r}, t)} \frac{f_d^m([\xi^3 - \zeta^3]^{1/3}, \mathbf{r}, t)}{m_d([\xi^3 - \zeta^3]^{1/3}, \mathbf{r}, t)} d\zeta \quad (5.15)$$

If the Eq. (5.9) - Eq. (5.15) are multiplied by $m_d(\xi, \mathbf{r}, t)$ and combined, the following equation results:

$$\begin{aligned} & \frac{\partial f_d^m(\xi, \mathbf{r}, t)}{\partial t} - \frac{f_d^m(\xi, \mathbf{r}, t)}{m_d(\xi, \mathbf{r}, t)} \frac{\partial m_d(\xi, \mathbf{r}, t)}{\partial t} + f_d^m(\xi, \mathbf{r}, t) \nabla_{\mathbf{r}} \cdot \mathbf{v}_{\mathbf{r}}(\xi, \mathbf{r}, t) + \mathbf{v}_{\mathbf{r}}(\xi, \mathbf{r}, t) \cdot \nabla_{\mathbf{r}} f_d^m(\xi, \mathbf{r}, t) \\ & - \frac{\mathbf{v}_{\mathbf{r}}(\xi, \mathbf{r}, t) f_d^m(\xi, \mathbf{r}, t)}{m_d(\xi, \mathbf{r}, t)} \cdot \nabla_{\mathbf{r}} m_d(\xi, \mathbf{r}, t) + f_d^m(\xi, \mathbf{r}, t) \frac{\partial v_{\xi}^n(\xi, \mathbf{r}, t)}{\partial \xi} + v_{\xi}^n(\xi, \mathbf{r}, t) \frac{\partial f_d^m(\xi, \mathbf{r}, t)}{\partial \xi} \\ & - \frac{v_{\xi}^n(\xi, \mathbf{r}, t) f_d^m(\xi, \mathbf{r}, t)}{m_d(\xi, \mathbf{r}, t)} \frac{\partial m_d(\xi, \mathbf{r}, t)}{\partial \xi} = -B_D^m(\xi, \mathbf{r}, t) + B_B^m(\xi, \mathbf{r}, t) - C_D^m(\xi, \mathbf{r}, t) + C_B^m(\xi, \mathbf{r}, t) \end{aligned} \quad (5.16)$$

By applying the chain rule in reverse, the two convection terms can be condensed once more. Additionally, the term $\frac{f_d^m(\xi, \mathbf{r}, t)}{m_d(\xi, \mathbf{r}, t)}$ is bracketed out before the partial derivatives of the particle mass; this yields the following result.

$$\begin{aligned} & \frac{\partial f_d^m(\xi, \mathbf{r}, t)}{\partial t} + \nabla_{\mathbf{r}} (\mathbf{v}_{\mathbf{r}}(\xi, \mathbf{r}, t) f_d^m(\xi, \mathbf{r}, t)) + \frac{\partial}{\partial \xi} (v_{\xi}^n(\xi, \mathbf{r}, t) f_d^m(\xi, \mathbf{r}, t)) \\ & - \frac{f_d^m(\xi, \mathbf{r}, t)}{m_d(\xi, \mathbf{r}, t)} \left(\frac{\partial m_d(\xi, \mathbf{r}, t)}{\partial t} + v_{\xi}^n(\xi, \mathbf{r}, t) \frac{\partial m_d(\xi, \mathbf{r}, t)}{\partial \xi} + \mathbf{v}_{\mathbf{r}}(\xi, \mathbf{r}, t) \cdot \nabla_{\mathbf{r}} m_d(\xi, \mathbf{r}, t) \right) \quad (5.17) \\ & = -B_D^m(\xi, \mathbf{r}, t) + B_B^m(\xi, \mathbf{r}, t) - C_D^m(\xi, \mathbf{r}, t) + C_B^m(\xi, \mathbf{r}, t) \end{aligned}$$

The use of the total time derivative, that is $\frac{d\phi(t, x_1(t), \dots, x_N(t))}{dt} = \frac{\partial \phi}{\partial t} + \sum_{i=1}^N \frac{dx_i}{dt} \frac{\partial \phi}{\partial x_i}$, enables the summarization of the partial derivatives related to the mass of a single particle, resulting in the final equation Eq. (5.18) that is subsequently referred in the following text as number to mass-based PBE (n2mPBE).

$$\begin{aligned} & \frac{\partial f_d^m(\xi, \mathbf{r}, t)}{\partial t} + \nabla_{\mathbf{r}} \cdot (\mathbf{v}_{\mathbf{r}}(\xi, \mathbf{r}, t) f_d^m(\xi, \mathbf{r}, t)) + \frac{\partial}{\partial \xi} (v_{\xi}^n(\xi, \mathbf{r}, t) f_d^m(\xi, \mathbf{r}, t)) \\ & = \frac{f_d^m(\xi, \mathbf{r}, t)}{m_d(\xi, \mathbf{r}, t)} \frac{dm_d(\xi, \mathbf{r}, t)}{dt} - B_D^m(\xi, \mathbf{r}, t) + B_B^m(\xi, \mathbf{r}, t) - C_D^m(\xi, \mathbf{r}, t) + C_B^m(\xi, \mathbf{r}, t) \end{aligned} \quad (5.18)$$

In which now:

$$B_D^m(\xi, \mathbf{r}, t) = b(\xi) f_d^m(\xi, \mathbf{r}, t) \quad (5.19)$$

$$B_B^m(\xi, \mathbf{r}, t) = m_d(\xi, \mathbf{r}, t) \int_{\xi}^{\xi_{\max}} \nu P(\xi, \zeta) b(\zeta) \frac{f_d^m(\zeta, \mathbf{r}, t)}{m_d(\zeta, \mathbf{r}, t)} d\zeta \quad (5.20)$$

$$C_D^m(\xi, \mathbf{r}, t) = f_d^m(\xi, \mathbf{r}, t) \int_{\xi_{\min}}^{(\xi_{\max}^3 - \xi^3)^{1/3}} c(\xi, \zeta) \frac{f_d^m(\zeta, \mathbf{r}, t)}{m_d(\zeta, \mathbf{r}, t)} d\zeta \quad (5.21)$$

$$C_B^m(\xi, \mathbf{r}, t) = \frac{\xi^2 m_d(\xi, \mathbf{r}, t)}{2} \int_{\xi_{\min}}^{(\xi^3 - \xi_{\min}^3)^{1/3}} \frac{c([\xi^3 - \zeta^3]^{1/3}, \zeta)}{(\xi^3 - \zeta^3)^{2/3}} \frac{f_d^m(\zeta, \mathbf{r}, t)}{m_d(\zeta, \mathbf{r}, t)} d\zeta \quad (5.22)$$

In order to be in line with the equations presented in [3, 16, 24–26], only the definition of the mass density of the dispersed phase ρ_d , that is $m_d(\xi, \mathbf{r}) = \rho_d(\xi, \mathbf{r}, t)V(\xi)$, where $V(\xi)$ is the volume of a single particle with size ξ , has to be applied. The term $dm_d(\xi, \mathbf{r}, t)/dt$ must be described with a appropriate closure.

5.4. Discussion

5.4.1. Extra Mass Transfer Term

The comparison of the nPBE (Eq. (5.3)) and the n2mPBE (Eq. (5.18)) shows that the transformation from a number-based PBE to a mass-based PBE leads to an additional term that appears on the right side of the n2mPBE (Eq. (5.18)), the extra mass transfer term that is $\frac{f_d^m(\xi, \mathbf{r}, t)}{m_d(\xi, \mathbf{r}, t)} \frac{dm_d(\xi, \mathbf{r}, t)}{dt}$. This term represents an additional mass transfer term beside the one within the convection term in the property space (growth). It accounts for the increase in total mass of the dispersed phase that is balanced in the PBE caused by a mass flux from outside, e.g. the continuous phase, into the dispersed phase.

In order to get a deeper understanding of the origin of the extra mass transfer term, we start with substituting ψ in the generalized PBE Eq. (5.1) with the mass density function f_d^m and assume only one inner coordinate, the particle size, so that the mass-based PBE (Eq. (5.23)), in the following just mPBE, directly follows:

$$\begin{aligned} \frac{\partial f_d^m(\xi, \mathbf{r}, t)}{\partial t} + \nabla_{\mathbf{r}} \cdot (\mathbf{v}_{\mathbf{r}}(\xi, \mathbf{r}, t) f_d^m(\xi, \mathbf{r}, t)) + \frac{\partial}{\partial \xi} (v_{\xi}^m(\xi, \mathbf{r}, t) f_d^m(\xi, \mathbf{r}, t)) \\ = -B_D^m(\xi, \mathbf{r}, t) + B_B^m(\xi, \mathbf{r}, t) - C_D^m(\xi, \mathbf{r}, t) + C_B^m(\xi, \mathbf{r}, t) \end{aligned} \quad (5.23)$$

Comparing the mPBE (Eq. (5.23)) with the one from the transformation of the number-based PBE the n2mPBE (Eq. (5.18)), the extra mass transfer term is also missing here. The fact that the extra mass transfer term appears in the mass-based PBE through the derivation of the number-based PBE with subsequent transformation and does not appear in the direct derivation via the generalized PBE Eq. (5.1), can be attributed to the conservation properties of the original equation. To study the conservation property of the original equations the generalized PBE Eq. (5.1) is integrated over the entire phase space and Gauss's theorem is applied.

$$\frac{\partial \Psi}{\partial t} = \int_{\Omega_{\mathbf{C}}(t)} \frac{\partial \psi}{\partial t} d\mathbf{C} = \int_{\Omega_{\mathbf{C}}(t)} \Phi d\mathbf{C} - \oint_{\delta\Omega_{\mathbf{r}}(t)} \psi \mathbf{v}_{\mathbf{r}} \cdot d\mathbf{r} - \oint_{\delta\Omega_{\mathbf{c}}(t)} \psi \mathbf{v}_{\mathbf{c}} \cdot d\mathbf{c} \quad (5.24)$$

This equation implies that the conserved quantity Ψ changes temporally by a source within the modeled system (first term) and due to convective (second and third term) across the boundary of the modeled system. Note the conserved quantity Ψ is also the total quantity of the modeled system.

Now, from the observation in Section 5.2 that the PBE is a single-phase equation, it follows that if mass is considered as a conserved quantity, the integral over the source must disappear, since there are no internal sources of mass in a single-phase system, neglecting relativistic phenomena. Consequently, the conserved quantity cannot change by convection within the domain, only by fluxes across the boundaries. This conclusion leads to two insights:

1. In a closed domain (no particles are added or withdrawn through fluxes across the boundary of the phase space) where no breakage and coalescence occurs, the following holds:

- both the nPBE (Eq. (5.3)) and the n2mPBE (Eq. (5.18)) conserve the total number and not necessarily the total mass
- the mPBE (Eq. (5.23)) conserves the total mass but not necessarily the total number

The fact that the nPBE (Eq. (5.3)) and the n2mPBE (Eq. (5.18)) have the same conservation properties is because Eq. (5.8) is a bijective mapping.

2. The velocities $\mathbf{v}_r, \mathbf{v}_c$ should be Ψ conservative, transporting it without generating or destroying it.¹ Hence, the growth rate v_ξ^n in the nPBE (Eq. (5.3)) is total number conserving, and in the mPBE (Eq. (5.23)), the growth rate v_ξ^m is total mass conserving.

Particle growth in one-dimensional length property space, without assumptions (refer to Supplementary Information D.2), correlates with changes in volume, which arise from changes in density and mass of the particle. Density changes maintain total mass and number. Mass changes can either preserve total number, involving mass transfer from outside modeled system e.g. from the continuous phase in to the dispersed phase due to phase changes or it can preserve total mass, involving mass transfer from within the modeled system, such as between neighboring particles sizes. Furthermore, it can preserve both total number and mass within the system, for instance, via mass transfer between non-neighboring particles sizes. Physically, only the number-conserving mass change due to phase change is pertinent, as the other mechanisms lack a phase boundary necessary for mass transfer or involve changes in the number of particles, typically modeled through breakage or coalescence. Therefore the number conserving growth rate v_ξ^n should contain both effects density change and mass change due to phase change and the mass conserving growth rate v_ξ^m only the density change:

$$v_\xi^n(\xi, \mathbf{r}, t) = -\frac{\xi}{3\rho_d(\xi, \mathbf{r}, t)} \frac{d\rho_d(\xi, \mathbf{r}, t)}{dt} + \frac{1}{\frac{\pi}{2}\xi^2\rho_d(\xi, \mathbf{r}, t)} \frac{dm_d(\xi, \mathbf{r}, t)}{dt} \quad (5.25)$$

$$v_\xi^m(\xi, \mathbf{r}, t) = -\frac{\xi}{3\rho_d(\xi, \mathbf{r}, t)} \frac{d\rho_d(\xi, \mathbf{r}, t)}{dt} \quad (5.26)$$

In summary, when considering mass transfer between phases leading to changes in the total mass of the dispersed phase, the use of either the nPBE (Eq. (5.3)) or the n2mPBE (Eq. (5.18)), is necessary, rather than relying on the mPBE (Eq. (5.23)). The n2mPBE (Eq. (5.18)) is superior to the nPBE (Eq. (5.3)) in most scenarios due to its aforementioned advantages, including scalability, interpretability, and the preservation of a conserved quantity.

If the previous findings and interpretations from the continuum mechanical model are compared with those from the kinetic gas theory model of Vik *et al.* [26], they are consistent. For instance, the model of Vik *et al.* [26] also features the extra mass transfer term. In terms of applicability, the KTAWSR already provides mass-based and size-dependent transport equations

¹At this point, this conclusion only applies strictly mathematically to mass as a conserved quantity, since the sources do not disappear after integration in the number-based PBE. However, if it is included that the behavior of the collective can be derived from the individual particle behavior and that the individual particle growth is number conserving, this statement applies again.

for the common conservation quantities (mass, species mass, momentum, energy). Whereas the approach from continuum mechanics presented in this chapter so far only applies to mass. A derivation based on a continuum mechanics approach, wherein the extra mass transfer is a direct outcome without detour over the number-based PBE, and in which new transport equations for the other conservation quantities, which also depend on the particle size, is currently absent in the literature. A potential avenue for this involves a derivation within the generalized phase space akin to that of multifluid equations (cf. Jakobsen [73]). However, this remains a subject for future work whereby the challenge must also be faced that the most of the experimental data or correlations available in the literature are for v_{ξ}^n and not for v_{ξ}^m .

5.4.2. Mass-based Breakage and Coalescence Sources and Sinks

As mentioned earlier, if mass is selected as the conserved quantity, the integral of ξ over Φ must vanish. Since breakage and coalescence are considered independent phenomena, this conclusion must also apply to both phenomena individually. Consequently, the mass of particles that undergo breakage or coalescence must be equivalent to the mass generated by breakage or coalescence. This ensures that, during the integration over the entire property space, the following relationship must hold:

$$0 = \int_{\xi_{\min}}^{\xi_{\max}} B_{\text{B}}^m(\xi, \mathbf{r}, t) - B_{\text{D}}^m(\xi, \mathbf{r}, t) \, d\xi \quad (5.27)$$

$$0 = \int_{\xi_{\min}}^{\xi_{\max}} C_{\text{B}}^m(\xi, \mathbf{r}, t) - C_{\text{D}}^m(\xi, \mathbf{r}, t) \, d\xi \quad (5.28)$$

Note that the mass-based terms Eq. (5.19) - Eq. (5.22) were obtained on the basis of a transformation of a number-based form. A direct derivation of the mass-based terms should be possible analogous to [73, 79, 80], but is not shown here.

The two relationships Eq. (5.27) and Eq. (5.28) of the mass-based breakage and coalescence kernels represents an additional advantage of the mass-based formulation over the number-based counterpart. For a number-based formulation with binary breakage or convalence, the ratio of the integrals over the entire property space of the birth and death terms is 2 and 1/2 respectively. However, this only applies to binary processes. For breakage and convalence phenomena in which different numbers of particles participate, e.g. size-dependent or location-dependent, this no longer applies, whereas in the mass-based formulation the relationship Eq. (5.27) and Eq.(5.28) is still valid.

Furthermore in the case of absent mass transfer the entire mass-based PBE is now in conservative form, ensuring that the system's conservation properties are rigorously preserved, enhancing numerical stability and accuracy. This characteristic facilitates the examination of kernel functions and employed numerical methods for mass conservation. It is important to note that this property extends to the general source Φ within the multidimensional property space.

Comparing the coalescence birth term in the mass-based formulation C_{B}^m with its number-based counterpart C_{B}^n , a noticeable difference, the single particle mass resp. the product

of volume and density, arises in the denominator of the integral due to the transformation (see Eq. (5.22)). Since ξ and ζ generally fall in the millimeter or micrometer range, their difference results in an exceedingly small number, further compounded by applying the volume. Consequently, the entire denominator (see Eq. (5.22)) becomes very small, particularly at the respective integration limits, posing several numerical challenges. Firstly, division by an extremely small number yields a large number, making the system highly sensitive to small disturbances in f_d^m . Secondly, pronounced step gradients at integration limits pose challenges for accurate integration, crucial for maintaining mass conservation. Additionally, higher-order interpolation schemes, such as orthogonal collocation [16, 25], face difficulty in approximating step gradients without introducing oscillations. A potential resolution involves scaling the property space, prompting the subsequent nondimensionalization of the PBE.

5.4.3. Nondimensionalization of the PBE

To nondimensionalize the PBE, the dependent variable is identified as f_d^m , while the independent variables include $\xi, \mathbf{r}, t, \zeta$. Each variable is then expressed in terms of a dimensionless variable (indicated by a hat over the symbol) and a scaling factor (indicated by a subscript s) with units corresponding to the original variable. In the present case it follows:

$$f_d^m = \hat{f}_d^m f_{d,s}^m \quad (5.29)$$

$$t = \hat{t} t_s \quad (5.30)$$

$$\mathbf{r} = \hat{\mathbf{r}} r_s \quad (5.31)$$

$$\xi = \hat{\xi} \xi_s \quad (5.32)$$

$$\zeta = \hat{\zeta} \xi_s \quad (5.33)$$

If the Eq. (5.29) - Eq. (5.33) are inserted into Eq. (5.18), where we applied the definition of the mass density of the dispersed phase, we get

$$\begin{aligned} & \frac{f_{d,s}^m}{t_s} \frac{\partial \hat{f}_d^m(\hat{\xi}, \hat{\mathbf{r}}, \hat{t})}{\partial \hat{t}} + \frac{f_{d,s}^m}{r_s} \nabla_{\hat{\mathbf{r}}} \cdot \left(\mathbf{v}_{\mathbf{r}}(\hat{\xi} \xi_s, \hat{\mathbf{r}} r_s, \hat{t} t_s) \hat{f}_d^m(\hat{\xi}, \hat{\mathbf{r}}, \hat{t}) \right) + \frac{f_{d,s}^m}{\xi_s} \frac{\partial}{\partial \hat{\xi}} \left(v_{\xi}(\hat{\xi} \xi_s, \hat{\mathbf{r}} r_s, \hat{t} t_s) \hat{f}_d^m(\hat{\xi}, \hat{\mathbf{r}}, \hat{t}) \right) \\ &= \frac{f_{d,s}^m}{\xi_s^3} \frac{\hat{f}_d^m(\hat{\xi}, \hat{\mathbf{r}}, \hat{t})}{V(\hat{\xi})} \frac{1}{\rho_d} \frac{dm_d(\xi, \mathbf{r}, t)}{dt} - B_D^m(\hat{\xi} \xi_s, \hat{\mathbf{r}} r_s, \hat{t} t_s) + B_B^m(\hat{\xi} \xi_s, \hat{\mathbf{r}} r_s, \hat{t} t_s) \\ & - C_D^m(\hat{\xi} \xi_s, \hat{\mathbf{r}} r_s, \hat{t} t_s) + C_B^m(\hat{\xi} \xi_s, \hat{\mathbf{r}} r_s, \hat{t} t_s) \end{aligned} \quad (5.34)$$

whereby the fact that the scaling factors are assumed to be constant was utilized. In the next step, the Eq. (5.34) is divided by the prefactor of the transient term.

$$\begin{aligned} & \frac{\partial \hat{f}_d^m(\hat{\xi}, \hat{\mathbf{r}}, \hat{t})}{\partial \hat{t}} + \frac{t_s}{r_s} \nabla_{\hat{\mathbf{r}}} \cdot \left(\mathbf{v}_r(\hat{\xi}\xi_s, \hat{\mathbf{r}}\mathbf{r}_s, \hat{t}t_s) \hat{f}_d^m(\hat{\xi}, \hat{\mathbf{r}}, \hat{t}) \right) + \frac{t_s}{\xi_s} \frac{\partial}{\partial \hat{\xi}} \left(v_\xi(\hat{\xi}\xi_s, \hat{\mathbf{r}}\mathbf{r}_s, \hat{t}t_s) \hat{f}_d^m(\hat{\xi}, \hat{\mathbf{r}}, \hat{t}) \right) \\ &= \frac{t_s}{\xi_s^3} \frac{\hat{f}_d^m(\hat{\xi}, \hat{\mathbf{r}}, \hat{t})}{V(\hat{\xi})} \frac{1}{\rho_d} \frac{dm_d(\xi, \mathbf{r}, t)}{dt} - \hat{B}_D^m(\hat{\xi}, \hat{\mathbf{r}}, \hat{t}) + \hat{B}_B^m(\hat{\xi}, \hat{\mathbf{r}}, \hat{t}) - \hat{C}_D^m(\hat{\xi}, \hat{\mathbf{r}}, \hat{t}) + \hat{C}_B^m(\hat{\xi}, \hat{\mathbf{r}}, \hat{t}) \end{aligned} \quad (5.35)$$

In which are

$$\hat{B}_D^m(\hat{\xi}, \hat{\mathbf{r}}, \hat{t}) = t_s b(\hat{\xi}\xi_s) \hat{f}_d^m(\hat{\xi}, \hat{\mathbf{r}}, \hat{t}) \quad (5.36)$$

$$\hat{B}_B^m(\hat{\xi}, \hat{\mathbf{r}}, \hat{t}) = \xi_s t_s \rho_d(\hat{\xi}\xi_s, \hat{\mathbf{r}}\mathbf{r}_s, \hat{t}t_s) V(\hat{\xi}) \int_{\hat{\xi}}^{\hat{\xi}_{\max}} \nu P(\hat{\xi}\xi_s, \hat{\zeta}\xi_s) b(\hat{\zeta}\xi_s) \frac{\hat{f}_d^m(\hat{\zeta}, \hat{\mathbf{r}}, \hat{t})}{\rho_d(\hat{\zeta}\xi_s, \hat{\mathbf{r}}\mathbf{r}_s, \hat{t}t_s) V(\hat{\zeta})} d\hat{\zeta} \quad (5.37)$$

$$\hat{C}_D^m(\hat{\xi}, \hat{\mathbf{r}}, \hat{t}) = \frac{f_{d,s}^m t_s}{\xi_s^2} \hat{f}_d^m(\hat{\xi}, \hat{\mathbf{r}}, \hat{t}) \int_{\hat{\xi}_{\min}}^{(\hat{\xi}_{\max} - \hat{\xi}^3)^{1/3}} c(\hat{\xi}\xi_s, \hat{\zeta}\xi_s) \frac{\hat{f}_d^m(\hat{\zeta}, \hat{\mathbf{r}}, \hat{t})}{\rho_d(\hat{\zeta}\xi_s, \hat{\mathbf{r}}\mathbf{r}_s, \hat{t}t_s) V(\hat{\zeta})} d\hat{\zeta} \quad (5.38)$$

$$\begin{aligned} \hat{C}_B^m(\hat{\xi}, \hat{\mathbf{r}}, \hat{t}) &= \frac{f_{d,s}^m t_s}{\xi_s^2} \frac{\hat{\xi}^2 \rho_d(\hat{\xi}\xi_s, \hat{\mathbf{r}}\mathbf{r}_s, \hat{t}t_s) V(\hat{\xi})}{2} \\ & \int_{\hat{\xi}_{\min}}^{(\hat{\xi}^3 - \hat{\xi}_{\min}^3)^{1/3}} \frac{c([\hat{\xi}^3 - \hat{\zeta}^3]^{1/3} \xi_s, \hat{\zeta}\xi_s)}{(\hat{\xi}^3 - \hat{\zeta}^3)^{2/3}} \frac{\hat{f}_d^m(\hat{\zeta}, \hat{\mathbf{r}}, \hat{t})}{\rho_d(\hat{\xi}\xi_s, \hat{\mathbf{r}}\mathbf{r}_s, \hat{t}t_s) V(\hat{\zeta})} \\ & \frac{\hat{f}_d^m([\hat{\xi}^3 - \hat{\zeta}^3]^{1/3}, \hat{\mathbf{r}}, \hat{t})}{\rho_d([\hat{\xi}^3 - \hat{\zeta}^3]^{1/3} \xi_s, \hat{\mathbf{r}}\mathbf{r}_s, \hat{t}t_s) V([\hat{\xi}^3 - \hat{\zeta}^3]^{1/3})} d\hat{\zeta} \end{aligned} \quad (5.39)$$

In a final step, the scaling factors are chosen. The following scaling factors are only suggestions and are generally case specific.

$$f_{d,s}^m = m_0 / \xi_{\max} \quad (5.40)$$

$$t_s = \tau \quad (5.41)$$

$$\mathbf{r}_s = (x_{\max}, y_{\max}, z_{\max})^T \quad (5.42)$$

$$\xi_s = \xi_{\max} \quad (5.43)$$

$$\zeta_s = \xi_{\max} \quad (5.44)$$

Here m_0 is initial mass of all particles in the modeled system per unit volume, τ the mean residence time of the particles in the modeled system. When extending this procedure to a number-based PBE, the prefactors remain consistent with mass-based PBEs for all terms except coalescence. The prefactor for the coalescence term in the number-based form becomes $f_{d,s}^n t_s \xi_s$. Note that the consecutive equations e.g. $\rho_d, b(\hat{\xi}\xi_s)$ are calculated with dimensional quantities and have a dimension themselves. The consecutive equations can also be nondimensionalized, although the prefactors must then be included in to the consecutive equation and any dimensional prefactors that occur in the consecutive equations must also be scaled.

From preliminary studies we were able to observe that the nondimensionalization reduces

the computing time but hardly affects the accuracy. However, the challenge associated with the denominator in the coalescence birth term persists partially, prompting consideration of alternative strategies, including additional operations on nondimensionalized coordinates, such as applying the natural logarithm. Alternatively, the PBE could be derived directly with dimensionless inner coordinates. This derivation requires careful reformulation of breakage and coalescence integrals from the general form (cf. Jakobsen [73]) and precise transformation of the corresponding kernels. Exploration of these approaches is pending and will be a focus of future investigations.

5.5. Conclusion and Outlook

In this chapter, the number-based PBE was derived on the basis of a generalized multidimensional transport equation stemming from continuum mechanics and then transformed into a mass-based PBE. This transformation revealed an additional term in the mass-based formulation, signifying the system's mass increase due to external mass transfer. We extensively discussed the origin and distinctions between this approach and the direct derivation of the mass-based PBE from the generalized transport equation. Our exploration demonstrated that growth rates in the property space are either mass or number conserving, depending on the derivation origin, a characteristic retained post-transformation, introducing an extra term in the PBE.

Based on a general growth velocity for particle lengths, we attribute the distinct conservation properties to mass transfer. The derivation of the number-based PBE is grounded in number-conserving mass transfer, leading to an increase in mass upon transformation into a mass-based PBE.

Furthermore, using our continuum mechanics approach, we derived the same PBE that includes the additional mass transfer term, consistent with the derivation by Vik *et al.* [26] from a kinetic gas theory approach.

Additionally, we addressed the numerical challenges arising from the denominator in the coalescence term after transformation, proposing nondimensionalization as a potential solution. Although this method partially resolved numerical issues, a notable enhancement in computational speed was observed.

In conclusion, this chapter significantly contributes to advancing the understanding of mass-based PBE modeling, unraveling intricacies in conservation properties and offering insights into addressing numerical challenges associated with certain terms.

6. Sensitivity and Parameter Analysis of Population Balance Applied to Non-Reactive Gas-Liquid Semi-Batch Stirred Tanks

Contributor Roles Taxonomy

Ferdinand Breit: conceptualization; formal analysis; methodology; project administration; software; validation; visualization; writing - original draft; writing - review & editing

This chapter is intended for submission to a peer-reviewed journal for publication.

Abstract

This chapter applies the multifluid population balance model (MPB) to a non-reactive gas-liquid semi-batch stirred tank reactor (STR) to describe the bubble size distribution and the interfacial area density. A robust numerical solution method for solving the population balance equation is essential for large parameter studies. We compare and evaluate three numerical methods from literature and a novel method developed in this chapter using analytical solutions of known test cases. While no method clearly outperforms others, the finite volume method with Gauss quadrature, proposed by us, demonstrates fast, robust, and precise results. To demonstrate the robustness and to investigate the STR, a large sensitivity and parameter study is carried out in which several parameters of the model are varied in a one-at-a-time analysis. The studies reveal strong dependencies on kernel parameters and process conditions. Our findings confirm trends from literature and highlight the importance of understanding the complex interaction of breakage and coalescence. Furthermore, we fitted the model parameters to experimental data in a preliminary study, showing good agreement with measured data. The presented MPB, in conjunction with our novel solution methodology proved to be a valuable tool for investigating the intricate behavior of the dispersed gas phase within the STR. However, the model also demonstrated shortcomings, as it lacked the capacity to describe the gas holdup. The primary objective of future research will be to identify and develop modelling approaches that address this shortcoming.

6.1. Introduction

In this chapter, the multfluid population balance model (MPB) is applied to a non-reactive gas-liquid semi-batch stirred tank reactor (STR) to describe the behavior of the dispersed gas phase. The gas feed is continuous while no in or out flow of liquid phase is considered (semi-batch mode). The usual assumption of STR models in process engineering of zero gradients is also adopted in this chapter, resulting in an ideally mixed system. However, in contrast to the previous chapters, we consider here the transient behavior of the reactor. Consequently, the kinetic theory approach with size resolution (KTAWSR) developed by Jakobsen and coworkers [24–26] results in the properties of the dispersed phase becoming functions of the bubble diameter and time. Furthermore, we extended the population balance equation (PBE) so that the influence of mass transfer between the phases on the bubble size distribution (BSD) can be explicitly accounted for. In our recent publication (see Chapter 5), we presented a detailed discussion on the consideration of mass transfer in the PBE.

In order to facilitate rapid and comprehensive parameter studies with the MPB, it is essential to devise a rapid, straightforward, and, in particular, robust methodology for solving the governing equations. Given that the PBE represents a transient integro-partial differential equation, it is crucial to select and optimize the solver for the specific task at hand. Basically, there are two approaches for solving the PBE, one is to solve for moments of the density function and the other is to solve directly for the density function. Methods based on moments such as [81–84] are often used [19, 85–88] as they are simple and efficient. The disadvantage, however, is that these methods are not very accurate and the density function can only be obtained by making further strong assumptions [73, 89]. As a result, important phenomena such as multimodal density functions and their effects on the system cannot be investigated. The methods that directly solve the density function can reproduce these phenomena, which is why this approach is further considered in this chapter.

Numerous methods within this class are described in the literature [32, 89–92]. One aim of the present chapter is to undertake a comparative evaluation of the performance of different solvers. For that reason, we implemented and compared four different methods: 1) spectral orthogonal collocation method, which were develop by Jakobsen and coworker [32, 93] and used in our previous studies [16], Chapter 3-4, 2) the classical fixed pivot technique [94] as it used e.g. in OpenFOAM [90], 3) a meshless radial basis method [89] and 4) a finite volume method with Gauss quadrature which was developed in this chapter. The solution methods were selected on the basis of the availability of information in the literature and the simplicity of implementation. It should be noted that this article does not aim to provide a comprehensive mathematical review of solution methods (for which the reader is referred to [95, 96]). Instead, the objective is to identify a method that enables engineers to easily and quickly navigate the complex landscape of advanced multiphase modelling involving PBE. The performance of the different methodologies was evaluated by benchmarking the numerical solutions of four straightforward and renowned PBE problems against their analytical solutions that are documented in the literature [97–103].

The best numerical solution method, the method proposed by us, was used to solve the MPB

of the STR. Given the model assumptions, it is not possible to determine the gas holdup in the reactor (see Section 6.3.1 for a detailed discussion). Therefore, the sensitivity and parameter analysis presented in this chapter is primarily intended to demonstrate the robustness of the numerical solution method. However, the trends found here, despite the artificial assumption of constant gas holdup, were compared with the corresponding trends from the literature, if available. In these parameter studies most parameters of the MPB were examined in a one-at-the-time analysis, e.g. the choice of the kernels and their parameters, as well as the influence of the process conditions, the design of the gas sparger and of the physicochemical properties of gas and liquid phase.

Despite the artificial constant gas holdup, most of the trends from the literature could be confirmed in the sensitivity and parameter analysis. But more important the results show that the solution method developed in this chapter is simple, fast and robust in comparison to the other methods investigated. For that reason, it is well suited for parameter studies in which the MPB must be solved for many different parameters.

Furthermore, the findings of a preliminary study are presented, wherein the parameters of the breakage and coalescence kernels were estimated through the utilisation of experimental measurements of the BSD in a STR. While the model is capable of reproducing the observed data, certain limitations are evident, which will be addressed in future studies.

In summary, this chapter illustrates the benefits of our MPB for the representation of multiphase STRs. The model is relatively inexpensive to compute, yet it can describe the interaction of different sub-processes, such as the breakage and coalescence of bubbles and mass transfer. This chapter represents a significant advancement in our efforts to develop a model that can adequately describe the complex behavior of a dispersed multiphase system in a STR, while requiring only a limited set of empirical equations and parameters.

6.2. Experimental Setup

The Fig. 6.1 illustrates the experimental setup used in this chapter. Compressed air from the utility supply was dispersed at the bottom of stainless steel vessel (1, the number refers to the Fig. 6.1) with a diameter of 0.3 m by a spider sparger (2) with a diameter of 0.15 m, four arms and six orifices per arm of 2 mm diameter each and exits the vessel at the top into the ambient.

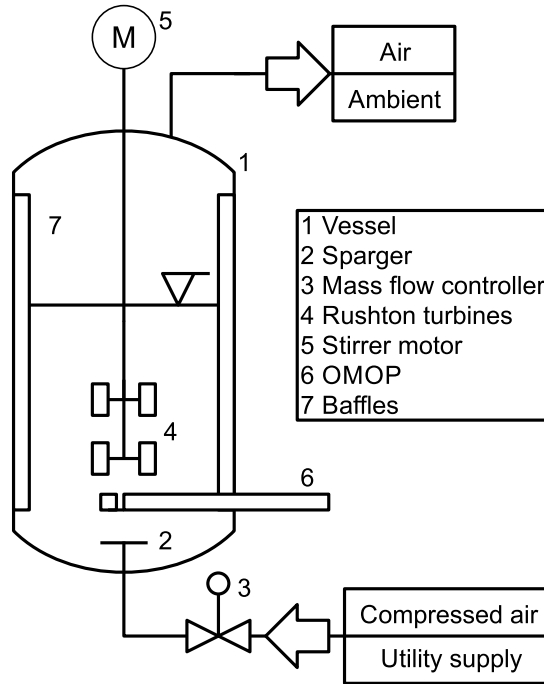


Figure 6.1.: Schematic illustration of the experimental setup.

The air flux was controlled by a mass flow controller (3) of type GF040 (GF040CXXC-0008051L-N2AVS5-XXXXXX-00C) from the manufacture Brooks Instrument (Dresden, Germany).

The continuous liquid phase was a mixture consisting of osmosis water (conductivity about 1100 μS adjusted with Na_2SO_4) and $w_{\text{c,EtOH}} = 0.01 \text{ kg kg}^{-1}$ ethanol (EtOH). This mixture was pre-filled (about 27 L) and remains in the vessel during the experiment. The possibility of ethanol being stripped out during the experiment was negated by a preliminary simulation study.

The STR was agitated with two 6-blade Rushton turbines (4) driven by a Hei-TORQUE Ultimate 400 stirrer motor (5) from the manufacture Heidolph Instruments GmbH & Co. KG (Schwabach, Germany), which also measures the torque on the shaft. To intensify the mixing, the STR has four baffles (7) equidistantly distributed around the vessel.

The in-house developed optical multimode online probe (OMOP, 6) was used to determine the BSD [104, 105]. It records telecentric shadowgraph images of the bubbly flow in a measuring gap (4 mm). Then, an pre-trained convolutional neural network developed by Weibel *et al.* [67]

automatically detects and evaluates the bubbles so that the BSD can be calculated. Details of the OMOP and evaluation procedure can be found elsewhere [3, 67, 104, 105]. The OMOP was located under the stirrer. In a preliminary study, it was found that the measured BSD to be independent of the measurement position, proving ideal mixed conditions. Further details of the geometry of the STR are summarized in the Supplementary Information Tab. E.6.

To carry out an experiment, the mixture was pre-filled, the stirrer was started and adjusted to the desired speed. As soon as the torque had stabilized, the gas was introduced, and simultaneously the measurement of the BSD was started. An experiment lasts 30 minutes, with an image being taken with the OMOP every second. The first 60 images were stacked to create the inlet BSD, and then subsequently every 120 images were stacked to create a BSD. The last BSD consists again only of 60 images to match the total number of recorded images (1800 pcs.). In summary, this results in 16 measured BSDs.

In the experiment, the mixture including the holdup, the gas flux including the gas type, the stirrer, the stirrer speed, the sparger and baffle plates can be varied. However, this chapter only serves as a preliminary study for a larger experimental study to be conducted in future to evaluate the prediction performance of the develop model, so only one experiment at $j_d = 0.6 \text{ cm s}^{-1}$ and 300 RPM is considered here.

The measured BSDs are summarized in the Supplementary Material of the publication.

6.3. Modelling and Simulation

6.3.1. System Description and Assumptions

To investigate the transient behavior of the BSD within the STR, it is assumed that a single-component gas enters the vessel through a bottom sparger at a specified mass flow rate $\dot{m}_{d,in}$, characterized by an inlet bubble size distribution $f_{d,in}^m$, and exits from the top with a mass flow rate $\dot{m}_{d,out}$ and distribution f_d^m , based on the assumption of ideal mixing. The liquid phase is neither fed nor withdrawn from the reactor, constituting a semi-batch process. Phase mixing is facilitated by a stirrer, ensuring ideal mixing conditions for both liquid and gas phase. The system maintains constant pressure and temperature, treating the physicochemical properties of the fluids enclosed as constant. Entrainment of gas phase by the stirrer is neglected. Furthermore, it is assumed that the mass change of the liquid phase due to mass transfer between the liquid and gas phases is negligible compared to the total mass of the liquid phase. As a result, the total mass/volume and the composition of the liquid phase remains constant within the reactor, rendering a mass and species balance of the liquid phase unnecessary. Together with the single-component gas case, only the mass balance of the gas phase, the mass-based PBE, needs to be considered. It is important to note that in this chapter, mass transfer is considered directly in the mass-based PBE because it completely replaces the mass balance of the gas phase. This approach contrasts with the usual ad hoc solution, in which the PBE is solved in addition to the gas phase mass balance in the two-fluid model to obtain a better estimate of the interfacial area density or bubble diameter [19].

For engineers, an understanding of the residence time of the dispersed phase within the reactor is of considerable significance. This information allows for the assessment of the conversion of reactants and the selectivity to target products in the reactor. In the bubble column, the residence time distribution as a function of the bubble diameter can be obtained from the axial phase velocity, which is determined from the momentum balance of the dispersed phase using the KTAWSR (see Chapter 3-4). Given the assumption of ideal mixing in the reactor, a global momentum balance over the STR cannot yield information about the velocity of the gas phase. In order to obtain this information, it would be necessary to consider the internal flow conditions of the gas and liquid phases, which are also influenced by a number of factors, including the type and speed of the stirrer, the design of the gas sparger and other internals, such as baffles. The development of such a model was not within the scope of the present chapter; however, it will be considered in future work. In this chapter, the residence time of the gas phase was fixed at a constant value to align with the experimentally correlated gas holdup in the reactor. It is acknowledged that this simplification is at odds with our general objective of developing a model approach that requires only a minimal number of measurement data from the considered process, thereby facilitating process optimization and scale-up. Nevertheless, the objective of this chapter is to develop and test a solution method for the MPB. In this context, this assumption is deemed acceptable.

As the gas holdup is set to a constant value, the overall volume of the enclosed fluids resp. the gasified volume is constant. Consequently, the mass flow rate of the gas phase exiting the reactor $\dot{m}_{d,out}$ is equal to the mass flow rate of the gas entering the reactor via the sparger

$\dot{m}_{d,in}$ minus the mass flow rate due to phase change (see Supplementary Information E.3.1).

6.3.2. Governing Equations

If the assumptions and conditions from Section. 6.3.1 are applied to the rigorous KTAWSR of [26], it is reduced to solely a simplified form of the PBE Eq. (6.1). A derivation can be found in the Supplementary Information E.3.2.

$$\begin{aligned} & \frac{\partial f_d^m(\xi, t)}{\partial t} + \frac{\dot{m}_{d,out}}{V_R} \frac{f_d^m(\xi, t)}{\int_{\xi_{min}}^{\xi_{max}} f_d^m(\xi, t) d\xi} - \frac{\dot{m}_{d,in}}{V_R} \frac{f_{d,in}^m(\xi, t)}{\int_{\xi_{min}}^{\xi_{max}} f_{d,in}^m(\xi, t) d\xi} + \frac{\partial}{\partial \xi} (v_\xi(\xi, t) f_d^m(\xi, t)) \\ & = \frac{f_d^m(\xi, t)}{V(\xi)} \frac{1}{\rho_d} \frac{dm_d}{dt} - B_D^m(\xi, t) + B_B^m(\xi, t) - C_D^m(\xi, t) + C_B^m(\xi, t) \end{aligned} \quad (6.1)$$

In which the growth rate due to phase change, the breakage death and birth term as well as the coalescence death and birth term are:

$$v_\xi(\xi, t) = \frac{1}{\frac{\pi}{2} \xi^2 \rho_d} \frac{dm_d}{dt} \quad (6.2)$$

$$B_D^m(\xi, t) = H\left(\xi - \sqrt[3]{2\xi_{min}^3}\right) b(\xi) f_d^m(\xi, t) \quad (6.3)$$

$$B_B^m(\xi, t) = H\left(\sqrt[3]{\xi_{max}^3 - \xi_{min}^3} - \xi\right) \rho_d V(\xi) \int_{\xi}^{\xi_{max}} \nu P(\xi, \zeta) b(\zeta) \frac{f_d^m(\zeta, t)}{\rho_d V(\zeta)} d\zeta \quad (6.4)$$

$$C_D^m(\xi, t) = H\left(\sqrt[3]{\xi_{max}^3 - \xi_{min}^3} - \xi\right) f_d^m(\xi, t) \int_{\xi_{min}}^{(\xi_{max}^3 - \xi^3)^{1/3}} c(\xi, \zeta) \frac{f_d^m(\zeta, t)}{\rho_d V(\zeta)} d\zeta \quad (6.5)$$

$$\begin{aligned} C_B^m(\xi, t) = H\left(\xi - \sqrt[3]{2\xi_{min}^3}\right) & \frac{\xi^2 \rho_d V(\xi)}{2} \int_{\xi_{min}}^{(\xi^3 - \xi_{min}^3)^{1/3}} \frac{c([\xi^3 - \zeta^3]^{1/3}, \zeta) f_d^m(\zeta, t)}{(\xi^3 - \zeta^3)^{2/3} \rho_d V(\zeta)} \\ & \frac{f_d^m([\xi^3 - \zeta^3]^{1/3}, t)}{\rho_d V([\xi^3 - \zeta^3]^{1/3})} d\zeta \end{aligned} \quad (6.6)$$

$$c(\xi, \zeta) = \lambda(\xi, \zeta) h(\xi, \zeta) \quad (6.7)$$

Eq. (6.1) is governed by the following initial and boundary conditions:

$$f_d^m(\xi, t = 0) = f_{d,ini}^m(\xi) \quad (6.8)$$

$$f_d^m(\xi = \xi_{min}, t) v_\xi(\xi_{min}, t) = J_d^m \quad (6.9)$$

$$f_d^m(\xi = \xi_{max}, t) v_\xi(\xi_{max}, t) = 0 \quad (6.10)$$

Here f_d^m is the mass density function of the dispersed phase, t is the time dimension, ξ is the bubble diameter (inner coordinate in the property space), $\dot{m}_{d,out}$, $\dot{m}_{d,in}$ are the outlet resp. inlet mass flow rate of the dispersed phase, V_R is the reactor volume, $f_{d,in}^m$ is the inlet mass density function of the dispersed phase, $v_\xi(\xi, t)$ is the velocity in property space in the following just growth rate, $V(\xi)$ volume of a bubble with size ξ , m_d mass of a bubble with size ξ , $B_B^m(\xi, t)$, $B_D^m(\xi, t)$ are sources regarding breakage birth and death events, $C_B^m(\xi, t)$, $C_D^m(\xi, t)$ are sources regarding coalescence birth and death events, $b(\xi)$ the breakage frequency, ξ_{max} , ξ_{min} are the maximal resp. minimal size of bubble size, ζ the integration variable resp. the

mother bubble, ν the average number of new bubbles after breakage, $P(\xi, \zeta)$ the daughter size distribution function, $c(\xi, \zeta)$ the coalescence frequency, $\lambda(\xi, \zeta)$ coalescence efficiency, $h(\xi, \zeta)$ collision frequency, $f_{d,ini}^m(\xi)$ initial mass density function, and J_d^m is the mass nucleation rate.

Eq. (6.1) has additional terms compared to the PBE that usually appear in the literature [73, 94]. The second and third term on the left-hand side of Eq. (6.1) appears due to the unresolved convective fluxes over the physical space and describe the change of f_d^m due to in and outflows of the system under consideration (see Supplementary Information E.3.1 for a derivation). The first term on the right-hand side of Eq. (6.1) describes the mass increase due to mass transfer from the continuous to the dispersed phase. This term results from the transformation of a number into a mass-based PBE. Derivation and a detailed discussion of this term can be found elsewhere (cf. Chapter 5). Furthermore, in Eq. (6.3) - Eq. (6.6) Heaviside functions appear in the equations these were introduced for strict mass conservation [32].

Eq. (6.1) has a first order differential operator with respect to ξ which requires a boundary condition to be set, here Eq. (6.9) which describes nucleation processes. Note that other authors [89, 90] add this process as a point source inside of Eq. (6.1). Depending on the solution method used, these two approaches are identical but they might also differ from each other, so attention must be paid. Eq. (6.10) is called regularity condition [79], which ensures that no mass can leave the system over the property domains boundary's. In a mathematical sense it is not a boundary condition that can be enforced, however it must be inherently satisfied by the system, which is a modeling problem. This can be fulfilled, for example, by ensuring that $v_\xi(\xi_{max})$ assumes zero, or that the domain with respect to ξ is chosen so large that f_d^m never assumes values greater than zero, presuming $f_d^m(\xi_{max})$ was initialized with zero.

6.3.3. Constitutive Equations

To close the model constitutive equations are needed for $\dot{m}_{d,out}$, $f_{d,in}^m(\xi)$, $\frac{dm_d}{dt}$, $\frac{d\rho_d}{dt}$, ν , $b(\xi)$, $P(\xi, \zeta)$, $\lambda(\xi, \zeta)$, $h(\xi, \zeta)$ and J_d^m . $\dot{m}_{d,out}$ is determined on the basis of an integral balance about the volume of the reactor (see Eq. (E.16)). A derivation is given in the Supplementary Information E.3.1, using the assumption that the volume of the fluids enclosed is constant in time, so that the mass outflow rate is the difference between the mass inflow rate minus the mass flow rate due to phase change. As inlet distribution $f_{d,in}^m(\xi)$ the initial $f_{d,ini}^m(\xi)$ is used since it is assumed that only the inlet distribution was present at $t = 0$. For $\frac{dm_d}{dt}$ a simple two-film theory approach with constant driving force (cf. assumptions Section 6.3.1) is used (see Eq. (E.15)), ν is constant and has the value two, meaning only a binary breakage, J_d^m is constant and assumes a value based on the investigated case, usually zero. For $b(\xi)$ the model according to Coualoglou *et al.* [53] (see Eq. (E.7)), for $P(\xi, \zeta)$ the distribution function according to Laakkonen *et al.* [106] (see Eq. (E.8)) and for $\lambda(\xi, \zeta)$, $h(\xi, \zeta)$ the model according to Coualoglou *et al.* [53] (see Eq. (E.3), Eq. (E.2)) are mainly used. The corresponding equations are summarized in the Supplementary Information E.2.

6.3.4. Methods of Solution

Overview

The four discretization methods for determining the density function directly from the PBE used in this chapter, are the weighed residual spectral orthogonal collocation (OC), the fixed pivot technique (FPT), the meshless radial basis method (RBM) and our develop method, called the finite volume method with Gauss quadrature (FVMG).

The following provides an overview of the mathematical details necessary for discussing the various methods. For more comprehensive insights please refer to the source publications [32, 89, 94] and textbooks [107, 108].

To compare the four methods, they can be roughly divided into six building blocks: discretization of the accumulation/transient term, grid points (in physical and in this chapter especially in property space), convection in physical space, convection in property space, integrals and the interpolation scheme within the integrals.

The transient term is discretized for all methods using a standard ordinary differential equation (ODE) time stepper (see Supplementary Information E.5 for details). Except for OC, the grid points in property space are all equidistant in the respective examined domain (see Eq. (E.46)). OC uses Gauss-Legendre-Lobatto (GLL) nodes as grid points. Integration is performed with the exception of the FPT by using a Gauss-Legendre quadrature rule. For further differences and the convection scheme, the four methods are briefly introduced.

Weighed Residual Spectral Orthogonal Collocation – OC

OC uses a truncated series expansion to approximate the solution function $f \approx f_{\text{approx}} = \sum_i^{N_\xi} \omega_i \varphi_i$, where f is the exact solution function, f_{approx} an approximate solution function, N_ξ is the number of grid points resp. basis functions and ω_i the coefficients of the basis functions φ_i . Lagrangian functions are chosen as basis functions, which have special properties such as orthogonality. Due to the available approximation function, the convection in the property and physical space can be obtained by analytical derivation of it and the function value at the integration points can be obtained directly by evaluating f_{approx} , resulting in a derivative resp. interpolation scheme of higher order accuracy. The unknown coefficients of the basis functions ω_i are determined using the method of weighted residuals utilizing a weighting function, in the case of OC Dirac delta functions.

Meshless Radial Basis Method – RBM

The RBM approximates f similarly to OC with an truncated series expansion. Radial basis functions such as multiquadrics are used as basis functions. This radial basis functions depend on the distance between the grid points and a shape factor κ . Alzyod *et al.* [89] uses Algorithm 7.1 according to Griffiths [109] to determine it. The algorithm aims to bring the condition number of the interpolant matrix, which is used to interpolate and determine the derivative,

into a given range. This requires an initial shape factor κ_0 and a step width $\delta\kappa = 1 \times 10^{-4}$. Due to the available approximation function, as with OC, the derivative can be easily determined and the function values can be determined directly at the integration points without the need for a separate interpolation scheme.

Fixed Pivot Technique – FPT

The FPT decomposes the PBE into classes resp. sections and chooses zero-order polynomials as the basis function, which leads to solving the PBE as a histogram. Further the integrals of the breakage and coalescence terms can be considered as a simple summation. Based on the derivation, a further an additional integral of the breakage and coalescence terms over the class width appears, which is determined using the mean value theorem for integrals. An interpolation scheme within the breakage and coalescence terms does not appear directly, rather the particles born between the centers of the classes are distributed to the neighboring classes using rules based on moment conservation. A convection scheme is not part of the standard method according to Kumar *et al.* [94]. Lehnigk *et al.* [90] uses a first order upwind finite volume scheme for the property space. However, other schemes for physical and property space should be possible.

Finite Volume Method With Gauss Quadrature – FVMG

Our FVMG method is characterized by the fact that it uses numerical procedures familiar to the engineer, is easy to understand and to implement and that the convection in the property and physical space is strictly mass conserving due to the FVM part. FVMG uses a Gauss-Legendre quadrature rule for the integration like OC and RBM ensuring higher order integration accuracy. For convection in physical and property space a high resolution finite volume scheme is used that is at least second order accurate in areas of smooth solution and does not oscillate around of discontinuities. As interpolation scheme to the integration nodes a piece-wise cubic Hermite spline interpolation. The equations required to implement the FVMG are summarized in the Supplementary Information E.4. For further details, please refer to the textbooks [110–112], for example.

6.3.5. Implementation Details and Tools

All methods were implemented in the Julia programming language in Version 1.10 [113]. A detailed list of the packages used including their version and some details of the used ODE and steady-state solver can be found in the Supplementary Information E.5. The number of grid points N_ξ and integration nodes $N_{\xi,\text{int}}$ used differ depending on the case and are listed in the Supplementary Information E.2.3.

6.3.6. Analytical Solutions and Error Measure

In order to analyze the performance of the different methods, some analytical solutions of simplified PBE from the literature [97–103] are used. As error measure the Euclidean norm of the

derivation between the normalized density function resulting from the simulation $\hat{f}_{d,\text{sim}}(\xi, t)$ and from an analytic solution $\hat{f}_{d,\text{ana}}(\xi, t)$ is used.

$$Error = \left\| \hat{f}_{d,\text{ana}}(\xi, t) - \hat{f}_{d,\text{sim}}(\xi, t) \right\|_2 \quad \text{for } t > 0 \quad (6.11)$$

It should be noted that the same time steps are employed for all solution methods, although the grid points in the property space may differ. Consequently, a separate analytical solution is calculated for each method. The normalized density function is obtained by division by its area (see Eq. (E.40)).

In this chapter four different test cases (A-D) are considered. In the first two cases, constant growth in the property space without breakage and coalescence is analyzed with: (A) constant growth with a multi-modal initial distribution [100] and (B) constant growth of a nucleation process [98]. In the third case (C) only breakage occurs [103] and in the fourth case (D) only breakage and coalescence [99]. The analytical solutions can be found in the source publications [98–100, 103]. The applied model parameters are listed in the Supplementary Information Tab. E.1.

6.3.7. Definition of Sensitivity and Parameter Studies

Based on a classical design strategy for STR using [114, 115] and in analogy to the experiments, a default case is defined, which is summarized in Tab. E.2. It was taken into account that in STR breakage dominates over coalescence. The gas holdup, which mainly results from the power input resp. the energy dissipation rate and gas flux, was calculated using the correlation according to Moucha *et al.* [116] for a single Rushton turbine. This default case serves as the basis for the sensitivity and parameter study, in which mainly steady-state solutions will be considered. In the study, almost all model parameters are varied in one-at-a-time analysis, which is divided into four parts:

The first study assesses the influence of kernel parameters and selection. The kernel parameters of the default case are varied to ascertain their sensitivity to changes, thereby providing insights for parameter estimation and model behaviour. In addition to the default case, a second kernel set comprising of Laakkonen *et al.* [106] for the breakage frequency, Prince *et al.* [117] for the collision frequency, R.B. Diemer [118] for the daughter size distribution function and Chester [119] for the coalescence efficiency is investigated. The second kernel set parameters were manually adjusted so that these conserved mass, satisfy the regularity condition and generate a similar integral amount of breakage (0.03 kg s^{-1}) and coalescence (0.01 kg s^{-1}) as the default case based on the inlet BSD.

In the second study, an existing reactor concept is optimized by varying the process conditions (gas holdup, gas flux, power input). The gas holdup in a STR is mainly influenced by two effects: first the rising velocity of the bubbles and second the recirculation of the gas phase. The first effect is determined by the size and shape as well as the property data of the fluids. The second effect depends on the flow field. The flow field depends on numerous parameters such as the type and dimensions of the stirrer, baffles, stirrer speed, property data of the fluids,

etc. Since we keep the gas holdup constant over time and assume that all bubbles have the same residence time, we cannot model the influence of the first effect. The second effect is investigated in an artificial study in which the gas holdup is varied at constant power input and gas flux. In the experiment, this study could not be carried out at least in the wide range, because as described the gas holdup depends on many parameters. However, the general behavior of the model should be investigated. When examining the gas flux and the power input, a distinction is made between two cases: in one case, the gas holdup is kept constant, as in all other studies, and in the other case, the influence of the gas flux or the power input is considered using the correlation presented by Moucha *et al.* [116] that describes the gas holdup ($\alpha_d = 0.01686 (\varepsilon \rho_c)^{0.6241} j_d^{0.5669}$). Note, it was ensured that the STR would not start to flood [115, 120].

In the third study, the influence of the gas sparger (mean, width and mode of the inlet resp. initial BSD) is investigated since the sparger is an essential component of any multiphase STR and its influence on the behavior of the dispersed phase is difficult to study with models that do not include the PBE.

In the fourth and final study, the influence of the physiochemical properties (surface tension, viscosity liquid phase, mass density gas and liquid phase, mass transfer) is examined.

The third and fourth studies are provided in the Supplementary Information E.1. The four studies are discussed based on the following (output) variables: the mass density function f_d^m , the Sauter mean diameter (SMD) ξ_{32} , and the interfacial area density a . The SMD and the interfacial area density are determined from the second and third moment of the predicted mass density function, see Eq. (E.20) and Eq. (E.19), respectively. All results of the studies are compared with findings from the literature, if available. The parameters applied in the studies are summarized in Supplementary Information E.2.

6.3.8. Preliminary Application to Measured BSD and Parameter Estimation

In order to apply the model to the experimentally investigated STR (cf. Section 6.2), the parameters in Tab. E.4 are utilized. Furthermore, the measured initial BSD and the inlet BSD, which is assumed to be the measured initial BSD, must be specified. As the kernels and their parameters are not yet predictive and are case-dependent, a known issue in the community [106, 121–123], they must be adapted to experiments. This was accomplished by minimizing the sum of the symmetric χ^2 -distance between the experimental and simulated normalized number density function over all time steps. Prior to the optimization, all kernel parameters are normalized to a scale of unity since they span over many orders of magnitude. In order to obtain only physical solutions (e.g. no artificial mass loss), a regularization was added, which acts as a penalty for high mass loss. Furthermore, a grid search was used to select suitable starting parameters and lower and upper parameter bounds so that the local minimum found by optimization coincides with the global minimum.

Details of the packages and solvers used are given in the Supplementary Information E.5.

6.4. Results and Discussion

6.4.1. Comparison of the Numerical Solution Methods

Fig. 6.2 depicts a dimensionless and scaled number density function f^s as a function of a dimensionless and scaled diameter ξ^s for the four test A-D cases described in Section 6.3.4. The nondimensionalization and scaling of the axes were implemented to facilitate a straightforward comparison of the four cases.

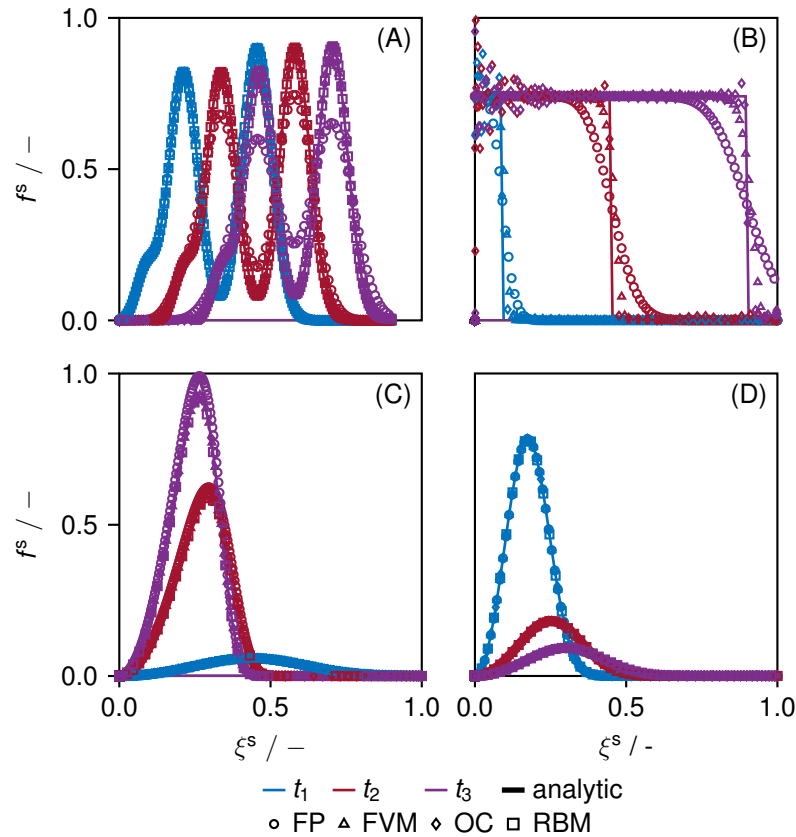


Figure 6.2.: Dimensionless and scaled number density function f^s as function of a dimensionless and scaled diameter ξ^s . Comparison of the numerical solutions (symbols) obtained from the four different solvers with the respective analytical solutions (lines) for the four test cases A-D. The color represents different points in time.

Fig. 6.2A shows the case according to Qamar *et al.* [100] of pure growth of a multi-modal distribution function. It can be seen that the OC, RBM and FVMG methods can reproduce the time evolution well: $Error = (0.015, 0.041, 0.340)$. The high accuracy of OC and RBM results from the available analytic derivative with higher order accuracy. But it should be noted if the algorithm of Griffiths [109] to determine the shape factor is initialized with $\kappa_0 = 0.01$ instead of $\kappa_0 = 10$, we obtain a shape factor of $\kappa = 0.064$ instead of $\kappa = 0.076$ which leads to an $Error = 2 \times 10^{52}$, which is far away from the solution and even smaller changes, e.g. an $\kappa = 0.071$, already produce nonphysical negative values ($Error = 1.806$). This means that the algorithm [109] does not provide unique solutions and that the accuracy depends strongly and very sensitively on the shape factor. The FVMG tends to underestimate the peaks despite

the high resolution scheme, but this is just second order accurate and could be replaced by a higher order scheme. FPT shows a strong numerical diffusion due to the first order upwind scheme ($Error = 2.349$).

Fig. 6.2B shows the case according to Hounslow *et al.* [98] of constant growth with simultaneous nucleation. FVMG and FPT can track the fronts, whereas OC is more prone to numerical diffusion due to the lower order scheme, $Error = (14.31, 21.31)$. OC shows strong oscillations especially at ξ_{\min} caused by the step gradient introduced by the nucleation process resp. the boundary condition, $Error = 18.61$. The oscillations originate from the higher order approximation function. RBM also produces oscillations, but more in the area of the front also caused by the higher order scheme $Error = 8.25$. Note that RBM and OC have a comparatively small error but the fronts are insufficiently tracked and they oscillate. The oscillation in particular amplifies with increasing time. Furthermore the OC and RBM provide strong solutions where the boundary conditions are rigorously enforced, ensuring their precise fulfillment. In conjunction with the PBE, which encompasses integrals that span the entire property space, particles that die due to coalescence or are born due to breakage are irretrievably lost. To prevent this mass loss, an integral boundary condition can be set. Alternatively, it can be imposed that the smallest particles can neither be born by breakage nor die by coalescence, e.g. by constraints or by appropriate choice and parameterization of the kernel functions. While the FVMG and FPT provide weak solutions, this is not a problem and nucleation is simply considered as an additional flux over the lower boundary of the property domain without any complicated time-dependent integral boundary condition or artificial constraints.

For the third case according to Ziff *et al.* [103], where only breakage and no coalescence and growth are considered, the methods RBM, FVMG and OC provide an accurate solution, $Error = (0.24, 0.23, 0.21)$ of the density functions, see Fig. 6.2C. The finding that all methods performed similarly well can be attributed to the fact that they all used the same quadrature rule for the breakage birth term. The differences result only from the interpolation scheme and the grid points. FPT, on the other hand, overestimates the trend caused by the zero-order approximation of the integration, $Error = 20.38$. The $Error$ can only be reduced to 10.08 when 300 grid points are used.

In the last case according to J. McCoy *et al.* [99], where simultaneous breakage and coalescence but no growth is considered (see Fig. 6.2C). The analytic solution was transformed to a mass-length based form and the domain was chosen to be $\xi = [2, 1000] \times 10^{-6}$ m to be closer to the experimentally investigated system of this chapter (cf. Section 6.2). The methods FPT, FVMG and OC provide an accurate numerical solution of the density function. The error of the OC method is lowest, and highest for the FPT method, $Error = (0.7, 3.8, 4.9) \times 10^{-3}$. However, it should be noted that the number of grid points in OC had to be reduced to 80 in order to obtain a stable solution. Since OC uses GLL grid points, which are very dense close to the domain boundaries, numerical problems arise when integrating and interpolating the denominator in the coalescence birth term. The hole denominator within in the coalescence birth term assumes very large values at the respective integration limits, which is difficult to integrate accurately and to interpolate stable with a higher order interpolation scheme. This problem is exacerbated by the use of property domains on smaller scales and denser grid

points. While nondimensionalization and scaling of the dependent and independent variables can mitigate this issue, it is not a complete solution. This is because the GLL points will remain closely spaced as the number of grid points increases, as is the case with breakage-dominated problems. Restricting the range permitted for breakage and coalescence only addresses this issue in certain instances. Another approach is to express the PBE in number length or number volume based form, which significantly simplifies the mathematical form of the breakage and coalescence terms. However, this approach also introduces new challenges. For instance, volume as a property leads to very small numbers, which can result in poorly prescribed grids and large numbers that must be balanced for a number-based PBE, increasing the susceptibility to round-off errors. Further research is needed to address these issues.

Nevertheless, it should be noted that only 80 points were necessary for the OC in contrast to 200 points for the other methods in order to achieve a high accuracy. No optimal shape factor could be found for the RBM, so no solution could be obtained. Important in contrast to Alzyod *et al.* [89] the PBE was solved mass length based in the domain $\xi = [2, 1000] \times 10^{-6}$ m instead of number length based in the scaled domain $\xi = [2, 5]$ μm . We assume that the algorithm [109] has problems with the domain on the small scales.

In conclusion, it can be stated that none of the examined methods demonstrated a clear superiority over the others. The FPT results in numerical diffusion, which may be improved by employing a different convection scheme. Due to the zero-order integration, an accurate calculation of the breakage and coalescence terms may necessitate the use of numerous classes, which are numerically demanding. RBM provides exact results for complex convection-dominated problems. However, there are issues with nucleation and small-scale property spaces. These issues are primarily attributed to the shape factor and its calculation. Mesh-free methods, in general, are promising methods to provide a robust solution of the PBE, as evidenced by the work of Garg *et al.* [124]. However, further work is needed to fully realize their potential. OC is by far the most accurate method, even for low grid point counts. Once the aforementioned issues are resolved, the highly accurate method can also become a robust numerical method. This is not the case, and further development of the method is not our primary objective; we leave this to other authors. Our proposed method, FVMG, has been demonstrated to be sufficiently accurate, robust, and easy to understand and implement. Consequently, an engineer can expeditiously adapt this method and, if necessary, specialize it to her / his problem with the assistance of well-known methods from the FVM environment, such as non-uniform grids, different convection and diffusion schemes, and specialized solvers, among others. Therefore, only our FVMG method is considered in the following parameter study.

6.4.2. Sensitivity and Parameter Analysis

Study on Breakage and Coalescence Kernels and Parameters

Fig. 6.3A and B illustrate the SMD ξ_{32} , and interfacial area density a , respectively, as functions of the linear scaling factor of breakage frequency C_{bf} and coalescence frequency C_{cf} (cf. Eq. (E.7)-(E.2)). Similarly, Fig. 6.3C and D present the mass density function f_d^m as a function of bubble size ξ for various linear scaling factor of breakage and coalescence frequency.

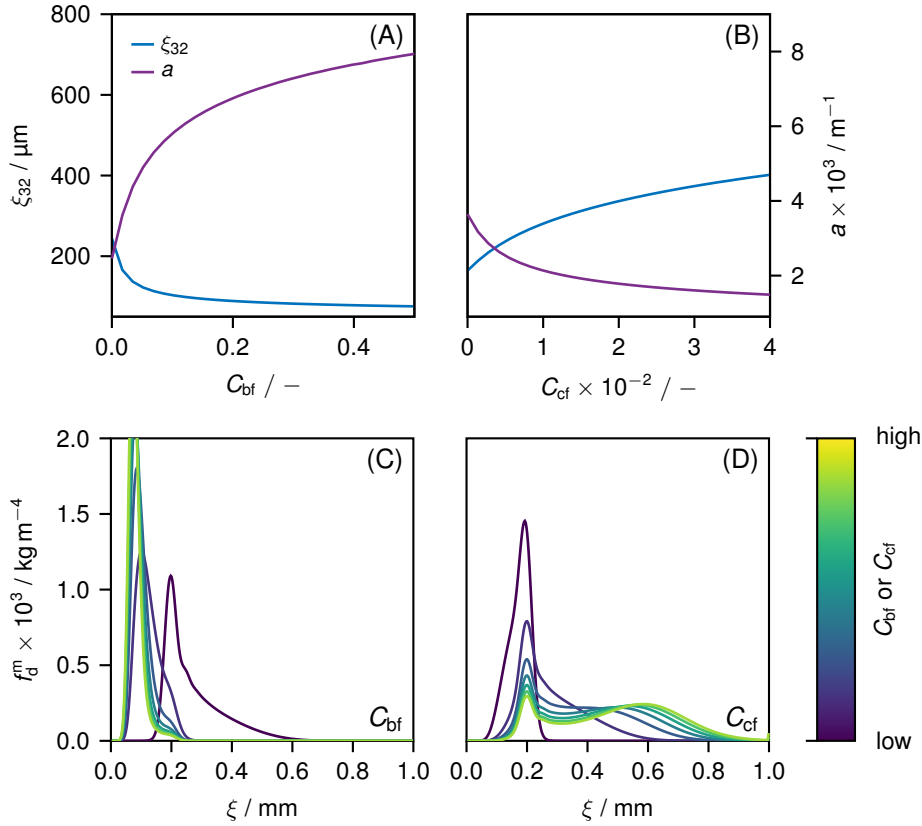


Figure 6.3.: (A-B): Sauter mean diameter ξ_{32} and the interfacial area density a as a function of linear scaling factor of breakage frequency C_{bf} (A) and coalescence frequency C_{cf} (B). (C-D): Mass density function f_d^m as a function of bubble size ξ for the different breakage frequency C_{bf} (C) and coalescence frequency C_{cf} (D). Applied parameters see Tab. E.2 and Tab. E.3.

As expected, the breakage frequency has a strong influence on the model predictions (see Fig. 6.3A and D). The SMD drops rapidly and converges slowly to a constant value from approx. $C_{bf} \approx 0.2$. The fact that the bubbles cannot become smaller is due to the breakage kernel used, which is parameterized in such a way that no breakage below a certain bubble size is possible (cf. Fig. 6.3C). It is known that a lower limit exists [125], but it depends strongly on the material system, power input and stirrer, for example. The re-increase at $\xi = 0.2$ mm in Fig. 6.3C after the maximum originates from the inlet distribution. Due to the constant gas holdup, the interfacial area density behaves inversely according to $a \propto \alpha_d / \xi_{32}$.

In consideration of the variation in coalescence frequency (see Fig. 6.3B and D), the inverse effect of breakage is observed: bubbles increase in size and the interfacial area density decreases

with rising coalescence. A comparable degree of sensitivity to that observed with breakage does not manifest, although a similar flattening of the slope can be discerned at higher coalescence frequencies.

This study helps to identify the range in which the BSD are sensitive to the breakage and coalescence parameters. This knowledge is important for selecting reasonable initial values or parameter ranges for parameter estimation when calibrating the model to measured data. This study was also carried out for the two other breakage and coalescence parameters that influence the bubble size dependence. The results are not shown here.

Fig. 6.4 shows the analysis of the influence of the kernel selection, where the SMD ξ_{32} is depicted as a function of time t and the mass density function f_d^m as function of the bubble diameter ξ for different time steps for the two investigated kernel sets (used kernels see Supplementary Information E.2.1).

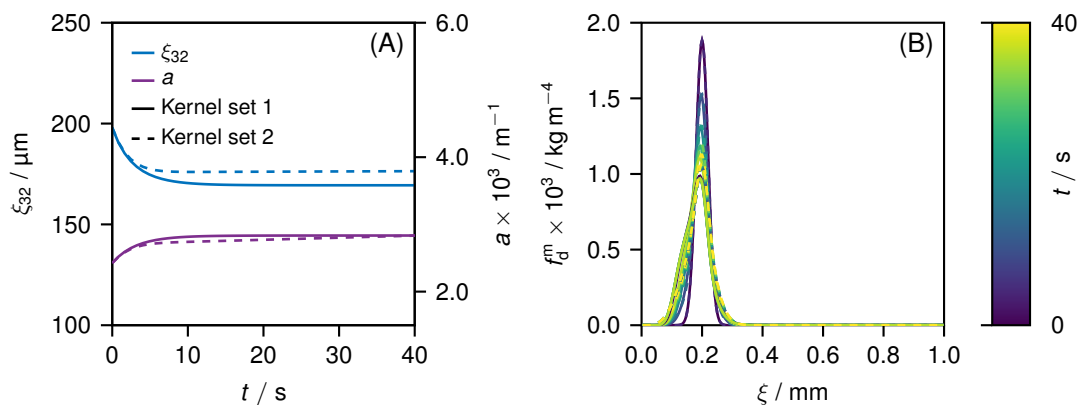


Figure 6.4.: (A): Sauter mean diameter ξ_{32} and the interfacial area density a as a function of time t for two different kernel sets (line style, used kernels see Supplementary Information E.2.1). (B): Mass density function f_d^m as a function of bubble size ξ for two different kernel sets.

It can be clearly seen that the two kernel sets differ just slightly from each other. The second kernel set predict a slightly higher steady-state SMD. A similar observation that different sets of kernels hardly differ from each other after a parameter adjustment has already been made in a previous publication of us [16]. Furthermore, if available, other kernel functions of the above-mentioned authors [53, 106, 117–119] and those of [126, 127] were varied, showing a similar behavior (not shown in this chapter). This behavior is due to the fact that the process is affected by the inlet distribution, that the kernels are very flexible, have a similar theoretical background and thus have similar model equations. However, this should not lead to a generally applicable statement that the choice of kernel is irrelevant. Other kernels such as multifractal [128], cascade kernel [129] or other kernels such as those summarized in [130, 131] could lead to different results.

Variation of Process Conditions

Fig. 6.5A-C depict the SMD ξ_{32} and the interfacial area density a as a function of different process conditions: gas holdup α_d , gas flux j_d , power input or energy dissipation rate ε . Fig. 6.5D-F shows the mass density function f_d^m as a function of bubble size ξ for the different process conditions. In the study of the gas flux and power input, as described in Section 6.3.7, two cases are distinguished: constant gas holdup (dashed line) and gas holdup according to the correlation of Moucha *et al.* [116] (solid line), whereby the non-varying parameter is kept constant, e.g. in the gas flux study, the power input is always constant. The BSDs for the constant gas holdup case could be found in the Supplementary Information Fig. E.5.

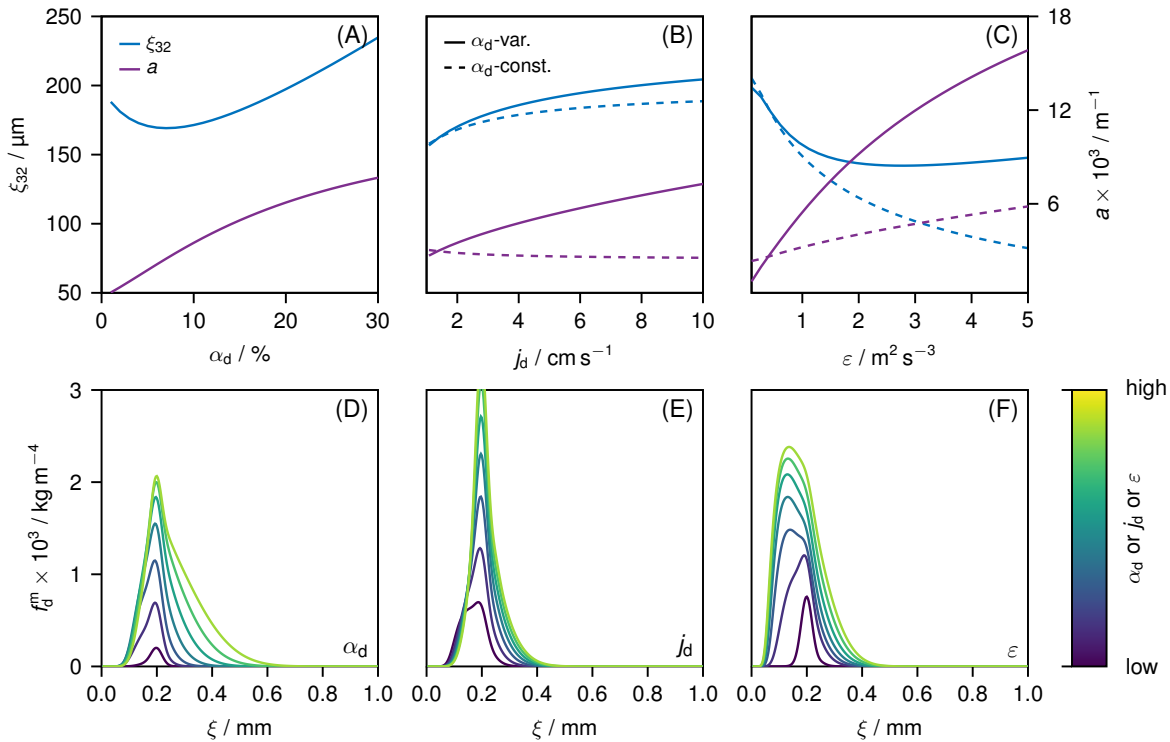


Figure 6.5.: (A-C): Sauter mean diameter ξ_{32} and the interfacial area density a as a function of different process conditions, with varying gas holdup according to Moucha *et al.* [116] (solid line) and constant gas holdup (dashed line) in B,C. (D-F): Mass density function f_d^m as a function of bubble size ξ for different process conditions. Process conditions: (A,D) - gas holdup α_d ; (B,E) - gas flux j_d ; (D,F) energy dissipation rate ε .

Fig. 6.5A and D demonstrate the influence of gas holdup at constant power input and gas flux on the SMD and the mass density function, respectively. The SMD initially exhibits a decrease and then an increase with rising gas holdup. The anticipated increase is consistent with the experimental findings reported by Alves *et al.* [132]. In the model, the coalescence rate (cf. Eq. (E.2) and Eq. (E.3)) increases with gas holdup as documented by Tsouris *et al.* [133]. The increase in the coalescence rate is responsible for the increase in the SMD. However, at very low values of gas holdup ($\alpha_d \leq 7\%$) the breakage rate obviously dominates over the coalescence, so that the SMD initially decreases.

As the gas flux is increased (see Fig. 6.5B and E), the SMD also increases in accordance with

the literature [134, 135]. This trend is observed irrespective of whether the gas holdup is regarded as constant or varying. In the case of constant gas holdup, the residence time of the bubbles in the reactor decreases directly with increasing gas flux. Given the short residence time, the impact of breakage and coalescence events within the reactor on the BSD is reduced, while the SMD is predominantly influenced by the inlet BSD with an SMD of $\approx 198 \mu\text{m}$. In the case of varying gas holdup, the fundamental behavior is analogous to that observed with a constant holdup. However, the predicted SMDs are higher with increasing gas flux than with a constant gas holdup. As the gas flux rises, the gas holdup increases, leading to an elevated incidence of coalescence events. In the case of a variable gas holdup, the interfacial area density increases. This phenomenon can be attributed to the fact that the gas holdup increases at a rate that is greater than that of the SMD. At constant gas holdup, the interfacial area density is inversely proportional to the SMD. Note that, depending on the parameterization of the kernel, the opposite behavior of decreasing SMD and increasing interfacial area density at constant gas holdup can also occur, once again emphasizing the importance of parameterizing the kernel correctly.

In the context of energy dissipation rate or power input, respectively (see Fig. 6.5C and F), it is evident that regardless of the gas holdup case, increasing the dissipation rate from $0.1 \text{ m}^2 \text{ s}^{-3}$ to about $2.5 \text{ m}^2 \text{ s}^{-3}$ leads to a reduction in bubble size. This behavior is consistent with the well-documented phenomenon that the breakage rate increases with energy dissipation rate, as observed in previous studies [132, 136, 137]. In the case of varying gas holdup, the SMD decreases less strongly than in the case of constant gas holdup. Indeed, for large power inputs, the SMD even increases once more ($\varepsilon > 2.5 \text{ m}^2 \text{ s}^{-3}$). This is due to the fact that, with an increase in gas holdup, coalescence also rises, as evidenced by Polli *et al.* [76] and Oolman *et al.* [138]. Consequently, this phenomenon effectively masks the impact of the power input. The behavior of the interfacial area density can be explained in a manner analogous to that employed in the analysis of the gas flux study.

In conclusion, the model demonstrates a correlation between the observed trends of increased gas holdup and gas flux, which result in larger bubbles, and the increased power input, which leads to smaller bubbles. Nevertheless, it is essential to address the limitation of the model, which is unable to predict the gas holdup. One potential approach to address this issue is the deployment of a size-dependent residence time model for the gas phase. This model should account for two key effects: the rising velocity of bubbles and the flow field, particularly the backmixing of the gas phase (cf. Section 6.3.7).

It is a prerequisite for future calibration of the model in a manner analogous to that employed in our previous work on the BCs (see Chapter 3-4). In that instance, we were able to calibrate the model for at single axial position for two gas fluxes and to predict both the BSD and the gas volume fraction for other gas fluxes outside the calibrated range.

The third and fourth study (cf. Section 6.3.7) on the influence of the sparger design and the physiochemical properties (surface tension, viscosity liquid phase, mass density gas and liquid phase, mass transfer) on the BSD are documented in the Supplementary Information E.1. These studies demonstrate that despite the limitations of the model, a considerable number of predicted trends are consistent with observations reported in the literature. Furthermore,

these simulation studies also confirm that our FVMG method is both robust and efficient for solving these systems of equations.

6.4.3. Model Demonstration: Application to Experimental Data

Fig. 6.6 illustrates the comparison between the experimentally measured BSD and the BSD predicted by the model at varying time points. The initial BSD value was utilized as both the initial and inlet condition. The four model parameters employed to fit the breakage and coalescence kernels were estimated using the BSDs derived from a time series measurement.

The results demonstrate that the model is capable of reproducing the BSD in principle. However, due to the model's inability to describe the gas holdup in the STR, it is not yet feasible to utilize this model for predicting the impact of process parameter variations on the behavior of the dispersed gas phase, as is possible with our bubble column model. Nevertheless, this result represents a significant initial step in the model development process.

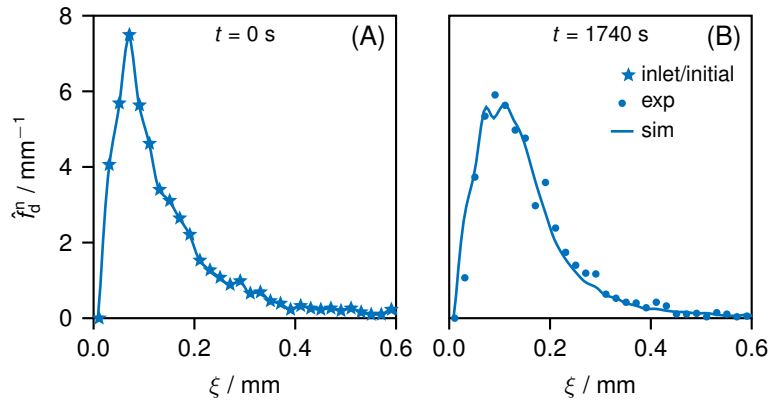


Figure 6.6.: Normalized number density function \hat{f}_d^n as a function of the bubble diameter ξ for different time steps t . Definitions: lines - simulations, symbols - experiments, star marker - inlet/initial value. Applied parameters see Tab. E.4. Experimental data see Supplementary Material of the publication.

6.5. Conclusion and Outlook

In this chapter, the multifluid population balance model (MPB) was employed to analyze a non-reactive two-phase stirred tank reactor (STR). The objective of this chapter was to identify a robust and efficient method for solving the resulting integro-partial differential equations. Four distinct solution methodologies were subjected to evaluation, with one, namely the finite volume method with Gauss quadrature (FVMG), being developed within the context of this investigation. The efficacy of the methods was evaluated through their application to problems for which analytical solutions are available. The results demonstrate that no single method emerges as a clear outperformer in comparison to the others. All methods have both advantages and disadvantages. The proposed method, FVMG, has been demonstrated to be sufficiently accurate, robust, and readily comprehensible and implementable. Consequently, this constitutes a valuable contribution to the field and has the potential to facilitate the application of the MPB for describing dispersed multiphase reactors.

The FVMG was utilized for parameter and sensitivity studies with the MPB of the STR. Four different studies were carried out. The first study investigated the influence of the breakage and coalescence kernels on the bubble size distribution (BSD). The simulation results show the expected trends. This study also provides information on the parameter ranges in which the calculated BSD is sensitive to the model parameters. This information is important for selecting reasonable initial values for parameter estimation when calibrating the model to measured data. The second study examined the influence of the variation of different process conditions on the BSD. The limitation of the model, namely its inability to describe the gas holdup in the STR, was addressed by considering two cases: one with a constant gas holdup and the other with a varying gas holdup according to an empirical correlation. The general trends are in accordance with the findings of experimental studies. The studies three and four presented in the Supplementary Information E.1 concerning the physicochemical properties and the design of the gas sparger largely confirm the trends described in the literature, although some limitations are apparent. It was also observed that the parameterization of kernel models has a significant impact on the predicted trends. Overall, the FVMG was demonstrated to be a robust and efficient method through the parameter and sensitivity analysis, exhibiting no numerical instabilities and rapid convergence of the solver.

Ultimately, the model parameters were calibrated to the experimental data obtained from the BSD in the STR. The simulation and experimental results were observed to be in close agreement with one another. In order to obtain a reliable prediction, it was necessary to utilize all BSDs of a given time series from an experiment in the preliminary parameter determination. Nevertheless, the model is not yet suitable for predicting large ranges of process parameters, as is possible with our MPB of the bubble column (BC). In contrast to the MPB for STRs, the MPB for BCs can describe the gas holdup.

In conclusion, the MPB of the STR, in conjunction with our novel solution methodology, FVMG, proved to be a valuable tool for investigating the intricate behavior of the dispersed gas phase within the STR. However, the model also exhibited limitations. The inability of the model to describe the gas holdup limits the applicability of the MBP for scale-up and design of

real reactors, as the influence of variation of parameters (design, process conditions, property data) on the properties of the gas phase (and on heat and mass transfer) cannot be adequately predicted. The primary objective of future work will be to identify modelling approaches that enable the description of this important property. Furthermore, the application to systems with reaction and/or heat and mass transfer will be carried out to further evaluate the performance of the model approach. This chapter represents a significant advancement in our efforts to develop a model that can describe the complex behavior of a dispersed multiphase system within a STR and that requires only a minimal number of empirical equations and parameters.

7. Conclusion and Outlook

This thesis focuses on the development of efficient and accurate modeling approaches for reactive dispersed multiphase systems, which are critical in industrial chemical processes such as hydrogenation, carboxylation, and hydroformylation. These processes take place in reactors such as jet loop reactors (JLRs), bubble columns (BCs), and stirred tank reactors (STRs). The main challenge is to balance the need for detailed, reliable insight into the behavior of these systems with the computational efficiency required for practical engineering applications like reactor design and optimization.

In Chapter 2, a one-dimensional model of a JLR has been developed based on a momentum balance. This model allows local resolution of important process variables such as species concentration, gas volume fraction, pressure, and phase velocities. It allows investigation of the influence of gas consumption on internal circulation and overall reactor performance. The simplicity of the model ensures fast and robust simulations, allowing extensive parameter studies. Key findings highlight that gas consumption significantly affects internal circulation, potentially leading to reactor instability under certain conditions. Furthermore, complex correlations between reactor geometry and operating conditions were found that need to be taken into account during design and optimization, suggesting that interphase couplings need to be considered simultaneously. Future work includes experimental validation and extension of the model to include bubble coalescence and phase slip.

A one-dimensional multifluid population balance model (MPB) has been developed to predict the behavior of dispersed flow in semi-batch bubble columns in Chapter 3, based on a previous study [16]. The model balances computational effort and accuracy, and requires calibration to experimental data. An optimal calibration method was identified using data from a single measurement position for two gas fluxes. The model effectively predicts key variables such as gas holdup and bubble size distribution (BSD), although deviations at lower and higher gas fluxes suggest limitations in the turbulence model. Future studies will extend the application of the model to board operating conditions and varying liquid fluxes.

The prediction performance of the MPB applied to BCs was further evaluated under semi-batch and continuous operation using different spargers and varying gas and liquid fluxes in Chapter 4. Fiber optic needle probes provided less invasive measurements compared to the previously used optical multimode online probe (OMOP) of Chapter 3. The model showed good prediction performance without recalibration of the model parameters, especially at medium gas and lower liquid fluxes. In addition, a modified sparger model derived from existing literature is presented as a means of circumventing the need to specify a measured inlet BSD. While this model does not completely eliminate the need for experimentation, it serves to reduce the number of experiments required and thus represents a promising avenue

for further investigation. Future work aims to refine the sparger model and the turbulence model to describe changes in the flow regime and to extrapolate to higher flow rates without recalibrating the model parameters.

In Chapter 5, a transformation from a number-based population balance equation (PBE) to a mass-based PBE revealed an additional mass transfer term, highlighting the mass increase due to external mass transfer. The study provided a deeper understanding of the conservation properties of the growth rate and the PBE in general. In addition, a nondimensionalization was proposed to address numerical challenges arising from the transformation, particularly for the coalescence birth term. The results contribute to the advancement of mass-based PBE modeling and provide insights for improving numerical stability and computational efficiency.

Finally, the MPB was applied to a non-reactive semi-batch STR for optimization and design purposes in Chapter 6. A new finite volume method with Gauss quadrature (FVMG) was proposed and compared with other numerical methods. The FVMG method was found to be fast, robust, and sufficiently accurate. In a parameter and sensitivity study, most trends from the literature could be confirmed and a deep process understanding necessary for design and optimization could be obtained. Preliminary experimental validation showed good agreement with simulation results, although further work is needed to generalize the model to other operating conditions and geometries. In future work, the prediction performance of the model should be further investigated and the species balance should be included to study reactive processes and their dependence on the BSD.

Despite the successes achieved in the thesis, four limitations of the MPB were identified:

- The semi-empirical functions describing breakage and coalescence phenomena are not universal; they are valid only for certain bubble size ranges and do not transfer well to different material systems. New universal kernels need to be developed that take into account e.g. changes of the composition of the phases.
- The BSD at the inlet must be specified as a boundary condition, which we derive from experiments. This limits the applicability of the model to other reactor types and dimensions and operating conditions where the inlet BSD is unknown. Although a sparger model has been proposed to reduce the need for experimental data, it does not completely solve the issue.
- Determining the size-dependent residence time behavior of the gas phase is challenging, especially when applying the MPB to stirred tanks, limiting prediction performance.
- Current estimation of the turbulent energy dissipation rate is based on simple integral models that rely solely on the inlet fluid fluxes or torque on the stirrer shaft. However, the lack of local information precludes accurate calculation of local values for bubble breakage and coalescence. A more sophisticated model that takes into account reactor geometry and other operating parameters is needed. Without it, the current model requires recalibration and new experiments when the flow regime changes. This more sophisticated model could be derived, for example, from non-reactive CFD simulations.

However, the content of this thesis contributes to a deeper understanding of dispersed multiphase reactive processes, which is essential for reactor design and optimization. For this purpose, simple, efficient and robust models have been developed, which can nevertheless represent the complex multiphase interactions, and have been validated by parameter studies and comparison with own experiments.

Nomenclature

Latin Letters

| Symbol | Description | Unit | Chapter |
|-----------------|---|----------------------------------|---------|
| a | Interfacial area density | m^{-1} | 3,6 |
| a | Order of the moment | - | 3,4 |
| a_i | Ratio of the cross-sectional area of compartment i to the cross-sectional area of the reactor | - | 2 |
| A | Cross-sectional area; see subscripts and superscripts for further variant | m^2 | 4, 6 |
| A_i | Cross-sectional area of compartment i | m^2 | 2 |
| $d\mathbf{A}$ | Vectorial surface element | m^2 | 6 |
| $b(\xi)$ | Breakage frequency | s^{-1} | 3,5,6 |
| b | Order of the moment | - | 3,4 |
| B_B | Mass-based breakage birth term | $\text{kg m}^{-4} \text{s}^{-1}$ | 3 |
| B_D | Mass-based breakage death term | $\text{kg m}^{-4} \text{s}^{-1}$ | 3 |
| B_B^n | Number-based breakage birth term; see subscripts and superscripts for further variants | $\text{m}^{-4} \text{s}^{-1}$ | 5,6 |
| B_D^n | Number-based breakage death term; see subscripts and superscripts for further variants | $\text{m}^{-4} \text{s}^{-1}$ | 5,6 |
| c | Sparger parameter | - | 4 |
| $c(\zeta, \xi)$ | Coalescence frequency | $\text{m}^3 \text{s}^{-1}$ | 3,5,6 |
| c_s | Concentration of species s in the aqueous solution | kg m^{-3} | 3 |
| c | c -coordinate of the property space | | 5 |
| \mathbf{c} | Property space with internal coordinates $\mathbf{c} = (c_1, c_2, c_3, \dots)^T$ | | 5 |
| $c_{1,A,i}$ | Molar concentration of species A in the liquid phase in compartment i | mol m^{-3} | 2 |
| $c_{1,A,IN,i}$ | Molar concentration of species A at the respective inlet of the compartment i | mol m^{-3} | 2 |
| C_B | Mass-based coalescence birth term | $\text{kg m}^{-4} \text{s}^{-1}$ | 3 |
| C_D | Mass-based coalescence death term | $\text{kg m}^{-4} \text{s}^{-1}$ | 3 |
| C_B^n | Number-based coalescence birth term; see subscripts and superscripts for further variants | $\text{m}^{-4} \text{s}^{-1}$ | 5,6 |
| C_D^n | Number-based coalescence death term; see subscripts and superscripts for further variants | $\text{m}^{-4} \text{s}^{-1}$ | 5,6 |
| C_i | Adjustable parameter of the breakage and coalescence kernel | | 3,4,6 |
| $C_{\sigma,i}$ | Parameter of the property data model describing the surface tension | - | 3 |

continued ...

... continued

| | | | |
|---------------------------------|--|----------------------------------|--------|
| $C_{\mu,i}$ | Parameter of the property data model describing the viscosity of the continuous phase | - | 3 |
| $C_{\rho,i}$ | Parameter of the property data model describing the mass density of the continuous phase | - | 3 |
| C^D | Drag coefficient | - | 3 |
| C^W | Wall friction factor | - | 3 |
| \mathbf{C} | Phase space | | 5 |
| C_{bf} | Linear scaling factor of the breakage frequency | - | 6 |
| C_{cf} | Linear scaling factor of the coalescence frequency | - | 6 |
| d_i | Hydraulic diameter of compartment i | m | 2 |
| d | Diameter, pipe diameter; see subscripts and superscripts for further variants | m | 2,4 |
| d_h | Orifice diameter | m | 4 |
| d_{BC} | Bubble column diameter | m | 3, 4 |
| Da_i | Damköhler number of first order of compartment i | - | 2 |
| \overline{Da}_i | Integral Damköhler number of first order of compartment i | - | 2 |
| $Eu(\xi, z)$ | Eötvös number defined | - | 3 |
| <i>Error</i> | Error measure according to Eq. (6.11) | - | 6 |
| f_{d}^{m} | Mass-based density function; see subscripts and superscripts for further variants | kg m^{-4} | 3-6 |
| f_{d}^{n} | Number-based density function; see subscripts and superscripts for further variants | kg m^{-4} | 3-6 |
| $\hat{f}_{\text{d}}^{\text{n}}$ | Normalized number based density function | m^{-1} | 3,4, 6 |
| f | Distribution function | | 4 |
| f | Exact solution function | | 6 |
| f_{approx} | Approximate solution function | | 6 |
| f_{model} | Model function | | 3 |
| f_{loss} | Loss function | | 3 |
| f_{r} | Recycling excess factor | - | 2 |
| f_{s} | Stoichiometric excess factor of species B | - | 2 |
| f^{s} | Dimensionless and scaled number density function | - | 6 |
| F_i | Flux at phase i | | 6 |
| F_1 | Friction force per unit volume acting on the liquid phase | N m^{-3} | 2 |
| F_c^W | Wall friction force acting on the continuous phase | N m^{-3} | 3 |
| g | Gravitational acceleration constant | m s^{-2} | 2-4 |
| g_i | Slope at grid point i | | 6 |
| h | Height | m | 4 |
| h_i | Height of compartment i | m | 2 |
| h_c | Ungasified liquid height, column height | m | 3, 4 |
| $h_{\text{c,cal}}$ | h_c to which the model was calibrated | m | 3 |
| $h(\zeta, \xi)$ | Collision frequency | $\text{m}^3 \text{s}^{-1}$ | 3, 6 |
| $h_{\text{BC}}^{\text{ini}}$ | Initial guess of the bubble column height (gasified height) | m | 3 |
| $\mathbb{H}(\phi)$ | Heavy side function of variable ϕ | - | 3, 6 |
| j_k | Superficial velocity resp. flux of the k -phase | m s^{-1} | 3,4,6 |
| \mathbf{J} | Non-convective diffusive fluxes in phase space | | 5 |
| J_{d}^{m} | Mass nucleation rate | $\text{kg m}^{-3} \text{s}^{-1}$ | 6 |
| k_{I} | Rate of reaction constant of Reaction I | s^{-1} | 2 |

continued ...

... continued

| | | | |
|----------------------------------|---|-----------------------------------|-------|
| k_{MT} | Mass transfer coefficient | m s^{-1} | 6 |
| \dot{m} | Mass flow rate; see subscripts and superscripts for further variants | kg s^{-1} | 6 |
| m_0 | Initial mass all particles in the system per unit volume | kg m^{-3} | 5 |
| $m_{a,b}$ | a, b -th moment ratio | | 3 |
| m_{d} | Size dependent interfacial momentum transfer to the dispersed gas phase | $\text{kg m}^{-4} \text{s}^{-2}$ | 3 |
| m_{d} | Mass of one particle with size ξ , mass of the dispersed phase | kg | 5, 6 |
| M_j | Molar mass of spices j | mol kg^{-1} | 2 |
| M_{c} | Interfacial momentum transfer to the continuous liquid phase | N m^{-3} | 3 |
| $MAPE$ | Mean absolute percentage error (see Eq. (3.6)) | % | 3, 4 |
| n | Normalizing index | - | 3,4 |
| n_{d} | Number density | m^{-3} | 6 |
| \mathbf{n}_{e} | Local outer normal vector of $\delta\Omega_{\text{e}}$ | | 5 |
| N_{circ} | Circulation number | - | 2 |
| N_j | Set of experiments (index j) included in the calculation of the $MAPE$ | - | 3 |
| N | Number incorporated moments and experiments | - | 4 |
| N | Number of dimensions | - | 5 |
| N_{h} | Number of orifices in a sparger | - | 4 |
| N_{ξ} | Number of discretization points in property space | - | 4,6 |
| $N_{\xi,\text{int}}$ | Number of integration points | - | 6 |
| N_z | Number of discretization points in physical space | - | 4 |
| p | Pressure | Pa | 2,3,6 |
| p_0 | Pressure in the headspace | bar | 2 |
| p^0 | Ambient pressure | Pa | 3,4 |
| p_1 | Slope parameter of the sparger function | s cm^{-1} | 4 |
| p_2 | y-intercept of the sparger function | - | 4 |
| Δp_{N} | Pressure drop over the nozzle | Pa | 2 |
| $p^{\text{ini}}(z_{\text{min}})$ | Initial guess of the pressure at z_{min} | Pa | 3 |
| P | Power introduced into the reactor | W | 2 |
| P_{ξ} | Number of collocation point in the ξ -domain | - | 3 |
| P_z | Number of collocation point in the z -domain | - | 3 |
| PE | Percentage error | % | 3 |
| $P(\xi, \zeta)$ | Daughter size distribution function | m^{-1} | 3,5,6 |
| q | Kernel parameter of Laakkonen <i>et al.</i> [106] | - | 6 |
| r_{I} | Rate of reaction per unit liquid volume of Reaction I | $\text{mol m}^{-3} \text{s}^{-1}$ | 2 |
| \mathbf{r} | Physical space with external coordinates $\mathbf{r} = (x, y, z)^{\text{T}}$; see subscripts and superscripts for further variants | m | 5,6 |
| $Re_{\text{d}}(\xi, z)$ | Reynolds number of the continuous phase | - | 2,3 |
| $Re_{\text{c}}(z)$ | Reynolds number of the dispersed phase bubbles | - | 3 |
| s_i | Smoothness indicator at phase i | - | 6 |
| t | Temperature | $^{\circ}\text{C}$ | 3 |
| t | Time dimension; see subscripts and superscripts for further variants | s | 5,6 |
| T^0 | Ambient temperature | K | 3,4 |

continued ...

... continued

| | | | |
|-------------------|--|----------------------------|-----|
| T | Temperature | K | 3 |
| u_k | Velocity of phase k | kg m^{-3} | 2 |
| $u_d(\xi, z)$ | Velocity in z -direction of the dispersed phase | m s^{-1} | 3 |
| $u_c(z)$ | Velocity in z -direction of the continuous phase | m s^{-1} | 3 |
| $\dot{V}_{k,i}$ | Volume flow rate of phase k in compartment i | $\text{m}^3 \text{s}^{-1}$ | 2 |
| V_i | Volume of compartment i | m^3 | 2 |
| $V(\xi)$ | Volume of a bubble of diameter ξ | m^3 | 3-6 |
| V_c | Volume of the liquid phase | m^3 | 3 |
| \mathbf{v}_r | Velocity in physical space | m s^{-1} | 5,6 |
| \mathbf{v}_c | Velocity in property space | | 5,6 |
| $V_d(\xi)$ | Volume of the particle with size ξ | m^3 | 5 |
| v_ξ | Velocity in property space particle size, growth rate; see subscripts and superscripts for further variants | m s^{-1} | 5,6 |
| \mathbf{v}_r | Velocity in physical space | m s^{-1} | 5 |
| $V(\xi)$ | Volume of a bubble of diameter ξ | m^3 | 6 |
| V_R | Reactor volume | m^3 | 6 |
| V_k | Volume of the k -phase | m^3 | 2,6 |
| \bar{V}_ξ | Average volume of the bubbles | m^3 | 6 |
| w_s | Mass fraction of species s ; see subscripts and superscripts for further variants | kg kg^{-1} | 3,6 |
| Δw | Mass transfer driving force | kg kg^{-1} | 6 |
| x | x -coordinate of the physical space | m | 5 |
| x_i | Dimension coordinate i | | 5 |
| x_s | Mole fraction of species s | mol mol^{-1} | 3 |
| \mathbf{X} | Independent variables | | 3 |
| y | y -coordinate of the physical space | m | 5 |
| \mathbf{Y} | Dependent variables | | 3 |
| z | Coordinate along the axial direction; z -coordinate of the physical space | m | 2-5 |
| $z_{\text{IN},i}$ | Initial position in flow path direction of compartment i | m | 2 |
| z_{min} | Lower bound of the z domain | m | 3 |
| z_{max} | Upper bound of the z domain | m | 3 |

Greek Letters

| Symbol | Description | Unit | Chapter |
|--|---|----------------------------------|---------|
| α_k | Volume fraction of phase k | $\text{m}^3 \text{m}^{-3}$ | 2-4,6 |
| $\bar{\alpha}_{k,i}$ | Gas holdup of phase k of compartment i , integral over $\alpha_{k,i}(z)$ along z | $\text{m}^3 \text{m}^{-3}$ | 2,3 |
| $\bar{\alpha}_d$ | Gas holdup | $\text{m}^3 \text{m}^{-3}$ | 3 |
| α_d^{ini} | Initial guess of the local gas volume fraction | $\text{m}^3 \text{m}^{-3}$ | 3 |
| $\Delta \bar{\alpha}_{g,\text{DT,AG}}$ | Difference between the gas holdup of compartment DT and AG; gas holdup difference | $\text{m}^3 \text{m}^{-3}$ | 2 |
| β | Unknown parameter vector | | 3 |
| Γ_d | Mass transfer rate per volume due to phase change | $\text{kg s}^{-1} \text{m}^{-3}$ | 6 |
| $\delta \Omega_C$ | Boundary of the phase space manifold; see subscripts and superscripts for further variants | | 5 |

continued ...

... continued

| | | | |
|---------------------|---|----------------------------|-------|
| $\delta\kappa_0$ | Step width of the algorithm proposed by [109] | - | 6 |
| δV_R | Surface of the reactor volume V_R | m^2 | 6 |
| $\Delta\xi$ | Cell width of the ξ -grid | m | 6 |
| ε | Turbulent energy dissipation rate | $\text{m}^2 \text{s}^{-3}$ | 3,4,6 |
| ϵ | Termination criteria of the Picard loop | | 3,4 |
| ϵ | Small number | | 6 |
| ζ | Pressure loss coefficient | - | 2 |
| ζ | Integration variable resp. the mother particle; see subscripts and superscripts for further variants | m | 3,5,6 |
| η_c | Kinematic viscosity of the continuous liquid phase | $\text{m}^2 \text{s}^{-1}$ | 3 |
| κ | Shape factor a the basis function of the RBM | - | 6 |
| κ_0 | Initial shape factor of the algorithm proposed by [109] | - | 6 |
| $\lambda(\zeta)$ | Coalescence efficiency | - | 3,6 |
| λ | Darcy friction factor | - | 2 |
| $\Lambda(\varphi)$ | Distribution function of variable φ | - | 3 |
| μ_k | Viscosity of the k -phase | Pa s | 2-4,6 |
| μ_{ab} | ab moment ratio of a distribution function | $\text{m}^{(a-b)}$ | 4 |
| μ_0 | Mean value of the inlet distribution | m | 6 |
| μ_1 | Value of the second peak of a bi-modal inlet distribution | m | 6 |
| ν_1 | Kinematic viscosity of the liquid phase | $\text{m}^2 \text{s}^{-1}$ | 2 |
| $\nu_{1,j}$ | Stoichiometric coefficient of chemical species j of the reaction I | - | 2 |
| ν | Average number of bubbles after breakage | - | 3,5,6 |
| ξ | Property space coordinate representing the bubble resp. particle diameter, child bubble; see subscripts and superscripts for further variants | m | 3-6 |
| $\dot{\xi}(\xi, z)$ | Growth rate | m s^{-1} | 3 |
| ξ_{\min} | Minimal bubble diameter | m | 3-6 |
| ξ_{\max} | Maximal bubble diameter | m | 3-6 |
| ξ_{eq} | Equivalent bubble diameter | m | 6 |
| ξ_0 | Variable around which the moment is formed | | 4 |
| ξ_{10} | Arithmetic mean | m | 3,4 |
| ξ_{30} | Volume-equivalent mean diameter | m | 4 |
| $\xi_{30,h}$ | Volume-equivalent mean diameter from at a sparger orifice | m | 4 |
| ξ_{32} | Sauter mean diameter | m | 3,4,6 |
| $\tilde{\xi}_i$ | Integration nodes in the reference domain | - | 6 |
| $\tilde{\xi}_i^*$ | Integration nodes in the property domain | m | 6 |
| ξ^s | Dimensionless and scaled diameter | - | 6 |
| ρ_k | Mass density of k -phase | kg m^{-3} | 2-6 |
| ρ_d^0 | Mass density of the dispersed phase at ambient conditions | kg m^{-3} | 3 |
| σ | Surface tension between of the continuous and dispersed phase | J m^{-2} | 3,4,6 |
| σ | Standard deviation of a distribution | m | 4 |
| σ^2 | Variance of a distribution | m | 3,4 |
| σ_0 | Standard deviation of the inlet distribution | m | 6 |
| τ_i | Residence time in compartment i | s | 2 |
| τ | Mean residence time of the particles in the system | s | 5 |

continued ...

| | | | |
|----------------------|--|-------------------|---|
| ... | continued | | |
| φ | Specific power input per reactor volume; power input | W m^{-3} | 2 |
| φ | Variable of a distribution function | | 3 |
| φ_i | Basis function | | 6 |
| φ_0 | Origin about the moment is evaluated | | 3 |
| ϕ | Arbitrary function | | 5 |
| Φ | Source or sink within the phase space | | 5 |
| $\Phi(s_i)$ | Flux limiter | - | 6 |
| χ | Second parameter of a log-normal distribution function | - | 4 |
| χ^2 | Chi-square distance | m^{-1} | 4 |
| ψ | Conserved density function | | 5 |
| $\dot{\psi}$ | Nucleation rate in phase space | | 5 |
| ψ | Basis functions of a truncated series expansion | | 6 |
| $\Psi(\xi)$ | Number based probability density function | m^{-1} | 3 |
| Ψ | Conserved quantity | | 5 |
| ω | Kurtosis of a distribution function | - | 3 |
| ω | First parameter of a log-normal distribution function, sparger function | - | 4 |
| ω_i | Basis function coefficients | | 6 |
| $\tilde{\omega}_i$ | Quadrature weights in the reference domain | - | 6 |
| $\tilde{\omega}_i^*$ | Quadrature weights in the property domain | - | 6 |
| Ω_C | Phase space manifold; see subscripts and superscripts for further variants | | 5 |

Subscripts

| Symbol | Description | Chapter |
|--------|---|---------|
| 0 | Quantity related to the inlet distribution | 6 |
| ab | Order of the μ_{ab} moment ratio | 3,4 |
| ana | Analytic solution | 6 |
| B | Birth/source term | 3,5,6 |
| batch | Quantity with reference to batch mode | 4 |
| c | Continuous (liquid) phase | 3,4,6 |
| conti | Quantity with reference to continuous co-current mode | 4 |
| c | Property space related quantity | 5 |
| circ | Circulation | 2 |
| D | Death/sink term | 3,5,6 |
| d | Dispersed (gas) phase | 3-6 |
| exp | Quantity resulting from an experiment | 4,6 |
| feed | Feed stream | 2 |
| g | Gas phase index | 2 |
| h | Quantity with reference to a sparger orifice | 4 |
| i | Compartment index | 2 |
| i | Unique experiment identifier | 3 |
| i | Index of incorporated moments and/or experiments | 4 |
| i | Dimension index | 5 |
| i | Index of the basis function | 6 |

continued ...

| | | |
|---------|--|-----|
| ... | continued | |
| i | Index of grid point | 6 |
| i | Index of adjustable parameter | 6 |
| IN | Inlet | 2 |
| I | Reaction I | 2 |
| in | Quantity at the inlet | 6 |
| ini | Initial value | 6 |
| inlet | Quantity at the inlet | 4 |
| j | Chemical species index | 2 |
| j | Data set identifier | 3 |
| j | Index of the bubble size class | 4 |
| k | Phase descriptor index: d-dispersed phase, c-continuous phase | 2-6 |
| l | Liquid phase index | 2 |
| max | Upper bound | 3-6 |
| min | Lower bound | 3-6 |
| mod | Mode of the inlet/initial distribution | 6 |
| OUT | Outlet | 2 |
| out | Quantity at the outlet | 6 |
| product | Product stream | 2 |
| purge | Purge stream | 2 |
| r | Physical space related quantity | 5 |
| ξ | Particle size related quantity | 5 |
| s | Quantity related to the wall of the draft tube | 2 |
| s | Chemical species | 3 |
| s | Scaling quantity | 5 |
| sim | Quantity resulting from a simulation | 3,6 |
| sim | Quantity resulting from a simulation with measured inlet BSD | 4 |
| sim-SPM | Quantity resulting from a simulation with a inlet BSD from the sparger model | 4 |

Superscripts

| Symbol | Description | Chapter |
|--------|-----------------------------------|---------|
| * | Current solution | 3 |
| * | Incompletely transformed quantity | 5 |
| ** | Previous solution | 3 |
| ^ | Normalized quantity | 3,4,6 |
| ^ | Dimensionless quantity | 5 |
| - | Averaged quantity | 4,6 |
| 0 | Reference state | 4 |
| D | Drag | 3 |
| ini | Initial guess value | 4 |
| ini | Initial quantity | 5 |
| m | Mass based quantity | 3-6 |
| M | Measuring position | 4 |
| n | Number based quantity | 3-6 |
| s | Dimensionless and scaled quantity | 6 |

continued ...

... continued

| | | |
|---|---------------------|---|
| T | Transposed quantity | 5 |
| W | Wall | 3 |

Abbreviations

| Symbol | Description | Chapter |
|------------|--|-----------|
| 0D | Zero-dimensional in physical space | 6 |
| 1D | One-dimensional in physical space | 3,4,6 |
| 2D | Two-dimensional in physical space | 4 |
| aq. | aqueous | 2 |
| A | High-boiling reactant A | 2 |
| AH | Aerate height | 2 |
| AG | Annular gap | 2 |
| B | Chemical species B | 2 |
| BC | Bubble column | 1,3,4 |
| BP | Baffle plate | 2 |
| BR | Bottom redirection zone | 2 |
| BS | Bottom space | 2 |
| BSD | Bubble size distribution | 1,3- 6 |
| C | High-boiling product C | 2 |
| CFD | Computational fluid dynamics | 1-4 |
| CLD | Chord length distribution | 4 |
| CSTR | Continuous stirred tank reactor | 2 |
| D | Calibration method which use the BSD as dependent variable | 3 |
| DT | Draft tube | 2 |
| ER | External recycle | 2 |
| EtOH | Ethanol | 3,6 |
| FPT | Fixed pivot technique | 6 |
| FVMG | Finite volume method with Gauss quadrature | 1,4,6 |
| GLL | Gauss-Legendre-Lobatto | 4,6 |
| Gly | Glycerol | 3 |
| H | Calibration method which use the gas holdup as dependent variable | 3 |
| HR | Head flow redirection | 2 |
| HS | Head space | 2 |
| JLR | Jet loop reactor | 1-3 |
| KTAWSR | Kinetic theory approach with size resolution | 1,3- 6 |
| KGT | Kinetic gas theory | 4 |
| mPBE | mass-based PBE | 5 |
| M1, M2, M3 | Measuring position | 4 |
| M2 | Calibration method which use two moments of a BSD as dependent variable | 3 |
| M2H | Calibration method which use two moments of a BSD and the gas holdup as dependent variable | 3 |

continued ...

| | | |
|---------------------------------|---|---------|
| ... continued | | |
| M3 | Calibration method which use three moments of a BSD as dependent variable | 3 |
| MUSIG | Multiple-size group approach | 1,3 |
| MUSCL | Monotonic upstream-centered scheme for conservation laws | 6 |
| MPB | Multifluid population balance model | 1,3,4,6 |
| nPBE | Number-based PBE | 5 |
| n2mPBE | Mass-based PBE resulting of a transformation of a number-based PBE | 5 |
| N | Nozzle | 2 |
| NaCl | Sodium chloride | 3 |
| Na ₂ SO ₃ | Sodium sulfite | 3 |
| Na ₂ SO ₄ | Sodium sulfate | 3,6 |
| NP | Needle probe | 4 |
| OC | Weighed residual spectral orthogonal collocation | 1,6 |
| ODE | Ordinary differential equation | 6 |
| OMOP | Optical multimode online probe | 1,3,4,6 |
| OPTOEM | Optoelectronic module | 4 |
| PBE | Population balance equation | 1-6 |
| PFR | Plug flow reactor | 2 |
| PMMA | Polymethylmethacrylat | 3 |
| PIS | Plate sparger | 4 |
| R | Reactor | 2,6 |
| RBM | Meshless radial basis method | 6 |
| SMD | Sauter mean diameter | 4,6 |
| SpS | Spider sparger | 4 |
| SPM | Sparger model | 4 |
| STR | Stirred tank reactor | 1,6 |

Note if a variable has no unit this is indicated by -, if no specification is made the unit of the variable can change.

Notation

The following notation is introduced to differentiate between scalar, vector, matrix and tensor:

Scalar: v ; Vector: \mathbf{v} ; Matrix: \mathbf{V} ; Tensor: \mathbf{V}

References

- [1] P. Harriott, *Chemical Reactor Design*. Boca Raton: CRC Press, 2002, ISBN: 978-0-429-22237-5. DOI: 10.1201/9780203910238.
- [2] S. V. Patankar, *Numerical Heat Transfer and Fluid Flow*. CRC Press, 2018. DOI: 10.1201/9781482234213.
- [3] F. Breit, C. Weibel, and E. von Harbou, "Application and parameterization of a one-dimensional multifluid population balance model to bubble columns," *AIChE Journal*, vol. 70, no. 7, 2024. DOI: 10.1002/aic.18424.
- [4] J. B. Joshi and V. V. Ranade, "Computational fluid dynamics for designing process equipment: Expectations, current status, and path forward," *Industrial & Engineering Chemistry Research*, vol. 42, no. 6, pp. 1115–1128, 2003. DOI: 10.1021/ie0206608.
- [5] C. K. Harris, D. Roekaerts, F. Rosendal, F. Buitendijk, P. Daskopoulos, A. Vreene-goor, and H. Wang, "Computational fluid dynamics for chemical reactor engineering," *Chemical Engineering Science*, vol. 51, no. 10, pp. 1569–1594, 1996. DOI: 10.1016/0009-2509(96)00021-8.
- [6] R. Vinuesa and S. L. Brunton, "Enhancing computational fluid dynamics with machine learning," *Nature Computational Science*, vol. 2, no. 6, pp. 358–366, 2022. DOI: 10.1038/s43588-022-00264-7.
- [7] Antony Jameson, Ed., *The present status , challenges , and future developments in computational fluid dynamics*, October 1995.
- [8] M. Baerns, *Technische Chemie*, 2nd ed. Weinheim: Wiley-VCH, 2013, ISBN: 3-527-33072-0.
- [9] H. Warmeling, A. Behr, and A. J. Vorholt, "Jet loop reactors as a versatile reactor set up - Intensifying catalytic reactions: A review," *Chemical Engineering Science*, vol. 149, pp. 229–248, 2016. DOI: 10.1016/j.ces.2016.04.032.
- [10] J. C. Bloor, G. K. Anderson, and A. R. Willey, "High rate aerobic treatment of brewery wastewater using the jet loop reactor," *Water Research*, vol. 29, no. 5, pp. 1217–1223, 1995. DOI: 10.1016/0043-1354(94)00310-4.
- [11] O. Bey and E. von Harbou, "Einfluss der Wechselwirkung von Reaktion und Fluid-dynamik auf das Verhalten von Strahlschlaufenreaktoren," *Chemie Ingenieur Technik*, vol. 93, no. 1-2, pp. 191–200, 2021. DOI: 10.1002/cite.202000156.
- [12] G.-Y. Zhu, A. Zamamiri, M. A. Henson, and M. A. Hjortsø, "Model predictive control of continuous yeast bioreactors using cell population balance models," *Chemical Engineering Science*, vol. 55, no. 24, pp. 6155–6167, 2000. DOI: 10.1016/S0009-2509(00)0208-6.

- [13] S. Shirazian, H. Y. Ismail, M. Singh, R. Shaikh, D. M. Croker, and G. M. Walker, “Multi-dimensional population balance modelling of pharmaceutical formulations for continuous twin-screw wet granulation: Determination of liquid distribution,” *International journal of pharmaceutics*, vol. 566, pp. 352–360, 2019. DOI: 10.1016/j.ijpharm.2019.06.001.
- [14] P. Seydel, J. Blömer, and J. Bertling, “Modeling particle formation at spray drying using population balances,” *Drying Technology*, vol. 24, no. 2, pp. 137–146, 2006. DOI: 10.1080/07373930600558912.
- [15] C. B. B. Costa, M. R. W. Maciel, and R. M. Filho, “Considerations on the crystallization modeling: Population balance solution,” *Computers & Chemical Engineering*, vol. 31, no. 3, pp. 206–218, 2007. DOI: 10.1016/j.compchemeng.2006.06.005.
- [16] F. Breit, A. Mühlbauer, E. von Harbou, M. W. Hlawitschka, and H.-J. Bart, “A one-dimensional combined multifluid-population balance model for the simulation of batch bubble columns,” *Chemical Engineering Research and Design*, vol. 170, pp. 270–289, 2021. DOI: 10.1016/j.cherd.2021.03.036.
- [17] E. Bilgili and B. Scarlett, “Population balance modeling of non-linear effects in milling processes,” *Powder Technology*, vol. 153, no. 1, pp. 59–71, 2005. DOI: 10.1016/j.powtec.2005.02.005.
- [18] M. M. Attarakih, H.-J. Bart, T. Steinmetz, M. Dietzen, and N. M. Faqir, “LlecmoD: A bivariate population balance simulation tool for liquid-liquid extraction columns,” *The Open Chemical Engineering Journal*, vol. 2, no. 1, pp. 10–34, 2008. DOI: 10.2174/1874123100802010010.
- [19] J. Gimbun, S. Y. Liew, Z. K. Nagy, and C. D. Rielly, “Three-way coupling simulation of a gas-liquid stirred tank using a multi-compartment population balance model,” *Chemical Product and Process Modeling*, vol. 11, no. 3, pp. 205–216, 2016. DOI: 10.1515/cppm-2015-0076.
- [20] E. Krepper, D. Lucas, T. Frank, H.-M. Prasser, and P. J. Zwart, “The inhomogeneous musig model for the simulation of polydispersed flows,” *Nuclear Engineering and Design*, vol. 238, no. 7, pp. 1690–1702, 2008. DOI: 10.1016/j.nucengdes.2008.01.004.
- [21] M. M. Attarakih, H.-J. Bart, and N. M. Faqir, “Numerical solution of the bivariate population balance equation for the interacting hydrodynamics and mass transfer in liquid-liquid extraction columns,” *Chemical Engineering Science*, vol. 61, no. 1, pp. 113–123, 2006. DOI: 10.1016/j.ces.2004.12.055.
- [22] S. A. Schmidt, M. Simon, M. M. Attarakih, L. Lagar G., and H.-J. Bart, “Droplet population balance modelling—hydrodynamics and mass transfer,” *Chemical Engineering Science*, vol. 61, no. 1, pp. 246–256, 2006. DOI: 10.1016/j.ces.2005.02.075.
- [23] B. H. Shah and D. Ramkrishna, “A population balance model for mass transfer in lean liquid-liquid dispersions,” *Chemical Engineering Science*, vol. 28, no. 2, pp. 389–399, 1973. DOI: 10.1016/0009-2509(73)80038-7.

- [24] A. K. Nayak, Z. Borcka, L. E. Patrino, F. Sporleder, C. A. Dorao, and H. A. Jakobsen, "A combined multifluid-population balance model for vertical gas–liquid bubble-driven flows considering bubble column operating conditions," *Industrial & Engineering Chemistry Research*, vol. 50, no. 3, pp. 1786–1798, 2011. DOI: 10.1021/ie101664w.
- [25] J. Solsvik and H. A. Jakobsen, "A combined multifluid-population balance model applied to dispersed gas–liquid flows," *Journal of Dispersion Science and Technology*, vol. 35, no. 11, pp. 1611–1625, 2014. DOI: 10.1080/01932691.2013.866901.
- [26] C. B. Vik, J. Solsvik, M. Hillestad, and H. A. Jakobsen, "A multifluid-pbe model for simulation of mass transfer limited processes operated in bubble columns," *Computers & Chemical Engineering*, vol. 110, pp. 115–139, 2018. DOI: 10.1016/j.compchemeng.2017.11.023.
- [27] E. von Harbou, M. Schmitt, C. Großmann, and H. Hasse, "A novel type of equipment for reactive distillation: Model development, simulation, sensitivity and error analysis," *AIChE Journal*, vol. 59, no. 5, pp. 1533–1543, 2013. DOI: 10.1002/aic.13947.
- [28] I. von Harbou, M. Imle, and H. Hasse, "Modeling and simulation of reactive absorption of CO₂ with MEA: Results for four different packings on two different scales," *Chemical Engineering Science*, vol. 105, pp. 179–190, 2014. DOI: 10.1016/j.ces.2013.11.005.
- [29] M. Mickler and H.-J. Bart, "Optical Multimode Online Probe: Erfassung und Analyse von Partikelkollektiven," *Chemie Ingenieur Technik*, vol. 85, no. 6, pp. 901–906, 2013. DOI: 10.1002/cite.201200139.
- [30] V. Jossen, R. Eibl, R. Pörtner, M. Kraume, and D. Eibl, "Stirred bioreactors," in *Current Developments in Biotechnology and Bioengineering*, Elsevier, 2017, pp. 179–215, ISBN: 978-0-444-63663-8. DOI: 10.1016/B978-0-444-63663-8.00007-0.
- [31] J. A. Conesa, *Chemical Reactor Design: Mathematical modeling and applications*. Weinheim Germany: Wiley, 2019, ISBN: 978-3-527-34630-1. DOI: 10.1002/9783527823376.
- [32] J. Solsvik and H. A. Jakobsen, "On the solution of the population balance equation for bubbly flows using the high-order least squares method: Implementation issues," *Reviews in Chemical Engineering*, vol. 29, no. 2, 2013. DOI: 10.1515/revce-2012-0018.
- [33] A. Babajimopoulos, D. N. Assanis, D. L. Flowers, S. M. Aceves, and R. P. Hessel, "A fully coupled computational fluid dynamics and multi-zone model with detailed chemical kinetics for the simulation of premixed charge compression ignition engines," *International Journal of Engine Research*, vol. 6, no. 5, pp. 497–512, 2005. DOI: 10.1243/146808705X30503.
- [34] J. Jung and I. K. Gamwo, "Multiphase CFD-based models for chemical looping combustion process: Fuel reactor modeling," *Powder Technology*, vol. 183, no. 3, pp. 401–409, 2008. DOI: 10.1016/j.powtec.2008.01.019.
- [35] H. Kruggel-Emden, F. Stepanek, and A. Munjiza, "A Study on the Role of Reaction Modeling in Multi-phase CFD-based Simulations of Chemical Looping Combustion," *Oil & Gas Science and Technology – Revue d'IFP Energies nouvelles*, vol. 66, no. 2, pp. 313–331, 2011. DOI: 10.2516/ogst/2010031.

- [36] M. Zandie, H. K. Ng, S. Gan, M. F. Muhamad Said, and X. Cheng, “Review of the advances in integrated chemical kinetics-computational fluid dynamics combustion modelling studies of gasoline-biodiesel mixtures,” *Transportation Engineering*, vol. 7, p. 100102, 2022. DOI: 10.1016/j.treng.2021.100102.
- [37] H. Blenke, K. Bohner, and W. Pfeiffer, “Hydrodynamische Berechnung von Schlaufenreaktoren für Einphasensysteme,” *Chemie Ingenieur Technik*, vol. 43, no. 1-2, pp. 10–17, 1971. DOI: 10.1002/cite.330430103.
- [38] P. Zehner, “Modellbildung für Mehrphasenströmungen in Reaktoren,” *Chemie Ingenieur Technik*, vol. 60, no. 7, pp. 531–539, 1988. DOI: 10.1002/cite.330600706.
- [39] P. Zehner and Benfer R., “Modelling fluid dynamics in multiphase reactors,” *Chemical Engineering Science*, vol. 51, no. 10, pp. 1735–1744, 1996. DOI: 10.1016/0009-2509(96)00032-2.
- [40] W. Reschetilowski, *Handbuch Chemische Reaktoren*. Berlin, Heidelberg: Springer Berlin Heidelberg, 2020, ISBN: 978-3-662-56433-2. DOI: 10.1007/978-3-662-56434-9.
- [41] P. Zehner, *Flüssigkeits/Feststoff-Strömungen in verfahrenstechnischen Apparaten: Fortschritt-Berichte VDI Reihe 3: Verfahrenstechnik Nr. 160*. Düsseldorf: VDI-Verlag gmbH, 1988.
- [42] Octave Levenspiel, *Chemical Reaction Engineering*. New York, NY: John Wiley & Sons, Inc., 1999, vol. 3, ISBN: 0-471-25424-X.
- [43] K. H. Tebel and P. Zehner, “Fluid dynamic description of jet-loop reactors in multiphase operation,” *Chemical Engineering & Technology - CET*, vol. 12, no. 1, pp. 274–280, 1989. DOI: 10.1002/ceat.270120138.
- [44] V. C. Kelessidis and A. E. Dukler, “Modeling flow pattern transitions for upward gas-liquid flow in vertical concentric and eccentric annuli,” *International Journal of Multiphase Flow*, vol. 15, no. 2, pp. 173–191, 1989. DOI: 10.1016/0301-9322(89)90069-4.
- [45] H. Blenke, K. Bohner, and S. Schuster, “Beitrag zur optimalen Gestaltung chemischer Reaktoren,” *Chemie Ingenieur Technik*, vol. 37, no. 3, pp. 289–294, 1965. DOI: 10.1002/cite.330370322.
- [46] Y. Gao, Du Hong, Y. Cheng, L. Wang, and X. Li, “CFD simulation for up flow jet-loop reactors by use of bi-dispersed bubble model,” *Chemical Engineering Research and Design*, vol. 141, pp. 66–83, 2019. DOI: 10.1016/j.cherd.2018.10.035.
- [47] P. K. Hui and H. J. Palmer, “Uncatalyzed oxidation of aqueous sodium sulfite and its ability to simulate bacterial respiration,” *Biotechnology and bioengineering*, vol. 37, no. 4, pp. 392–396, 1991. DOI: 10.1002/bit.260370416.
- [48] A. Mühlbauer, O. Böck, R. Raab, M. W. Hlawitschka, and H.-J. Bart, “Solid particle effects in centi-scale slurry bubble columns,” *Chemie Ingenieur Technik*, vol. 93, no. 1-2, pp. 318–325, 2021. DOI: 10.1002/cite.202000136.
- [49] M. Lichti, J. Schulz, and H.-J. Bart, “Quantification of entrainment using an optical inline probe,” *Chemie Ingenieur Technik*, vol. 91, no. 4, pp. 429–434, 2019. DOI: 10.1002/cite.201800045.

- [50] J. Schulz, K. Schäfer, and H.-J. Bart, “Entrainment control using a newly developed telecentric inline probe,” *Chemie Ingenieur Technik*, vol. 92, no. 3, pp. 256–265, 2020. DOI: 10.1002/cite.201900112.
- [51] M. Koch, T. M. Dang, F. Justen, F. Breit, and E. von Harbou, “Experimental Investigation of the Bubble Size Distribution in a Mini Plant Batch Bubble Column With Variation of Gas Flux, Bubble Column Height and Composition of the Liquid Phase,” *Zenodo*, Nov. 2023. DOI: 10.5281/zenodo.7774678.
- [52] G. Besagni and F. Inzoli, “Bubble size distributions and shapes in annular gap bubble column,” *Experimental Thermal and Fluid Science*, vol. 74, pp. 27–48, 2016. DOI: 10.1016/j.expthermflusci.2015.11.020.
- [53] C. A. Coualaloglou and L. L. Tavlarides, “Description of interaction processes in agitated liquid-liquid dispersions,” *Chemical Engineering Science*, vol. 32, no. 11, pp. 1289–1297, 1977. DOI: 10.1016/0009-2509(77)85023-9.
- [54] M. Baird and R. G. Rice, “Axial dispersion in large unbaffled columns,” *The Chemical Engineering Journal*, vol. 9, no. 2, pp. 171–174, 1975. DOI: 10.1016/0300-9467(75)80010-4.
- [55] J. Solsvik and H. A. Jakobsen, “Solution of the dynamic population balance equation describing breakage-coalescence systems in agitated vessels: The least-squares method,” *The Canadian Journal of Chemical Engineering*, vol. 92, no. 2, pp. 266–287, 2014. DOI: 10.1002/cjce.21882.
- [56] J. E. Botello-Álvarez, S. A. Baz-Rodríguez, R. González-García, A. Estrada-Baltazar, J. A. Padilla-Medina, G. González-Alatorre, and J. L. Navarrete-Bolaños, “Effect of electrolytes in aqueous solution on bubble size in gas-liquid bubble columns,” *Industrial & Engineering Chemistry Research*, vol. 50, no. 21, pp. 12 203–12 207, 2011. DOI: 10.1021/ie200452q.
- [57] D. Pjontek, V. Parisien, and A. Macchi, “Bubble characteristics measured using a monofibre optical probe in a bubble column and freeboard region under high gas holdup conditions,” *Chemical Engineering Science*, vol. 111, pp. 153–169, 2014. DOI: 10.1016/j.ces.2014.02.024.
- [58] J. J. Quinn, J. M. Sovechles, J. A. Finch, and K. E. Waters, “Critical coalescence concentration of inorganic salt solutions,” *Minerals Engineering*, vol. 58, pp. 1–6, 2014. DOI: 10.1016/j.mineng.2013.12.021.
- [59] K. Samaras, M. Kostoglou, T. D. Karapantsios, and P. Mavros, “Effect of adding glycerol and tween 80 on gas holdup and bubble size distribution in an aerated stirred tank,” *Colloids and Surfaces A: Physicochemical and Engineering Aspects*, vol. 441, pp. 815–824, 2014. DOI: 10.1016/j.colsurfa.2013.02.031.
- [60] D. K. R. Nambiar, R. Kumar, and K. S. Gandhi, “Breakage and coalescence of drops in turbulent stirred dispersions,” *Sadhana*, vol. 15, no. 2, pp. 73–103, 1990. DOI: 10.1007/BF02760469.

- [61] D. Li, A. Buffo, W. Podgórska, D. L. Marchisio, and Z. Gao, "Investigation of droplet breakup in liquid–liquid dispersions by cfd–pbm simulations: The influence of the surfactant type," *Chinese Journal of Chemical Engineering*, vol. 25, no. 10, pp. 1369–1380, 2017. DOI: 10.1016/j.cjche.2017.01.014.
- [62] S. Falzone, A. Buffo, M. Vanni, and D. L. Marchisio, "Simulation of turbulent coalescence and breakage of bubbles and droplets in the presence of surfactants, salts, and contaminants," in *Bridging scales in modelling and simulation of non-reacting and reacting flows*, ser. Advances in Chemical Engineering, A. Parente and J. de Wilde, Eds., vol. 52, Cambridge, MA et al.: Elsevier Academic Press, 2018, pp. 125–188, ISBN: 978-0-12-815096-2. DOI: 10.1016/bs.ache.2018.01.002.
- [63] N. W. Geary and R. G. Rice, "Bubble size prediction for rigid and flexible spargers," *AIChE Journal*, vol. 37, no. 2, pp. 161–168, 1991. DOI: 10.1002/aic.690370202.
- [64] N. Kantarci, F. Borak, and K. O. Ulgen, "Bubble column reactors," *Process Biochemistry*, vol. 40, no. 7, pp. 2263–2283, 2005. DOI: 10.1016/j.procbio.2004.10.004.
- [65] W.-D. Deckwer, *Reaktionstechnik in Blasensäulen*, 1. Aufl., ser. Grundlagen der chemischen Technik. Frankfurt am Main: Salle, 1985, ISBN: 978-3-7941-2606-4.
- [66] A. Lefebvre, Y. Mezui, M. Obligado, S. Gluck, and A. Cartellier, "A new, optimized doppler optical probe for phase detection, bubble velocity and size measurements: Investigation of a bubble column operated in the heterogeneous regime," *Chemical Engineering Science*, vol. 250, p. 117359, 2022. DOI: 10.1016/j.ces.2021.117359.
- [67] C. F. Weibel, M. C. Hofmann, C. Garth, H.-J. Bart, and E. von Harbou, "A new image evaluation method for disperse multiphase processes using synthetic training data," *Industrial & Engineering Chemistry Research*, vol. 63, no. 28, pp. 12561–12573, 2024. DOI: 10.1021/acs.iecr.4c01546.
- [68] M. Schlüter, "Lokale Messverfahren für Mehrphasenströmungen," *Chemie Ingenieur Technik*, vol. 83, no. 7, pp. 992–1004, 2011. DOI: 10.1002/cite.201100039.
- [69] C. P. Ribeiro and P. L. Lage, "Population balance modeling of bubble size distributions in a direct-contact evaporator using a sparger model," *Chemical Engineering Science*, vol. 59, no. 12, pp. 2363–2377, 2004. DOI: 10.1016/j.ces.2004.01.060.
- [70] M. Alonzo, A. Lefebvre, Z. Huang, S. Gluck, and C. Alain, "Monofiber optical probe using doppler signals detection for drop size and velocity measurement in air assisted atomization," *International Conference on Liquid Atomization and Spray Systems (ICLASS)*, vol. 1, no. 1, 2021. DOI: 10.2218/iclass.2021.5909.
- [71] M. Li and D. Wilkinson, "Determination of non-spherical particle size distribution from chord length measurements. part 1: Theoretical analysis," *Chemical Engineering Science*, vol. 60, no. 12, pp. 3251–3265, 2005. DOI: 10.1016/j.ces.2005.01.008.
- [72] W. Liu and N. N. Clark, "Relationships between distributions of chord lengths and distributions of bubble sizes including their statistical parameters," *International Journal of Multiphase Flow*, vol. 21, no. 6, pp. 1073–1089, 1995. DOI: 10.1016/0301-9322(95)00039-Z.

- [73] H. A. Jakobsen, *Chemical Reactor Modeling*. Cham: Springer International Publishing, 2014, ISBN: 978-3-319-05091-1. DOI: 10.1007/978-3-319-05092-8.
- [74] A. Mandal, G. Kundu, and D. Mukherjee, “Gas-holdup distribution and energy dissipation in an ejector-induced downflow bubble column: The case of non-newtonian liquid,” *Chemical Engineering Science*, vol. 59, no. 13, pp. 2705–2713, 2004. DOI: 10.1016/j.ces.2004.04.012.
- [75] J. Zahradník, J. Kratochvíl, F. Kaštanek, and M. Rylek, “Energy effectiveness of bubble-column reactors with sieve-tray and ejector-type gas distributors,” *Chemical Engineering Communications*, vol. 15, no. 1-4, pp. 27–40, 1982. DOI: 10.1080/00986448208911057.
- [76] M. Polli, M. Di Stanislao, R. Bagatin, E. A. Bakr, and M. Masi, “Bubble size distribution in the sparger region of bubble columns,” *Chemical Engineering Science*, vol. 57, no. 1, pp. 197–205, 2002. DOI: 10.1016/S0009-2509(01)00301-3.
- [77] F. Sporleder, C. A. Dorao, and H. A. Jakobsen, “Model based on population balance for the simulation of bubble columns using methods of the least-square type,” *Chemical Engineering Science*, vol. 66, no. 14, pp. 3133–3144, 2011. DOI: 10.1016/j.ces.2011.02.062.
- [78] N. J. Higham, *Accuracy and Stability of Numerical Algorithms*. Society for Industrial and Applied Mathematics, 2002, ISBN: 978-0-89871-521-7. DOI: 10.1137/1.9780898718027.
- [79] D. Ramkrishna, *Population balances: Theory and applications to particulate systems in engineering*. New York: Acad. Press, 2000, ISBN: 978-0-12-391148-3. DOI: 10.1016/B978-0-12-576970-9.X5000-0.
- [80] J. Solsvik and H. A. Jakobsen, “The foundation of the population balance equation: A review,” *Journal of Dispersion Science and Technology*, vol. 36, no. 4, pp. 510–520, 2015. DOI: 10.1080/01932691.2014.909318.
- [81] A. D. Randolph and M. A. Larson, *Theory of particulate processes: Analysis of techniques of continuous crystallization*. New York, NY: Acad. Press, 1971, ISBN: 978-0-12-579650-7. DOI: 10.1016/B978-0-12-579650-7.X5001-5.
- [82] D. L. Marchisio, J. T. Piktorna, R. O. Fox, R. D. Vigil, and A. A. Barresi, “Quadrature method of moments for population-balance equations,” *AIChE Journal*, vol. 49, no. 5, pp. 1266–1276, 2003. DOI: 10.1002/aic.690490517.
- [83] D. L. Marchisio and R. O. Fox, “Solution of population balance equations using the direct quadrature method of moments,” *Journal of Aerosol Science*, vol. 36, no. 1, pp. 43–73, 2005. DOI: 10.1016/j.jaerosci.2004.07.009.
- [84] M. M. Attarakih, C. Drumm, and H.-J. Bart, “Solution of the population balance equation using the sectional quadrature method of moments (sqmom),” *Chemical Engineering Science*, vol. 64, no. 4, pp. 742–752, 2009. DOI: 10.1016/j.ces.2008.05.006.

- [85] E. Askari, G. St-Pierre Lemieux, and P. Proulx, "Application of extended quadrature method of moments for simulation of bubbly flow and mass transfer in gas-liquid stirred tanks," *The Canadian Journal of Chemical Engineering*, vol. 97, no. 9, pp. 2548–2564, 2019. DOI: 10.1002/cjce.23470.
- [86] A. Buffo, M. Vanni, and D. L. Marchisio, "Multidimensional population balance model for the simulation of turbulent gas-liquid systems in stirred tank reactors," *Chemical Engineering Science*, vol. 70, pp. 31–44, 2012. DOI: 10.1016/j.ces.2011.04.042.
- [87] D. Li, A. Buffo, W. Podgórska, D. L. Marchisio, and Z. Gao, "Investigation of droplet breakup in liquid-liquid dispersions by cfd-pbm simulations: The influence of the surfactant type," *Chinese Journal of Chemical Engineering*, vol. 25, no. 10, pp. 1369–1380, 2017. DOI: 10.1016/j.cjche.2017.01.014.
- [88] M. Petitti, M. Vanni, D. L. Marchisio, A. Buffo, and F. Podenzani, "Simulation of coalescence, break-up and mass transfer in a gas-liquid stirred tank with cqmom," *Chemical Engineering Journal*, vol. 228, pp. 1182–1194, 2013. DOI: 10.1016/j.cej.2013.05.047.
- [89] S. Alzyod and S. Charton, "A meshless radial basis method (rbm) for solving the detailed population balance equation," *Chemical Engineering Science*, vol. 228, p. 115 973, 2020. DOI: 10.1016/j.ces.2020.115973.
- [90] R. Lehnigk, W. Bainbridge, Y. Liao, D. Lucas, T. Niemi, J. Peltola, and F. Schlegel, "An open-source population balance modeling framework for the simulation of polydisperse multiphase flows," *AIChE Journal*, vol. 68, no. 3, 2022. DOI: 10.1002/aic.17539.
- [91] J. Kumar, G. Warnecke, M. Peglow, and S. Heinrich, "Comparison of numerical methods for solving population balance equations incorporating aggregation and breakage," *Powder Technology*, vol. 189, no. 2, pp. 218–229, 2009. DOI: 10.1016/j.powtec.2008.04.014.
- [92] F. Filbet and P. Laurençot, "Numerical simulation of the smoluchowski coagulation equation," *SIAM Journal on Scientific Computing*, vol. 25, no. 6, pp. 2004–2028, 2004. DOI: 10.1137/S1064827503429132.
- [93] C. A. Dorao and H. A. Jakobsen, "Time-space-property least squares spectral method for population balance problems," *Chemical Engineering Science*, vol. 62, no. 5, pp. 1323–1333, 2007. DOI: 10.1016/j.ces.2006.11.016.
- [94] S. Kumar and D. Ramkrishna, "On the solution of population balance equations by discretization—i. a fixed pivot technique," *Chemical Engineering Science*, vol. 51, no. 8, pp. 1311–1332, 1996. DOI: 10.1016/0009-2509(96)88489-2.
- [95] D. Li, Z. Li, and Z. Gao, "Quadrature-based moment methods for the population balance equation: An algorithm review," *Chinese Journal of Chemical Engineering*, vol. 27, no. 3, pp. 483–500, 2019. DOI: 10.1016/j.cjche.2018.11.028.
- [96] H. M. Omar and S. Rohani, "Crystal population balance formulation and solution methods: A review," *Crystal Growth & Design*, vol. 17, no. 7, pp. 4028–4041, 2017. DOI: 10.1021/acs.cgd.7b00645.

- [97] C. A. Dorao and H. A. Jakobsen, “A least squares method for the solution of population balance problems,” *Computers & Chemical Engineering*, vol. 30, no. 3, pp. 535–547, 2006. DOI: 10.1016/j.compchemeng.2005.10.012.
- [98] M. J. Hounslow, R. L. Ryall, and V. R. Marshall, “A discretized population balance for nucleation, growth, and aggregation,” *AIChE Journal*, vol. 34, no. 11, pp. 1821–1832, 1988. DOI: 10.1002/aic.690341108.
- [99] B. J. McCoy and G. Madras, “Analytical solution for a population balance equation with aggregation and fragmentation,” *Chemical Engineering Science*, vol. 58, no. 13, pp. 3049–3051, 2003. DOI: 10.1016/S0009-2509(03)00159-3.
- [100] S. Qamar and G. Warnecke, “Numerical solution of population balance equations for nucleation, growth and aggregation processes,” *Computers & Chemical Engineering*, vol. 31, no. 12, pp. 1576–1589, 2007. DOI: 10.1016/j.compchemeng.2007.01.006.
- [101] W. T. Scott, “Analytic studies of cloud droplet coalescence i,” *Journal of the Atmospheric Sciences*, vol. 25, no. 1, pp. 54–65, 1968. DOI: 10.1175/1520-0469(1968)025<0054:ASOCDC>2.0.CO;2.
- [102] J. Solsvik and H. A. Jakobsen, “Solution of the dynamic population balance equation describing breakage–coalescence systems in agitated vessels: The least-squares method,” *The Canadian Journal of Chemical Engineering*, vol. 92, no. 2, pp. 266–287, 2014. DOI: 10.1002/cjce.21882.
- [103] R. M. Ziff and E. D. McGrady, “The kinetics of cluster fragmentation and depolymerisation,” *Journal of Physics A: Mathematical and General*, vol. 18, no. 15, pp. 3027–3037, 1985. DOI: 10.1088/0305-4470/18/15/026.
- [104] M. Lichti and H.-J. Bart, “Bubble size distributions with a shadowgraphic optical probe,” *Flow Measurement and Instrumentation*, vol. 60, pp. 164–170, 2018. DOI: 10.1016/j.flowmeasinst.2018.02.020.
- [105] M. Mickler and H.-J. Bart, “Optical multimode online probe: Detection and analysis of particle collectives,” *Chemie Ingenieur Technik*, vol. 85, no. 6, pp. 901–906, 2013. DOI: 10.1002/cite.201200139.
- [106] M. Laakkonen, V. Alopaeus, and J. Aittamaa, “Validation of bubble breakage, coalescence and mass transfer models for gas–liquid dispersion in agitated vessel,” *Chemical Engineering Science*, vol. 61, no. 1, pp. 218–228, 2006. DOI: 10.1016/j.ces.2004.11.066.
- [107] T. Hillen, I. E. Leonard, and H. van Roessel, *Partial differential equations: Theory and completely solved problems*. Hoboken, N.J.: Wiley, 2012, ISBN: 978-1-118-06330-9.
- [108] D. G. Duffy, *Transform methods for solving partial differential equations*, 2. ed. Boca Raton, Fla.: Chapman & Hall/CRC, 2004, ISBN: 978-1-58488-451-4. [Online]. Available: <http://www.loc.gov/catdir/enhancements/fy0646/2004049448-d.html>.
- [109] G. W. Griffiths, *Numerical analysis using R: Solutions to ODEs and PDEs*. Cambridge: Cambridge University Press, 2016, ISBN: 1-107-11561-2. DOI: 10.1017/CB09781316336069.

- [110] P. J. Davis and P. Rabinowitz, *Methods of numerical integration*, 2. ed., ser. Computer Science and applied mathematics. New York: Acad. Pr, 1984, ISBN: 978-0-12-206360-2. DOI: 10.1016/C2013-0-10566-1.
- [111] F. Moukalled, L. Mangani, and M. Darwish, *The Finite Volume Method in Computational Fluid Dynamics: An Advanced Introduction with OpenFOAM® and Matlab*, 1st ed. 2016, ser. Fluid Mechanics and Its Applications. Cham: Springer International Publishing, 2016, vol. 113, ISBN: 978-3-319-16874-6. DOI: 10.1007/978-3-319-16874-6.
- [112] S. Lu, Y. Wang, and Y. Wu, “Novel high-precision simulation technology for high-dynamics signal simulators based on piecewise hermite cubic interpolation,” *IEEE Transactions on Aerospace and Electronic Systems*, vol. 54, no. 5, pp. 2304–2317, 2018. DOI: 10.1109/TAES.2018.2814278.
- [113] J. Bezanson, A. Edelman, S. Karpinski, and V. B. Shah, “Julia: A fresh approach to numerical computing,” *SIAM Review*, vol. 59, no. 1, pp. 65–98, 2017. DOI: 10.1137/141000671.
- [114] M. Zlokarnik, *Stirring: Theory and practice*. Weinheim et al.: Wiley-VCH, 2001, ISBN: 978-3-527-29996-6.
- [115] M. Kraume, *Transportvorgänge in der Verfahrenstechnik*. Berlin, Heidelberg: Springer Berlin Heidelberg, 2012, ISBN: 978-3-642-25148-1. DOI: 10.1007/978-3-642-25149-8.
- [116] T. Moucha, V. Linek, and E. Prokopová, “Gas hold-up, mixing time and gas–liquid volumetric mass transfer coefficient of various multiple-impeller configurations: Rushton turbine, pitched blade and techmix impeller and their combinations,” *Chemical Engineering Science*, vol. 58, no. 9, pp. 1839–1846, 2003. DOI: 10.1016/S0009-2509(02)00682-6.
- [117] M. J. Prince and H. W. Blanch, “Bubble coalescence and break-up in air-sparged bubble columns,” *AIChE Journal*, vol. 36, no. 10, pp. 1485–1499, 1990. DOI: 10.1002/aic.690361004.
- [118] J. O. R.B. Diemer, “A moment methodology for coagulation and breakage problems: Part 3—generalized daughter distribution functions,” *Chemical Engineering Science*, vol. 57, no. 19, pp. 4187–4198, 2002. DOI: 10.1016/S0009-2509(02)00366-4.
- [119] A. K. Chester, “The modelling of coalescence processes in fluid-liquid dispersions : A review of current understanding,” *Chemical Engineering Research and Design*, vol. 69, pp. 259–270, 1991.
- [120] A. Bombač and I. Žun, “Individual impeller flooding in aerated vessel stirred by multiple-rushton impellers,” *Chemical Engineering Journal*, vol. 116, no. 2, pp. 85–95, 2006. DOI: 10.1016/j.cej.2005.10.009.
- [121] J. Solsvik, P. J. Becker, N. Sheibat-Othman, and H. A. Jakobsen, “Population balance model: Breakage kernel parameter estimation to emulsification data,” *The Canadian Journal of Chemical Engineering*, vol. 92, no. 6, pp. 1082–1099, 2014. DOI: 10.1002/cjce.21928.

- [122] F. Maluta, F. Alberini, A. Paglianti, and G. Montante, “Hydrodynamics, power consumption and bubble size distribution in gas-liquid stirred tanks,” *Chemical Engineering Research and Design*, vol. 194, pp. 582–596, 2023. DOI: 10.1016/j.cherd.2023.05.006.
- [123] M. M. Ribeiro, P. F. Regueiras, M. M. L. Guimarães, C. M. N. Madureira, and J. J. C. Cruz_Pinto, “Optimization of breakage and coalescence model parameters in a steady-state batch agitated dispersion,” *Industrial & Engineering Chemistry Research*, vol. 50, no. 4, pp. 2182–2191, 2011. DOI: 10.1021/ie100368t.
- [124] S. Garg and M. Pant, “Meshfree methods: A comprehensive review of applications,” *International Journal of Computational Methods*, vol. 15, no. 04, p. 1830001, 2018. DOI: 10.1142/S0219876218300015.
- [125] C. Martínez-Bazán, J. L. Montañés, and J. C. Lasheras, “On the breakup of an air bubble injected into a fully developed turbulent flow. part 1. breakup frequency,” *Journal of Fluid Mechanics*, vol. 401, pp. 157–182, 1999. DOI: 10.1017/S0022112099006680.
- [126] Eleni G. Chatzi, Asterios D. Gavrielides, Costas Kiparissides, “Generalized model for prediction of the steady-state drop size distributions in batch stirred vessels,” *Industrial & Engineering Chemistry Research*, vol. 28, pp. 1704–1711, 1989. DOI: 10.1021/ie00095a022.
- [127] F. Lehr, M. Millies, and D. Mewes, “Bubble-size distributions and flow fields in bubble columns,” *AIChE Journal*, vol. 48, no. 11, pp. 2426–2443, 2002. DOI: 10.1002/aic.690481103.
- [128] J. Baldyga and W. Podgórska, “Drop break-up in intermittent turbulence: Maximum stable and transient sizes of drops,” *The Canadian Journal of Chemical Engineering*, vol. 76, no. 3, pp. 456–470, 1998. DOI: 10.1002/cjce.5450760316.
- [129] H. K. Foroushan and H. A. Jakobsen, “Experimental study of single bubble breakage in turbulent flow field: Evaluation of breakage models,” *Chemical Engineering Science*, vol. 253, p. 117584, 2022. DOI: 10.1016/j.ces.2022.117584.
- [130] Y. Liao and D. Lucas, “A literature review of theoretical models for drop and bubble breakup in turbulent dispersions,” *Chemical Engineering Science*, vol. 64, no. 15, pp. 3389–3406, 2009. DOI: 10.1016/j.ces.2009.04.026.
- [131] Y. Liao and D. Lucas, “A literature review on mechanisms and models for the coalescence process of fluid particles,” *Chemical Engineering Science*, vol. 65, no. 10, pp. 2851–2864, 2010. DOI: 10.1016/j.ces.2010.02.020.
- [132] S. S. Alves, C. I. Maia, J. Vasconcelos, and A. J. Serralheiro, “Bubble size in aerated stirred tanks,” *Chemical Engineering Journal*, vol. 89, no. 1-3, pp. 109–117, 2002. DOI: 10.1016/S1385-8947(02)00008-6.
- [133] C. Tsouris and L. L. Tavlarides, “Breakage and coalescence models for drops in turbulent dispersions,” *AIChE Journal*, vol. 40, no. 3, pp. 395–406, 1994. DOI: 10.1002/aic.690400303.

- [134] R. S. Mahmood, A. A. Alsarayreh, and A. S. Abbas, "Measurement and analysis of bubble size distribution in the electrochemical stirred tank reactor," *Iraqi Journal of Chemical and Petroleum Engineering*, vol. 24, no. 1, pp. 27–31, 2023. DOI: 10.31699/IJCPE.2023.1.4.
- [135] M. Laakkonen, P. Moilanen, V. Alopaeus, and J. Aittamaa, "Modelling local bubble size distributions in agitated vessels," *Chemical Engineering Science*, vol. 62, no. 3, pp. 721–740, 2007. DOI: 10.1016/j.ces.2006.10.006.
- [136] S. Li, R. Yang, C. Wang, H. Han, S. Shen, and H. Wang, "Cfd-pbm simulation on bubble size distribution in a gas-liquid-solid flow three-phase flow stirred tank," *ACS omega*, vol. 7, no. 2, pp. 1934–1942, 2022. DOI: 10.1021/acsomega.1c05406.
- [137] M. Barigou and M. Greaves, "Bubble-size distributions in a mechanically agitated gas—liquid contactor," *Chemical Engineering Science*, vol. 47, no. 8, pp. 2009–2025, 1992. DOI: 10.1016/0009-2509(92)80318-7.
- [138] T. O. Oolman and H. W. Blanch, "Bubble coalescence in air-sparged bioreactors," *Biotechnology and bioengineering*, vol. 28, no. 4, pp. 578–584, 1986. DOI: 10.1002/bit.260280415.
- [139] I. E. Idel chik, *Handbook of hydraulic resistance*, 4th ed. Redding CT: Begell House, 2007, ISBN: 978-1-56700-251-5.
- [140] Z. Borka and H. A. Jakobsen, "Least squares higher order method for the solution of a combined multifluid-population balance model: Modeling and implementation issues," *Procedia Engineering*, vol. 42, pp. 1121–1132, 2012. DOI: 10.1016/j.proeng.2012.07.504.
- [141] A. Tomiyama, "Struggle with computational bubble dynamics," *Multiphase Science and Technology*, vol. 10, no. 4, pp. 369–405, 1998. DOI: 10.1615/MultScienTechn.v10.i4.40.
- [142] Z. Zhu, C. A. Dorao, D. Lucas, and H. A. Jakobsen, "On the coupled solution of a combined population balance model using the least-squares spectral element method," *Industrial & Engineering Chemistry Research*, vol. 48, no. 17, pp. 7994–8006, 2009. DOI: 10.1021/ie900088q.
- [143] I. S. Khattab, F. Bandarkar, M. A. A. Fakhree, and A. Jouyban, "Density, viscosity, and surface tension of water+ethanol mixtures from 293 to 323k," *Korean Journal of Chemical Engineering*, vol. 29, no. 6, pp. 812–817, 2012. DOI: 10.1007/s11814-011-0239-6.
- [144] K. Takamura, H. Fischer, and N. R. Morrow, "Physical properties of aqueous glycerol solutions," *Journal of Petroleum Science and Engineering*, vol. 98-99, pp. 50–60, 2012. DOI: 10.1016/j.petrol.2012.09.003.
- [145] M. Laliberté, "Model for calculating the viscosity of aqueous solutions," *Journal of Chemical & Engineering Data*, vol. 52, no. 2, pp. 321–335, 2007. DOI: 10.1021/je0604075.

- [146] M. Laliberté and W. E. Cooper, “Model for calculating the density of aqueous electrolyte solutions,” *Journal of Chemical & Engineering Data*, vol. 49, no. 5, pp. 1141–1151, 2004. DOI: 10.1021/je0498659.
- [147] M. Sadeghi, V. Taghikhani, and C. Ghotbi, “Measurement and correlation of surface tension for single aqueous electrolyte solutions,” *International Journal of Thermophysics*, vol. 31, no. 4-5, pp. 852–859, 2010. DOI: 10.1007/s10765-010-0725-9.
- [148] V. Cappello, C. Plais, C. Vial, and F. Augier, “Bubble size and liquid-side mass transfer coefficient measurements in aerated stirred tank reactors with non-newtonian liquids,” *Chemical Engineering Science*, vol. 211, p. 115280, 2020. DOI: 10.1016/j.ces.2019.115280.
- [149] T. Kracík and T. Moucha, “Influence of viscosity on gas holdup formation in stirred tank reactors,” *Chemical Papers*, vol. 76, no. 1, pp. 301–307, 2022. DOI: 10.1007/s11696-021-01857-8.
- [150] D. Pinelli and F. Magelli, “Analysis of the fluid dynamic behavior of the liquid and gas phases in reactors stirred with multiple hydrofoil impellers,” *Industrial & Engineering Chemistry Research*, vol. 39, no. 9, p. 3211, 2000. DOI: 10.1021/ie991088w.
- [151] M. Nocentini, D. Fajner, G. Pasquali, and F. Magelli, “Gas-liquid mass transfer and holdup in vessels stirred with multiple rushton turbines: Water and water-glycerol solutions,” *Industrial & Engineering Chemistry Research*, vol. 32, no. 1, pp. 19–26, 1993. DOI: 10.1021/ie00013a003.
- [152] V. Machon, A. W. Pacek, and A. W. Nienow, “Bubble sizes in electrolyte and alcohol solutions in a turbulent stirred vessel,” *Chemical Engineering Research and Design*, vol. 75, no. 3, pp. 339–348, 1997. DOI: 10.1205/026387697523651.
- [153] P. Rollbusch, M. Becker, M. Ludwig, A. Bieberle, M. Grünwald, U. Hampel, and R. Franke, “Experimental investigation of the influence of column scale, gas density and liquid properties on gas holdup in bubble columns,” *International Journal of Multiphase Flow*, vol. 75, pp. 88–106, 2015. DOI: 10.1016/j.ijmultiphaseflow.2015.05.009.
- [154] D. Laupsien, C. Le Men, A. Cockx, and A. Liné, “Effects of liquid viscosity and bubble size distribution on bubble plume hydrodynamics,” *Chemical Engineering Research and Design*, vol. 180, pp. 451–469, 2022. DOI: 10.1016/j.cherd.2021.09.025.
- [155] P. Zahedi, R. Saleh, R. Moreno-Atanasio, and K. Yousefi, “Influence of fluid properties on bubble formation, detachment, rising and collapse; investigation using volume of fluid method,” *Korean Journal of Chemical Engineering*, vol. 31, no. 8, pp. 1349–1361, 2014. DOI: 10.1007/s11814-014-0063-x.
- [156] P. M. Wilkinson, A. van Schayk, J. P. Spronken, and L. L. van Dierendonck, “The influence of gas density and liquid properties on bubble breakup,” *Chemical Engineering Science*, vol. 48, no. 7, pp. 1213–1226, 1993. DOI: 10.1016/0009-2509(93)81003-E.
- [157] H. Zhang, Y. Wang, A. Sayyar, and T. Wang, “Experimental study on breakup of a single bubble in a stirred tank: Effect of gas density and liquid properties,” *AIChE Journal*, vol. 69, no. 1, 2023. DOI: 10.1002/aic.17511.

- [158] K. Hecht, O. Bey, J. Ettmüller, P. Graefen, R. Friehmelt, and M. Nilles, “Effect of gas density on gas holdup in bubble columns,” *Chemie Ingenieur Technik*, vol. 87, no. 6, pp. 762–772, 2015. DOI: 10.1002/cite.201500010.
- [159] R. Parthasarathy and N. Ahmed, “Bubble size distribution in a gas sparged vessel agitated by a rushton turbine,” *Industrial & Engineering Chemistry Research*, vol. 33, no. 3, pp. 703–711, 1994. DOI: 10.1021/ie00027a032.
- [160] A. V. Kulkarni and J. B. Joshi, “Design and selection of sparger for bubble column reactor. part i: Performance of different spargers,” *Chemical Engineering Research and Design*, vol. 89, no. 10, pp. 1972–1985, 2011. DOI: 10.1016/j.cherd.2011.01.004.
- [161] D. D. McClure, C. Wang, J. M. Kavanagh, D. F. Fletcher, and G. W. Barton, “Experimental investigation into the impact of sparger design on bubble columns at high superficial velocities,” *Chemical Engineering Research and Design*, vol. 106, pp. 205–213, 2016. DOI: 10.1016/j.cherd.2015.12.027.
- [162] S. Whitaker, *The Method of Volume Averaging*, 1st ed. Dordrecht: Springer, Nov. 1999, ISBN: 978-0-7923-5486-4. DOI: 10.1007/978-94-017-3389-2.
- [163] B. van Leer, “Towards the ultimate conservative difference scheme. v. a second-order sequel to godunov’s method,” *Journal of Computational Physics*, vol. 32, no. 1, pp. 101–136, 1979. DOI: 10.1016/0021-9991(79)90145-1.
- [164] B. van Leer, “Towards the ultimate conservative difference scheme. ii. monotonicity and conservation combined in a second-order scheme,” *Journal of Computational Physics*, vol. 14, no. 4, pp. 361–370, 1974. DOI: 10.1016/0021-9991(74)90019-9.
- [165] A. C. Hindmarsh, P. N. Brown, K. E. Grant, S. L. Lee, R. Serban, D. E. Shumaker, and C. S. Woodward, “Sundials: Suite of nonlinear and differential/algebraic equation solvers,” *ACM Transactions on Mathematical Software*, vol. 31, no. 3, pp. 363–396, 2005. DOI: 10.1145/1089014.1089020.
- [166] D. J. Gardner, D. R. Reynolds, C. S. Woodward, and C. J. Balos, “Enabling new flexibility in the sundials suite of nonlinear and differential/algebraic equation solvers,” *ACM Transactions on Mathematical Software*, 2022. DOI: 10.1145/3539801.
- [167] V. K. Dixit and C. Rackauckas, *Optimization.jl: A unified optimization package*, 2023. DOI: 10.5281/zenodo.7738525.
- [168] C. Rackauckas, Y. Ma, J. Martensen, C. Warner, K. Zubov, R. Supekar, D. Skinner, A. Ramadhan, and A. Edelman, “Universal differential equations for scientific machine learning,” *Preprint, Research Square*, 2021. DOI: 10.21203/rs.3.rs-55125/v1.
- [169] P. K Mogensen and A. N Riseth, “Optim: A mathematical optimization package for julia,” *Journal of Open Source Software*, vol. 3, no. 24, p. 615, 2018. DOI: 10.21105/joss.00615.
- [170] L. Allen, A. O’Connell, and V. Kiermer, “How can we ensure visibility and diversity in research contributions? how the contributor role taxonomy (credit) is helping the shift from authorship to contributorship,” *Learned Publishing*, vol. 32, no. 1, pp. 71–74, 2019. DOI: 10.1002/leap.1210.

A. Supplementary Information for Chapter 2

A.1. Parameter Applied in the Simulation Studies

A.1.1. Constant Parameters

Tab. A.1 summarizes constant parameters applied in the simulations: property data, reactor geometry and process conditions.

Table A.1.: Left: Property data applied in the simulations. Center: Constant reactor geometry parameter. Right: Constant process conditions.

| <i>Property data</i> | | | <i>Reactor geometry</i> | | | <i>Process conditions</i> | | |
|----------------------|--------------------------------|--------------------|-------------------------|----------------|-------|---------------------------|--------------------------------|--------------------|
| Parameter | Unit | Value | Parameter | Unit | Value | Parameter | Unit | Value |
| ρ_l | kg m ⁻³ | 1000 | V_R | m ³ | 3.12 | f_s | - | 1.1 |
| ρ_g | kg m ⁻³ | 8.17 | V_{ER} | m ³ | 0.2 | p_0 | bar | 11.11 |
| M_A | kg kmol ⁻¹ | 40 | ζ_N | - | 1.08 | $V_{l,feed}$ | m ³ s ⁻¹ | 1×10^{-4} |
| M_B | kg kmol ⁻¹ | 28 | d_s | m | 0.002 | | | |
| $\nu_{A,I}$ | - | -1 | h_{BS} | m | 1.50 | | | |
| $\nu_{B,I}$ | - | -1 | h_{HS} | m | 0.80 | | | |
| ν_l | m ² s ⁻¹ | 1×10^{-6} | h_{BR} | m | 0.25 | | | |
| | | | h_{HR} | m | 0.35 | | | |

Where, ν_l is the kinematic viscosity of the liquid phase and d_s is the wall thickness of the draft tube.

A.1.2. Parameters Study I

Tab. A.2 summarizes the applied parameters of study I.

Table A.2.: Applied parameters of study I.

| Parameter | Unit | Values/Range |
|--------------|--------------------|------------------|
| f_r | - | 1.0 |
| k_I | s ⁻¹ | [0,2] |
| φ | kW m ⁻³ | (1.13,1.70,4.00) |
| d_N | cm | 2.5 |
| d_R | m | 0.70 |
| d_{DT} | m | 0.35 |
| h_R | m | 8.1 |
| h_{DT} | m | 6.0 |
| d_{DT}/d_R | - | 0.5 |
| h_R/d_R | - | 11.6 |

A.1.3. Parameters Study II

Tab. A.3 summarizes the applied parameters of study II where the diameter ratio is varied.

Table A.3.: Applied parameters of study II where the diameter ratio is varied.

| Parameter | Unit | Values/Range |
|----------------|--------------|----------------|
| f_r | - | 1.0 |
| k_I | s^{-1} | (0.0,0.2,2.0) |
| φ | $kW m^{-3}$ | (1.13,1.7,4.0) |
| \dot{V}_{ER} | $m^3 s^{-1}$ | 0.0177 |
| d_R | m | 0.7 |
| d_{DT} | m | [0.12,0.37] |
| h_R | m | 8.1 |
| h_{DT} | m | 6.0 |
| d_{DT}/d_R | - | [0.175,0.525] |
| h_R/d_R | - | 11.6 |

Tab. A.4 summarizes the applied parameters of study II where the slenderness ratio is varied.

Table A.4.: Applied parameters of study II where the slenderness ratio is varied.

| Parameter | Unit | Values/Range |
|----------------|--------------|----------------|
| f_r | - | 1.0 |
| k_I | s^{-1} | (0.0,0.2,2.0) |
| φ | $kW m^{-3}$ | (1.13,1.7,4.0) |
| \dot{V}_{ER} | $m^3 s^{-1}$ | 0.0177 |
| d_R | m | Eq. (A.1) |
| d_{DT} | m | Eq. (A.2) |
| h_R | m | Eq. (A.3) |
| h_{DT} | m | Eq. (A.4) |
| d_{DT}/d_R | - | 0.5 |
| h_R/d_R | - | [7,15] |

To keep the reactor volume constant, the Eq. (A.1) - Eq. (A.4) are applied.

$$d_R = \left(\frac{V_R}{\frac{\pi}{4} \frac{h_R}{d_R}} \right)^{1/3} \quad (A.1)$$

$$d_{DT} = \frac{d_{DT}}{d_R} d_R \quad (A.2)$$

$$h_R = \frac{h_R}{d_R} d_R \quad (A.3)$$

$$h_{DT} = h_R - h_{BR} - h_{BS} - h_{HS} \quad (A.4)$$

A.1.4. Parameters Study III

Tab. A.5 summarizes the applied parameters of study III.

Table A.5.: Applied parameters of study III.

| Parameter | Unit | Values/Range |
|----------------|--------------|----------------|
| f_r | - | (0, 7] |
| k_I | s^{-1} | (0,0.2,2) |
| φ | $kW m^{-3}$ | (1.13,1.7,4.0) |
| \dot{V}_{ER} | $m^3 s^{-1}$ | 0.0177 |
| d_R | m | 0.7 |
| d_{DT} | m | (0.21,0.35) |
| h_R | m | 8.1 |
| h_{DT} | m | 6.0 |
| d_{DT}/d_R | - | (0.3,0.5) |
| h_R/d_R | - | 11.6 |

A.2. Modeling Details

A.2.1. Pressure Loss Coefficient

The pressure loss coefficient ζ within compartments DT and AG are calculated according to Idel chik [139] with:

$$\zeta_i = \lambda \frac{z}{d_i} \quad \text{for } i \in \{\text{DT}, \text{AG}\} \quad (\text{A.5})$$

where λ is the Darcy friction factor, which is computed using Eq. (A.6).

$$\lambda = \begin{cases} 64/Re & Re \leq 3200 \\ 0.03 & Re > 3200 \end{cases} \quad (\text{A.6})$$

Here, Re is the Reynolds number which is defined by:

$$Re_i = \frac{u_1 d_i}{\nu_1} \quad \text{for } i \in \{\text{DT}, \text{AG}\} \quad (\text{A.7})$$

For compartment DT, the pipe diameter d_{DT} is equal to the hydraulic diameter because it is a cylindrical pipe. For compartment AG, the hydraulic diameter of the circular section is calculated according to Eq. (A.8).

$$d_{\text{AG}} = d_{\text{R}} - d_{\text{DT}} - 2 d_{\text{s}} \quad (\text{A.8})$$

An additional pressure loss occurs during the transition from compartment DT to AG and vice versa due to the flow redirection. The pressure loss coefficient in JLR was intensively investigated by Zehner [41] and resulted into the applied formulas:

$$\zeta_{\text{DT} \rightarrow \text{AG}} = 1.8 a_{\text{DT}} + 3.0 \left(\frac{a_{\text{DT}}}{a_{\text{AG}}} \right) \exp\left(-100 \frac{d_{\text{s}}}{d_{\text{R}}}\right) \quad (\text{A.9})$$

$$\zeta_{\text{AG} \rightarrow \text{DT}} = 3.6 a_{\text{DT}} + 1.5 \left(\frac{a_{\text{DT}}}{a_{\text{AG}}} \right) \exp\left(-50 \frac{d_{\text{s}}}{d_{\text{R}}}\right) \quad (\text{A.10})$$

where, a_i is the ratio of the cross-sectional area of the compartment i to the cross-sectional area of the reactor (see Eq. (A.11)) and d_{R} is the diameter of the reactor.

$$a_i = \frac{A_i}{A_{\text{R}}} \quad \text{for } i \in \{\text{DT}, \text{AG}\} \quad (\text{A.11})$$

Here, A_{R} is the cross-sectional area of the reactor.

A.2.2. Ideal Reactor Models

In following sections the plug flow reactor model (PFR) and the continuous stirred tank reactor (CSTR) model for the calculation of the concentrations present in the compartments are presented. A detailed derivation of the subsequent equations can be found in Octave Levenspiel [42].

Plug Flow Reactor Model

Based on the plug flow model, the Eq. (A.12) describing the propagation of the concentration of species A can be derived under additional assumptions: isothermal conditions (k_I is constant), single, irreversible reaction of first-order.

$$c_{1,A,i} = c_{1,A,IN,i} \exp(-Da_i) \quad (\text{A.12})$$

Here $c_{1,A,IN,i}$ is the molar concentration of species A at the respective inlet of the compartment i , Da_i is the first-order Damköhler number of the compartment i .

Applying the Eq. (A.12) to the compartments results in the following equations. Thereby it is assumed that the concentration at the outlet of compartment DT is the same as the inlet of compartment AG.

$$c_{1,A,DT} = c_{1,A,DT,IN} \exp(-Da_{DT}) \quad (\text{A.13})$$

$$c_{1,A,AG} = c_{1,A,DT,OUT} \exp(-Da_{AG}) \quad (\text{A.14})$$

$$c_{1,A,ER} = c_{1,A,BS} \exp(-Da_{ER}) \quad (\text{A.15})$$

with

$$c_{1,A,AG,IN} = c_{1,A,DT,OUT} \quad (\text{A.16})$$

Continuous Stirred Tank Reactor Model

Based on the continuous stirred tank reactor model, the Eq. (A.17) describing the molar concentration of species A in the liquid phase can be derived by assuming the same additional assumptions as in Section A.2.2.

$$c_{1,A,i} = c_{1,A,IN,i} \frac{1}{1 + Da_i} \quad (\text{A.17})$$

If the Eq. (A.17) is applied to the compartment BS, it follows:

$$c_{1,A,BS} = c_{1,A,DT,OUT} \frac{1}{1 + Da_{BS}} \quad (\text{A.18})$$

A.2.3. Inlet Conditions Draft Tube

Concentration of Species A

To calculate the concentration at the inlet of the draft tube, it is assumed that the incoming flows ($\dot{V}_{1,feed}$, $\dot{V}_{1,AG}$, \dot{V}_{ER}) are instantaneously mixed with each other and no reaction takes place. From the mass and species balance it follows:

$$c_{1,A,DT,IN} = \frac{\dot{V}_{1,feed} \frac{\rho_1}{M_A}}{\dot{V}_{1,DT,IN} - \dot{V}_{1,AG} \exp(-(\overline{Da}_{AG} + \overline{Da}_{DT})) - \dot{V}_{ER} \frac{\exp(-\overline{Da}_{DT})}{1 + Da_{BS}}} \quad (\text{A.19})$$

Here, \overline{Da}_i is the integral Damköhler number of the compartment i .

Velocity of the Liquid Phase

To determine the velocity of the liquid phase at the inlet of the draft tube, a momentum flow balance is drawn around an infinitely small control volume (see Eq. (A.20)). Where the momentum flow of the liquid feed was neglected.

$$\dot{V}_{1,DT,IN} u_{1,DT,IN} = \dot{V}_{ER} u_{1,ER} + \dot{V}_{1,AG} u_{1,AG,DT,IN} - \frac{\zeta_{AG \rightarrow DT}}{2} A_{DT} u_{1,DT,IN}^2 \quad (A.20)$$

Here $u_{1,AG,DT,IN}$ is a fictive velocity of the liquid phase of the volume flow coming from the annular gap into the draft tube. This volume flow is not related to the entire cross-sectional area of the draft tube, but to the annulus created by the nozzle mouth area. The Eq. (A.21) is used to calculate this fictive velocity.

$$u_{1,AG,DT,IN} = \frac{u_{1,AG,OUT} A_{AG}}{A_{DT,IN}} \quad (A.21)$$

Where the cross-sectional area of the draft tube inlet is defined as:

$$A_{DT,IN} = A_{DT} - A_N \quad (A.22)$$

A.2.4. Damköhler Number

The first-order Damköhler number describes the ratio of the rate constant of the reaction to the rate constant of the convective mass transport. It could be shown that:

$$Da_i(z) = k_I \tau_i(z) \quad (A.23)$$

is valid. Here, $\tau(z)$ is the residence time in the compartment i . The integral Damköhler number of the compartment i is calculated as follow:

$$\overline{Da}_i = \frac{1}{h_i} \int_0^{h_i} Da_i(z) dz \quad (A.24)$$

A.2.5. Residence Behavior

The residence time in compartment i describes the ratio between reaction volume and volume flow rate through the reaction volume. The volume flow rate of the liquid phase in the different compartments are calculated as follows. In addition the equations for $\dot{V}_{1,product}$ and $\dot{V}_{g,purge}$ are given.

$$\dot{V}_{1,DT,IN} = \dot{V}_{1,N} + \dot{V}_{1,feed} + \dot{V}_{1,AG} \quad (A.25)$$

$$\dot{V}_{1,DT} = \dot{V}_{1,DT,IN} \quad (A.26)$$

$$\dot{V}_{1,BS} = \dot{V}_{1,N} + \dot{V}_{1,feed} \quad (A.27)$$

$$\dot{V}_{1,product} = \dot{V}_{1,feed} \quad (A.28)$$

$$\dot{V}_{g,purge} = \dot{V}_{g,feed} (f_s - 1) \quad (A.29)$$

Using this the residence time in the different compartments results in:

$$\tau_{\text{DT}}(z) = \alpha_{1,\text{DT}}(z) \frac{V_{\text{DT}}(z)}{\dot{V}_{1,\text{DT}}} \quad (\text{A.30})$$

$$\tau_{\text{BS}} = \frac{V_{\text{BS}}}{\dot{V}_{\text{BS}}} \quad (\text{A.31})$$

$$\tau_{\text{AG}}(z) = \alpha_{1,\text{AG}}(z) \frac{V_{\text{AG}}(z)}{\dot{V}_{1,\text{AG}}} \quad (\text{A.32})$$

$$\tau_{\text{ER}} = \frac{V_{\text{ER}}}{\dot{V}_{1,\text{ER}}} \quad (\text{A.33})$$

where V_i is the reaction volume in compartment i , which are summarized in Eq. (A.34) - Eq. (A.36).

$$V_{\text{DT}}(z) = A_{\text{DT}} z \quad (\text{A.34})$$

$$V_{\text{BS}} = A_{\text{BS}} h_{\text{BS}} \quad (\text{A.35})$$

$$V_{\text{AG}}(z) = A_{\text{AG}} z \quad (\text{A.36})$$

The occurring cross-sectional areas A_i in Eq. (A.22) and Eq. (A.34) - Eq. (A.36) are calculated according to the following equations:

$$A_{\text{R}} = \frac{\pi}{4} d_{\text{R}}^2 \quad (\text{A.37})$$

$$A_{\text{N}} = \frac{\pi}{4} d_{\text{N}}^2 \quad (\text{A.38})$$

$$A_{\text{DT}} = \frac{\pi}{4} d_{\text{DT}}^2 \quad (\text{A.39})$$

$$A_{\text{BS}} = A_{\text{R}} \quad (\text{A.40})$$

$$A_{\text{AG}} = A_{\text{R}} - A_{\text{DT}} - \pi d_{\text{DT}} d_{\text{s}} \quad (\text{A.41})$$

A.3. Additional Figures

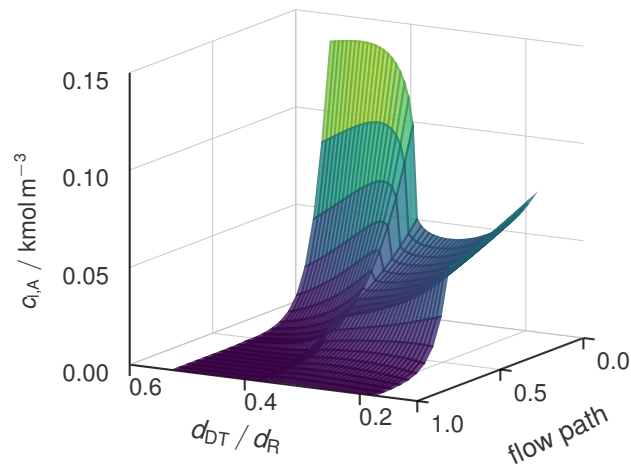


Figure A.1.: Molar concentration of species A in the liquid phase $c_{l,A}$ as a function of the diameter ratio d_{DT}/d_R and the normalized flow path using the parameters specified in Tab. A.1 and Tab. A.3 with $k_I = 0.2 \text{ s}^{-1}$ where the reactor volume where kept constant.

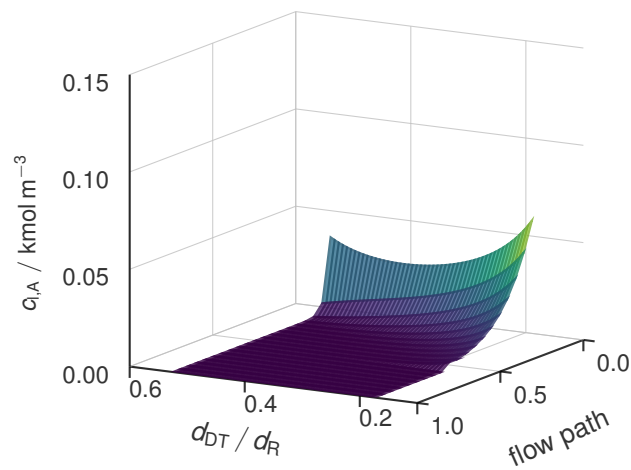


Figure A.2.: Molar concentration of species A in the liquid phase $c_{l,A}$ as a function of the diameter ratio d_{DT}/d_R and the normalized flow path using the parameters specified Tab. A.1 and Tab. A.3 with $k_I = 2.0 \text{ s}^{-1}$ where the reactor volume where kept constant.

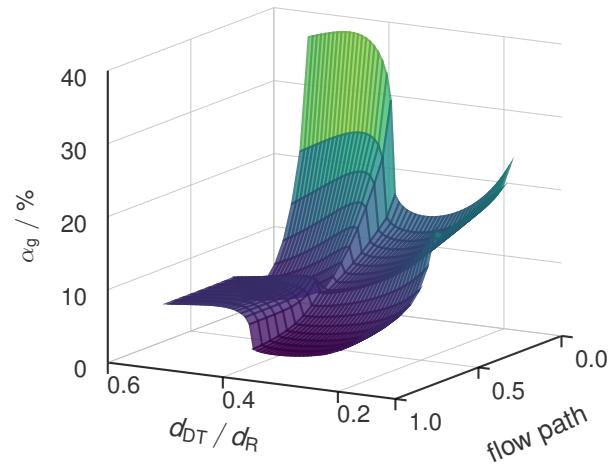


Figure A.3.: Gas volume fraction α_g as a function of the diameter ratio d_{DT}/d_R and the normalized flow path using the parameters specified in Tab. A.1 and Tab. A.3 with $k_I = 0.2 \text{ s}^{-1}$ where the reactor volume where kept constant.

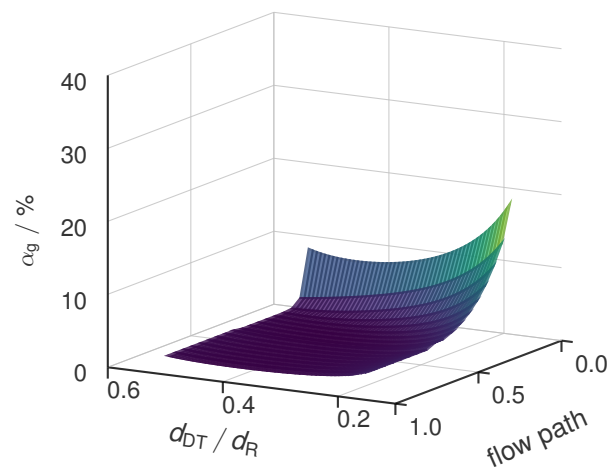


Figure A.4.: Gas volume fraction α_g as a function of the diameter ratio d_{DT}/d_R and the normalized flow path using the parameters specified in Tab. A.1 and Tab. A.3 with $k_I = 2.0 \text{ s}^{-1}$ where the reactor volume where kept constant.

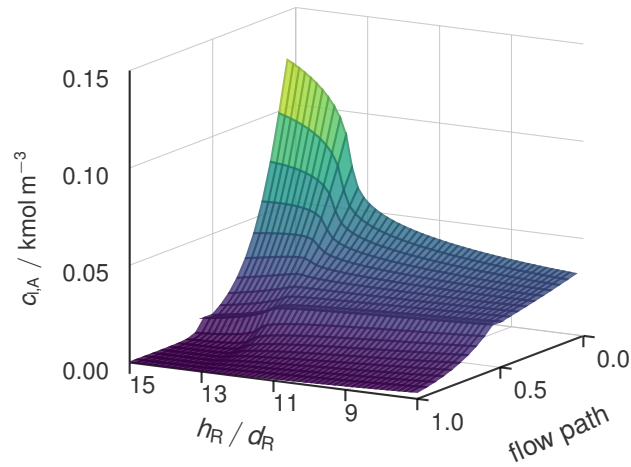


Figure A.5.: Molar concentration of A in the liquid phase $c_{l,A}$ as a function of the slenderness ratio h_R/d_R and the normalized flow path using the parameters specified in Tab. A.1 and Tab. A.4 with $k_l = 0.2 \text{ s}^{-1}$ whereby the diameter ratio $d_{DT}/d_R = 0.5$ and the reactor volume were kept constant.

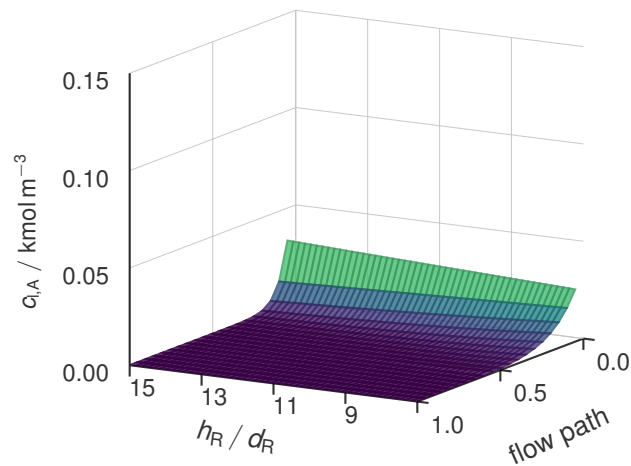


Figure A.6.: Molar concentration of A in the liquid phase $c_{l,A}$ as a function of the slenderness ratio h_R/d_R and the normalized flow path using the parameters specified in Tab. A.1 and Tab. A.4 with $k_l = 2.0 \text{ s}^{-1}$ whereby the diameter ratio $d_{DT}/d_R = 0.5$ and the reactor volume were kept constant.

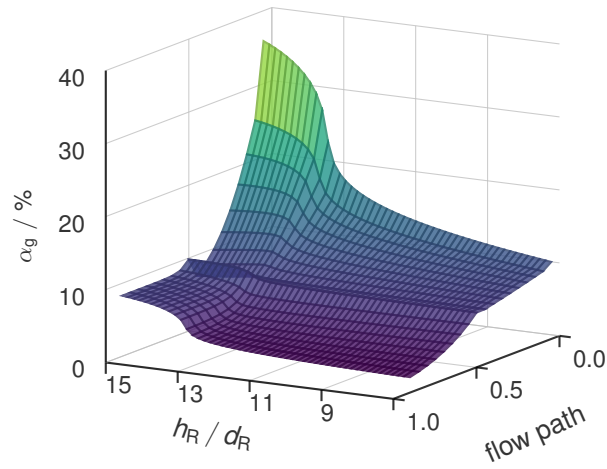


Figure A.7.: Gas volume fraction α_g as a function of the slenderness ratio h_R/d_R and the normalized flow path using the parameters specified in Tab. A.1 and Tab. A.4 with $k_I = 0.2 \text{ s}^{-1}$ whereby the diameter ratio $d_{DT}/d_R = 0.5$ and the reactor volume were kept constant.

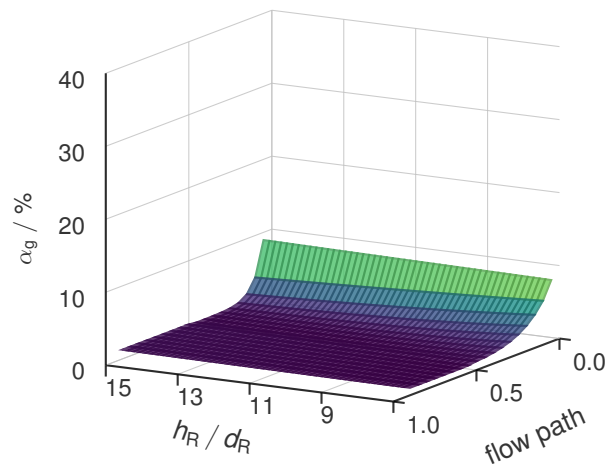


Figure A.8.: Gas volume fraction α_g as a function of the slenderness ratio h_R/d_R and the normalized flow path using the parameters specified in Tab. A.1 and Tab. A.4 with $k_I = 2.0 \text{ s}^{-1}$ whereby the diameter ratio $d_{DT}/d_R = 0.5$ and the reactor volume were kept constant.

A.4. Implementation Details

Fig. A.9 shows a flowchart of the solution procedure. On average, a single simulation takes less than a minute on an office notebook (CPU: AMD Ryzen 7 PRO4750 U with max. 4.1 GHz; RAM: 16 GB with 3200 MHz).

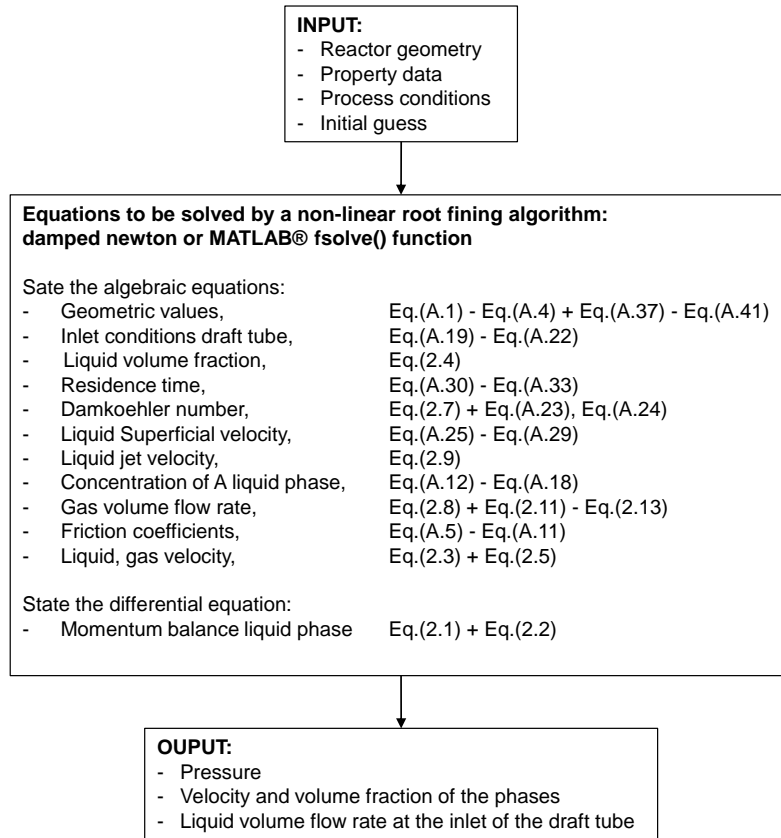


Figure A.9.: Flowchart of the solution procedure.

B. Supplementary Information for Chapter 3

B.1. Overview Experimental Data

Tab. B.1 summarizes all performed experiments. The corresponding experimental data can be taken from [51].

Table B.1.: Overview of the performed experiments. Full data available at [51].

| s | $c_s / \text{g L}^{-1}$ | j_d / cm^{-1} | h_c / m | $z_{\text{exp}} / \text{cm}$ | Sum |
|---------------------------------|---|------------------------------|------------------|---|------------|
| EtOH | 0.007, 0.012, 0.062, 0.125, 0.249, 0.373, 0.933 | 1.0, 2.0, 3.0, 3.5, 4.0, | 1.8 | 35, 120, 175 | 105 |
| NaCl | 3.58, 6.27, 8.95, 17.9, 35.8, 71.6 | 1.0, 2.0, 3.0, 4.0, | 1.8 | 30, 111.5, 180 | 72 |
| Na ₂ SO ₃ | 0.73, 2.2, 5.5, 11.0, 22.0 | 1.0, 2.0, 3.0, 3.5, 4.0, 4.5 | 1.8 | 35, 120, 175 | 90 |
| Gly | 4.998, 155.7, 25.12, 323.4, 76.36, 503.0, 694.6 | 1.0, 2.0, 3.0, 3.5, 4.0, | 1.8 | 35, 120, 175 | 105 |
| none | - | 1.0, 2.0, 3.0, 4.0 | 0.6 | 20, 30, 40, 50, 60 | 20 |
| none | - | 1.0, 2.0, 3.0, 4.0 | 0.8 | 20, 30, 40, 50, 60, 80 | 24 |
| none | - | 1.0, 2.0, 3.0, 4.0 | 1.0 | 20, 30, 40, 50, 60, 80, 105 | 27 |
| none | - | 1.0, 2.0, 3.0, 4.0 | 1.2 | 20, 30, 40, 50, 60, 80, 105, 120 | 32 |
| none | - | 1.0, 2.0, 3.0, 4.0 | 1.4 | 20, 30, 40, 50, 60, 80, 105, 120, 140 | 36 |
| none | - | 1.0, 2.0, 3.0, 4.0 | 1.6 | 20, 30, 40, 50, 60, 80, 105, 120, 140, 160 | 40 |
| none | - | 1.0, 2.0, 3.0, 4.0 | 1.8 | 20, 30, 40, 50, 60, 80, 105, 120, 140, 160, 180 | 44 |
| Overall experiments | | | | | 595 |

B.2. Constitutive and Additional Equations

In order to close, the model presented in Section 3.3 in Chapter 3 the following constitutive equations are applied:

Sources and sinks of the PBE [16, 26, 140]:

$$\dot{\xi}(\xi, z) = -\frac{\xi u_d(\xi, z)}{3\rho_d(z)} \frac{\partial \rho_d(z)}{\partial z} \quad (\text{B.1})$$

$$\dot{\xi}(\xi_{\min}, z) = \dot{\xi}(\xi_{\max}, z) = 0 \quad (\text{B.2})$$

$$B_D(\xi, z) = H\left(\xi - (2\xi_{\min}^3)^{1/3}\right) b(\xi) f_d^m(\xi, z) \quad (\text{B.3})$$

$$B_B(\xi, z) = H\left((\xi_{\max}^3 - \xi_{\min}^3)^{1/3} - \xi\right) \rho_d(z) V(\xi) \int_{\xi}^{\xi_{\max}} \nu P(\xi, \zeta) b(\zeta) \frac{f_d^m(\zeta, z)}{\rho_d(z) V(\zeta)} d\zeta \quad (\text{B.4})$$

$$C_D(\xi, z) = H\left((\xi_{\max}^3 - \xi_{\min}^3)^{1/3} - \xi\right) f_d^m(\xi, z) \int_{\xi_{\min}}^{(\xi_{\max}^3 - \xi^3)^{1/3}} c(\xi, \zeta) \frac{f_d^m(\zeta, z)}{\rho_d(z) V(\zeta)} d\zeta \quad (\text{B.5})$$

$$C_B(\xi, z) = H\left(\xi - (2\xi_{\min}^3)^{1/3}\right) \frac{\xi^2 \rho_d(z) V(\xi)}{2} \int_{\xi_{\min}}^{(\xi^3 - \xi_{\min}^3)^{1/3}} \frac{c([\xi^3 - \zeta^3]^{1/3}, \zeta)}{(\xi^3 - \zeta^3)^{2/3}} \frac{f_d^m(\zeta, z)}{\rho_d(z) V(\zeta)} \frac{f_d^m([\xi^3 - \zeta^3]^{1/3}, z)}{\rho_d(z) V([\xi^3 - \zeta^3]^{1/3})} d\zeta \quad (\text{B.6})$$

Ideal gas law:

$$\rho_d(z) = \rho_d^0 \frac{p(z)}{p^0} \quad (\text{B.7})$$

Volume of a sphere:

$$V(\xi) = \frac{\pi}{6} \xi^3 \quad (\text{B.8})$$

Volume fraction constrain:

$$\alpha_c(z) = 1 - \alpha_d(z) \quad (\text{B.9})$$

$$\alpha_d(z) = \int_{\xi_{\min}}^{\xi_{\max}} \frac{f_d^m(\xi, z)}{\rho_d(z)} d\xi \quad (\text{B.10})$$

Coalescence kernel [53]:

$$h(\xi, \zeta) = C_1 \frac{\varepsilon^{1/3}}{1 + \alpha_d(z)} (\xi + \zeta)^2 \sqrt{\xi^{2/3} + \zeta^{2/3}} \quad (\text{B.11})$$

$$\lambda(\zeta) = \exp\left(-C_2 \frac{\mu_c \rho_c \varepsilon}{\sigma(1 + \alpha_d(z))^3} \left(\frac{\xi \zeta}{\xi + \zeta}\right)^4\right) \quad (\text{B.12})$$

$$c(\xi, \zeta) = h(\xi, \zeta) \lambda(\zeta) \quad (\text{B.13})$$

Breakage kernel [53]:

$$b(\xi) = C_3 \frac{\varepsilon^{1/3}}{\xi^{2/3}} \exp\left(-\frac{\sigma C_4}{\rho_c \varepsilon^{2/3} \xi^{5/3}}\right) \quad (\text{B.14})$$

$$P(\xi, \zeta) = \frac{2.4 \left(\frac{\pi}{2} \xi^2\right)}{V(\zeta)} \exp\left(-4.5 \frac{(2V(\xi) - V(\zeta))^2}{V(\zeta)^2}\right) \quad (\text{B.15})$$

$$\nu = 2.0 \quad (\text{B.16})$$

Turbulent energy dissipation rate [54]:

$$\varepsilon = j_d(z_{\min})g \quad (\text{B.17})$$

Momentum transfer [16, 140–142]:

$$m_d(\xi, z) = -\frac{3}{4\xi} \frac{\rho_c C^D(\xi, z) f_d^m(\xi, z)}{\rho_d(z)} (u_d(\xi, z) - u_c(z)) |u_d(\xi, z) - u_c(z)| \quad (\text{B.18})$$

$$M_c(z) = F_c^W(z) - \int_{\xi_{\min}}^{\xi_{\max}} m_d(\xi, z) d\xi \quad (\text{B.19})$$

$$F_c^W(z) = -\frac{\alpha_c(z) \rho_c}{2d_{\text{BC}}} C^W(z) u_c(z)^{-2} \quad (\text{B.20})$$

$$C^W(z) = (0.79 \ln(Re_c(z)) - 1.64)^{-2} \quad (\text{B.21})$$

$$Re_c(z) = \frac{\rho_c |u_c(z)| d_{\text{BC}}}{\mu_c} \quad (\text{B.22})$$

$$C^D(\xi, z) = \max\left(\min\left(\frac{16}{Re_d(\xi, z)} (1 + 0.15 Re_d(\xi, z)^{0.687}), \frac{48}{Re_d(\xi, z)}\right), \frac{8}{3} \frac{Eo(\xi, z)}{Eo(\xi, z) + 4}\right) \quad (\text{B.23})$$

$$Eo(\xi, z) = \frac{g(\rho_c - \rho_d(z)) \xi^2}{\sigma} \quad (\text{B.24})$$

$$Re_d(\xi, z) = \frac{\rho_c |u_d(\xi, z) - u_c(z)| \xi}{\mu_c} \quad (\text{B.25})$$

Boundary condtions [16, 25]:

$$f_d^m(\xi, z_{\min}) = \frac{\Psi(\xi) V(\xi)}{\int_{\xi_{\min}}^{\xi_{\max}} \Psi(\xi) V(\xi) d\xi} \alpha_d^{**}(z_{\min}) \rho_d^*(z_{\min}) \quad (\text{B.26})$$

$$f_d^m(\xi_{\min}, z) = 0 \quad (\text{B.27})$$

$$u_d(\xi, z_{\min}) = u_d^*(\xi, z_{\min}) \quad (\text{B.28})$$

$$u_d(\xi_{\min}, z) = u_c(z) \quad (\text{B.29})$$

$$p(z_{\max}) = p^0 \quad (\text{B.30})$$

$$u_c(z_{\min}) = u_c^*(z_{\min}) \quad (\text{B.31})$$

Mixtrue properties continious phase:

aq. EtOH [143]:

$$\ln(\rho_c) = x_W \ln(\rho_W(T)) + x_{\text{EtOH}} \ln(\rho_{\text{EtOH}}(T)) - 30.808 \frac{x_W x_{\text{EtOH}}}{T} \quad (\text{B.32})$$

$$-18.274 \frac{x_W x_{\text{EtOH}}(x_W - x_{\text{EtOH}})}{T} + 13.890 \frac{x_W x_{\text{EtOH}}(x_W - x_{\text{EtOH}})^2}{T}$$

$$\ln(\eta_c) = x_W \ln(\eta_W(T)) + x_{\text{EtOH}} \ln(\eta_{\text{EtOH}}(T)) + 724.652 \frac{x_W x_{\text{EtOH}}}{T} \quad (\text{B.33})$$

$$+729.357 \frac{x_W x_{\text{EtOH}}(x_W - x_{\text{EtOH}})}{T} + 976.050 \frac{x_W x_{\text{EtOH}}(x_W - x_{\text{EtOH}})^2}{T}$$

$$\ln(\sigma) = x_W \ln(\sigma_W(T)) + x_{\text{EtOH}} \ln(\sigma_{\text{EtOH}}(T)) - 488.012 \frac{x_W x_{\text{EtOH}}}{T} \quad (\text{B.34})$$

$$-640.785 \frac{x_W x_{\text{EtOH}}(x_W - x_{\text{EtOH}})}{T} - 1073.310 \frac{x_W x_{\text{EtOH}}(x_W - x_{\text{EtOH}})^2}{T}$$

aq. Glycerol [144]:

$$\rho_c = w_W \rho_W(T) + w_{\text{Gly}} \rho_{\text{Gly}}(T) \quad (\text{B.35})$$

$$\mu_c = \mu_W \frac{1 - w_{\text{Gly}}/1.2}{1 - ((-0.012 T + 4.74)1.2 - 1)w_{\text{Gly}}/1.2} \left(\frac{-2.5 \cdot 1.2}{2 - (-0.012 T + 4.74)1.2} \right) \quad (\text{B.36})$$

$$\sigma = w_W \sigma_W(T) + w_{\text{Gly}} \sigma_{\text{Gly}}(T) \quad (\text{B.37})$$

aq. NaCl or aq. Na₂SO₃[145–147]:

$$\mu_c = \mu_W^{w_W} \mu_s^{w_s} \quad (\text{B.38})$$

$$\mu_W = \frac{t/^\circ\text{C} + 246}{(0.0559t/^\circ\text{C} + 5.2842)t/^\circ\text{C} + 137.37} \text{ mPa} \quad (\text{B.39})$$

$$\mu_s = \exp \left(\frac{C_{\mu,1}(1 - w_W)^{C_{\mu,2}} + C_{\mu,3}}{(C_{\mu,4}t/^\circ\text{C} + 1)(C_{\mu,5}(1 - w_W)^{C_{\mu,6}} + 1)} \right) \text{ mPa} \quad (\text{B.40})$$

$$\rho_c = (w_W \rho_W^{-1} w_s \rho_s^{-1})^{-1} \quad (\text{B.41})$$

$$\rho_s = \left(\frac{w_s + C_{\rho,2} + C_{\rho,3} t}{(C_{\rho,0} + w_s + C_{\rho,1}) e^{1 \times 10^{-6}(t/^\circ\text{C} + C_{\rho,4})^2}} \right)^{-1} \quad (\text{B.42})$$

$$\sigma_s = \sigma_W + C_{\sigma,1} + C_{\sigma,2} w_s + C_{\sigma,3} w_s T + C_{\sigma,4} w_s^2 + C_{\sigma,5} T^2 \quad (\text{B.43})$$

The nomenclature summarizes the descriptions of the symbols introduced in the above equations. Quantities with one asterisk denote the current solution, and those with two asterisks denote quantities from a previous iteration (see Breit *et al.* [16] Section 3.2 for details). The mass and mole fractions of the continuous phase were estimated iteratively from the concentrations c_s using the density model. The parameters for the calculation of the mass density, viscosity and surface tension in the mixtures of water and NaCl and Na₂SO₃ can be found in Tab. B.2. The parameters for Na₂SO₄ were used instead of Na₂SO₃ for the surface tension calculation, as they were not available and should not differ much from those for Na₂SO₄ due to their chemical similarity. Tab. B.4 summarizes the initial conditions of the non-linear solver presented in [16], the boundary conditions and further model parameters. Tab. B.3 presents the substance data of pure water and air together with solver related parameters.

Table B.2.: Parameters for calculating the mass density, viscosity and surface tension of aqueous solution of NaCl and Na₂SO₃.

| | C_1 | C_2 | C_3 | C_4 | C_5 | C_6 |
|-----------------------------------|-------------------------|-------------------------|---------|------------|---------|---------|
| $\sigma_{\text{Na}_2\text{SO}_3}$ | -2.8938 | 2.4971 | 0.1162 | -0.0069 | 0.8162 | -0.0009 |
| $\mu_{\text{Na}_2\text{SO}_3}$ | 0.000044078 | -2.2823 | 5.5871 | 0.1463 | -0.259 | 4.7169 |
| $\rho_{\text{Na}_2\text{SO}_3}$ | 1.5197×10^{-5} | 4.3766×10^{-7} | 0.10296 | -0.0015271 | -4500.9 | |
| σ_{NaCl} | -1.9744 | 3.6460 | -0.0254 | -0.0128 | -0.3033 | 0.0008 |
| μ_{NaCl} | 16.222 | 1.3229 | 1.4849 | 0.0074691 | 30.78 | 2.0583 |
| ρ_{NaCl} | -0.00433 | 0.06471 | 1.0166 | 0.014624 | 3315.6 | |

Table B.3.: Left: Property data pure water and air. Right: solver related parameter applied in the simulations.

| <i>Property data</i> | | | <i>Solver related parameter</i> | | |
|----------------------|--------------------|-------------------------|---------------------------------|------|---------------------|
| Parameter | Unit | Value | Parameter | Unit | Value |
| μ_c | Pas | 9.7754×10^{-4} | ξ_{\min} | m | 1×10^{-3} |
| μ_d | Pas | 18×10^{-6} | ξ_{\max} | m | 20×10^{-3} |
| σ | J m^{-2} | 0.072 | z_{\min} | m | (0.2, 0.3, 0.35) |
| ρ_d^0 | kg m^{-3} | 1.188 | $\{\epsilon\}$ | - | 1×10^{-6} |
| ρ_c | kg m^{-3} | 998 | P_ξ | - | 49-69 |
| T^0 | K | 298 | P_z | - | 14 |

Table B.4.: Initial and boundary conditions and model parameters used in the simulations.

| Parameter | Unit | Value |
|------------------------------|--------------------|--------------------|
| d_{BC} | m | 0.1 |
| V_c | l | 4.7 - 14.1 |
| h_c | m | 06 - 1.8 |
| j_c | m s^{-1} | 1×10^{-6} |
| j_d | cm s^{-1} | 1 - 4.5 |
| p^0 | Pa | 101500 |
| $\alpha_d^{\text{ini}}(z)$ | - | 0.1 |
| $h_{\text{BC}}^{\text{ini}}$ | - | 2.4 |
| $p^{\text{ini}}(z_{\min})$ | Pa | 120884 |
| g | m s^{-2} | 9.81 |

B.3. Additional Equations

B.3.1. Moments

The a, b -th moment ratio $m_{a,b}$ of a distribution function $\Lambda(\varphi - \varphi_0)$ of a variable φ about φ_0 is defined as:

$$m_{a,b} = \left(\frac{\int_{-\infty}^{+\infty} \varphi^a \Lambda(\varphi - \varphi_0) d\xi}{\int_{-\infty}^{+\infty} \varphi^b \Lambda(\varphi - \varphi_0) d\xi} \right)^{n/(a-b)} \quad (\text{B.44})$$

where a, b are the order of the moment ratio and n is the normalizing index with $n = 1$ - normalized and $n = 0$ non-normalized. In order to calculate some characteristic quantities of a distribution derived from the moment ratio Tab. B.5 is used.

Table B.5.: Characteristic quantities of a distribution derived from the moment ratio.

| a | b | n | φ | Λ | φ_0 | Name | Symbol |
|-----|-----|-----|---------------------------|-----------|-------------|----------------------------------|------------|
| 1 | 0 | 1 | ξ | f_d^n | 0 | Arithmetic mean | ξ_{10} |
| 2 | 0 | 1 | ξ | f_d^n | ξ_{10} | Standard deviation | |
| 2 | 0 | 0 | ξ | f_d^n | ξ_{10} | Variance | σ^2 |
| 3 | 0 | 0 | $(\xi - \xi_{10})/\sigma$ | f_d^n | 0 | Skewness | |
| 4 | 0 | 0 | $(\xi - \xi_{10})/\sigma$ | f_d^n | 0 | Kurtosis | ω |
| 3 | 2 | 1 | ξ | f_d^n | 0 | Sauter mean diameter | ξ_{32} |
| 2 | 0 | 1 | ξ | f_d^n | 0 | Surface-equivalent mean diameter | |
| 3 | 0 | 1 | ξ | f_d^n | 0 | Volume-equivalent mean diameter | |

B.3.2. Normalization

In order to compare the experimental and simulated BSD, the simulated mass based BSD $f_d^m(\xi, z)$ must be converted to a number based BSD $f_d^n(\xi, z)$ using Eq. (B.45) and then normalized using Eq. (B.46).

$$f_d^n(\xi, z) = \frac{f_d^m(\xi, z)}{V(\xi)\rho_d(z)} \quad (\text{B.45})$$

$$\hat{f}_d^n = \frac{f_d^n}{\int_{\xi_{\min}}^{\xi_{\max}} f_d^n d\xi} \quad (\text{B.46})$$

Here \hat{f}_d^n is the normalized number based distribution function.

B.3.3. Interfacial Area Density

Based on the mass density function $f_d^m(\xi, z)$ the interfacial area density could be calculated based on the following equation.

$$a(z) = \pi \int_{\xi_{\min}}^{\xi_{\max}} \xi^2 f_d^m(\xi, z) d\xi \quad (\text{B.47})$$

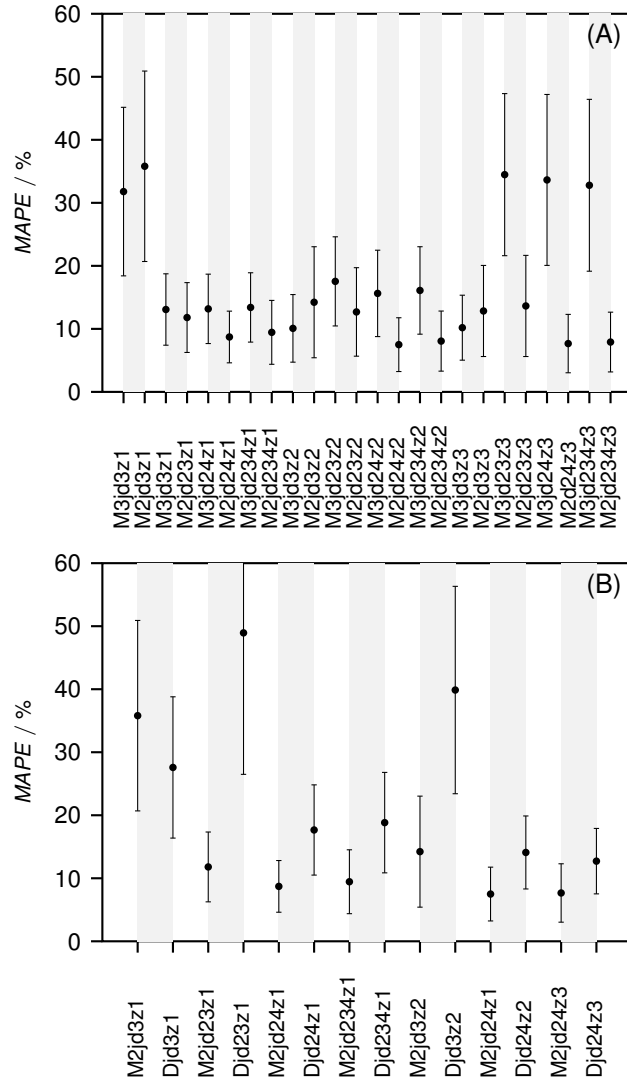


Figure B.2.: Comparison of calibration methods considering an additional moment (kurtosis). **(A):** Mean absolute percentage error $MAPE$ (see Eq. (3.6)) and **(B):** percentage error PE with respect to the gas holdup $\bar{\alpha}_g$ for different calibration methods (see Section 3.3.3). Evaluation data set: $h_c = 140$ cm.

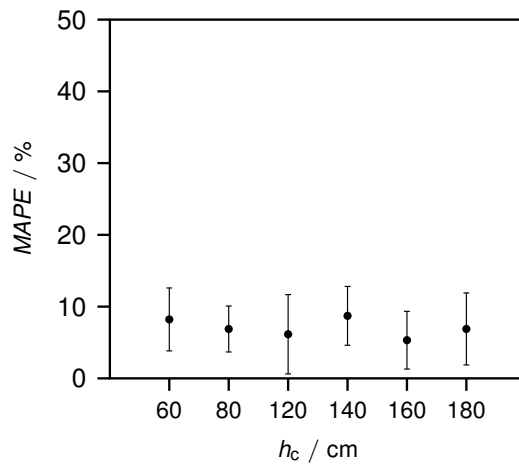


Figure B.3.: Mean absolute percentage error $MAPE$ (see Eq. (3.6)) as function of the un-gasified liquid heights h_c with previous calibration of the model with method M2jd24z1hc140. The $MAPE$ is evaluated within each h_c individually.

C. Supplementary Information for Chapter 4

C.1. Additional Equations

C.1.1. Transformation of Mass to Number Based Density Function

In order to calculate the number weighted moments, the mass density function f_d^m is transformed into a number density function f_d^n using the Eq. (C.1).

$$f_d^n(\xi, z) = \frac{f_d^m(\xi, z)}{V(\xi)\rho_d(z)} \quad (C.1)$$

$$(C.2)$$

Where $V(\xi)$ is the volume of a spherical bubble with size ξ and $\rho_d(z)$ is the mass density of the dispersed phase.

C.1.2. Moments

The ab -th moment ratio μ_{ab} of a distribution function $f(\xi - \xi_0)$ of a variable ξ about ξ_0 is defined as:

$$\mu_{ab} = \left(\frac{\int_{-\infty}^{+\infty} \xi^a f(\xi - \xi_0) d\xi}{\int_{-\infty}^{+\infty} \xi^b f(\xi - \xi_0) d\xi} \right)^{n/(a-b)} \quad (C.3)$$

where ab are the order of the moment ratio and n is the normalizing index with $n = 1$ - normalized and $n = 0$ non-normalized. In order to calculate some characteristic quantities of a distribution derived from the moment ratio Tab. C.1 is used.

Table C.1.: Characteristic quantities of a distribution derived from the moment ratio.

| a | b | n | ξ | f | ξ_0 | Name | Symbol |
|-----|-----|-----|---------------------------|---------|------------|----------------------------------|------------|
| 1 | 0 | 1 | ξ | f_d^n | 0 | Arithmetic mean | ξ_{10} |
| 2 | 0 | 1 | ξ | f_d^n | ξ_{10} | Standard deviation | |
| 2 | 0 | 0 | ξ | f_d^n | ξ_{10} | Variance | σ^2 |
| 3 | 0 | 0 | $(\xi - \xi_{10})/\sigma$ | f_d^n | 0 | Skewness | |
| 4 | 0 | 0 | $(\xi - \xi_{10})/\sigma$ | f_d^n | 0 | Kurtosis | |
| 3 | 2 | 1 | ξ | f_d^n | 0 | Sauter mean diameter | ξ_{32} |
| 2 | 0 | 1 | ξ | f_d^n | 0 | Surface-equivalent mean diameter | |
| 3 | 0 | 1 | ξ | f_d^n | 0 | Volume-equivalent mean diameter | ξ_{30} |

C.1.3. Normalization

In order to compare the experimental and predicted BSD, the simulated mass based density function $f_d^m(\xi, z)$ must be converted to a number based density function $f_d^n(\xi, z)$ using Eq. (C.1) and then normalized using Eq. (C.4).

$$\hat{f}_d^n(\xi, z) = \frac{f_d^n(\xi, z)}{\int_{\xi_{\min}}^{\xi_{\max}} f_d^n(\xi, z) d\xi} \quad (\text{C.4})$$

Here \hat{f}_d^n is the normalized number based density function.

C.1.4. Local Gas Volume Fraction

The local gas volume fraction α_d follows directly from the mass density function using the Eq. (C.5).

$$\alpha_d(z) = \frac{\int_{\xi_{\min}}^{\xi_{\max}} f_d^m(\xi, z) d\xi}{\rho_d(z)} \quad (\text{C.5})$$

Here ξ_{\min}, ξ_{\max} are the minimal resp. the maximal bubble size considered in the calculations.

C.2. Sparger Model

In the following, a five-step modification of the sparger model according to Ribeiro *et al.* [69], which consists only of steps (1,2,5), is presented in order to determine the inlet BSD $\hat{f}_{d,\text{inlet}}^n$.

1. In the first step, the volume mean diameter $\xi_{30,h}$ is calculated using the model according to Geary *et al.* [63] based on property data (liquid, gas mass density and viscosity, surface tension) and the sparger geometry consisting of the orifice diameter d_h and the number of orifices N_h . The number of orifices is used to calculate the volume flow rate through the single orifice for which the model according to Geary *et al.* [63] was developed.
2. In the second step, the two parameters (χ, ω) of a log-normal distribution Eq. (C.6) are fitted to measured inlet BSD for different gas fluxes in our case $j_d = (2, 4) \text{ cm s}^{-1}$ to be in line with the available gas fluxes of the breakage and coalescence parameter calibration (cf. Chapter 3). For this purpose, the minimization problem Eq. (C.7) is solved.

$$\hat{f}_{d,\text{inlet}}^n(\xi, \chi, \omega) = \frac{1}{\sqrt{2\pi}\xi\chi} \exp\left(-\left(\frac{\ln(\xi) - \chi}{\sqrt{2}\omega}\right)^2\right) \quad (\text{C.6})$$

$$\min_{\chi, \omega} \left\| \sum_{i,j} \hat{f}_{d,\text{inlet}}^n(\xi_j, \chi_i, \omega_i) - \hat{f}_{d,\text{inlet},\text{exp}}^n(\xi_j, j_{d,i}) \right\|_2^2 \quad (\text{C.7})$$

3. In the third step, the resulting value pairs of $j_{d,i}, \omega_i$ of the previous step are fitted via linear regression to the gas flux dependent sparger function Eq. (C.8).

$$\omega(j_d) = p_1 j_d + p_2 \quad (\text{C.8})$$

4. In the fourth step, the parameter c is determined by solving the minimization problem Eq. (C.9).

$$\min_{\chi, c} \left\| \int_{\xi_{\min}}^{\xi_{\max}} \xi^3 \hat{f}_{d,\text{inlet}}^n(\xi, \chi_i, \omega) d\xi - c \xi_{30,h,i} + \frac{1}{2} \left(\frac{|\xi_{32,i,\text{exp}} - \xi_{32,i}|}{\xi_{32,i,\text{exp}}} + \frac{|\sigma_{i,\text{exp}} - \sigma_i|}{\sigma_{i,\text{exp}}} \right) \right\|_2^2 \quad (\text{C.9})$$

In addition to the ξ_{30} of the distribution $\hat{f}_{d,\text{inlet}}^n(\xi, \chi_i, \omega)$, further moments namely the SMD ξ_{32} and the standard deviation σ in comparison to experiments using the *MAPE* were included in the minimization, so that further moments of the distribution are also optimized. It was found that the best results could be achieved when $\omega(j_d = 4 \text{ cm}^{-1})$ was kept constant.

5. In the fifth and final step, the minimization problem Eq. (C.10) is solved with the now determined sparger parameter c and sparger function $\omega(j_d)$ in order to obtain the final χ of the log-normal distribution.

$$\min_{\chi} \left\| \int_{\xi_{\min}}^{\xi_{\max}} \xi^3 \hat{f}_{d,\text{inlet}}^n(\xi, \chi_i, \omega(j_d)) d\xi - c \xi_{30,h,i} \right\|_2^2 \quad (\text{C.10})$$

This polishing step was additionally carried out because due to the now constant c , better χ can be found which has led to an overall better prediction performance.

Note that despite the multiple minimizations, only the measured distributions for the gas fluxes $j_d = (2, 4) \text{ cm s}^{-1}$ are used.

After the procedure has been run once, an inlet BSD can be obtained at any gas flux using the parameter c , the sparger function $\omega(j_d)$ and step 1 and 5 of the procedure. However, the limitation of

the model according to Geary *et al.* [63] must be considered, which only applies up to $Re = 500$, which is still fulfilled for $j_d = 4 \text{ cm s}^{-1}$ and is slightly exceeded for $j_d = 5 \text{ cm s}^{-1}$, it was nevertheless used.

The sparger model was implemented in MATLAB[®] in Version R2023a (9.14.0.2286388) from the publisher The MathWorks Inc. (Natick, Massachusetts, USA) using the functions: `fsolve` (step 1), `lsqcurvefit` (step 2), `polyfit` (step 3) and `lsqnonlin` (step 4,5).

The result of the sparger model using the property data, Tab. C.3 and the sparger geometry, Tab. C.7 is summarized in Tab. C.5 and Tab. C.6.

C.3. Applied Parameters in the Simulations

Tab. C.2 summarizes the initial conditions of the non-linear solver presented in Breit *et al.* [16], the boundary conditions and further model parameters. Tab. C.3 presents the property data of pure water and air together with solver related parameters and the calibrated parameter of the breakage and coalescence parameter of the model according to Coualoglou *et al.* [53] calibrated in Chapter 3. Tab. C.5 shows the parameters of the sparger function Eq. (C.8) and sparger parameter c resulting from the sparger model, presented in Section C.2. The corresponding parameters of the log-normal distribution Eq. (C.6) are depicted in Tab. C.5. The measured inlet BSD as a boundary condition for f_d^m are summarized in the Supplementary Material of the publication.

Table C.2.: Initial and boundary conditions and model parameters used in the simulations.

| Parameter | Unit | Value |
|---------------------|-------------|--------------------|
| d_{BC} | m | 0.10635 |
| $h_{c,semi-batch}$ | m | 1.8 |
| $h_{c,conti}$ | m | result of calc. |
| $h_{BC,semi-batch}$ | m | result of calc. |
| $h_{BC,conti}$ | m | 2.535 |
| $j_{c,semi-batch}$ | $m s^{-1}$ | 1×10^{-6} |
| $j_{c,conti}$ | $cm s^{-1}$ | 1 - 3 |
| j_d | $cm s^{-1}$ | 1 - 5 |
| p^0 | Pa | 101500 |
| $\alpha_d^{ini}(z)$ | - | 0.1 |
| h_{BC}^{ini} | - | 2.4 |
| $p^{ini}(z_{min})$ | Pa | 120884 |
| g | $m s^{-2}$ | 9.81 |

Table C.3.: Left: Property data pure of water and of air. Right: solver related parameter applied in the simulations.

| <i>Property data</i> | | | <i>Solver related parameter</i> | | |
|----------------------|-------------|-------------------------|-------------------------------------|------|---------------------|
| Parameter | Unit | Value | Parameter | Unit | Value |
| μ_c | Pas | 9.7754×10^{-4} | ξ_{min} | m | 5×10^{-5} |
| μ_d | Pas | 18×10^{-6} | ξ_{max} | m | 20×10^{-3} |
| σ | $J m^{-2}$ | 0.072 | $z_{min,semi-batch}, z_{min,conti}$ | m | 0.195, 0.162 |
| ρ_d^0 | $kg m^{-3}$ | 1.188 | $\{\epsilon\}$ | - | 1×10^{-6} |
| ρ_c | $kg m^{-3}$ | 998 | N_ξ | - | 89 |
| T^0 | K | 293 | N_z | - | 14 |

Table C.4.: Parameters of the used breakage and coalescence kernel according to Coualoglou *et al.* [53] adapted from Chapter 3.

| <i>Breakage and coalescence</i> | | |
|---------------------------------|----------|--------|
| Parameter | Unit | Value |
| C_1 | - | 0.0111 |
| C_2 | m^{-2} | 1 |
| C_3 | - | 0.2130 |
| C_4 | - | 4.4704 |

Table C.5.: Parameters of the sparger function Eq. (C.8) and the sparger parameter c resulting from the sparger model presented in Section C.2.

| Sparger | $p_1/\text{s cm}^{-1}$ | $p_2/-$ | $c/-$ |
|------------|------------------------|---------|--------|
| PIS-04-187 | 0.0354 | 0.3958 | 0.7003 |
| PIS-05-120 | 0.0196 | 0.4231 | 0.5533 |
| SpS-04-56 | 0.0324 | 0.3788 | 0.5143 |

Table C.6.: Parameters of the log-normal distribution Eq. (C.6) resulting from the sparger model (cf. Section C.2).

| $j_d/\text{cm s}^{-1}$ | Log-normal parameter χ, ω | | |
|------------------------|-------------------------------------|----------------|----------------|
| | PIS-04-187 | PIS-05-120 | SpS-04-56 |
| 1 | 0.4500, 0.4112 | 0.4111, 0.4428 | 0.4499, 0.4112 |
| 2 | 0.5942, 0.4667 | 0.5013, 0.4624 | 0.5453, 0.4436 |
| 3 | 0.6140, 0.5021 | 0.5553, 0.4820 | 0.5784, 0.4760 |
| 4 | 0.6141, 0.5375 | 0.5888, 0.5016 | 0.5797, 0.5084 |
| 5 | 0.6000, 0.5729 | 0.6087, 0.5212 | - |

The name of a sparger is made up of three parts: firstly the type plate sparger (PIS) or spider sparger (SpS), secondly the single orifice diameter in tenths of a millimeter and thirdly the number of orifices.

C.4. Detail about the Experimental Setup

Tab. C.7 provides the abbreviations of the spargers and details of their design. Tab. C.8 summarizes the set parameters of the OPTOEM and the associated software M2 Analyzer for Bubbles v2.25 from the publisher A2 Photonic Sensors (Grenoble, France). The geometric dimensions of the needle probes used in Chapter 4 are depicted in Fig. C.1. The exact axial measuring position of the needle probes is shown in Tab. C.9.

Table C.7.: Geometric dimensions used for the plate sparger (PlS) and the spider sparger (SpS). Here d_h is the single orifice diameter, the number of orifices N_h and the ratio of the total orifice area to the cross-sectional area of the bubble column A_h/A_{BC} .

| Disperser | d_h / mm | N_h / - | A_h/A_{BC} / - |
|------------|------------|-----------|------------------|
| PlS-04-187 | 0.4 | 187 | 0.0106 |
| PlS-05-120 | 0.5 | 120 | 0.0106 |
| SpS-04-56 | 0.4 | 56 | 0.00317 |

Table C.8.: Parameter settings of the optoelectronic module and the software.

| Parameter | Value | Unit |
|--|--------|---------|
| Refractive index of the continuous phase | 1.33 | - |
| Refractive index of the dispersed phase | 1.00 | - |
| Sampling frequency during gas fraction measurement | 801.28 | kHz |
| Pretrigger | 500 | μ s |
| Velocity filter | - | - |
| Size filter | - | - |
| Duration filter | - | - |
| FFT amplitude filter | - | - |
| Deviation factor of the liquid threshold (start value autosest parameters) | 10 | - |
| Minimum number of strips (start value autosest parameters) | 30 | - |
| Spectral-temporal homogeneity (start value autosest parameters) | 90 | % |
| Liquid threshold (start value autosest parameters) | 0 | mV |
| Bandpass low frequency (start value autosest parameters) | 100 | kHz |
| Bandpass high frequency (start value autosest parameters) | 100 | kHz |
| Trigger level of the gas fraction measurement | 0.25 | V |
| Laser Intensity | [1,4] | V |

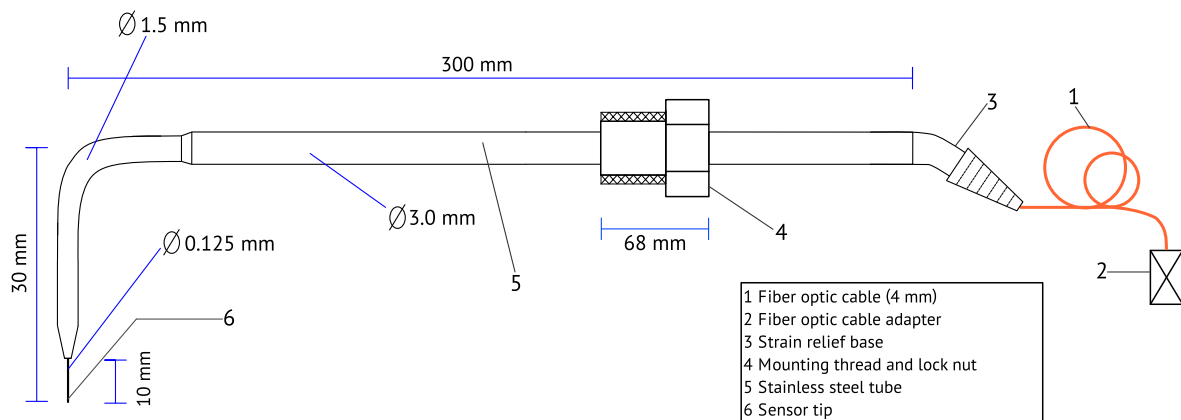


Figure C.1.: Design and dimensions of the needle probe used.

Table C.9.: Heights of the measuring positions, measured from the sparger.

| Measuring position | Semi-batch | Continuous | Unit |
|--------------------|------------|------------|------|
| M1 | 0.195 | 0.162 | m |
| M2 | 0.967 | 0.934 | m |
| M3 | 1.715 | 1.682 | m |

C.5. Additional Figures

This section summarizes all additional figures.

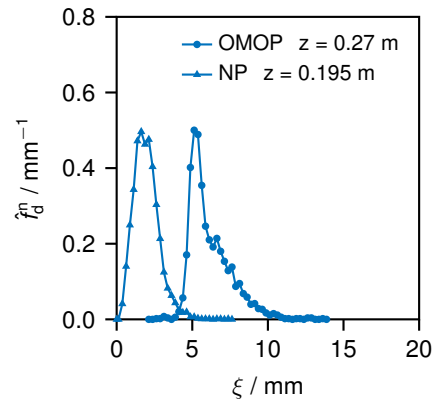


Figure C.2.: Normalized number density distribution \hat{f}_d^n as a function of bubble diameter ξ measured with the OMOP (solid line with point marker) and with the NP (solid line with triangle marker) at gas flux j_d above the PIS-04-187 sparger. Substance System: water-air.

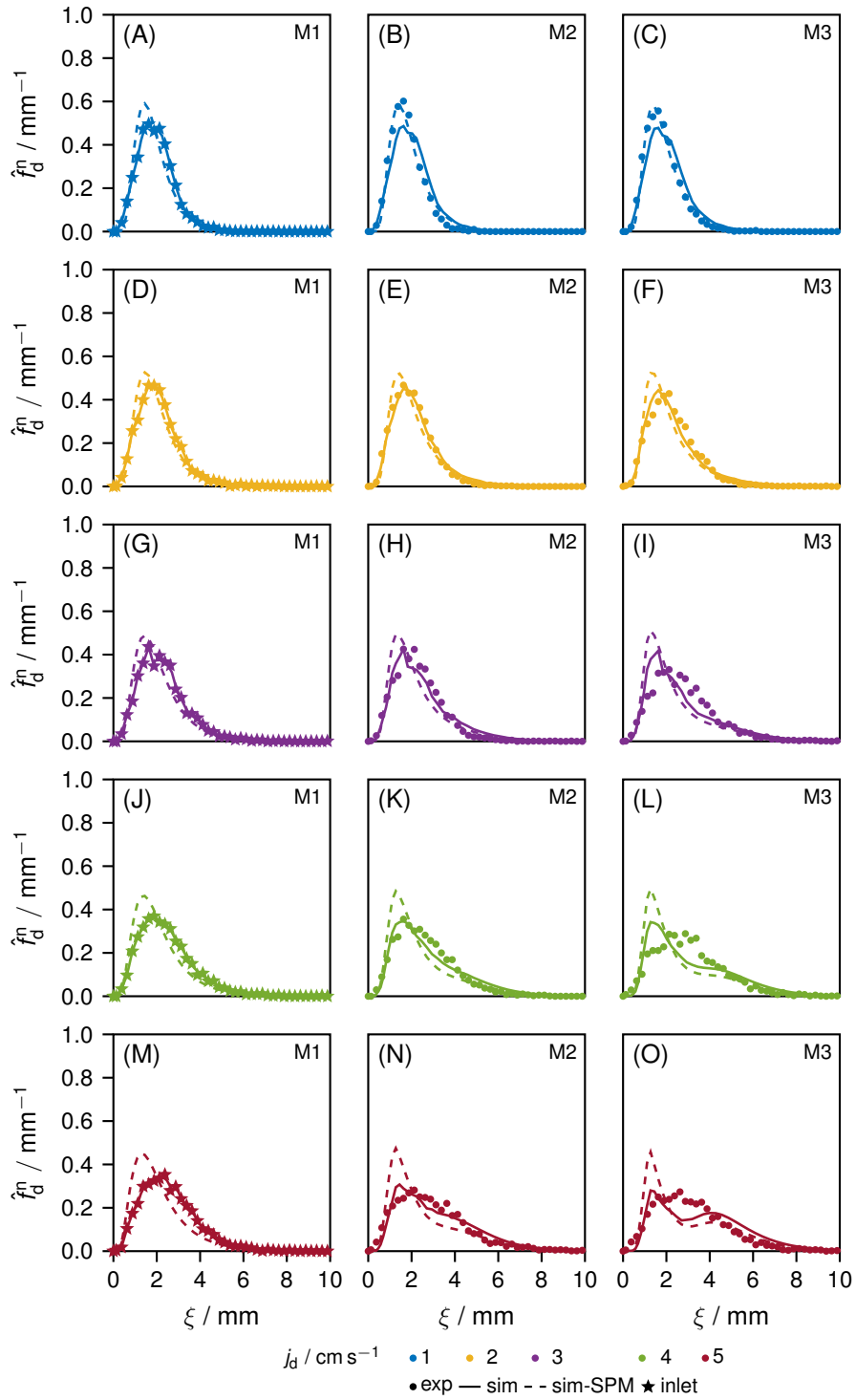


Figure C.3.: Normalized number density distribution \hat{f}_d^n as a function of bubble diameter ξ for different gas fluxes j_d (color, along rows) and axial positions z (along columns) for the PIS-04-187 sparger. Symbols: experiments, inlet marked with star. Solid lines: simulation with measured inlet BSD. Dashed line: simulation with inlet BSD obtained by the sparger model.

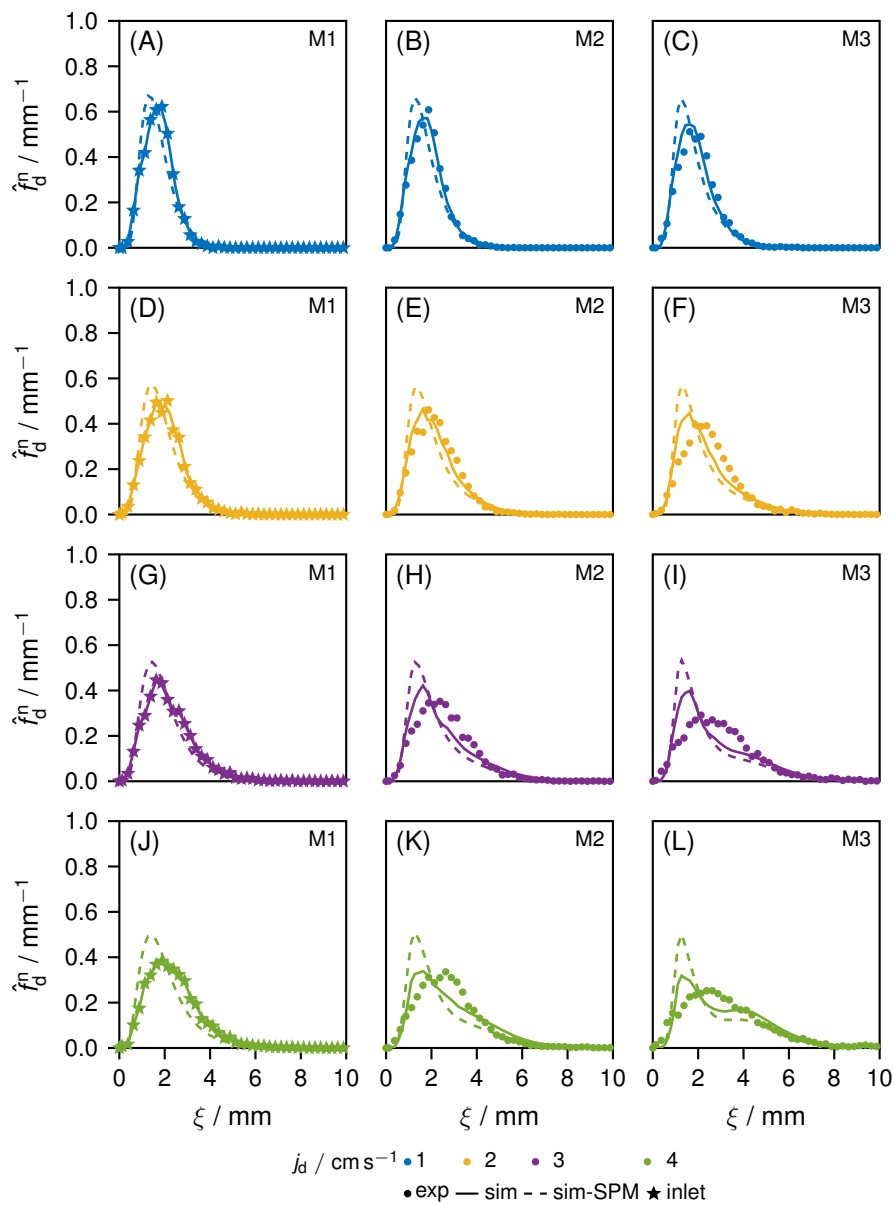


Figure C.4.: Normalized number density distribution \hat{f}_d^n as a function of bubble diameter ξ for different gas fluxes j_d (color, along rows) and axial positions z (along columns) for the liquid flux $j_c = 1 \text{ cm s}^{-1}$. Symbols: experiments, inlet marked with star. Solid lines: simulation with measured inlet BSD. Dashed line: simulation with inlet BSD obtained by the sparger model.

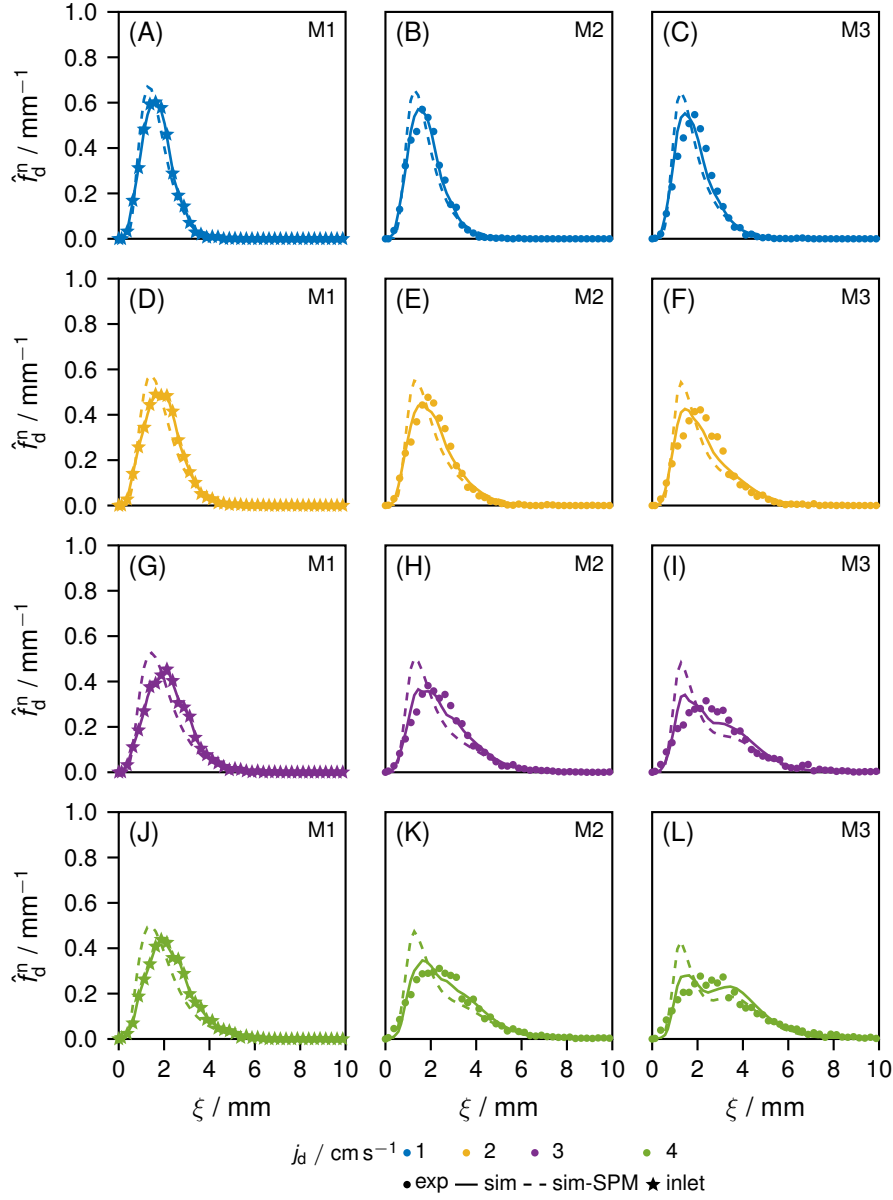


Figure C.5.: Normalized number density distribution \hat{f}_d^n as a function of bubble diameter ξ for different gas fluxes j_d (color, along rows) and axial positions z (along columns) for the liquid flux $j_c = 3 \text{ cm s}^{-1}$. Symbols: experiments, inlet marked with star. Solid lines: simulation with measured inlet BSD. Dashed line: simulation with inlet BSD obtained by the sparger model.

D. Supplementary Information for Chapter 5

D.1. Derivation of a Generalized Transport Equation in \mathbb{R}^N

D.1.1. Mathematical Preamble

Gauss's Theorem

The Gauss's theorem can be generalized as follows:

$$\int_{\Omega} \nabla \cdot \psi \, d^N \mathbf{C} = \oint_{\delta\Omega} \psi \cdot d^{N-1} \mathbf{C} \quad (\text{D.1})$$

where Ω is a bounded manifold in \mathbb{R}^N with N as the number of independent dimensions, ψ is a conserved density function and can be scalar or tensorial, \mathbf{C} is the phase space and $\delta\Omega$ is the boundary of the manifold Ω .

Total Time Derivative

The total (time) derivative is defined as follows:

$$\frac{d\phi(t, x_1(t), \dots, x_N(t))}{dt} = \frac{\partial\phi}{\partial t} + \sum_{i=1}^N \frac{dx_i}{dt} \frac{\partial\phi}{\partial x_i} \quad (\text{D.2})$$

where ϕ is a differential function, N is the number of dimensions and x_i a coordinate.

Generalized Leibniz's Rule

The Leibniz's rule can be generalized as follows:

$$\frac{d}{dt} \int_{\Omega(t)} \psi \, d^N \mathbf{C} = \int_{\Omega(t)} \frac{\partial\psi}{\partial t} d^N \mathbf{C} + \oint_{\delta\Omega(t)} \psi \mathbf{v} \cdot d^{N-1} \mathbf{C} \quad (\text{D.3})$$

$$= \int_{\Omega(t)} \left[\frac{\partial\psi}{\partial t} + \nabla \cdot (\psi \mathbf{v}) \right] d^N \mathbf{C} \quad (\text{D.4})$$

where Eq. (D.1) was used.

D.1.2. Model Development

Fig. D.1 shows a finite control volume in the Lagrangian frame of reference for single phase flow.

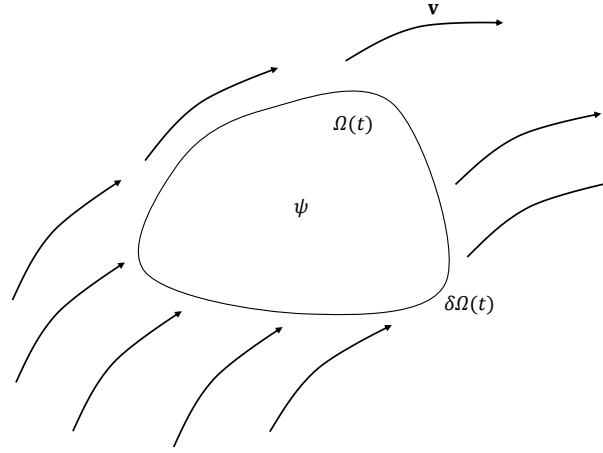


Figure D.1.: Finite control volume in the Lagrangian frame of reference.

Form the balance of the conserved quantity, Ψ the Eq. (D.5) can be formulated. The conserved quantity Ψ can change in time by sources inside Φ or by non-convective fluxes \mathbf{J} across the interface of Ω .

$$\frac{d\Psi}{dt} = \int_{\Omega(t)} \Phi d^N \mathbf{C} - \oint_{\delta\Omega(t)} \mathbf{J} \cdot d^{N-1} \mathbf{C} \quad (\text{D.5})$$

Note that the axiom of continuum mechanics applies here, which states that quantities like Φ is continuous in the control volume, so that the integral can be formulated and applied without jumps. The conserved quantity Ψ is determined from the conserved density function ψ :

$$\Psi = \int_{\Omega(t)} \psi d^N \mathbf{C} \quad (\text{D.6})$$

If Eq. (D.6) is substituted into Eq. (D.5), it follows:

$$\frac{d}{dt} \int_{\Omega(t)} \psi d^N \mathbf{C} = \int_{\Omega(t)} \Phi d^N \mathbf{C} - \oint_{\delta\Omega(t)} \mathbf{J} \cdot d^{N-1} \mathbf{C} \quad (\text{D.7})$$

Apply the Gauss's theorem Eq. (D.1) to the non-convective flux term:

$$\frac{d}{dt} \int_{\Omega(t)} \psi d^N \mathbf{C} = \int_{\Omega(t)} \Phi d^N \mathbf{C} - \int_{\Omega(t)} \nabla \cdot \mathbf{J} d^N \mathbf{C} \quad (\text{D.8})$$

Apply the generalized Leibniz's rule Eq. (D.4) on the left hand side of Eq. (D.8) results:

$$\int_{\Omega(t)} \left[\frac{\partial \psi}{\partial t} + \nabla \cdot (\psi \mathbf{v}) \right] d^N \mathbf{C} = \int_{\Omega(t)} \Phi d^N \mathbf{C} - \int_{\Omega(t)} \nabla \cdot \mathbf{J} d^N \mathbf{C} \quad (\text{D.9})$$

The volume integral must be fulfilled for every manifold Ω so that the following applies:

$$\frac{\partial \psi}{\partial t} + \nabla \cdot (\psi \mathbf{v}) + \nabla \cdot \mathbf{J} = \Phi \quad (\text{D.10})$$

The Eq. (D.10) is a local instantaneous transport equation of the conserved density function ψ in multidimensional phase space in single phase flow.

For a practical application, the phase space \mathbf{C} is conventionally partitioned into physical space, characterized by external coordinates $\mathbf{r} = (x, y, z)^T$, and property space, defined by internal coordinates $\mathbf{c} = (c_1, c_2, c_3, \dots)^T$. Since the individual dimensions of the phase space are in-dependent to each other, it can be separated as follows:

$$\mathbf{C} = \{\mathbf{r}, \mathbf{c}\} \quad \text{with} \quad \mathbf{r} \in \mathbb{R}^3 \quad \text{and} \quad \mathbf{c} \in \mathbb{R}^{N-3} \quad (\text{D.11})$$

$$\mathbf{v} = \{\mathbf{v}_r, \mathbf{v}_c\} \quad (\text{D.12})$$

$$\nabla = \{\nabla_r, \nabla_c\} \quad (\text{D.13})$$

So that we get the generalized transport equation:

$$\frac{\partial \psi}{\partial t} + \nabla_r \cdot (\psi \mathbf{v}_r) + \nabla_c \cdot (\psi \mathbf{v}_c) + \nabla \cdot \mathbf{J} = \Phi \quad (\text{D.14})$$

With respect to population balance modeling, usually no diffusion is considered. If the influence of turbulence or dispersion is to be incorporated in the PBE, a diffusion term occurs. However, in general $\mathbf{J} = \mathbf{0}$ is set so that the generalized PBE appears:

$$\frac{\partial \psi}{\partial t} + \nabla_r \cdot (\psi \mathbf{v}_r) + \nabla_c \cdot (\psi \mathbf{v}_c) = \Phi \quad (\text{D.15})$$

It should be noted that the conclusions drawn in Chapter 5 remain valid even without taking diffusion into account.

D.1.3. Initial and Boundary Conditions

For the time $t = t_{\min}$, the conserved density function must be specified for the entire phase space

$$\psi(\mathbf{c}, \mathbf{r}, t) = \psi_{\text{ini}}(\mathbf{c}, \mathbf{r}) \quad t \in t_{\min} \quad (\text{D.16})$$

where t_{\min} is the lower boundary of the time domain. Since Eq. (5.1) contains two first-order partial differential operators, boundary conditions must be set for each dimension of the physical and property space. For a better discussion of the boundary conditions, Eq. (5.1) is integrated over the entire phase space and Gauss's theorem Eq. (D.1) is applied.

$$\frac{\partial \Psi}{\partial t} = \int_{\Omega(t)} \frac{\partial \psi}{\partial t} d\mathbf{C} = \int_{\Omega(t)} \Phi d\mathbf{C} - \oint_{\delta\Omega_r(t)} \psi \mathbf{v}_r \cdot d\mathbf{r} - \oint_{\delta\Omega_c(t)} \psi \mathbf{v}_c \cdot d\mathbf{c} \quad (\text{D.17})$$

For the physical space, if we have an open domain, parts of the boundary surface is usually defined as inflow $\psi \mathbf{v}_r$ at $\delta\Omega_{r,\text{part}}^{\text{inlet}}$ and others as outflow $\psi \mathbf{v}_r$ at $\delta\Omega_{r,\text{part}}^{\text{outlet}}$. Only one of these two flows is set by the boundary condition usually the inflow the other the outflow is calculated by the differential equation. However, if we have a closed domain, the fluxes must be zero everywhere at the boundaries $\delta\Omega_r$. But since only one can be set to zero by the boundary condition, the other must become zero by the model formulation, e.g. by a suitable choice of model parameters and the constitutive equations. If these are not chosen correctly and there is a flux greater than zero at this boundary, the conservation quantity Ψ is lost, which contradicts the assumption of a closed domain. This applies in particular to the property space, because this is usually regarded as closed or partially closed or open. Partially closed or open means that one of the boundaries is open and the other is closed. A common case is nucleation of particles at the lower boundary. Then we apply:

$$\dot{\psi}_0 = -(\mathbf{v}_c(\mathbf{c}, \mathbf{r}, t) \cdot \mathbf{n}_c) \psi(\mathbf{c}, \mathbf{r}, t) \quad \mathbf{c} \in \delta\Omega_{\mathbf{c},\text{min}} \quad (\text{D.18})$$

$$0 = (\mathbf{v}_c(\mathbf{c}, \mathbf{r}, t) \cdot \mathbf{n}_c) \psi(\mathbf{c}, \mathbf{r}, t) \quad \mathbf{c} \in \delta\Omega_{\mathbf{c},\text{max}} \quad (\text{D.19})$$

where $\dot{\psi}_0$ is the nucleation rate and \mathbf{n}_c is the local outer normal vector of $\partial\Omega_c$. Eq. (D.18) then acts as the boundary condition and Eq. (D.19) must be fulfilled by the model formulation and is called regularity condition [79].

D.2. Derivation of Growth Velocity

The growth velocity is defined as the total (time) derivative of the inner coordinate. For the one-dimensional case of the particle length it applies:

$$v_\xi = \frac{d\xi}{dt} \quad (\text{D.20})$$

The change in particle length over time can also be calculated by the change in its volume using the total time derivative (cf. Eq. (D.2)):

$$v_\xi = \frac{\partial V_d(\xi)}{\partial \xi}^{-1} \frac{dV_d(\xi)}{dt} \quad (\text{D.21})$$

If the definition of mass density $\rho_d(\xi, \mathbf{r}, t)$ is used, the change in particle volume over time can be related to a change in density and particle mass $m_d(\xi, \mathbf{r}, t)$ over time.

$$\frac{dV_d(\xi)}{dt} = \frac{d}{dt} \left(\frac{m_d(\xi, \mathbf{r}, t)}{\rho_d(\xi, \mathbf{r}, t)} \right) \quad (\text{D.22})$$

$$= \rho_d(\xi, \mathbf{r}, t)^{-1} \frac{dm_d(\xi, \mathbf{r}, t)}{dt} - \rho_d(\xi, \mathbf{r}, t)^{-2} m_d(\xi, \mathbf{r}, t) \frac{d\rho_d(\xi, \mathbf{r}, t)}{dt} \quad (\text{D.23})$$

$$= \rho_d(\xi, \mathbf{r}, t)^{-1} \frac{dm_d(\xi, \mathbf{r}, t)}{dt} - \rho_d(\xi, \mathbf{r}, t)^{-1} V_d(\xi) \frac{d\rho_d(\xi, \mathbf{r}, t)}{dt} \quad (\text{D.24})$$

If Eq. (D.24) is inserted into Eq. (D.21), the final equation for the growth rate for the one-dimensional length property case follows.

$$v_\xi = \left(\frac{dm_d(\xi, \mathbf{r}, t)}{dt} - V_d(\xi) \frac{d\rho_d(\xi, \mathbf{r}, t)}{dt} \right) \left(\frac{\partial V_d(\xi)}{\partial \xi} \rho_d(\xi, \mathbf{r}, t) \right)^{-1} \quad (\text{D.25})$$

This implies that growth can be attributed to changes in mass over time, resulting from mass transfer, or to changes in density over time, resulting from changes in temperature, pressure, or composition.

It is important to note that no additional assumptions were made during the derivation process. The resulting Eq. (D.25) is generally applicable to a one-dimensional length property that is affiliated with the particle's volume.

For spherical particles with $V_d(\xi) = \frac{\pi}{6} \xi^3$ it results:

$$v_\xi(\xi, \mathbf{r}, t) = -\frac{\xi}{3\rho_d(\xi, \mathbf{r}, t)} \frac{d\rho_d(\xi, \mathbf{r}, t)}{dt} + \frac{1}{\frac{\pi}{2} \xi^2 \rho_d(\xi, \mathbf{r}, t)} \frac{dm_d(\xi, \mathbf{r}, t)}{dt} \quad (\text{D.26})$$

E. Supplementary Information for Chapter 6

E.1. Additional Studies

E.1.1. Variation of Physiochemical Properties

Fig. E.3 illustrate the SMD ξ_{32} and interfacial area density a , respectively, as functions of different property data. The figure of the mass density function was omitted and can be found in Supplementary Information Fig. E.4.

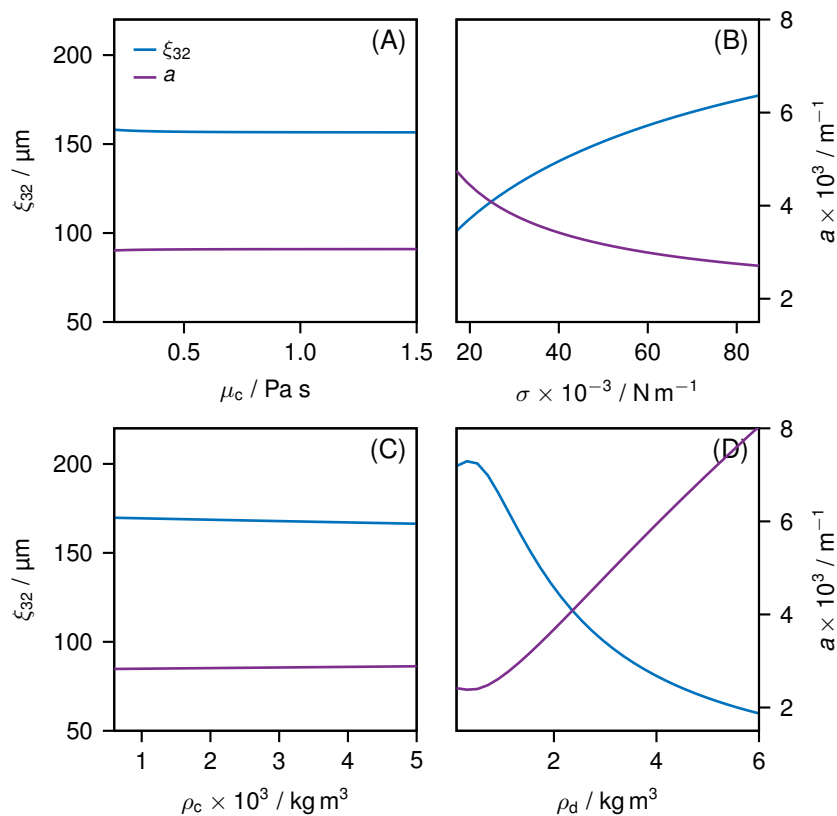


Figure E.1.: Sauter mean diameter ξ_{32} and the interfacial area density a as a function of different property data: (A) - viscosity of the continuous phase μ_c , (B) - surface tension σ , (C) - mass density of the continuous phase ρ_c , (D) - mass density of the dispersed phase ρ_d .

Despite the large viscosity range investigated, virtually no dependence of the SMD or interfacial area density could be found in the simulation (see Fig. E.1A). Experimentally, however, a strong influence towards larger bubbles is known [59, 148]. It should be noted once more that, in a real STR, the

alteration of liquid phase viscosity frequently results in changes to the gas holdup. The literature presents findings indicating both a proportional and an anti-proportional relationship between gas holdup and viscosity [149–151]. The results presented illustrate the relevance of adequate modeling of the influence of parameter variations on all variables (BSD, gas holdup) in order to ensure a valid description of the conditions in the real STR.

With respect to the surface tension (see Fig. E.1B), the fact that the diameter increases and thus the interfacial density decreases is in agreement with the experimental trend [59, 132, 152].

The slight trend of increasing breakage at increased liquid mass density shown here is also indicated by experimental observations described in literature, even if no experimental study with the liquid density as single varied parameter could be found [153, 154]. A numerical analysis of single bubble formation at an orifice according to Zahedi *et al.* [155] also confirms this trend of higher liquid density causing smaller bubbles [155]. Most likely, the movement of turbulent eddies is more efficient in highly dense liquids causing bubble breakage [155]. Although the trend observed here is less pronounced, which is due to the parameterization of the kernel.

The behavior of the SMD with regard to mass density of the gas phase is somewhat different. The SMD first increases until approx. 0.7 kg m^{-3} and then it decreases. The fact that more breakage occurs for gas densities $< 1.0 \text{ kg m}^{-3}$ is due to the fact that the gas density appears in the denominator in the breakage kernel used. Experimental values with such a high resolution to be able to reproduce this trend could not be found. However, the general trend that the bubbles become smaller with increasing gas density is in line with the experimental findings [156–158].

Figures E.3A and B illustrate the SMD ξ_{32} and interfacial area density a , respectively, as functions of the mass transfer coefficient k_{MT} for a condensation and evaporation of the gas phase.

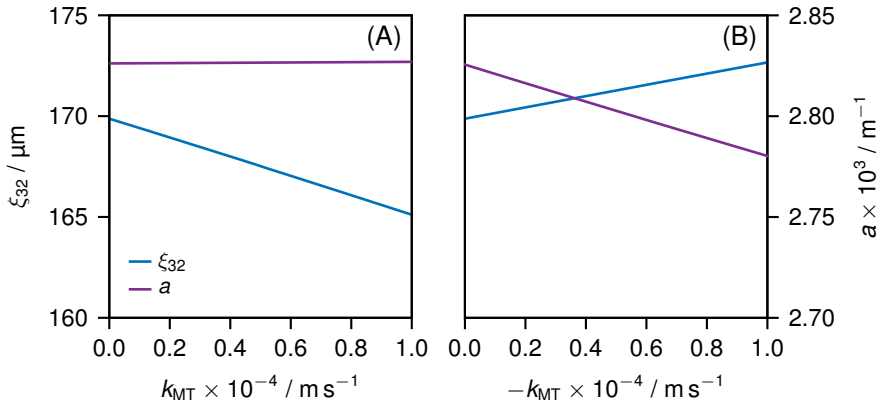


Figure E.2.: Sauter mean diameter ξ_{32} and the interfacial area density a as a function of the mass transfer coefficient k_{MT} for a (A) condensation and (B) evaporation of the gas phase.

If the scale of the y-axis is considered, it can be seen in both cases that the influence of the mass transfer is only very small, but corresponds to the expected behaviour that the bubbles become smaller in the case of condensation (cf. Fig. E.2A) and larger in the case of evaporation (cf. Fig. E.2B). The distributions are not shown because they hardly change noticeably.

Except for viscosity, the model, in particular the breakage and coalescence kernel of Coulaloglou *et al.* [53] used, can reproduce the general trends with respect to the variation of the physicochemical properties. It should be noted, however, that the trends shown are less pronounced than those found experimentally, especially for the liquid density. Apart from the influence of the artificial assumption

of constant gas holdup, we attribute this on one hand to our parameterization of the kernel and on the other hand to the fact that the kernels do not yet represent all phenomena correctly enough. Further intensive research is needed to develop generalized kernels and possibly standardized parameter estimation methods.

E.1.2. Design of the Gas Sparger

Fig. E.3A-C illustrate the SMD ξ_{32} and interfacial area density a , respectively, as functions of inlet distribution parameters: mean diameter μ_0 , standard deviation σ_0 and mean diameter of the second peak μ_1 of a bi-modal inlet distribution (see Eq. (E.13) with $mod = 2$) expressed as ratio $\frac{\mu_1}{\mu_0}$. Similarly, Fig. 6.5D-F present the mass density function f_d^m as a function of bubble size ξ for the various inlet distribution parameters.

Note that in this study, too, the gas holdup was kept constant, so the physical effect of larger bubbles created by larger sparger orifices having less residence time and thus less overall gas holdup cannot be reflected. However, it is acceptable for a robustness and sensitivity study.

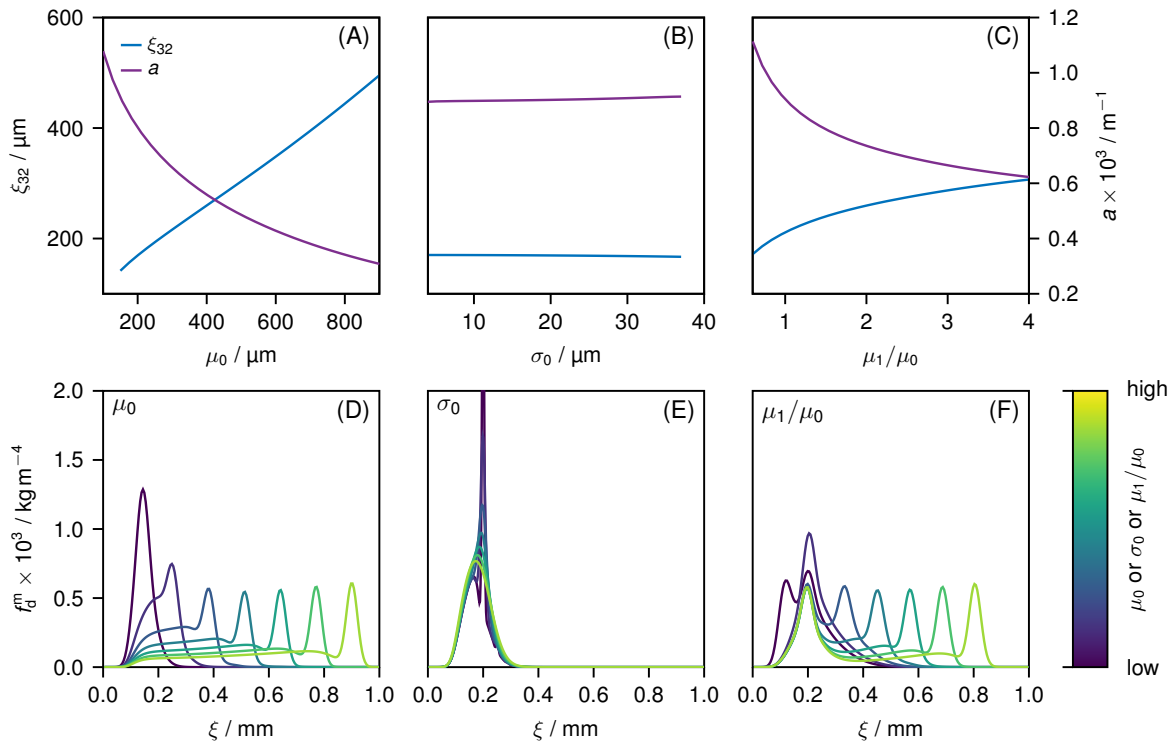


Figure E.3.: (A-C): Sauter mean diameter ξ_{32} and the interfacial area density a as a function of the inlet distribution parameters. (D-F): Mass density function f_d^m as a function of bubble size ξ for the inlet distribution parameters. Inlet distribution parameters: (A,D) - mean diameter μ_0 ; (B,E) - σ_0 standard deviation; (C,F) - mean diameter of the second peak μ_1 of a bi-modal inlet distribution (see Eq. (E.13) with $mod = 2$) expressed as ratio $\frac{\mu_1}{\mu_0}$. Applied parameters see Tab. E.2 and Tab. E.3.

Fig. E.3A and D demonstrate the significant influence of the mean value of the inlet distribution on the SMD and the shape of the BSD. A notable decrease in interfacial area density alongside a considerable increase in bubble diameter is observed with increasing mean value of the inlet distribution. This model prediction is consistent with experimental findings reported in the literature for stirred tank reactors [159] or with respect to bubble columns [160, 161].

In contrast to the mean value, the width of the inlet distribution has a minimal impact on the SMD and interfacial area density (Fig. E.3B), indicating that breakage and coalescence occur in appear equally strong. Peaks at approx. $\xi = 0.16$ mm and hardly to see at approx. $\xi = 0.25$ mm in some distributions result from a cascading effect of binary breakage and coalescence (cf. Fig. E.3E). The occurrence of narrow distributions is associated with an elevated probability of breakage or coalescence at the peak, which in turn gives rise to the formation of new peaks at smaller or larger bubbles. These new peaks are also prone to breakage or coalescence, thereby perpetuating the cascade. However, distributions that are wider and more continuous mitigate this effect. In any case, the numerical simulation method FVMG is capable of accurately capturing these sharp peaks without any smearing or oscillation.

In the process of designing spargers, it is typical to utilize a variety of orifice diameters to account for pressure loss within the sparger (such as within the arms of a spider sparger) and to ensure an even distribution of gas flux through all orifices. This design could result (in average) in bi-modal or multi-modal inlet distributions. Fig. E.3C and F show the influence of a bi-modal inlet distribution. It can be observed that the SMD increases as the diameter of the second peak increases and the interfacial area density decreases accordingly. An examination of Fig. E.3F reveals that while the two peaks of the inlet distribution persist, a broad transition is established, which becomes increasingly diminished as the distance between the peaks increases.

In summary, the mean value and the mode of distribution have a large influence on the BSD. However, the effect on the gas holdup, which can strongly influence the observed trends (see Section 6.4.2), cannot be neglected. Thus, these two values are likely to have a significant influence on the gas-liquid mass transfer in the reactor and thus, as expected, on the overall reactor performance. On the other hand, the width of the inlet BSD generated by the sparger seems to have little influence on the BSD. Although the estimation of the initial and inlet distribution from the sparger geometry is difficult [3], the MPB tool now offers a simple and quick way to clarify the question of how different spargers could affect the process in principle.

E.2. Model Details

E.2.1. Constitutive Equations

To close the model, the following constitutive equations were applied.

Volume of a sphere:

$$V(\xi) = \frac{\pi}{6} \xi^3 \quad (\text{E.1})$$

Coalescence kernel set 1 [53]:

$$h(\xi, \zeta) = C_{cf} \frac{\varepsilon^{1/3}}{1 + \alpha_d(z)} (\xi + \zeta)^2 \sqrt{\xi^{2/3} + \zeta^{2/3}} \quad (\text{E.2})$$

$$\lambda(\xi, \zeta) = \exp\left(-C_1 \frac{\mu_c \rho_c \varepsilon}{\sigma(1 + \alpha_d)^3} \left(\frac{\xi \zeta}{\xi + \zeta}\right)^4\right) \quad (\text{E.3})$$

Coalescence kernel set 2 [117, 119]:

$$h(\xi, \zeta) = \exp\left(-700 \left(\frac{\rho_c \varepsilon^{2/3} \xi_{eq}^{5/3}}{4\sigma}\right)^{1/2}\right) \quad (\text{E.4})$$

$$\lambda(\xi, \zeta) = 0.07 \exp\left(-\frac{\rho_c^{1/2} \xi_{eq}^{5/6} \varepsilon^{1/3}}{4\sigma^{1/2}} \ln\left(\frac{10^{-4}}{10^{-8}}\right)\right) \quad (\text{E.5})$$

$$\xi_{eq} = \frac{1}{4} \left(\frac{1}{\xi} + \frac{1}{\zeta}\right)^{-1} \quad (\text{E.6})$$

Breakage kernel set 1 [53, 106]:

$$b(\xi) = C_{bf} \frac{\varepsilon^{1/3}}{\xi^{2/3}} \exp\left(-\frac{\sigma C_2}{\rho_d \varepsilon^{2/3} \xi^{5/3}}\right) \quad (\text{E.7})$$

$$P(\xi, \zeta) = \frac{2.4 \left(\frac{\pi}{2} \xi^2\right)}{V(\zeta)} \exp\left(-4.5 \frac{(2V(\xi) - V(\zeta))^2}{V(\zeta)^2}\right) \quad (\text{E.8})$$

$$\nu = 2.0 \quad (\text{E.9})$$

Breakage kernel set 2 [106, 118]:

$$b(\xi) = 0.3784 \varepsilon^{1/3} \operatorname{erf}\left(\sqrt{10^{-6} \frac{\sigma}{\rho_c \varepsilon^{5/3}} + 10^{-5} \frac{\mu_d}{\rho_d \rho_c \varepsilon^{1/3} \xi^{4/3}}}\right) \quad (\text{E.10})$$

$$P(\xi, \zeta) = \left(\frac{\Gamma(q\nu)}{\Gamma(q)\Gamma(q(\nu-1))}\right) \left(\frac{\xi}{\zeta}\right)^{3(q-1)} \left(1 - \left(\frac{\xi}{\zeta}\right)^3\right)^{q(\nu-1)-1} \frac{\xi^2}{\zeta^3} \quad (\text{E.11})$$

$$\nu = 2.0, q = 2.0 \quad (\text{E.12})$$

Initial/Inlet Distribution:

$$f_{d,ini}^m(\xi) = \frac{\rho_d \alpha_{d,ini}}{mod} \sum_{i=0}^{mod-1} \frac{1}{\sqrt{2\pi\sigma_i^2}} \exp\left(-\frac{1}{2} \frac{(\xi - \mu_i)^2}{\sigma_i^2}\right) \quad (\text{E.13})$$

$$f_{d,in}^m(\xi) = f_{d,ini}^m(\xi) \quad (\text{E.14})$$

Mass transfer:

$$\frac{dm_d}{dt} = \pi \xi^2 \rho_d(t) k_{MT} \Delta w \quad (\text{E.15})$$

Outlet mass flow rate:

$$\dot{m}_{out} = \dot{m}_{in} + V_R \left(\int_{\xi_{min}}^{\xi_{max}} \frac{f_d^m(\xi, t)}{V(\xi)} \frac{1}{\rho_d} \frac{dm_d}{dt} d\xi + J_d^m \right) - \alpha_d V_R \frac{\partial \rho_d(t)}{\partial t} \quad (\text{E.16})$$

The new symbols introduced in the above equations are specified in the nomenclature. A derivation of Eq. (E.16) can be found in the Supplementary Information E.3.1.

E.2.2. Additional Equations

The additional equations used are listed below.

Number-based to mass-based density function:

$$f_d^n(\xi, t) = \frac{f_d^m(\xi, t)}{\rho_d V(\xi)} \quad (\text{E.17})$$

Gas volume fraction:

$$\alpha_d(t) = \int_{\xi_{min}}^{\xi_{max}} \frac{f_d^m(\xi, t)}{\rho_d(t)} d\xi \quad (\text{E.18})$$

Interfacial area density:

$$a = \pi \int_{\xi_{min}}^{\xi_{max}} \xi^2 f_d^n(\xi, t) d\xi \quad (\text{E.19})$$

Sauter mean diameter:

$$\xi_{32} = \frac{\int_{\xi_{min}}^{\xi_{max}} \xi^3 f_d^n(\xi, t) d\xi}{\int_{\xi_{min}}^{\xi_{max}} \xi^2 f_d^n(\xi, t) d\xi} \quad (\text{E.20})$$

E.2.3. Applied Parameters in the Simulations

The following tables summarize the parameters used in the simulations.

Table E.1.: Applied parameters in the comparison of numerical solution methods. Analytical solution and model equations given in the reference below and Alzyod *et al.* [89].

| Symbol | Values | | | |
|----------------------|-----------------|--------------------|---------------|-----------------------|
| | <i>Case 1</i> | <i>Case 2</i> | <i>Case 3</i> | <i>Case 4</i> |
| ξ_{\min} | 1 | 5×10^{-4} | 0.01 | 2×10^{-6} |
| ξ_{\max} | 180 | 2.0 | 2.0 | 1000×10^{-6} |
| N_{ξ} | 100 | 100 | 100 | 200* |
| $N_{\xi,\text{int}}$ | | | 100 | 200* |
| t | (0,50) | (0,1) | (0,15) | (0,10) |
| (a, b, c) | (0.0, 1.0, 0.0) | (1.8, 0.0, 0.0) | | |
| J | 0 | 20 | 0 | 0 |
| C_{bf} | | | | 10.2×10^8 |
| C_{cf} | | | | 8×10^{-7} |
| Reference | [100] | [98] | [103] | [99] |

* $N_{\xi}=80$, $N_{\xi,\text{int}}=100$ for OC

Table E.2.: Applied default parameters in the parameter studies.

| <i>Property data</i> | | | <i>Process conditions</i> | | |
|-------------------------|--------------------|--------------------|---------------------------|---------------------|----------------------------|
| Symbol | Value | Unit | Symbol | Value | Unit |
| ρ_{d} | 1.18 | kg m^{-3} | ε | 0.6 | $\text{m}^2 \text{s}^{-3}$ |
| ρ_{c} | 1000 | kg m^{-3} | $\alpha_{\text{d,ini}}$ | 0.08 | - |
| σ | 72 | mJ m^{-2} | $\dot{m}_{\text{d,in}}$ | 0.02 | kg s^{-1} |
| μ_{c} | 0.001 | Pas | Δw | -6×10^{-6} | kg kg^{-1} |
| k_{MT} | 1×10^{-5} | m s^{-1} | J_{d}^{m} | 0.0 | kg m^{-3} |
| | | | <i>mod</i> | 1 | - |
| <i>Reactor Geometry</i> | | | <i>Dispersed Phase</i> | | |
| Symbol | Value | Unit | Symbol | Value | Unit |
| V_{R} | 1.0 | m^3 | C_{cf} | 1×10^{-3} | - |
| μ_0 | 200 | μm | C_1 | 5×10^{12} | m^{-2} |
| σ_0 | 20 | μm | C_{bf} | 6×10^{-3} | - |
| | | | C_2 | 1×10^{-5} | - |
| | | | ξ_{\min} | 2 | μm |
| N_{ξ} | 500 | | ξ_{\max} | 1000 | μm |
| $N_{\xi,\text{int}}$ | 500 | | | | |

Table E.3.: Varied and applied parameter ranges in the parameter studies.

| Symbol | Min. Value | Max. Value | Unit |
|-------------------------|----------------------|---------------------|-------------------------|
| ε | 0.1 | 5.0 | $\text{m}^2 \text{s}^3$ |
| $\alpha_{\text{d,ini}}$ | 0.01 | 0.3 | - |
| $\dot{m}_{\text{d,in}}$ | 0.01 | 0.1 | kg s^{-1} |
| k_{MT} | 1×10^{-8} | 1×10^{-4} | m s^{-1} |
| k_{MT} | -1×10^{-8} | -2×10^{-4} | m s^{-1} |
| μ_0 | 150 | 900 | μm |
| σ_0 | 4 | 37 | μm |
| μ_1 | 120 | 800 | μm^* |
| μ_{c} | 0.2×10^{-3} | 1.5 | Pa s |
| σ | 17 | 85 | mJ m^{-2} |
| ρ_{c} | 600 | 5000 | kg m^{-3} |
| ρ_{d} | 0.1 | 6 | kg m^{-3} |
| C_{bf} | 5×10^{-5} | 0.5 | - |
| C_{cf} | 3×10^{-5} | 0.013 | - |

* $\text{mod} = 2$

Table E.4.: Applied parameters in the model application.

| <i>Property data</i> | | | <i>Process conditions</i> | | |
|----------------------|-------|---------------------|---------------------------|-------|----------------------------|
| Symbol | Value | Unit | Symbol | Value | Unit |
| ρ_{d} | 1.2 | kg m^{-3} | ε | 0.156 | $\text{m}^2 \text{s}^{-3}$ |
| ρ_{c} | 1000 | kg m^{-3} | $\alpha_{\text{d,ini}}$ | 0.06 | - |
| σ | 72 | mJ m^{-2} | $\dot{m}_{\text{d,in}}$ | 0.055 | g s^{-1} |
| μ_{c} | 1.0 | mPa s | Δw | 0 | kg kg^{-1} |
| μ_{d} | 0.18 | mPa s | J_{d}^{m} | 0 | kg m^{-3} |
| $w_{\text{c,EtOH}}$ | 0.01 | kg kg^{-1} | | | |

| <i>Reator Geometry</i> | | | <i>Dispersed Phase</i> | | |
|------------------------|-------|--------------|------------------------|-----------------------|-----------------|
| Symbol | Value | Unit | Symbol | Value | Unit |
| V_{R} | 0.027 | m^3 | C_{cf} | 1.89×10^{-6} | - |
| d_{R} | 0.3 | m | C_1 | 4.28×10^{11} | m^{-2} |
| | | | C_{bf} | 6.24×10^{-3} | - |
| | | | C_2 | 5.00×10^{-6} | - |
| | | | ξ_{min} | 1 | μm |
| | | | ξ_{max} | 2000 | μm |

| <i>Numerics</i> | | |
|----------------------|-----|--|
| N_{ξ} | 400 | |
| $N_{\xi,\text{int}}$ | 400 | |

E.3. Model Derivations

E.3.1. Derivation of the Outlet Mass Flow Rate

To derive an expression for \dot{m}_{out} , the assumption that the reactor volume V_{R} is constant and does not move is used (the substantial derivative reduces to a partial derivative). Furthermore, the reactor volume can be represented as the sum of the enclosed fluids. So it follows:

$$\frac{dV_{\text{R}}}{dt} = \frac{\partial V_{\text{R}}}{\partial t} = 0 \quad (\text{E.21})$$

$$= \frac{\partial V_{\text{d}}}{\partial t} + \frac{\partial V_{\text{c}}}{\partial t} \quad (\text{E.22})$$

The liquid phase can generally be regarded as incompressible, from which follows $\frac{\partial V_{\text{c}}}{\partial t} = 0$. If this is used

$$\frac{\partial V_{\text{d}}}{\partial t} = 0 \quad (\text{E.23})$$

$$\hat{=} \frac{\partial \alpha_{\text{d}}}{\partial t} \quad (\text{E.24})$$

it can be concluded that the volume of the dispersed phase in the reactor is always constant respectively the gas holdup. If the definition of mass density and the chain rule are applied to Eq. (E.23) we get:

$$\frac{\partial V_{\text{d}}}{\partial t} = \frac{\partial}{\partial t} \left(\frac{m_{\text{d}}}{\rho_{\text{d}}} \right) \quad (\text{E.25})$$

$$= \frac{1}{\rho_{\text{d}}} \frac{\partial m_{\text{d}}}{\partial t} - \frac{m_{\text{d}}}{\rho_{\text{d}}^2} \frac{\partial \rho_{\text{d}}}{\partial t} \quad (\text{E.26})$$

Now an expression for the total mass of the dispersed phase (m_{d}) follows from a simple mass balance.

$$\frac{\partial m_{\text{d}}}{\partial t} + \nabla \cdot (\mathbf{v}_{\text{r}} m_{\text{d}}) = \Gamma_{\text{d}} V_{\text{R}} \quad (\text{E.27})$$

Where Γ_{d} is the mass transfer rate per volume due to phase change and where $m_{\text{d}} = \rho_{\text{d}} \alpha_{\text{d}} V_{\text{R}}$ and constant V_{R} was used. If the Eq. (E.27) integrated and divided over/by the reactor volume it follows:

$$\dot{m}_{\text{d}} + \dot{m}_{\text{d,out}} - \dot{m}_{\text{d,in}} = \Gamma_{\text{d}} V_{\text{R}} \quad (\text{E.28})$$

where $\frac{\partial m_{\text{d}}}{\partial t} = \dot{m}_{\text{d}}$ and $\dot{m}_{\text{d,out}} = A_{\text{R}}/V_{\text{R}} v_{\text{r,out}} m_{\text{d,out}}$ was used. If Eq. (E.28) is inserted into Eq. (E.26) and converted to $\dot{m}_{\text{d,out}}$ using Eq. (E.23), we obtain:

$$\dot{m}_{\text{d,out}} = \dot{m}_{\text{d,in}} + \Gamma_{\text{d}} V_{\text{R}} - \frac{m_{\text{d}}}{\rho_{\text{d}}} \frac{\partial \rho_{\text{d}}}{\partial t} \quad (\text{E.29})$$

The term before the temporal mass density changes can be converted to $\alpha_{\text{d}} V_{\text{R}}$ by applying the definition of the mass density and the gas volume fraction. The mass transfer rate Γ_{d} can be determined as the sum over the change in mass of the individual bubbles. Instead of summing over the individual bubbles, it can also be integrated over the BSD distribution. Since nucleation occurs in the system, this is taken into account as an additional term.

$$\Gamma_{\text{d}} = \sum_i \frac{1}{V_{\text{R}}} \frac{dm_{\text{d}}}{dt} + J_{\text{d}}^{\text{n}} \quad (\text{E.30})$$

$$= \int_{\xi_{\text{min}}}^{\xi_{\text{max}}} f_{\text{d}}^{\text{n}}(\xi, t) \frac{dm_{\text{d}}}{dt} d\xi + J_{\text{d}}^{\text{n}} \quad (\text{E.31})$$

Finally, if the number based BSD $f_d^n(\xi, t)$ is converted into a mass-based one with the formula Eq. (E.17), Eq. (E.16) follows.

E.3.2. Simplification of the Generalized PBE to STR Application

Instead of simplifying the very lengthy KTAWSR [26], we start from a generalized PBE. However, the result is the same. Starting from a generalized PBE [73] with 1D particle size property space we get:

$$\begin{aligned} & \frac{\partial f_d^m(\xi, \mathbf{r}, t)}{\partial t} + \nabla_{\mathbf{r}} \cdot (\mathbf{v}_{\mathbf{r}}(\xi, \mathbf{r}, t) f_d^m(\xi, \mathbf{r}, t)) + \frac{\partial}{\partial \xi} (v_{\xi}(\xi, \mathbf{r}, t) f_d^m(\xi, \mathbf{r}, t)) \\ & = \frac{f_d^m(\xi, \mathbf{r}, t)}{V(\xi)} \frac{1}{\rho_d(\xi, \mathbf{r}, t)} \frac{dm_d}{dt} - B_D^m(\xi, \mathbf{r}, t) + B_B^m(\xi, \mathbf{r}, t) - C_D^m(\xi, \mathbf{r}, t) + C_B^m(\xi, \mathbf{r}, t) \end{aligned} \quad (\text{E.32})$$

If the Eq. (E.32) is averaged over the reactor volume, which means integrated and divided by the averaging volume, the reactor volume, and Gauss' theorem is applied to the convection term in physical space, the following results:

$$\begin{aligned} & \frac{1}{V_R} \int_{V_R} \frac{\partial f_d^m(\xi, \mathbf{r}, t)}{\partial t} dV + \frac{1}{V_R} \int_{\delta V_R} (\mathbf{v}_{\mathbf{r}}(\xi, \mathbf{r}, t) f_d^m(\xi, \mathbf{r}, t)) \cdot d\mathbf{A} + \frac{1}{V_R} \int_{V_R} \frac{\partial}{\partial \xi} (v_{\xi}(\xi, \mathbf{r}, t) f_d^m(\xi, \mathbf{r}, t)) dV \\ & = \frac{1}{V_R} \int_{V_R} \frac{f_d^m(\xi, \mathbf{r}, t)}{V(\xi)} \frac{1}{\rho_d(\xi, \mathbf{r}, t)} \frac{dm_d}{dt} - B_D^m(\xi, \mathbf{r}, t) + B_B^m(\xi, \mathbf{r}, t) - C_D^m(\xi, \mathbf{r}, t) + C_B^m(\xi, \mathbf{r}, t) dV \end{aligned} \quad (\text{E.33})$$

Strictly speaking, this corresponds to volume averaging, and the volume averaging theorems [162] should be applied. Next, the averages of products would have to be related to products of averages. This results in new unclosed terms that either have to be described or neglected. We abbreviate these steps for the sake of brevity and assume that the values within the volume integrals do not depend on the location, so that these can be omitted. Furthermore, we refrain from labeling these now volume-averaged values separately. It follows:

$$\begin{aligned} & \frac{\partial f_d^m(\xi, t)}{\partial t} + \frac{1}{V_R} \int_{\delta V_R} (\mathbf{v}_{\mathbf{r}}(\xi, \mathbf{r}, t) f_d^m(\xi, \mathbf{r}, t)) \cdot d\mathbf{A} + \frac{\partial}{\partial \xi} (v_{\xi}(\xi, t) f_d^m(\xi, t)) \\ & = \frac{f_d^m(\xi, t)}{V(\xi)} \frac{1}{\rho_d(\xi, t)} \frac{dm_d}{dt} - B_D^m(\xi, t) + B_B^m(\xi, t) - C_D^m(\xi, t) + C_B^m(\xi, t) \end{aligned} \quad (\text{E.34})$$

Only the second term on the right-hand side of Eq. (E.34) needs to be further processed. Since the boundary area δV_R of V_R is only permeable on two surfaces, the inlet and the outlet, this surface integral breaks down into two parts. Taking into account the surface normal of the surface element and assuming that the values within the integral are constant on the respective surface resp. we do the same trick as before with now area averaging, we get:

$$\frac{1}{V_R} \int_{\delta V_R} (\mathbf{v}_{\mathbf{r}}(\xi, \mathbf{r}, t) f_d^m(\xi, \mathbf{r}, t)) \cdot d\mathbf{A} = \frac{A_{\text{out}}}{V_R} v_{\mathbf{r}, \text{out}}(\xi, t) f_{d, \text{out}}^m(\xi, t) - \frac{A_{\text{in}}}{V_R} v_{\mathbf{r}, \text{in}}(\xi, t) f_{d, \text{in}}^m(\xi, t) \quad (\text{E.35})$$

The inlet distribution $f_{d, \text{in}}^m(\xi, t)$ is assumed to be known. Due to the ideal mixed assumption, $f_{d, \text{out}}^m(\xi, t) = f_d^m(\xi, t)$ follows. The terms preceding the distribution functions can now be converted into a volume flow rate by expanding them by the gas volume fraction and into a mass flow rate by further expanding them by the mass density. This results in the following expression for the outlet term:

$$\frac{A_{\text{out}}}{V_R} v_{\mathbf{r}, \text{out}}(\xi, t) f_{d, \text{out}}^m(\xi, t) = \frac{A_{\text{out}} \alpha_d(t) v_{\mathbf{r}, \text{out}}(\xi, t)}{V_R \alpha_d(t)} f_d^m(\xi, t) = \frac{\dot{V}_{d, \text{out}}(\xi, t)}{V_R \alpha_d(t)} f_d^m(\xi, t) \quad (\text{E.36})$$

$$= \frac{\dot{V}_{d, \text{out}}(\xi, t) \rho_d(\xi, t)}{V_R \alpha_d(t) \rho_d(\xi, t)} f_d^m(\xi, t) = \frac{\dot{m}_{d, \text{out}}(\xi, t) \rho_d(\xi, t)}{V_R \alpha_d(t)} f_d^m(\xi, t) \quad (\text{E.37})$$

If the Eq. (E.18) is employed to calculate the gas volume fraction from the mass density function, the Eq. (E.37) could be further simplified to:

$$\frac{\dot{m}_{d,\text{out}}(\xi, t)\rho_d(\xi, t)}{V_R\alpha_d}f_d^m(\xi, t) = \frac{\dot{m}_{d,\text{out}}(\xi, t)}{V_R} \frac{f_d^m(\xi, t)}{\int_{\xi_{\min}}^{\xi_{\max}} f_d^m(\xi, t)d\xi} \quad (\text{E.38})$$

$$\approx \frac{\dot{m}_{d,\text{out}}(t)}{V_R} \frac{f_d^m(\xi, t)}{\int_{\xi_{\min}}^{\xi_{\max}} f_d^m(\xi, t)d\xi} \quad (\text{E.39})$$

The inlet flow term follows analogously. This means that only the size-dependent mass or volume flow rate of the gas phase at inlet and outlet remain unknown (cf. Eq. (E.38)). These flow rates could now be determined using experimental results or an additional model. For the sake of simplicity, however, we assume that the in- and outlet mass or volume flow rate is independent of the bubble size, which corresponds to the assumption that all bubbles have the same effective velocity or residence time resulting in the finale Eq. (E.39).

E.3.3. Conversion Rules for Comparison Experiment and Simulation

In order to use experimentally measured BSD $\hat{f}_{d,\text{exp}}^n$ for the simulation, e.g. as initial distribution, it must be converted into a number or mass density function. Since the experimentally measured BSD represents a normalized distribution without information on how many bubbles or how much dispersed phase mass is in the system, further information is needed to represent this, the gas holdup provides this information. In order to use this, we derive the necessary equation below.

Starting from the definition of the normalized number density distribution Eq. (E.40).

$$\hat{f}_d^n(\xi, t) = \frac{f_d^n(\xi, t)}{\int_{\xi_{\min}}^{\xi_{\max}} f_d^n(\xi, t)d\xi} \quad (\text{E.40})$$

$$= \frac{f_d^n(\xi, t)}{n_d(t)} \quad (\text{E.41})$$

where the definition of the number density or the number of particles per volume $n_d(t) = \int_{\xi_{\min}}^{\xi_{\max}} f_d^n(\xi, t)d\xi$ was used. The definition of the gas volume fraction Eq. (E.42) is used to determine the number density.

$$\alpha_d = n_d\bar{V}_\xi \quad (\text{E.42})$$

This is obtained from the product of the n_d number density and the mean bubble volume \bar{V}_ξ . The mean bubble volume can be calculated on the basis of Eq. (E.43), which only requires a normalized distribution.

$$\bar{V}_\xi = \frac{\pi}{6} \int_{\xi_{\min}}^{\xi_{\max}} \xi^3 \hat{f}_d^n(\xi, t)d\xi \quad (\text{E.43})$$

If the Eq. (E.43), Eq. (E.42) and Eq. (E.41) are inserted into each other, the conversion rule follows:

$$f_d^n = \hat{f}_d^n \frac{\alpha_d}{\frac{\pi}{6} \int_{\xi_{\min}}^{\xi_{\max}} \xi^3 \hat{f}_d^n(\xi, t)d\xi} \quad (\text{E.44})$$

Here \hat{f}_d^n could be an experimental BSD. The conversion to a mass density function is then carried out using Eq. (E.17). The other way around is simply accomplished by using Eq. (E.40).

E.4. Finite Volume Method with Gauss Quadrature – FVMG

E.4.1. Grid points

A cell-centered equidistant grid with a cell width of $\Delta\xi$ according to Eq.(E.46) is used.

$$\Delta\xi = \frac{\xi_{\max} - \xi_{\min}}{N_\xi} \quad (\text{E.45})$$

$$\xi \in \xi_{\min} + \frac{2i-1}{2}\Delta\xi \quad \text{for } i = 1, 2, \dots, N_\xi \quad (\text{E.46})$$

The function `range(start, stop, length)` from `Base.jl` was used to calculate the grid points.

E.4.2. Convection

A high-resolution scheme with a flux limiter was used to discretize the convection term in property space, see Eq. (E.47) and following. An application to the convection term in physical space should also be possible, perhaps with a different flux limiter. In Chapter 6 we used a monotonic upstream-centered scheme for conservation laws (MUSCL) according to van Leer [163] scheme which is total variation diminishing. Based on the slope, which is determined by the smoothness indicator Eq. (E.49), a high resolution scheme switches to a non oscillating low order scheme, e.g. first order upwind, in areas with a large slope, e.g. around discontinuities, and to an more accurate higher order scheme with less numerical diffusion, e.g. central scheme, in areas with a small slope (smooth areas). The extent to which the two methods, lower and higher order, are "mixed" is determined by the flux limiter Eq. (E.50). The MUSCL scheme according to [163] is summarized below with a flux limiter according to van Leer [164].

$$\frac{\partial(v_\xi(\xi_i)f(\xi_i))}{\partial\xi} \approx \frac{1}{\Delta\xi_i} (F_{i+1/2} - F_{i-1/2}) \quad (\text{E.47})$$

$$F_i = v_\xi(\xi_i)f(\xi_i) \quad (\text{E.48})$$

$$s_i = \frac{F_i - F_{i-1} + \epsilon}{F_{i+1} - F_i + \epsilon} \quad (\text{E.49})$$

$$\Phi(s_i) = \frac{|s_i| + s_i}{1 + |s_i|} \quad (\text{E.50})$$

$v_\xi(\xi_i) > 0$

$$F_{i+1/2} = F_i + \frac{1}{2}\Phi(s_i)(F_{i+1} - F_i) \quad (\text{E.51})$$

$$F_{i-1/2} = F_{i-1} + \frac{1}{2}\Phi(s_{i-1})(F_i - F_{i-1}) \quad (\text{E.52})$$

$v_\xi(\xi_i) < 0$

$$F_{i+1/2} = F_{i+1} + \frac{1}{2}\Phi(s_{i+1})(F_{i+2} - F_{i+1}) \quad (\text{E.53})$$

$$F_{i-1/2} = F_i + \frac{1}{2}\Phi(s_i)(F_{i-1} - F_i) \quad (\text{E.54})$$

$$(\text{E.55})$$

Where ϵ was added to the smoothness indicator Eq. (E.49) to avoid diving by zero, $\epsilon = 1 \times 10^{-32}$. The above scheme is not applicable for the first two and the last cell nodes resp. the last two and the the first (depending on the sign of v_ξ), otherwise ghost points would have to be introduced, instead a

first order upwind scheme is used.

$v_\xi(\xi_i) > 0$

$$\frac{\partial (v_\xi(\xi_1)f(\xi_1))}{\partial \xi} \approx \frac{1}{\Delta \xi_1} (F_1 - F_0) \quad (\text{E.56})$$

$$\frac{\partial (v_\xi(\xi_2)f(\xi_2))}{\partial \xi} \approx \frac{1}{\Delta \xi_2} (F_{2+1/2} - F_1) \quad (\text{E.57})$$

$$\frac{\partial (v_\xi(\xi_{N_\xi})f(\xi_{N_\xi}))}{\partial \xi} \approx \frac{-F_{N_\xi-1/2}}{\Delta \xi_{N_\xi}} \quad (\text{E.58})$$

$v_\xi(\xi_i) < 0$

$$\frac{\partial (v_\xi(\xi_1)f(\xi_1))}{\partial \xi} \approx \frac{1}{\Delta \xi_1} (F_{1+1/2} + F_0) \quad (\text{E.59})$$

$$\frac{\partial (v_\xi(\xi_{N_\xi-1})f(\xi_{N_\xi-1}))}{\partial \xi} \approx \frac{1}{\Delta \xi_{N_\xi-1}} (F_{N_\xi} - F_{N_\xi-1-1/2}) \quad (\text{E.60})$$

$$\frac{\partial (v_\xi(\xi_{N_\xi})f(\xi_{N_\xi}))}{\partial \xi} \approx \frac{-F_{N_\xi}}{\Delta \xi_{N_\xi}} \quad (\text{E.61})$$

Where F_0 is a boundary flux i.e. the nucleation rate.

E.4.3. Interpolation

In Chapter 6 we used piece-wise cubic Hermite spline interpolation [112] because it preserves the monotonicity (i.e. it will not under- or overshoot). The scheme is summarized in Eq. (E.62) - Eq. (E.68) where a three point finite difference was used in order to determine the slope g_i .

$$f(\xi) \approx \psi_{00}(\xi')\xi_i f_i + \psi_{10}(\xi')(\xi_{i+1} - \xi_i)s_i + \psi_{01}(\xi')f_{\xi_{i+1}} + \psi_{11}(\xi')(\xi_{i+1} - \xi_i)s_{i+1} \quad (\text{E.62})$$

$$\psi_{00}(\xi') = (1 + 2\xi')(1 - \xi')^2 \quad (\text{E.63})$$

$$\psi_{10}(\xi') = \xi'(1 - \xi')^2 \quad (\text{E.64})$$

$$\psi_{01}(\xi') = \xi'^2(3 - 2\xi') \quad (\text{E.65})$$

$$\psi_{11}(\xi') = \xi'^2(\xi' - 1) \quad (\text{E.66})$$

$$\xi' = \frac{\xi - \xi_i}{\xi_{i+1} - \xi_i} \quad (\text{E.67})$$

$$g_i = \frac{1}{2} \left(\frac{f_{i+1} - f_i}{\xi_{i+1} - \xi_i} + \frac{f_i - f_{i-1}}{\xi_i - \xi_{i-1}} \right) \quad (\text{E.68})$$

Instead of an own implementation the package `PCHIPInterpolation.jl` was used. Due to the fact that a cell center scheme was used but the breakage and coalescence spans the entire domain including the boundary points, it is necessary to extrapolate towards them. To accomplish this, a constant slope based on linear interpolation was assumed wherefore the package `Interpolations.jl` was used.

E.4.4. Gauss Quadrature

For the approximation of integrals a Gauss quadrature rule [110] was used which is defined on a limited interval $[-1,1]$, e.g. Gauss-Legendre or Gauss-Legendre-Lobatto. The only difference between these two is that Gauss-Legendre-Lobatto includes the boundary points $-1,1$ and Gauss-Legendre does not. Gauss-Legendre was used in Chapter 6, as the boundary values in the coalescence birth term assume very large values that are difficult to integrate. Eq. (E.69) shows the integration rule, where the standard interval $[-1,1]$ has already been transformed to an arbitrary $[\xi_{\min}, \xi_{\max}]$ interval (indicated with *) using Eq. (E.70) and Eq. (E.71). The nodes $\tilde{\xi}_i$ and weights $\tilde{\omega}_i$ on the interval $[-1,1]$ were calculated with the function `gausslegendre($N_{\xi,\text{int}}$)` from the packet `FastGaussQuadrature.jl`.

$$\int_{\xi_{\min}}^{\xi_{\max}} f(\xi) d\xi \approx \sum_{i=1}^{N_{\xi,\text{int}}} f(\xi_i^*) \omega_i^* \quad (\text{E.69})$$

$$\tilde{\xi}_i^* = \frac{\xi_{\max} - \xi_{\min}}{2} \tilde{\xi}_i + \frac{\xi_{\max} + \xi_{\min}}{2} \quad (\text{E.70})$$

$$\tilde{\omega}_i^* = \frac{\xi_{\max} - \xi_{\min}}{2} \tilde{\omega}_i \quad (\text{E.71})$$

E.5. Used Packages and Version

The programming language Julia [113] in the Version 1.10 was used to implement the MPB. The `DifferentialEquations.jl` package with the algorithm `CVODE_BDF(linear_solver = :GMRES)` from the `Sundials.jl` [165, 166] package was used for solving the system of ODEs. In order to calculate a steady-state solution the functionality of the `DifferentialEquations.jl` package was used. There a transient problem can be transformed into a steady-state problem using the same algorithm as before within the steady-state algorithm `DynamicSS()` with $abstol = 10^{-4}$, $reltol = 10^{-3}$, $dt_{ini} = 10^{-6}$. Higher accuracies were also possible but slowed down the calculation considerably without any significant change in the result.

The package `Optimization.jl` [167] in the Version 3.19.3 offers a unified interface to formulate optimization problems and integrates various optimization libraries. `SciMLSensitivity.jl`, in the Version 7.51.0 enables rapid derivative calculations through automatic differentiation and serves as a comprehensive ecosystem for scientific machine learning [168]. The LBFGS and Nelder-Mead algorithms are provided in the `Optim.jl` package in the version 1.9.2 [169]. In the case of the parameter estimation procedure the number of grid and intergration points were reduced to $N_\xi = 100$ and $N_{\xi,int} = 100$, due to computational time. In addition, the algorithm for solving the systems of ODEs was chosen automatically by the package `DifferentialEquations.jl`, as `CVODE_BDF` algorithm with the linear `solver=:GMRES` is not compatible with the parameter estimation procedure. It is important to mention that the NaN safemode feature of the `ForwardDiff.jl` package (included in `SciMLSensitivity.jl`) was enabled to prevent the optimization procedure from halting when NaN values arise when the step sizes becomes very small.

Tab. E.5 summarizes all used packages within the programming language Julia including the Version number.

Table E.5.: Used packages in the programming language Julia.

| Package | Version |
|-----------------------|----------|
| CSV | v0.10.13 |
| DataFrames | v1.6.1 |
| DelimitedFiles | v1.9.1 |
| DifferentialEquations | v7.11.0 |
| FastGaussQuadrature | v1.0.2 |
| Interpolations | v0.15.1 |
| NLSolve | v4.5.1 |
| NumericalIntegration | v0.2.0 |
| Optim | v1.9.2 |
| OptimizationOptimJL | v0.1.14 |
| Optimization | v3.19.3 |
| PCHIPInterpolation | v0.2.0 |
| Plots | v1.40.1 |
| Preferences | v1.4.3 |
| Revise | v3.5.14 |
| SciMLSensitivity | v7.51.0 |
| SpecialFunctions | v2.3.1 |
| SpecialPolynomials | v0.4.9 |
| StatsFuns | v1.3.1 |
| Sundials | v4.24.0 |
| XLSX | v0.10.1 |

E.6. Geometric Dimension of STR Used in the Experiments

Table E.6.: Summary of the geometric dimension of the STR used in the experiments.

| Quantity | Value | Unit |
|--------------------------|-------|------|
| Diameter | 300 | mm |
| Height | 940 | mm |
| Baffle plate thickness | 44 | mm |
| Length baffle plate | 838 | mm |
| Length stirrer shaft | 900 | mm |
| Diameter stirrer shaft | 20 | mm |
| Spacing between turbines | 140 | mm |
| Stirrer diameter | 100 | mm |
| Turbine blade height | 20 | mm |
| Turbine blade width | 25 | mm |

E.7. Additional Figures

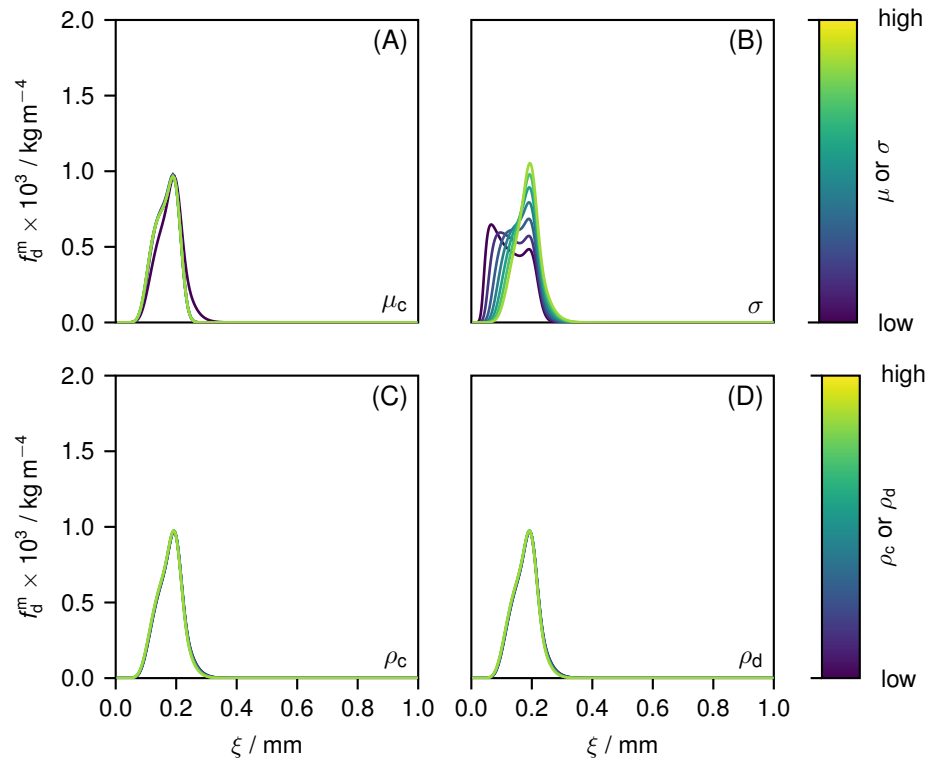


Figure E.4.: Mass density function f_d^m as a function of bubble size ξ for different property data: **(A)** - viscosity of the continuous phase μ_c , **(B)** - surface tension σ , **(C)** - mass density of the continuous phase ρ_c , **(D)** mass density of the dispersed phase ρ_d .

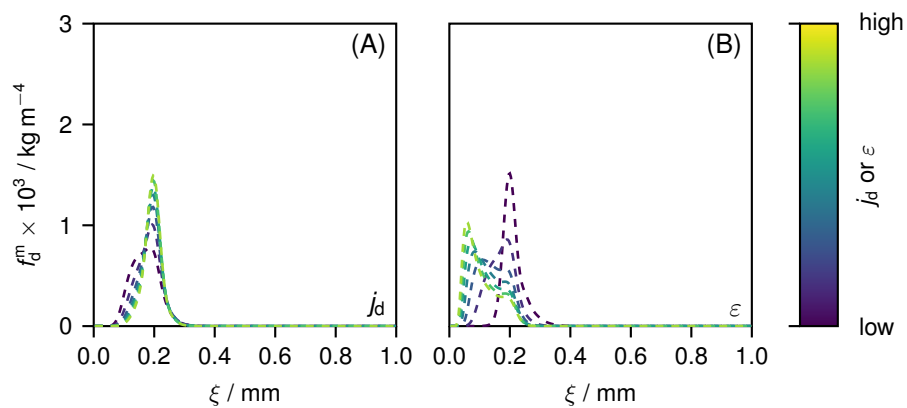


Figure E.5.: Mass density function f_d^m as a function of bubble size ξ for different **(A)** - gas fluxes j_d and **(B)** - energy dissipation rates ϵ for the case with constant gas holdup.

Detailed Contributor Roles Taxonomy

This chapter provides a detailed contributor roles taxonomy according to Allen *et al.* [170] of the publications and manuscripts redrafted in Chapters 2-6 including there Supplementary Information A-E. The remaining chapters were written solely by the author of the dissertation, using elements from aforementioned publications and manuscripts.

Chapter 2: Jet Loop Reactor

Ferdinand Breit: conceptualization; methodology; software; validation; formal analysis; investigation; data curation; writing - original draft; writing - review & editing; visualization

Oliver Bey: conceptualization; validation; writing - review & editing

Erik von Harbou: conceptualization; methodology; software; validation; resources; writing - review & editing; supervision; project administration

Chapter 3: Bubble Column Study I

Ferdinand Breit: conceptualization; data curation; investigation; methodology; software; validation; visualization; writing – original draft; writing – review & editing

Christian Weibel: data curation; formal analysis; investigation; methodology; project administration; validation; writing – review & editing

Erik von Harbou: conceptualization, formal analysis, funding acquisition, investigation; methodology; project administration, resources, supervision, writing – original draft, writing – review & editing

Chapter 4: Bubble Column Study II

Ferdinand Breit: conceptualization; formal analysis; investigation; methodology; project administration; software; validation; visualization; writing - original draft; writing - review & editing

Christina Zipp: data curation; formal analysis; investigation; validation; visualization

Christian Weibel: data curation

Erik von Harbou: funding acquisition; project administration; resources; supervision; writing - review & editing

Chapter 5: Insights Into PBE Modelling

Ferdinand Breit: conceptualization; formal analysis; investigation; methodology; project administration; validation; visualization; writing - original draft; writing - review & editing

Hugo Atle Jakobsen: formal analysis; validation; writing - review & editing

Erik von Harbou: formal analysis; funding acquisition; resources; supervision; validation; writing - review & editing

Chapter 6: Stirred Tank Reactor

Ferdinand Breit: conceptualization; formal analysis; methodology; project administration; software; validation; visualization; writing - original draft; writing - review & editing

Marc Hofmann: data curation; project administration; validation

Eduard Kharik: data curation; formal analysis; investigation; methodology; software; validation

Erik von Harbou: funding acquisition; resources; supervision; writing - review & editing

Publication List

The following scientific works were published by the author of the present dissertation as part of his research.

Journal Articles

- F. Breit, C. Weibel, S. Eberweiser, A. Reihle, and J. Stüber, “chemPhone 2019 – Konzepte zum nachhaltigen Handyrecycling der Zukunft,” *CITplus*, vol. 23, no. 1-2, pp. 16–17, 2020. DOI: 10.1002/citp.202000111.
- F. Breit, A. Mühlbauer, E. von Harbou, M. W. Hlawitschka, and H.-J. Bart, “A one-dimensional combined multifluid-population balance model for the simulation of batch bubble columns,” *Chemical Engineering Research and Design*, vol. 170, pp. 270–289, 2021. DOI: 10.1016/j.cherd.2021.03.036.
- F. Breit, O. Bey, and E. von Harbou, “Model-based investigation of the interaction of gas-consuming reactions and internal circulation flow within jet loop reactors,” *Processes*, vol. 10, no. 7, 2022. DOI: 10.3390/pr10071297.
- F. Breit, C. Weibel, and E. von Harbou, “Application and parameterization of a one-dimensional multifluid population balance model to bubble columns,” *AIChE Journal*, 2024. DOI: 10.1002/aic.18424.
- F. Breit, H. A. Jakobsen, and E. von Harbou, “Formulation of a mass-based population balance equation: Insights into derivation, mass transfer, and nondimensionalization,” *Chemical Engineering Communications*, 2024. DOI: 10.1080/00986445.2024.2445228.

Lectures and Speeches

- F. Breit, E. von Harbou, and O. Bey, Conference Lecture, Topic: “Interaction of Reaction and Internal Fluid Dynamics in Jet Loop Reactors”, Presented at: 13th European Congress of Chemical Engineering and 6th European Congress of Applied Biotechnology (ECCE13/ECAB6), Online, Sep. 21, 2021. DOI: 10.5281/zenodo.7787843.
- F. Breit, C. Weibel, and E. von Harbou, Conference Lecture, Topic: “Application and Parameterization of a 1D Multifluid Population Balance Model for Gas-Liquid Processes”, Presented at: Jahrestreffen der DECHEMA Fachgruppen der Mehrphasenströmung und Partikelmesstechnik, Paderborn, Germany, Mar. 30, 2023. DOI: 10.5281/zenodo.7787742.

- F. Breit, J. Hofinger, C. Weibel, H. Müller, A. Atalay, O. Bey, K. Ehrhardt, and E. von Harbou, Conference Lecture, Topic: “1D MPB Model for reactive gas-liquid flows & applications to industrial scale”, Presented at: Annual Meeting on Reaction Engineering and Electrochemical Processes 2024, Würzburg, Germany, May 6, 2024. DOI: 10.5281/zenodo.11209411.
- C. Weibel, F. Breit, and E. von Harbou, Conference Lecture, Topic: “Insights into Jet Loop Reactors: A 1D Model Approach and Experimental Validation for Enhanced Understanding and Design Optimization”, Presented at: Jahrestreffen der DECHEMA/VDI-Fachgruppen Mehrphasenströmung , Computational Fluid Dynamics und Aerosoltechnik, Bremen, Germany, Mar. 21, 2024. DOI: 10.5281/zenodo.10876923.

Conference Posters

- F. Breit, O. Bey, and E. von Harbou, “Interaction of Reaction and Fluid Dynamics on the Performance of Jet Loop Reactors,” Presented at: Jahrestreffen der ProcessNet-Fachgruppen Fluidverfahrenstechnik und Wärme- und Stoffübertragung, Online, Feb. 24, 2021. DOI: 10.5281/zenodo.7774624.
- F. Breit, A. Mühlbauer, E. von Harbou, M. Hlawitschka, and H.-J. Bart, “A 1D Combined Multifluid-Population Balance Model for the Simulation of Batch Bubble Columns,” Presented at: Jahrestreffen der ProcessNet-Fachgruppen Computational Fluid Dynamics und Mehrphasenströmungen, Online, Sep. 3, 2021. DOI: 10.5281/zenodo.7787785.
- M. Hofmann, F. Breit, E. von Harbou, and H.-J. Bart, “Fluid Dynamic Investigations of a Biotechnological System via a Shadowgraphic Inline Probe,” Presented at: Jahrestreffen der DECHEMA Fachgruppen der Mehrphasenströmung und Partikelmesstechnik, Paderborn, Germany, Mar. 29, 2023. DOI: 10.5281/zenodo.7766428.
- F. Breit, M. Hofmann, and E. von Harbou, “1D PBE Modelling for Mass Transfer in Gas-Liquid Stirred Tank Reactors,” Presented at: Jahrestreffen der DECHEMA/VDI-Fachgruppen Mehrphasenströmung , Computational Fluid Dynamics und Aerosoltechnik, Bremen, Germany, Mar. 21, 2024. DOI: 10.5281/zenodo.10782034.

Data Sets

- M. Koch, T. M. Dang, F. Justen, F. Breit, and E. von Harbou, “Experimental Investigation of the Bubble Size Distribution in a Mini Plant Batch Bubble Column With Variation of Gas Flux, Bubble Column Height and Composition of the Liquid Phase,” *Zenodo*, Nov. 2023. DOI: 10.5281/zenodo.7774678.

Supervised Student Theses

The following student theses were prepared under the supervision of the author of the present dissertation as part of the author's research program.

- M. Koch, "Optimization of the calibration routine of a coupled one-dimensional multifluid population balance model for the description of a water-air batch bubble column," Student Research Project, Laboratory of Reaction and Fluid Process Engineering, RPTU Kaiserslautern, Germany, May 2021.
- S. Ettmüller, "Characterization of electrical resistance tomography systems for industrial applications," Bachelor Thesis, Laboratory of Reaction and Fluid Process Engineering, RPTU Kaiserslautern, Germany, Mar. 2022.
- T. Simon, "Design and initial tests of a laboratory jet loop reactor," Bachelor Thesis, Laboratory of Reaction and Fluid Process Engineering, RPTU Kaiserslautern, Germany, Mar. 2022.
- F. Justen, "Application of an optical probe for the determination of the bubble size distribution as a soft sensor for process monitoring," Bachelor Thesis, Laboratory of Reaction and Fluid Process Engineering, RPTU Kaiserslautern, Germany, Jul. 2022.
- K. Aldabbousi, "Construction and commissioning of a laboratory jet loop reactor," Bachelor Thesis, Laboratory of Reaction and Fluid Process Engineering, RPTU Kaiserslautern, Germany, Aug. 2022.
- N. Kessel, "Investigation of the extrapolability of a coupled one-dimensional multifluid population balance model for the description of bubble columns," Student Research Project, Laboratory of Reaction and Fluid Process Engineering, RPTU Kaiserslautern, Germany, Sep. 2022.
- J. Arweiler, "Sensitivity and parameter study of the population balance equation applied to chemical multiphase reactors," Master Thesis, Laboratory of Reaction and Fluid Process Engineering, RPTU Kaiserslautern, Germany, Sep. 2022.
- P. Mavaddat, "Investigation of the invasivity of the optical multimode online probe to measure the bubble size distribution using computational fluid dynamics," Student Research Project, Laboratory of Reaction and Fluid Process Engineering, RPTU Kaiserslautern, Germany, Nov. 2022.
- M. Usslar, "Investigation of the operating behavior of an ideally mixed gas-liquid stirred tank reactor using population balance modeling," Master Thesis, Laboratory of Reaction and Fluid Process Engineering, RPTU Kaiserslautern, Germany, Dec. 2022.

- P. Schiller, “Erstellung eines kpi-dashboards für die chemische industrie,” Student Research Project, Laboratory of Reaction and Fluid Process Engineering, RPTU Kaiserslautern, Germany, Dec. 2022.
- J. Ludorf, “Investigation of the influence of the optical multimode online probe on two-phase flows using cfd,” Student Research Project, Laboratory of Reaction and Fluid Process Engineering, RPTU Kaiserslautern, Germany, Aug. 2023.
- E. Kharik, “Extension and investigation of a reactive 1D jet loop reactor model,” Student Research Project, Laboratory of Reaction and Fluid Process Engineering, RPTU Kaiserslautern, Germany, Nov. 2023.
- C. Zipp, “Investigation of the scale-up behavior of a 1D multifluid population balance model applied to bubble columns,” Master Thesis, Laboratory of Reaction and Fluid Process Engineering, RPTU Kaiserslautern, Germany, Jan. 2024.
- E. Kharik, “Application and parameter estimation of a 1D population balance model in multiphase stirred tank reactors,” Master Thesis, Laboratory of Reaction and Fluid Process Engineering, RPTU Kaiserslautern, Germany, 2024.
- T. Melchior, “Parameterisation and application of a 1D two-phase model to non-reactive jet loop reactors,” Student Research Project, Laboratory of Reaction and Fluid Process Engineering, RPTU Kaiserslautern, Germany, 2024.
- J. Krewin, “Construction of a test rig for the investigation of needle probes,” Student Research Project, Laboratory of Reaction and Fluid Process Engineering, RPTU Kaiserslautern, Germany, 2024.

Ferdinand Breit

Curriculum Vitae



Work Experience

- 01/2021 - 12/2024 **Scientific Assistant**
Laboratory of Reaction and Fluid Process Engineering
University of Kaiserslautern-Landau, Kaiserslautern, Germany
- 09/2019 – 02/2020 **Intern** as Part of a Research Project
BASF SE, Ludwigshafen am Rhein, Germany
- 04/2018 – 08/2018 **Intern**
KSB SE, Frankenthal, Germany

Education

- 10/2019 – 10/2020 **Technische Universität Kaiserslautern**
Course: Energy and Process Engineering
Degree: Master of Science
- 10/2015 – 10/2019 **Technische Universität Kaiserslautern**
Course: Energy and Process Engineering
Degree: Bachelor of Science